UNIVERSITY OF CALIFORNIA

Santa Barbara

Active Site Mobility Dictates Reactivity of $Rh(CO)_2$ for Ethylene Hydroformylation

A Dissertation submitted in partial satisfaction of the

requirements for the degree Doctor of Philosophy

in Chemical Engineering

by

Gregory Paul Zakem

Committee in charge:

Professor Phillip Christopher, Chair

Professor Brad Chmelka

Professor Mahdi Abu-Omar

Professor Christopher Bates

Professor Lior Sepunaru

March 2023

The dissertation of Gregory Paul Zakem is approved.

_____

Lior Sepunaru

_____

Christopher Bates

_____

Mahdi Abu-Omar

_____

Brad Chmelka

_____

Phillip Christopher, Committee Chair

March 2023

Active Site Mobility Dictates Reactivity of $Rh(CO)_2$ for Ethylene Hydroformylation

by

Gregory Paul Zakem

ACKNOWLEDGEMENTS

I would like to thank my family, most of all my mother and father, for always encouraging me to pursue my interests and supporting my decisions to explore higher education. A special thanks goes to my wife, Taylor, whom has always been my greatest supporter. Her emotional support has been key to my successes, and I would not be here without her. Thank you as well to my dog, Scooby for making sure I get my exercise, and to my unborn child, Lila, for the extra motivation.

I would like to thank my friends from undergrad and my childhood for always being there when I needed to take my mind off work. Thank you to David, James, Andrew, Josh, Sean, and Vlad for being my friends since childhood, my life would be missing something important without you guys. Thank you to Rob, Matt, and Peter for making the time and effort to keep in touch with me after undergrad. A special thanks to Peter for his emotional support.

I would like to thank my advisor Dr. Phillip Christopher for his mentorship, time, knowledge, energy, and most of all, his patience and understanding. I would also like to acknowledge my committee for their time and advice. I would like to acknowledge the support that UCSB has provided, as my work would not have been possible without the assistance of the administrative staff and shared facilities.

I would also like to thank my professors at Villanova University for their mentorship. Specifically, thank you to Dr. Charles Coe and Dr. Justinus Satrio for allowing me the opportunity to perform research in their labs, and their encouragement of my interest in catalysis. Thank you to Dr. Mike Smith and Dr. Rees Rankin for their career guidance, and an extra thank you to Dr. Mike Smith for recommending Dr. Phillip Christopher as an advisor. Thank you to Brendon Shea for his mentorship as he completed his master's degree.

I would like to acknowledge all of my labmates for their help, advice, and support throughout my PhD. I would like to thank Chithra Asokan, Leo DeRita, Insoo Ro, Ji Qi, and Sergei Hanukovich for their mentorship. A special thanks to Insoo Ro specifically, who set the standard of rigor and reproducibility for me. Thank you to all my labmates, past and present for being awesome people in general. You've all contributed to my personal and professional growth, and I wouldn't be the same without all of you.

VITA OF GREGORY PAUL ZAKEM
March 2023

EDUCATION

PhD in Chemical Engineering Expected Winter 2023
University of California Santa Barbara, Santa Barbara CA
Advisor: Dr. Phillip Christopher

B.S. in Chemical Engineering May 2017
Villanova University, Villanova PA

PUBLICATIONS

Ro, I., Qi, J., Lee, S., Xu, M., Yan, X.,Xie, Z., **Zakem, G.**, et al. Bifunctional hydroformylation on heterogeneous Rh-WOx pair site catalysts. *Nature* (2022)

Hoffman, A., Asokan, C., Gadinas, N., Schroeder, E., **Zakem, G.**, Nystrom, S., Getsoian, A., Christopher, P., & Hibbitts, D. Experimental and theoretical characterization of Rh single-atoms supported on γ-Al2O3 with varying hydroxyl content during NO reduction by CO. *ACS Catalysis (2022)*

Zakem, G., Ro, I., Finzel, J. & Christopher, P. Support functionalization as an approach for modifying activation entropies of catalytic reactions on atomically dispersed metal sites. *Journal of Catalysis* (2021).

Zhang, J., Asokan, C., **Zakem, G.**, Christopher, P. & Medlin, J. W. Enhancing sintering resistance of atomically dispersed catalysts in reducing environments with organic monolayers. *Green Energy and Environment* (2021).

Zakem, G., Christopher, P. *Active Site Entropy of Atomically Dispersed Rh/Al_2O_3 Catalysts Dictates Activity for Ethylene Hydroformylation*, Submitted to ACS Catalysis

CONFERENCES/PRESENTATIONS

Gregory Zakem, Insoo Ro, Phillip Christopher. Support Functionalization as an Approach for Modifying Activation Entropies of Catalytic Reactions on Atomically Dispersed Metal Sites. *Presented (Poster) North American Catalysis Society. May 2022*

Gregory Zakem, Phillip Christopher. Support Functionalization as an Approach for Modifying Activation Entropies of Catalytic Reactions on Atomically Dispersed Metal Sites. *Presented (Oral) UCSB Graduate Student Symposium. September 2021*

Gregory Zakem, Insoo Ro, Phillip Christopher. Modifying the Entropy of Adsorbates Bound to Atomically Dispersed Metals by Support Functionalization. *Presented (Oral) AICHE. November 2020*

ABSTRACT

Active Site Mobility Dictates Reactivity of $Rh(CO)_2$ for Ethylene Hydroformylation

by

Gregory Paul Zakem

The design of heterogeneous catalysts typically emphasizes modifications of the electronic state of the active metal to control catalytic reactivity. Changes in the electronic structure of active metals often is correlated with changes in the enthalpies of adsorbed species and enthalpic reaction barriers, but inherent limitations exist on the activity and selectivity of a catalyst that cannot be overcome by these modifications alone. Less often, non-covalent interactions are considered in modifying catalysts. These interactions typically limit the degrees of freedom that reactants, transition states, and products can exhibit, often resulting in modified entropies of adsorbed species and entropic barriers. Even less commonly, the mobility of the active site is relevant to catalytic activity.

Here, we present a system in which atomically dispersed Rh/Al_2O_3 catalysts are modified with straight chain alkylphosphonic acid self-assembled monolayers, such that the mobility of atomically dispersed Rh is altered. Careful kinetic measurements of CO desorption from $Rh(CO)_2$, and ethylene hydroformylation evidence that $Rh(CO)_2$ is mobile on unmodified Rh/Al_2O_3, which results in entropic barriers for reactions that is lowered when the mobility of $Rh(CO)_2$ is decreased by the phosphonic acid self-assembled monolayers. This results in improved activity and selectivity for ethylene hydroformylation with negligible changes to the enthalpic barriers. Further, the extent by which $Rh(CO)_2$ mobility is decreased was modified by changing the length of alkylphosphonic acid tails, in which longer tailed phosphonic acids

formed more rigid self-assembled monolayers due to intermolecular attractions, resulting in lower $Rh(CO)_2$ mobility.

Despite the unique reactivity of atomically dispersed catalysts, the low active metal loadings often results in low catalyst productivity. By modifying existing synthetic protocols, changing support morphology, and using gentle and dispersive pretreatments, the Rh loading was increased by up to 80x (0.25% Rh to 20% Rh) while maintaining atomic dispersion. Additionally, phosphonic acids were used to stabilize atomically dispersed species at elevated pressures and temperatures. Overall, these studies establish the relevancy of active site mobility in atomically dispersed heterogeneous catalysts, methodologies by which to modify active site mobility, and methods to increase the loading and stability of atomically dispersed catalysts.

TABLE OF CONTENTS

LIST OF FIGURES/TABLES

Chapter 1: Introduction

1.1 HETEROGENEOUS CATALYSIS

Catalysts are materials that alter the pathway of a chemical reaction without being consumed itself. These properties allow for small quantities of catalysts to facilitate the conversion of large quantities of reactants. Typically, catalysts are used to improve the rates, selectivities, and operating conditions of a particular reaction.[1] Broadly, catalysts can be divided into heterogeneous and homogeneous catalysts. Homogeneous catalysts exist in the same phase as the reactants/products, such that it must typically be separated from products after the reaction occurs. By contrast, heterogeneous catalysts exist in a different phase than the reactants/products (typically a solid catalyst with a fluid reactant/products). This allows for continual usage of the catalyst without separation, and heterogeneous catalysts generally allow for harsher reaction conditions.[1,2] Heterogeneous catalysts contribute in some way to approximately 35% of the worlds GDP, while over 90% of chemicals produced involve heterogeneous catalysts during at least one step of synthesis.[3] Some notable industrial reactions necessary to modern life include ammonia synthesis for the production of fertilizers,[4,5] olefin polymerization for the production of plastics,[6,7] and hydrogen production via steam reforming.[8,9]

While many types of heterogeneous catalysts exist, supported metals are one of the most common. Supported metals typically consist of a chemically active metal dispersed onto a high surface area, thermally and physically stable support. Oxide supports (such as Al_2O_3, SiO_2, TiO_2, etc.) are commonly used, while the active metal forms metal particles on the support surface. Much of catalytic design involves modifying the active metal composition, structure, or adding dopants to improve the activity and selectivity of the active metal for the

desired chemistry. These modifications are generally covalent in nature, but non-covalent modifications can be exploited as well.

1.2 NON-COVALENT INTERACTIONS IN HETEROGENEOUS CATALYSIS

Typically, modifications to heterogeneous catalysts are motivated by expected changes in the electronic structure of active sites[10–15] These changes in electronic structure typically result in changes in reaction enthalpies for specific elementary steps, which can be correlated with the overall catalytic activity.[16–21] These correlations exhibit linear relationships between adsorption enthalpies of similar species and between the reaction enthalpies and transition state enthalpies (often referred to as Bronsted-Evans-Polanyi (BEP) relations).[22] While these relations are helpful for predicting how changes in catalyst composition may affect reactivity, they also impose inherit limits on the maximum activity and selectivity that a catalyst can exhibit.[23]

These inherent limitations have motivated the study of methodologies to create active sites that deviate from BEP relations. The primary goal of these methods is to decouple reaction enthalpies from transition state enthalpies, such that the maxima defined by BEP relations can be surpassed. Some examples of means to overcome scaling relations include the creation of bifunctional active sites with different scaling relations, [24–26] the use of electronic promoters,[27][28] straining active sites,[27] dynamically modifying active site properties,[29,30] and others.[4]

Less commonly, non-covalent interactions are used to modify the activity of heterogeneous catalysts. These interactions usually present themselves as changes in entropic barriers and can provide an alternative means to improve reactivity than changing the electronic structure. Below we will discuss two different types of heterogeneous catalytic

systems that often exploit these non-covalent interactions: zeolites and self-assembled monolayers (SAMs).

1.2.1 Non-Covalent Interactions in Zeolites

Zeolites are aluminosilicate frameworks made of tetrahedral networks of Si and Al cations surrounded by four O atoms (Figure 1.1).[31] Since each O is shared with other cations, a three-dimensional framework of SiO_2 and AlO_2 units. Since some Si^{4+} cations are substituted with Al^{3+} cations, the network has a net negative charge, additional cations are required to balance the charge. Many zeolites occur naturally with extra-framework Na, K, or Ca cations bound via electrostatic bonds. These extra-framework cations exist in cavities formed by the three dimensional arrangement of the tetrahedral framework (Figure 1.2).[31–35]

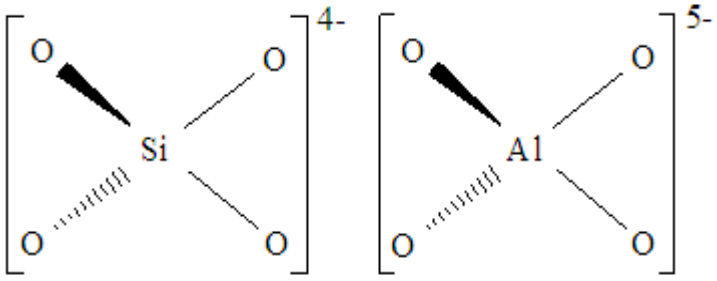

Figure 1.1: Tetrahedral SiO_4 and AlO_4 units that zeolites consist of.[31]

The three-dimensional structures formed from the tetrahedral network result in zeolites being porous materials. The pore structures are often microporous (having pores sizes less than 2nm, a property that lends itself to a variety of applications).[36] In particular, zeolites make excellent molecular sieves, and are applied in chemical sensors, environmental air-quality monitoring, auto-exhaust and effluent control, medical monitoring, and many other applications. An application of particular interest in driving regioselective chemistry is the ability to separate linear hydrocarbons from branched hydrocarbons.[31,37,38] This property, along with the ability to act as a solid-acid, has allowed zeolites to be used since the 1960s in a variety of catalytic applications.[39–42] The effects of Si/Al ratio on the strength and quantity

of acids sites, and the subsequent effects on reactivity, have been heavily studied,[31,43–45] but is outside of the scope of this introduction.

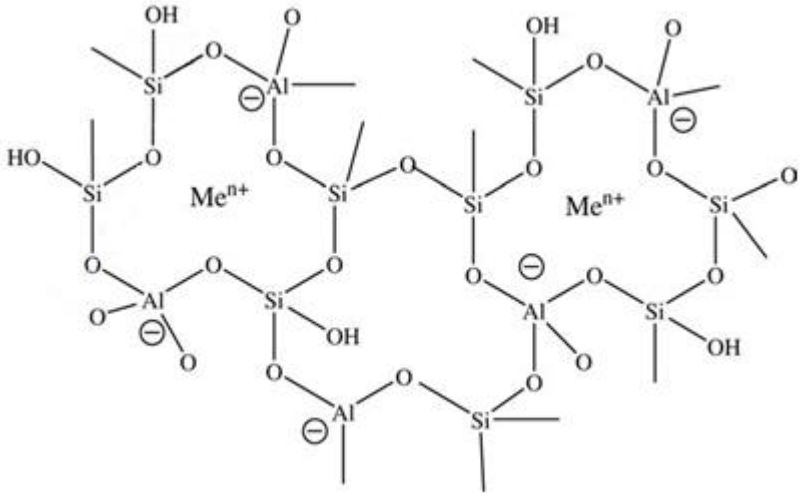

Figure 1.2: An illustration of a zeolite framework. Me^{n+} represents extra-framework cations.[31]

The effect of pore size on product reactivity is relevant to the discussion of regioselectivity in heterogeneous catalysis. Studies have demonstrated that the activation enthalpy and entropy of reaction are modified in narrow pores.[46–48] This results in different rates and chemoselectivities for reactions on zeolites with different pore sizes. Zeolites with larger pores tend to be more active, but with a higher propensity to deactivation, while zeolites with smaller pores tend to exhibit lower overall activities, but with longer lifetimes.[49–51] In addition to the modification of these kinetic parameters, the microporosity of zeolites can also result in a property known as shape or size selectivity.[52,53] Shape selective reaction in zeolites can broadly be categorized into three types: reactant selective, product selective, or transition-state selective.[52–55]

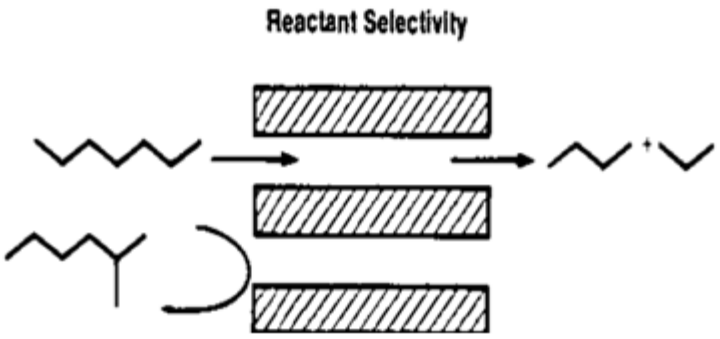

Figure 1.3: An illustration of reactant selectivity in catalytic cracking of alkanes, allowing linear alkanes to react, but excluding branched alkanes.[31]

Reactant selectivity is exhibited in zeolites when the active site is only accessible to reactants of a certain size or shape, such that only those reactants are converted to products. One example of this is the dehydration of butanol, in which n-butanol can enter the zeolite pores and react, while iso-butanol does not react as the branched structure does not allow it to enter the pores. This allows the zeolite to selectively dehydrate n-butanol, resulting in only linear olefin products that can be easily separated from the unreacted iso-butanol. Another example is in the cracking of long chain hydrocarbons, in which linear long-chain paraffins are broken down into smaller products, while aromatic and branched reactants are left unreacted (Figure 1.3).[54]

Product selectivity is exhibited in zeolites when only specific products are capable of diffusing through pores due to their shapes/size relative to the microporous framework. In these processes, products that cannot diffuse through the pores can either react/isomerize at the active site until the product is the correct shape/size to diffuse, or it can accumulate in the pores, ultimately poisoning and deactivating the catalyst. An important application of this is in toluene disproportionation,[56] in which methanol and toluene react to form para, ortho, and meta xylene, which readily isomerize inside of the pores. The ortho and para xylene products diffuse much more slowly out of the catalyst than the para products, resulting in the para

product leaving that catalyst, while the ortho and meta products will remain inside the pores until they isomerize to the para product (Figure 1.4). This leads to a unique feature of this system in which the rate-limiting step is diffusion, rather than any particular kinetic steps.

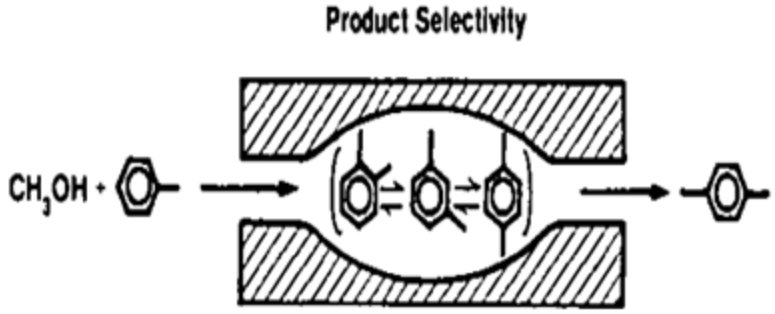

Figure 1.4: An illustration of product selectivity in toluene disproportionation, in which only the para product can diffuse through the pores and ultimately leave the catalyst.[31]

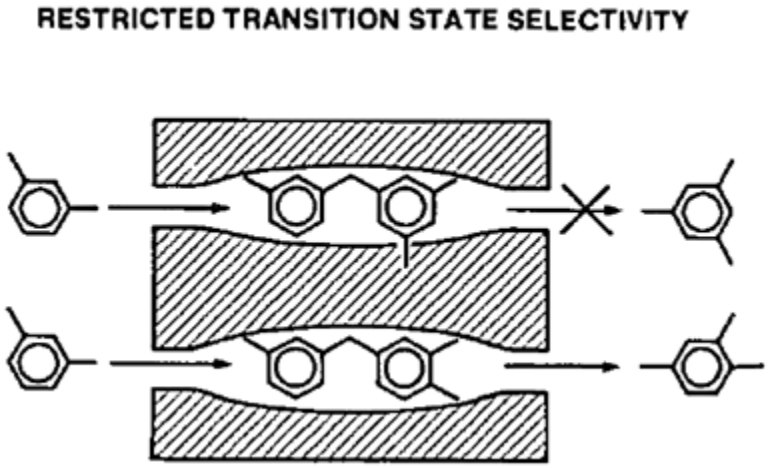

Figure 1.5: An illustration of transition state selectivity, in which certain transition states are more favorable due to confinement.[31]

Transition-state selectivity occurs when the size of the zeolite pores are similar to the size of reaction transition states. This results in the certain transition states or intermediates being less favored due to their size or shape, driving selectivity towards products that form through smaller or more favorably shaped transition states (Figure 1.5). This type of shape-selectivity seems the most promising for altering activities and selectivies at the active site, but it still synthetically difficult to site-selectively introduce metals into zeolites (control where in

the pore the metal sites are) such that only the reactivity towards desired products are enhanced.[47,57–59]

1.2.2 SELF-ASSEMBLED MONOLAYERS IN HETEROGENEOUS CATALYSIS

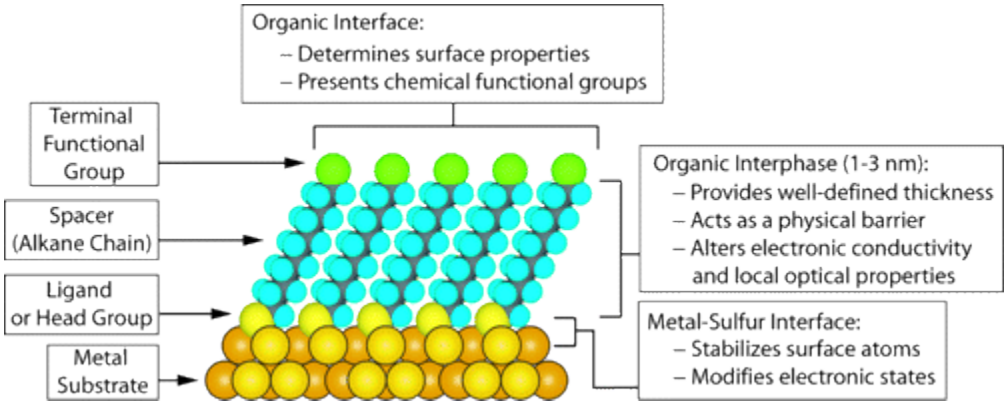

Figure 1.6: An illustration of an ideal alkylthiol SAM on a (111) Au surface.[63]

Under the right conditions, bare metal and metal oxide surfaces readily adsorb organic materials in order to lower surface free energy.[60–63] For surfactant-like molecules, with polar and reactive head groups and less reactive tail groups, self-assembled monolayers

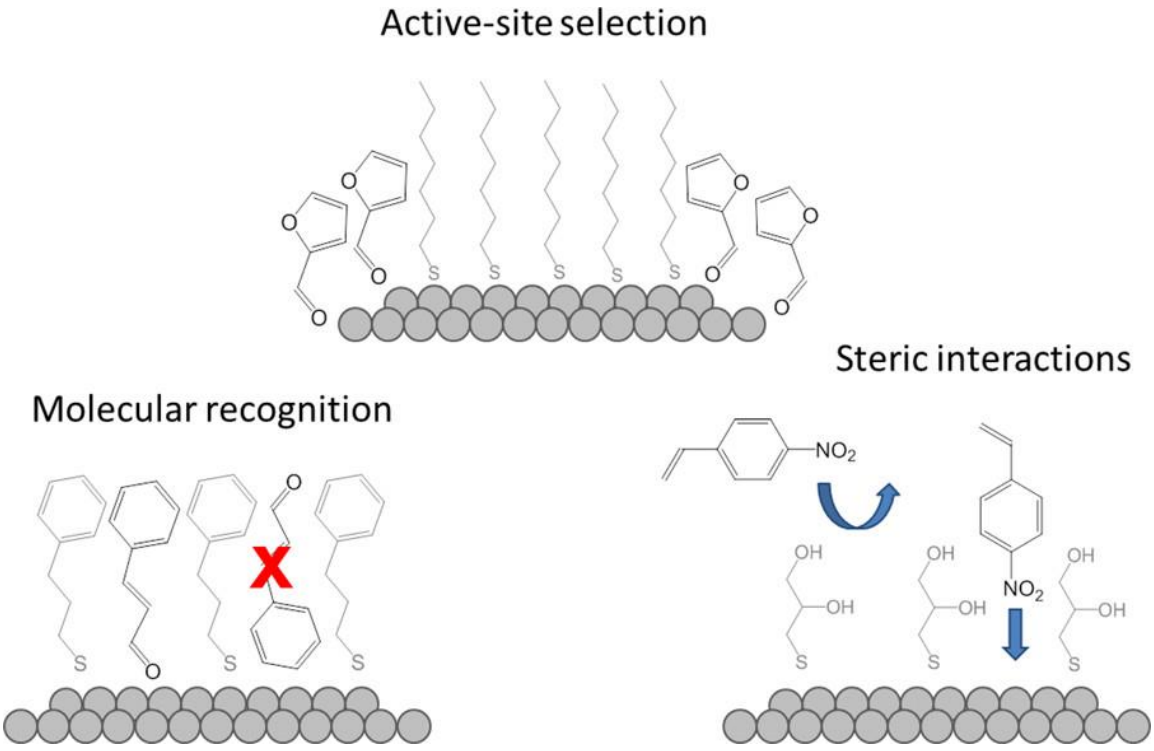

Figure 1.7: Illustration of the three different methodologies identified by Medlin et al. for changing the reactivity of metal nanoparticles using organosulfur SAMs.[60]

(SAMs) can form, in which these molecules adsorb in semicrystalline surface structures. The interfacial properties and stability of the surface can be drastically altered by SAMs, altering the electronic, optical, and physical behavior of a material. The field and study of SAMs began in 1946 when Zisman demonstrated the formation of a monomolecular layer of a surfactant on a metal substrate.[64] Despite this early observation, SAMs did not receive very much attention in literature until the 1980s, in which studies largely focused on the formation of organosulfur SAMs on single-crystal Au or Ag substrates.[65–67] Figure 1.6 depicts an illustration of an organosulfur SAM. While there is an abundance of literature on using SAMs to change the physical, optical, and electronic properties of materials, this section will focus on its use in heterogeneous catalysts.

SAMs are of interest in heterogeneous catalysis as a means to introduce uniform and highly ordered structures that can be reliably studied and systematically modified.[60] To such an end, SAMs on catalytic materials have been studied. In one case, thiol modified palladium was found to improve selectivity in hydrogenation reactions.[68] In this particular case, the enhancement in selectivity was demonstrated to be independent of the tail used, and was instead attributed to the change in the electronic structure of palladium sites adjacent to adsorbed thiols.[69] Medlin et al. have demonstrated several ways that SAMs can be used to modify heterogeneous catalysts. Broadly, they have classified these methodologies into the categories of active-site selection, molecular recognition, and steric interactions (Figure 1.7).

Active site selection described the use of SAMs to selectively block certain sites, while leaving other exposed. Figure 1.7 depicts this as the SAM formation on terrace sites, while leaving edge and step sites exposed. This effect was demonstrated by comparing olefin hydrogenation on a surface functionalized with an octadecyl thiol and a surface functionalized with adamantanethiol (Figure 1.8) The bulkier adamantanethiol groups resulted in greater spacing between thiols. It was demonstrated that ethylene preferentially adsorbed and reacted on edge sites for the more densely packed octadecyl thiol surface but was able to react on terrace sites for the adamantanethiol surface.

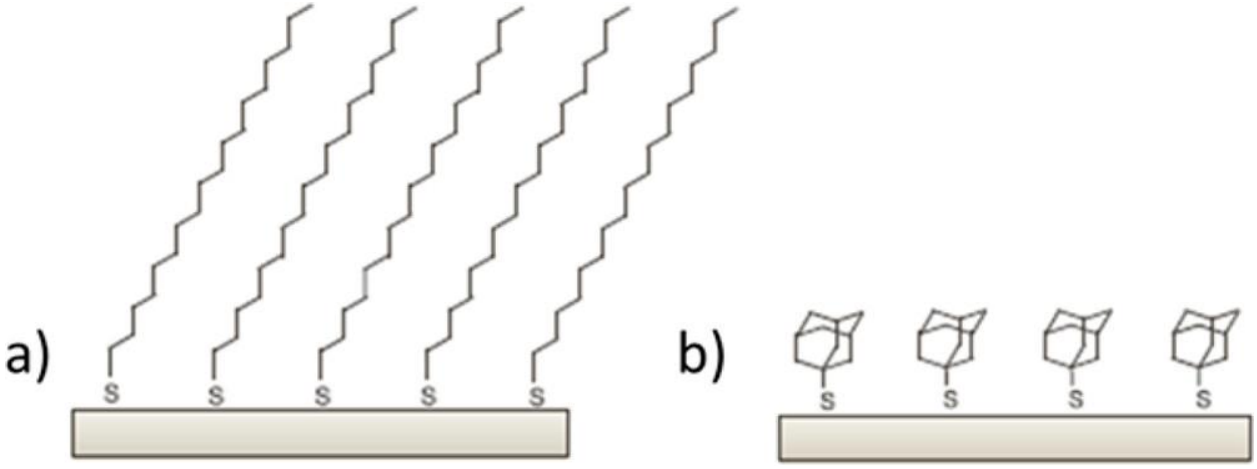

Figure 1.8: Illustration of octadecylthiol and adamantane thiol functionalized surfaces. [60]

Using the information gleamed from ethylene hydrogenation, it was hypothesized that furfural hydrogenation (Figure 1.9), which literature suggests requires a "lying-down" conformation for ring hydrogenation,[70,71] should be more selective for aldehyde hydrogenation on octadecyl thiol functionalized samples than the adamantanethiol functionalized samples. There experiments confirmed these hypotheses, as they observed a decrease in ring hydrogenation, with no loss in aldehyde hydrogenation rates, suggesting that this reaction occurred preferentially on edge sites.[72]

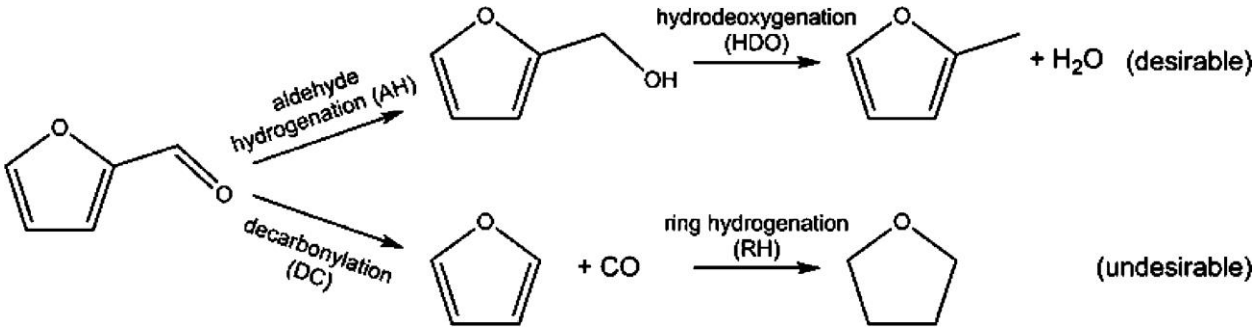

Figure 1.9: Competing pathways for hydrogenation of furfural.[60]

Molecular recognition uses molecular interactions between the SAM molecule and the reactant molecule to enable catalytic selectivity. This technique was demonstrated using the selective hydrogenation of cinnamaldehyde to cinnamyl alcohol (Figure 1.10).[73] To produce cinnamyl alcohol from cinnamaldehyde, the aldehyde must be hydrogenated, without the central olefin being hydrogenated. On unmodified Pt surfaces, the most abundant product is 3-phenyl-1-propanol. Upon modification with alkanethiols, a small increase in selectivity was observed, but this increase was attributed to changes in the electronic structure of Pt, rather than interactions between the reactant and the SAM tail. When phenyl thiols of different lengths were examined, it was found that 3-phenyl-1-propyl thiol exhibited 95% selectivity towards cinnamyl alcohol. This was attributed to π-π stacking between the reactant and the SAM at the correct height such that the reactant adsorbed on the surface vertically, only allowing for hydrogenation of the terminal aldehyde.

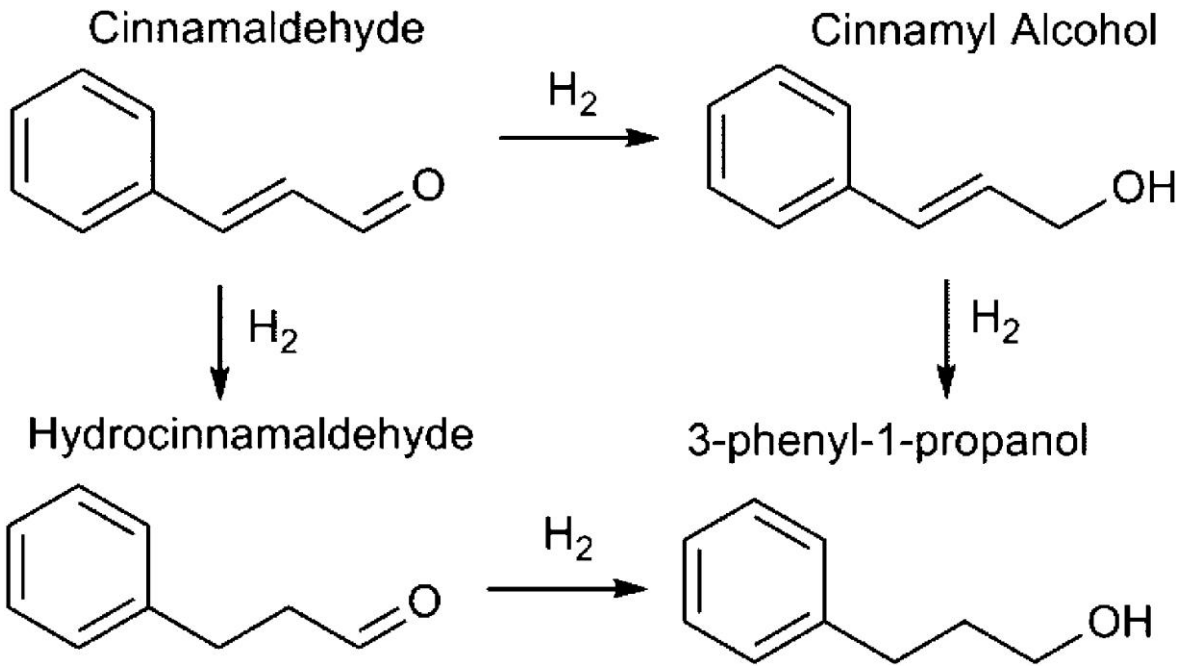

Figure 1.10: Hydrogenation pathways for cinnamaldehyde. The desired product is cinnamyl alcohol.[73]

The previous approaches used SAMs to create relatively well-defined interactions between the reactant or surface in order to modify selectivity. In the case of steric interactions, non-specific interactions are used to exclude certain sizes, conformations, or structures from reaching the catalyst surface (similar to the reactant selectivity in zeolites discussed earlier). These steric interactions were exploited in the hydrogenation of unsaturated fatty acids, a feedstock to produce biodiesel.[74] Fatty acids often occur naturally as polyunsaturated fatty acids, which are hydrogenated before conversion to fuel. Partial hydrogenation to monounsaturated fatty acids is preferable, as fully saturated fatty acids have high melting points, making them unsuitable for application in fuel synthesis. It was found that functionalizing a Pd/Al_2O_3 catalyst with dodecane thiol improve selectivity towards monounsaturated fatty acids. It was argued that the monounsaturated fatty acid is more sterically hindered than the polyunsaturated fatty acid, such that the active site was less accessible to the monounsaturated fatty acids.

There are additional challenges in the use and characterization of SAMs in heterogeneous catalysis. The stability of the SAM is of concern, especially under high temperatures and pressures. In one example, examination of the hydrocarbon stretching region in FTIR suggests that the monolayer degrades over time, evidenced by decreased stretch areas and shifts to higher wavenumbers.[72] This suggests that a portion of the SAM desorbed, and that it became less crystalline. Another issue with SAM functionalized catalysts is a loss in activity due to the blocking of active sites. Many studies have observed a loss in total catalytic activity upon functionalization, but often SAMs suppress undesired pathways, resulting in similar production rates of the desired products. This also makes counting of active sites difficult, as probe molecules used for site counting are often much smaller than reactant molecules, such that available active sites may be fewer than site counting suggests. Finally, characterization of heterogeneous catalysts modified by SAMs is difficult as nanoparticle curvature introduces complexity.[75–77] Most studies of SAMs have been performed on flat, single-crystal Au surfaces using linear alkylthiols, but the dynamic nature of catalytic surfaces make these systems more complex.

Despite extensive study of theses systems, the specific role of SAMs on the entropy of adsorbates has not been well investigated. This is partially due to the heterogeneity in active site environments inherent to supported metals. Careful kinetic studies of a well-defined system may provide additional insights into how SAMs can alter the kinetics of a reaction.

1.2.3 Active Site Mobility

In the previously described cases of non-covalent interactions, the active site is assumed to be stationary on the timescale of individual catalytic turnovers. In some rare cases, active site mobility has been observed to be significant in determining the catalytic

activity.[78,79] One specific case is atomically dispersed Cu in Chabazite zeolites used for reduction of NO_x from diesel engines. In this case, the rate of reaction was dependent on the spatial density of Cu within the zeolite. It was determined that two Cu ions needed to "find" each other for the reaction to occur, such that the mobility of the active site itself was kinetically relevant up to a certain Cu density, at which point the rates no longer changed with Cu density. While these works establish the mobility of active sites can be relevant in heterogeneous catalysis, the specific influence of mobility on entropic barriers has not been investigated.

This example is relevant to the work presented in this thesis, as we will be examining the behavior of atomically dispersed $Rh(CO)_2$ on Al_2O_3, a system in which $Rh(CO)_2$ is believed to be highly mobile,[80–82] such that individual turnovers may occur on a timescale slower than the timescale of $Rh(CO)_2$ mobility. Hydroformylation is used as a probe reaction to examine how restricting this mobility can affect reactivity, so the following section will review this chemistry.

1.3 BACKGROUND OF HYDROFORMYLATION CHEMISTRY

Hydroformylation chemistry was first reported in 1938 by the German scientist Otto Roelen.[83–85] Since then, with a global production of 14 billion kg/yr, hydroformylation reactions have become one of the largest scale reactions that use a homogeneous catalyst.[85–90] The hydroformylation of propylene to produce n-butanal accounts for the majority of hydroformylation production (~50%), ethylene and butene account for approximately ~20%, while C_5+ olefin hydroformylation accounts for the remaining ~30% of hydroformylation processes.[90,91]

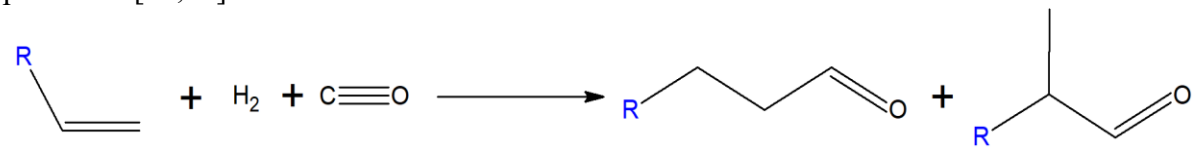

Figure 1.11: Hydroformylation of a terminal olefin leading to the formation of a linear (n) (left) aldehyde and a branched (iso) (right) aldehyde.

Figure 1.12: Hydrogenation of a terminal olefin to an alkane.

Hydroformylation is a CO insertion reaction that transforms olefins into aldehydes in the presence of a catalyst. When CO insertion occurs at a terminal carbon, a linear aldehyde is formed, while CO insertion at a non-terminal carbon results in a branched aldehyde. (Figure 1.11) Olefin hydroformylation competes with olefin hydrogenation to alkanes (Figure 1.12). Alkane formation is the most thermodynamically favorable reaction, followed by branched aldehyde formation, while normal aldehyde formation is the least favorable.[88,92] As such, catalysts for olefin hydroformylation must have electronic structures that result in the chemoselective formation of aldehydes, while also having a steric environment that results in regioselective formation of the desired aldehyde isomer.[93]

Aldehydes are valuable products for use as solvents or as intermediates in the production of alcohols, carboxylic acid, and amines (Figure 1.13).[85] In particular, the highest volume aldehyde product (n-butanal) is mostly used in the manufacturing of 2-ethylhexanol for use in the synthesis of the bis(2-ethylhexyl) phthalate, a plasticizer used in polyvinyl chloride (PVC) pipes.[87,90,91]

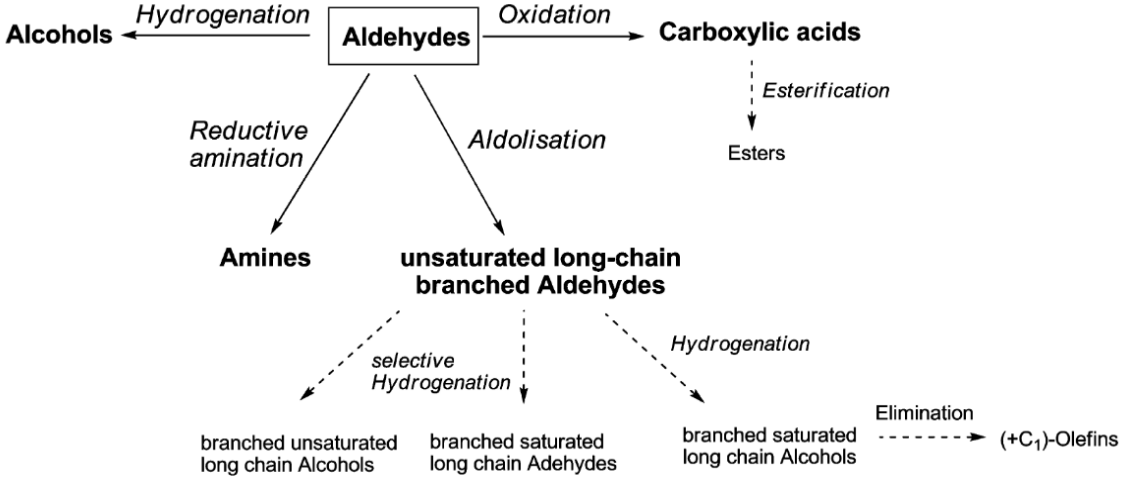

Figure 1.13: Scheme of products derived from aldehydes.[85]

First generation hydroformylation processes (known then as Oxo processes) used Co-based catalysts for higher olefin hydroformylation with production not exceeding 10 million kg/yr.[94] In the second generation of hydroformylation processes, advances in catalyst recovery[95] allowed for the use of $HCo(CO)_4$ as a catalyst at higher temperatures and pressures (up to 190°C and 300 bar), and most new plants were used for propylene hydroformylation. These unmodified Co catalysts exhibited low regioselectivity towards normal aldehydes. Attempts to improve regioselectivity with phosphine ligands resulted in decreased activity and undesired side reactions. Third generation hydroformylation processes operate using a Rh catalyst modified with monodentate P ligands at lower temperatures and pressures (up to 130°C and 60bar). These processes are operated with high excesses of P ligands to stabilize the Rh complex and promote regioselectivity. Rh based processes use

different technologies for the separation of the product and catalysts than Co-based processes due to the high cost of Rh. The price of Rh is much greater than Co and is very volatile (ranging from $475 per ounce to $18,074 per ounce since 2000)[96] while Co prices, are much lower and less volatile (ranging from $0.70 per ounce to $2.66 per oz)[97,98]. As such, Co-based processes are still economical with incomplete recycling of Co, while even small losses in Rh catalyst result in uneconomical processes. To ensure minimal losses, many plants operate under an excess of syngas to strip the volatile products from the reactor, leaving behind the heavier catalysts. Fourth generation hydroformylation plants operate under similar conditions to third generation plants but use sulfonated phosphine ligands to immobilize the catalyst in an aqueous phase[99].

Typical homogeneous hydroformylation catalysts have the general form $HM(CO)_xL_y$ where M is the metal center, and L is an organic ligand. Although many different metals have been surveyed for hydroformylation activity, only Rh and Co have seen industrial use as the activity of unmodified metals for hydroformylation is as follows: Rh>>Co>Ir, Ru>Os> Pt>Pd>>Fe>Ni.[100–104] Rh and Co are the most active due to their ability to promote CO insertion into the olefin (the rate limiting step in the catalytic cycle). Due to its high relative activity, Rh catalysts are used for <10 C olefins, as they can be up to 1000 times more active than Co catalysts.[105,106]. For >10 C olefins, Co catalysts are often used as separation of the catalyst from the product becomes more difficult without exposing the catalyst to harsh separation conditions, resulting in some loss of catalyst.

Unlike with Co catalysts which exhibit a loss in activity upon coordination to ligands, Rh catalysts exhibited improved activity, selectivity, and regioselectivity. In order of effectiveness, these different triphenyl ligands have been investigated: $Ph_3P>>Ph_3N>Ph_3As,Ph_3Sb>Ph_3Bi$.[107–109]. In particular, triphenylphosphine ligands have been found to be highly effective, inexpensive, and widely available. One particular catalyst discovered in the early development of Rh hydroformylation processes is tris(triphenylphosphine) Rh carbonyl hydride.[110] The triphenylphosphine ligands are

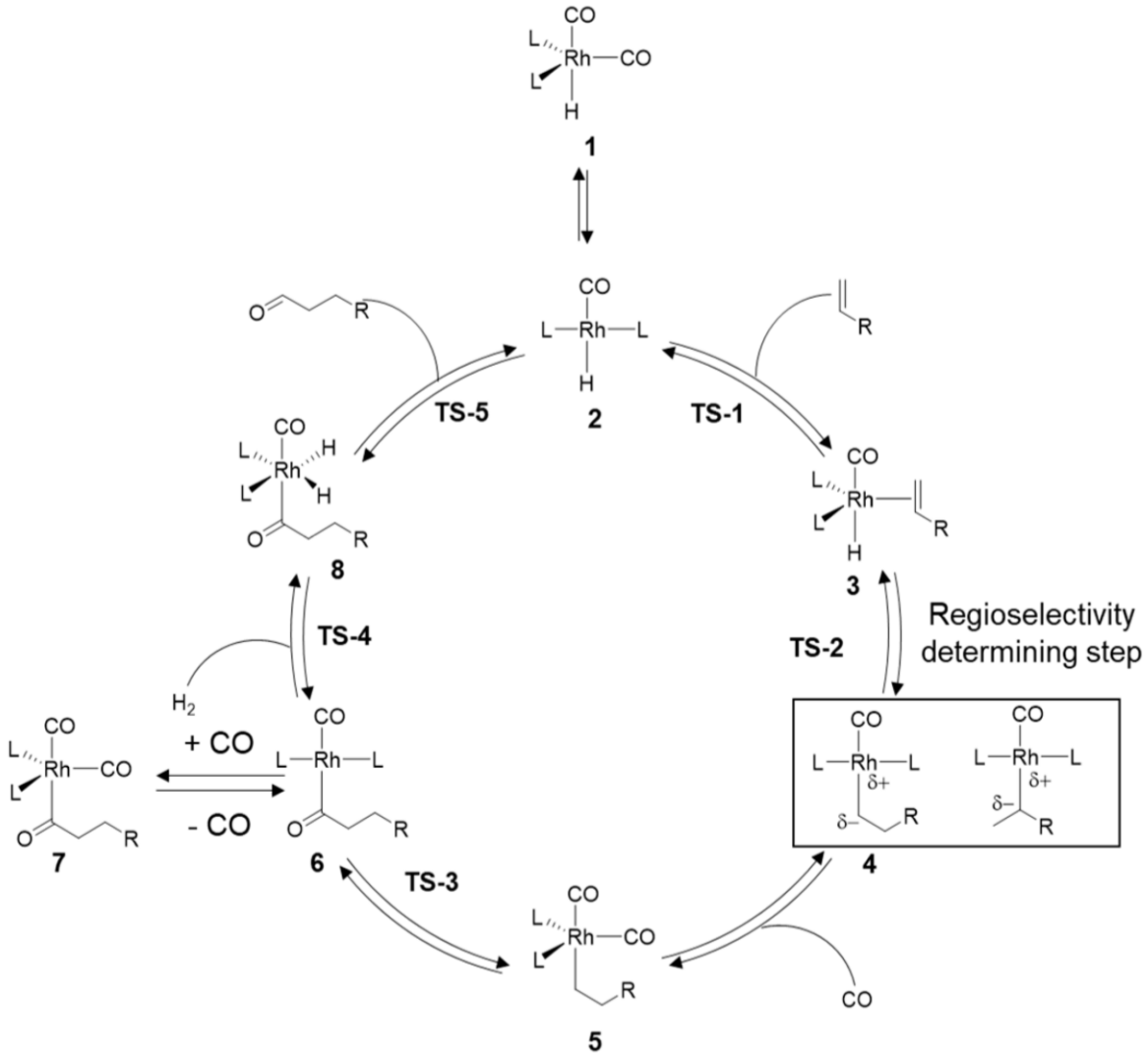

Figure 1.14: Generally accepted mechanism for terminal linear olefin hydroformylation on monodentate ligand modified Rh catalysts.[88]

believed to enhance activity of Rh catalysts by donating σ electrons and sterically promoting desorption of species, promoting turnover. Even this early catalyst exhibited excellent chemoselectivity (near 100%) and sufficient regioselectivity (>95%).

The catalytic mechanism has been extensively studied for this system,[93,111–114] a scheme of which is presented as Figure 1.14.[88] Most studies have focused on the mechanism of Rh catalysts due to the greater performance they exhibit. It is still debated whether the catalytically active species are mono or disubstituted by ligands, but it is widely accepted that a ligand must first be removed to initiate the catalytic cycle (1→2). This opens the metal center for coordination to the olefin (2→3), upon which hydrometallation occurs (3→4) which is often considered the regioselective determining step. The electronic state and the ligand environment of the Rh catalyst both influence the regioselectivity of this step.[93] Followed by coordination to CO (4→5), the rate determining step, CO insertion occurs (5→6). This state can form a dead-end structure (6→7) under sufficient CO partial pressure, but oxidative addition of hydrogen can occur (6→8) to continue the catalytic cycle. Finally, the reductive

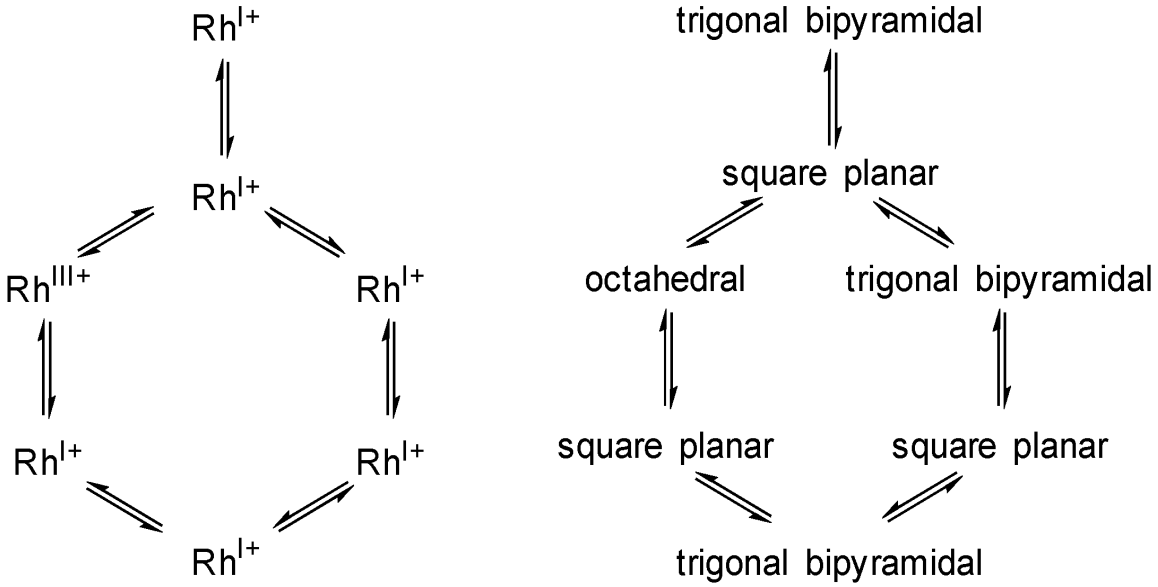

Figure 1.15: Rh oxidation states (left) and molecular geometries (right) throughout the hydroformylation catalytic cycle depicted in Figure 1.14 [88]

elimination of the olefin can occur, completing the catalytic cycle (8→2). The oxidation state and molecular geometry of this complex changes throughout the catalytic cycle (Figure 1.15)[88]

1.4 HETEROGENEOUSLY CATALYZED HYDROFORMYLATION

Despite the continual development and optimization of homogeneous processes for this reaction,[85][93] significant efforts have and are still being made to develop heterogeneous analogues. Given the scale of this reaction, it could be economically advantageous to implement a continuous gas phase process using a heterogeneous catalyst with comparable reactivity to the currently-used homogeneous catalysts.[85,87,115] So far, attempts to make heterogeneous analogues have been unable to exhibit comparable activity, selectivity, regioselectivity, or stability compared to the industrially used homogeneous catalysts. This section will focus on ethylene and propylene hydroformylation specifically, as gas phase continuous processes are not studied for larger substrates, and the chapters presented in this work will focus on ethylene as the substrate of interest.

Heterogeneous hydroformylation catalysts can roughly be categorized into four categories: supported organometallic complexes (immobilized molecular catalysts), supported metal clusters/nanoparticles, supported metal atoms, and metal complexes supported in organic media (Figure 1.16).[88] While there have been hundreds of studies and variations on heterogeneous catalysts for this process, the performance of a select few heterogeneous hydroformylation catalysts that represent a variety of catalyst types and design strategies are presented in Table 1.1. This table includes only gas phase processes, in which less success has been achieved, and that this thesis will focus on.

Table 1.1: Performance of chosen examples of gas phase heterogeneous hydroformylation catalysts.

Catalyst Description	Olefin	Alkane Rate	n-Aldehyde Rate	iso-Aldehyde Rate	Units	Chemoselectivity (%)	Regioselectivity (%)	Conversion	Pressure (atm)	Feed (CO:H2:Olefin)	Temp (°C)	Year	DOI
Carbon-supported Ru-CO Carbonyl Clusters	C_2H_4	1.1E+00	1.3E-01	N/A	TOF (1/min)	5.0	N/A	Near 0	1	1_1_1	172	1971	10.1021/ja00741a050
RhCl(CO)(PPh3)2 immobilized on SiO2	C_2H_4	1.8E-03	4.3E-04	N/A	mol/(hr*g_cat)	19.2	N/A	Near 0	1	1_3_3	130	1978	10.1016/0021-9517(78)90286-5
3.7% Rh_13Y	C_2H_4	7.5E-03	1.4E-03	N.A	mol/(hr*g_cat)	15.7	N/A	Near 0	1	1_3_3	150	1982	10.1016/0021-9517(82)90134-8
LaRhO3	C_2H_4	1.7E-01	5.9E-01	N/A	mol/(hr*g_cat)	78.0	N/A	3% or less	17	1_1_1	150	1987	10.1016/0021-9517(87)90132-1
Fe3Rh2(CO)14C	C_2H_4	2.2E-01	2.2E-01	N/A	mol/(min*mol_Rh)	44.0	N/A	Near 0	1	1_1_1	135	1988	10.1016/S0277-5387(00)86353-6
S-Ni/SiO2	C_2H_4	1.5E+01	9.9E+00	N/A	mol/(kg*hr)	40.3	N/A	Near 0	30	1_1_1	240	1990	10.1007/BF00764006
S-Rh/SIO2	C_2H_4	3.6E+01	1.5E+01	N/A	mol/(kg*hr)	29.3	N/A	Near 0	10	1_1_1	270	1990	10.1016/S0166-9834(00)81619-X
Membrane Supported Rh Complex	C_2H_4	7.9E-03	5.1E-01	N/A	TOF (1/min)	98.5	N/A	10%	1	2_2_3	82	1990	10.1016/0304-5102(90)85145-8
[TMBA]2[Fe2Rh4(CO)16] on SiO2	C_2H_4	4.6E-02	8.8E-02	N/A	mol/(min*mol_Rh)	47.0	N/A	7%	1	1_1_1	135	1990	10.1016/0304-5102(90)85145-8
Rh Dimer on SiO2	C_2H_4	8.8E-04	3.1E-04	N/A	TOF(1/min)	26.1	N/A	Near 0	1	1_1_1	140	1990	10.1039/C39900000253
H2[Ru3(CO)9(CCO)] on MgO	C_2H_4	3.0E-02	1.1E-02	N/A	TOF (1/min)	14.6	N/A	Near 0	1	1_1_1	172	1990	10.1007/BF00764003
Ru/SiO2	C_2H_4	1.7E+00	6.0E-03	N/A	mol/(kg*hr)	0.4	N/A	Near 0	30	1_1_1	240	1991	10.1016/0304-5102(91)80090-P
S-Ru/SiO2	C_2H_4	4.2E-01	1.1E-01	N/A	mol/(kg*hr)	20.8	N/A	Near 0	30	1_1_1	240	1991	10.1016/0304-5102(91)80090-P
Rh-containing aluminum pillared smectite clay	C_2H_4	1.4E-01	1.2E-01	N/A	mol/(hr*g_cat)	43.1	N/A	Near 0	1	1_3_1	125	1992	10.1016/0304-5102(92)80032-C
K2[Rh12(CO)30] on SiO2	C_2H_4	3.2E-01	1.9E-01	N/A	TOF (1/min)	37.0	N/A	Near 0	1	1_1_1	180	1993	10.1016/S0167-2991(08)64296-2
K2[Rh12(CO)30] on Al2O3	C_2H_4	2.6E-01	4.7E-02	N/A	TOF (1/min)	15.0	N/A	Near 0	1	1_1_1	180	1993	10.1016/S0167-2991(08)64296-2
K2[Rh12(CO)30] on MgO	C_2H_4	2.1E-01	4.0E-02	N/A	TOF (1/min)	16.0	N/A	Near 0	1	1_1_1	180	1993	10.1016/S0167-2991(08)64296-2
Rh-B on SiO2	C_2H_4	1.0E+00	2.2E+00	N/A	mol/(hr*g_Rh)	64.7	N/A	Near0	1	1_1_1	125	1993	10.1016/0304-5102(93)87063-E
RhCo3(CO)12 on SiO2	C_2H_4	1.0E-01	2.6E+00	N/A	TOF (1/min)	90.0	N/A	4%	1	1_1_1	110	1994	10.1007/BF00812134
Rh/SiO2	C_2H_4	1.8E-01	2.5E-02	N/A	TOF (1/min)	11.9	N/A	Near 0	1	1_1_1	210	1995	10.1006/jcat.1995.1027
Rh6(CO)16 on SiO2	C_2H_4	3.2E+00	6.6E+00	N/A	TOF (1/min)	68.0	N/A	Near 0	1	1_1_1	150	1995	10.1007/BF00806102
Co2(CO)8 on ZnO	C_2H_4	0.0E+00	1.4E+00	N/A	TOF (1/min)	99.2	N/A	6%	77	1_1_1	160	1995	10.1016/1381-1169(94)00050-6
Rh-Mn/SiO2	C_2H_4	5.8E-01	1.5E-01	N/A	TOF(1/min)	27	N/A	Near 0	1	1_1_1	210	1995	10.1006/jcat.1995.1026
Rh-Co on SiO2	C_2H_4	3.0E+00	4.8E+00	N/A	mol/(min*mol_Rh)	56	N/A	8%	1	1_1_1	150	1998	10.1023/a:1019055517372
Rh on Graphite Nano Fiber	C_2H_4	-	-	N/A	-	50	N/A	30%	1	1_1_1	240	2001	10.1016/S0920-5861(00)00541-1
Ru-Co/SiO2	C_2H_4	1.7E+00	9.9E-01	N/A	mol/(min*mol_Ru)	31	N/A	Near 0	1	1_1_1	150	2001	10.1016/S0926-860X(00)00573-1
RhCl(PPh3)3 Powder	C_2H_4	3.0E-07	5.8E-05	N/A	TOF (1/min)	76	N/A	Near 0	3	1_1_1	185	2004	10.1007/s10562-004-3747-8
Rh on Phosphine Containing Fibercat™	C_2H_4	-	-	N/A	-	96	N/A	20%	5	1_1_1	100	2005	10.1016/j.apcata.2005.02.010
PPh3 Modified Rh/SiO2	C_2H_4	-	-	N/A	-	99.7	N/A	95%	10	1_1_1	100	2005	10.1016/j.apcata.2005.02.010
V-Rh/SiO2	C_2H_4	5.2E+00	1.3E+00	N/A	TOF (1/min)	8	N/A	Near 0	1	1_1_1	115	2005	10.1016/j.catcom.2005.03.008
Polymer Supported Rh-PPh3	C_2H_4	8.0E+00	1.6E+02	N/A	TOF (1/min)	95.4	N/A	89%	10	1_1_1	120	2015	10.1016/j.molcata.2015.05.008
Rh Phosphide on SiO2	C_2H_4	9.5E-01	2.2E+00	N/A	TOF (1/min)	70	N/A	48%	20	5_1_1	210	2017	10.1021/acscatal.7b00499
Rh-ReOx on Al2O3	C_2H_4	1.2E-01	6.0E-02	N/A	TOF (1/min)	3.4E+01	N/A	Near 0	1	1_1_1	150	2019	10.1021/acscatal.9b02111
Rh-Co on SiO2	C_2H_4	1.3E+03	2.1E+01	N/A	TOF (1/hr)	46	N/A	<10%	10	1_1_1	180	2020	10.1021/acs.iecr.0c03437
Carbon-supported Ru-CO Carbonyl Clusters	C_3H_6	5.5E-01	6.2E-03	2.6E-04	TOF (1/min)	1.0	96	Near 0	1	1_1_1	194	1971	10.1021/ja00741a050
RhCl(CO)(PPh3)2 immobilized on SiO2	C_3H_6	9.2E-05	2.8E-05	4.6E-06	mol/(hr*g_cat)	26	86	Near 0	1	1_3_3	130	1978	10.1016/0021-9517(78)90286-5
3.7% Rh_13Y	C_3H_6	2.6E-03	3.7E-03	3.2E-03	mol/(s*g_cat)	39	54	Near 0	1	1_3_3	150	1982	10.1016/0021-9517(82)90134-8
Rh-Na/SiO2 (40% Dispersion)	C_3H_6	3.0E-05	4.9E-06	1.4E-06	TOF (1/s)	16	74	Near 0	1	2_4_1	177	1989	10.1246/cl.1987.941
Membrane Supported Rh Complex	C_3H_6	0.0E+00	4.7E-02	3.1E-03	TOF (1/min)	100	94	1%	1	2_2_3	88	1990	10.1016/0304-5102(90)85145-8
Rh-containing aluminum pillared smectite clay	C_3H_6	1.8E-02	9.1E-03	2.5E-03	mol/(hr*g_cat)	39	78	Near 0	1	1_3_1	125	1992	10.1016/0304-5102(92)80032-C
Rh-B on Alumina-Silica Support	C_3H_6	1.0E-04	2.2E-04	3.2E-05	mol/(hr*g_Rh)	72	87	Near 0	1	1_1_1	120	1993	10.1016/0304-5102(93)85105-3
RhCo3(CO)12 on SiO2	C_3H_6	2.0E-01	3.4E-01	-	TOF (1/min)	26	-	4%	1	1_1_1	110	1994	10.1007/BF00812134
Rh-Co-B on SiO2	C_3H_6	7.0E-05	1.5E-04	-	mol/(hr*g_Rh)	68	100	Near 0	5	1_1_1	130	1996	10.1016/1381-1169(96)00243-9

1.4.1 Supported Organometallic Complexes

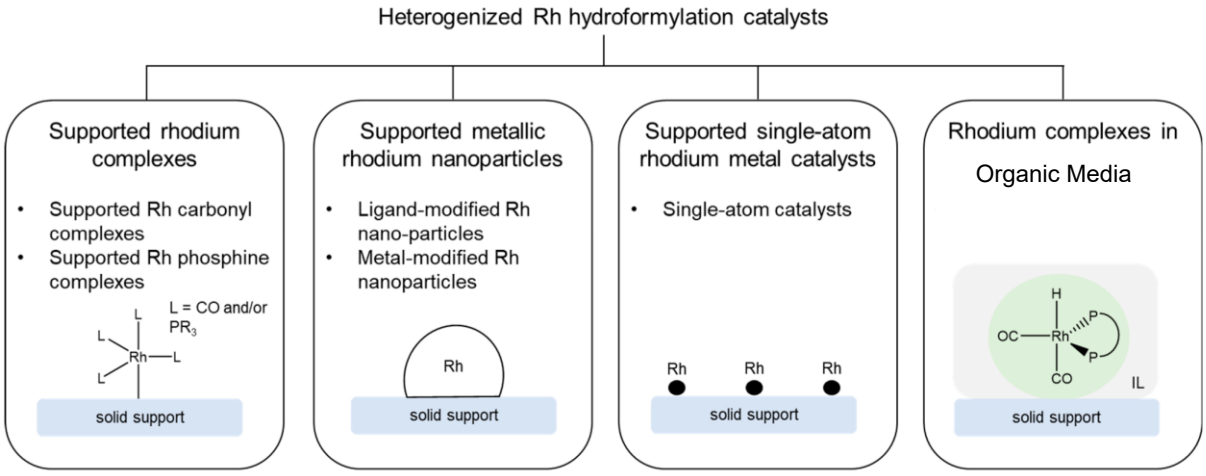

Figure 1.16: Categorizations of different heterogeneous catalysts for hydroformylation. [88]

Early studies into the heterogenization of hydroformylation catalysts used molecular organometallic catalysts immobilized on solid supports.[86,88,115–118] The solid supports in these systems must be highly stable (thermally, chemically, mechanically) and have sufficiently high surface area and a pore structure that minimizes mass transfer limitations. In general, four methods have been explored for the immobilization of molecular complexes (Figure 1.17)[88]: These methodologies include covalent coordination between the molecular catalyst and the support, electrostatic interactions between the molecule and support, physical adsorption of the molecule to the support, and entrapment of the molecule within porous supports.

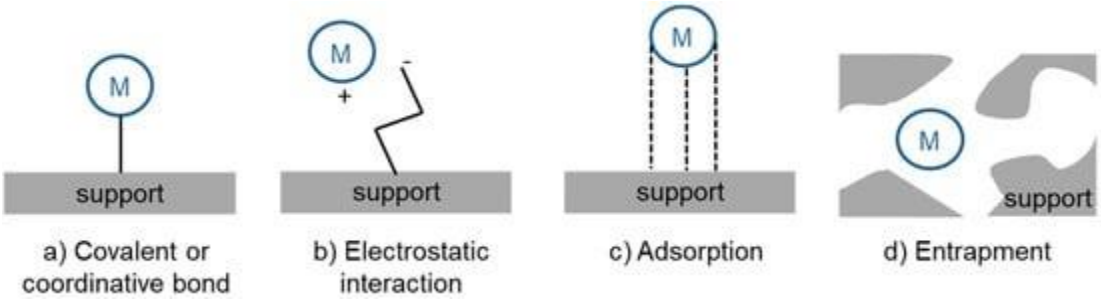

Figure 1.17: Methodologies for immobilizing organometallic complexes on solid supports. [88]

Covalent coordnation has been an attractive methodology as strong support-molecule interactions increase the stability of these materials. The covalent bond may be between the

support and the ligands of the molecular complex, between the support and the metal itself, or both.[115] This kind of immobilization requires special functional groups on the support or ligand, making it synthetically challenging. As such, non-covalent methodologies have also received great attention. One such non-covalent method is entrapment via electrostatic interactions, in which the organometallic complex is ionic, and is attached to cationic or anionic sites of supports such as zeolites, clays, and ion-exchange resins. This methodology tends to result in less stable catalysts, as competition with other ionic species can lead to leaching. Another methodolgy in which instability is an issue is the physical adsorption of the organometallic complex via Van-Der-Waals interactions. This methodology can only be applied in gas phase, low temperature processes to avoid leaching. Finally, entrapment of organometallic complexes in the pores of solid supports has been applied with some success. This methodology requires careful control over the pore size of the solid support, such that the organometallic complex is trapped, while still allowing the reactants and products to enter and leave pores without mass transfer limitations. Ultimately, despite the extensive study of these materials, they generally fail to exhibit comparable activity, selectivity, or stability to homogeneous organometallic complexes.[119–123] While gas phase processes may prevent leaching of the metal complexes, solvent enviroments and the ability to desorb and readsorb ligands have have significant effects on reactivity. This discrepancy between the performance of supported organometallic complexes and organometallic complexes in the liquid phase has been attributed to electronic changes in the metal centers, changes in the coordination of the metal center, and changes in the local concentration of ligands.

1.4.2 Supported Metal Nanoparticles

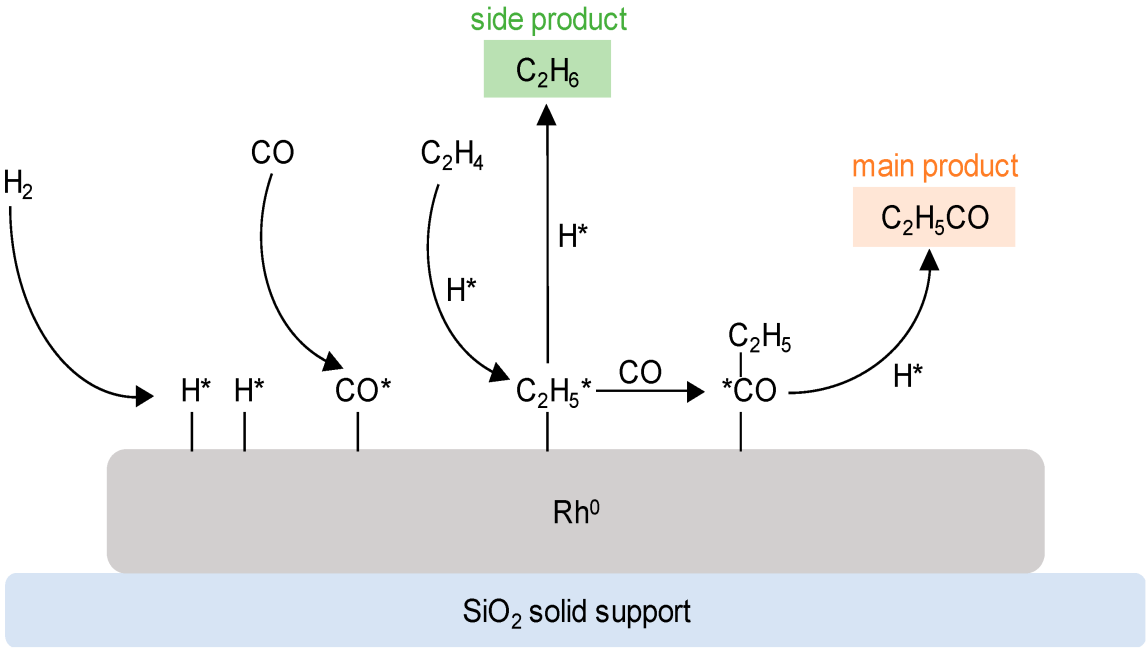

Figure 1.18: Proposed pathways for ethylene hydrogenation and hydroformylation on Rh nanoparticles.[88]

Another methodology for the design of heterogeneous hydroformylation catalysts has been to support metal (usually Rh) nanoparticles or clusters on solid supports (usually SiO_2). Nanoparticles are inherently different than homogeneous catalysts due to the existence of contiguous metal sites (allowing for molecules to adsorb on more than one site at once), resulting in different electronic structures. Additionally, metal sites will exhibit different electronic structures and activities depending on the geometry and coordination of the metal site. These types of catalysts can further be divided into two categories: modified or unmodified. Unmodified Rh/SiO_2 nanoparticle catalysts have been extensively studied.[28,124–130]. These catalysts are usually synthesized via impregnation using metal chloride or nitrate precursors, followed by calcination and reduction. These materials inherently lack uniformity, with well-coordinated sites primarily being Rh^0, and undercoordinated sites having partial positive charges. These sites have significantly different

reactivity, with undercoordinated sites having greater activity for CO insertion reactions. Additionally, vicinal terrace sites allow CO dissociation, olefin dissociation, olefin isomerization, olefin hydrogenation, and aldehyde hydrogenation to occur more facilely than on undercoordinated sites (See Figures 1.18 and 1.19, for proposed ethylene hydroformylation pathways and side reactions).[88,128] This ultimately results in low selectivity and activity for hydroformylation, in addition to creating a multitude of undesired products that aren't normally observed when using mononuclear homogeneous catalysts. Studies of ethylene hydroformylation on different particle sizes or Rh supported on SiO_2 demonstrated that unmodified Rh has the highest CO insertion activity at a Rh particle size of ~2.5nm.[131] Changes in CO insertion activity with decreased particle size were attributed to an increased proportion of under-coordinated sites to well-coordinated sites, while the loss in activity on smaller particle sizes than the optimum was attributed to the formation of dispersed Rh(CO)H species. It should be noted that ethylene hydroformylation is approximately 10x more active than propylene hydroformylation on supported metal nanoparticles.[132,133] This is attributed to more facile adsorption of ethylene than propylene, resulting in propylene adsorption limiting the total reaction rate.

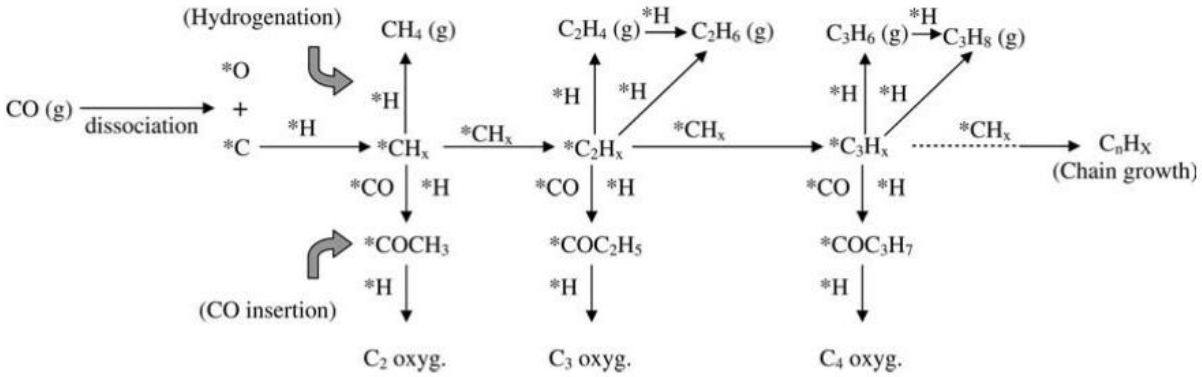

Figure 1.19: Proposed pathways for undesired products from CO dissociation on metal surfaces.[128]

. In response to these phenomena, many nanoparticle catalysts designed for hydroformylation aim to disrupt the continuity of sites, often inducing partial positive charges

on the metallic sites.[28,124,130,134–137] These efforts can be roughly divided into ligand-modified nanoparticles, and promoter modified nanoparticles. Some of the simpler modifications include introducing sulfides to the catalysts to partially poison the surface, introducing chlorides to withdraw electron density from metal sites which promotes CO insertion, and doping Ag onto the metal nanoparticles to disrupt surface continuity with a non-reactive metal. More complex modifications include forming bimetallic clusters, usually of Rh and another metal. Some metals that have been studied include B, Co, Fe, La, Se, and Ru.[119,138–141]. Nearly all of these modifications improved catalytic performance through one mechanism or another, again emphasizing the importance of breaking the continuity of Rh metal surfaces in improving activity and selectivity for hydroformylation reactions. Of particular note, is a K-Rh system in which the authors propose that K on top of Rh blocked active site in such a way that favored terminal adsorption of olefins, increasing regioselectivity.[142] This is unique in that regioselectivity is driven by a structure built by a single element, rather than ligands.

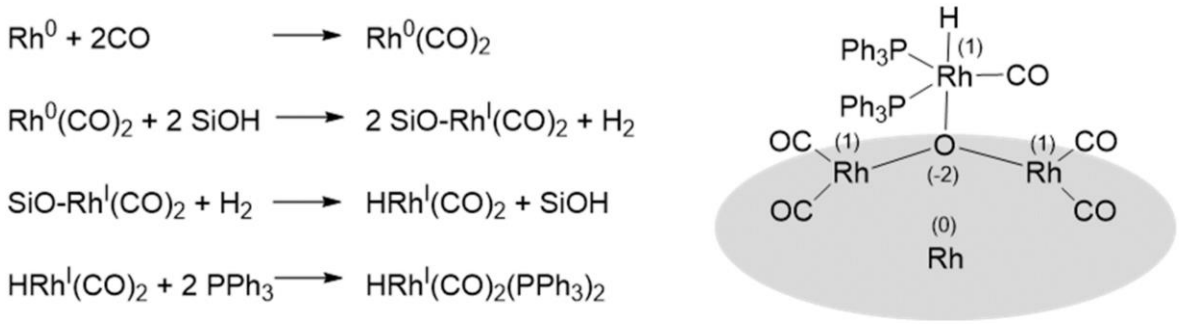

Figure 1.20: Proposed pathway for the in-situ formation of $HRh(CO)_2(PPh_3)_2$ species on Rh/SiO_2 catalysts treated with PPh_3 ligands.[145]

In an attempt to imbue Rh nanoparticles with the steric and electronic properties of the homogeneous catalyst, phosphine ligands have been attached to the nanoparticles by a variety of means.[143–150]. This differs from the supported organometallic complexes in that, at least initially, the Rh exists in a metallic state as part of a nanoparticle. One study treated an existing

Rh/SiO_2 catalyst with a solution containing triphenylphosphine (PPh_3), in which for propylene hydroformylation, the PPh_3-modified catalyst was ~100 times more active than the unmodified catalyst on a per-site basis, but the large portion of inactive Rh makes this catalyst uneconomical for use. This increase in activity was ascribed to the production of $HRh(CO)_2(PPh_3)_2$ on the catalyst surface under reaction conditions (Figure 1.20).[145] The formation of these species was evidenced by NMR, XPS, and FTIR, and was shown to prevent Rh leaching, and to increase catalyst stability with the occasional addition of PPh_3.

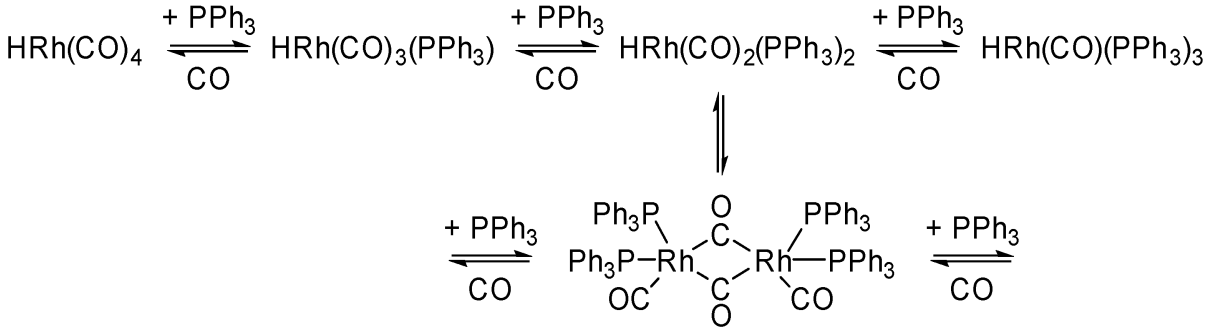

Figure 1.21: Proposed pathways for the formation of surface PPh_3 species on Rh/SiO_2 nanoparticles.[145]

Further studies on ligand dependency sampled triphenylphosphines, phosphites, fluorinated ligands, methoxy triphenylphosphines, and bidentate phosphorous ligands. Ultimately the bidentate phosphorous ligands were found to be approximately twice as active as the PPh_3 ligands for propylene hydroformylation, which was attributed to increase formation of Rh^{1+} species. This system shares the problem that the PPh_3 modified system exhibited, in which too large of a fraction of the Rh is left unused. Various Rh species hypothesized under reaction conditions for ligand modified Rh nanoparticles are presented in Figure 1.21.[145]

An alternative approach to attaching ligands directly to the nanoparticle surface is to attach ligands to the SiO_2 support (referred to from this point on as tethered ligand-modified catalysts). In one such study, tethered ligand modified catalyst were synthesized using either 2-(diphenylphosphino)ethyltriethoxysilane (DPPTS) or diphenylethylphosphine (DPEP),

which were mixed as a slurry with Rh/SiO_2. From NMR and FTIR, it was evidenced that the ligands bond directly to the support, and active Rh species were either attached to the support via Rh-O bonds, or to metal nanoparticles via Rh-Rh bonds (Figure 1.22).[147]

The DPEP modified Rh/SiO_2 catalysts were observed to rapidly deactivate under ethylene hydroformylation reaction conditions. Conversely, the DPPTS modified Rh/SiO_2 catalyst was stable for over 1000 hours. It was later demonstrated that increasing the length of the alkyl spacer between the support and ligand resulted in a significant enhancement of catalytic activity which was attributed to improved ligand flexibility, promoting formation of the active species.[148] Later, Al^{3+} dopants were introduced into the Rh/SiO_2 catalysts, and then modified with DPPTS ligands. A Rh/Al molar ratio of one was observed to exhibit the highest turnover frequencies (TOF), in which the enhancement was attributed to increased electron density at the ligand P bridgeheads, as evidenced by ^{31}P and ^{27}Al NMR.

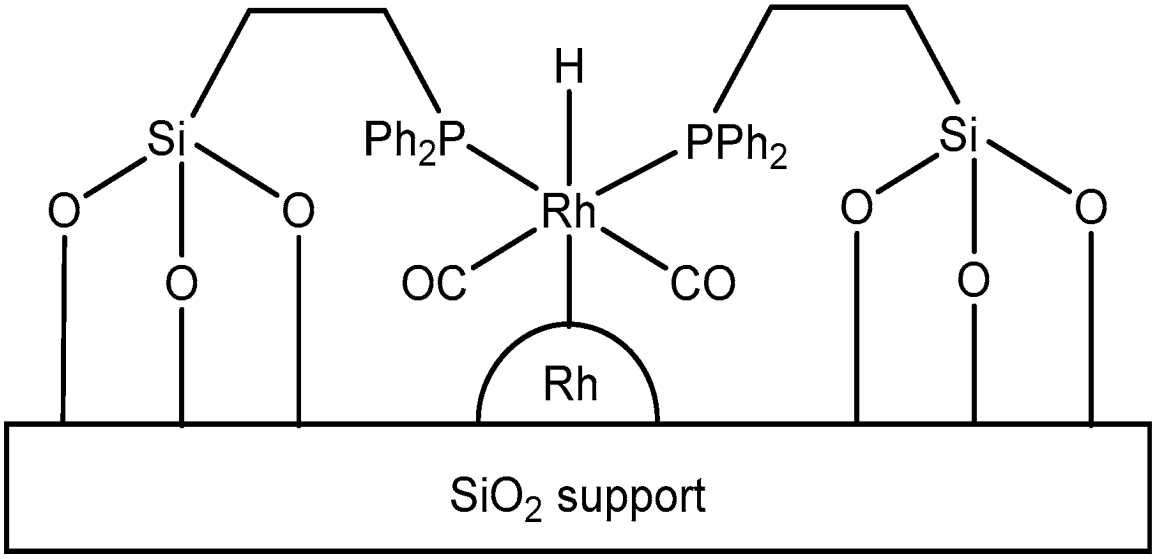

Figure 1.22: Potential structure of tethered ligand modified DPEP Rh/SiO_2 catalysts. [147]

1.4.3 Rh Complexes in Organic Media

Another strategy for heterogenizing hydroformylation catalysts has been to support Rh in organic media. This generally can be divided into Rh supported on polymers[116,118,151–153] (usually phosphorous containing polymers) and organometallic Rh complexes solubilized in ionic liquids (ILs).[145,154–156]

Polymeric materials have been proposed to support Rh in more homogeneous environments, with better control over the steric and electronic environment of the active site. These systems usually present themselves as porous organic networks with Rh atoms or complexes bound to specific functionalities on the polymer.[151] The fine control over the local environment of Rh has allowed for heterogeneous catalysts that can perform asymmetric, enantiomerically selective chemistries. Despite high turnover frequencies, the spatial density of Rh is often low in polymeric systems, making them less competitive for low-value products. As such, the primary interest for these catalysts has been for hydroformylation of larger olefins, to make high-value products.

While there exists some debate on the exact definition of an ionic liquid, generally they can be described as organic salts that exist as liquids at ambient temperatures (below 100°C by some definitions).[157,158] ILs supported on solids are stable under mild conditions, and have been used to solvate organometallic complexes. In such scenarios, they are often called supported ionic liquid phase (SILP) catalysts.[154,155,157–161] These catalysts are categorized separately from other supported organometallic complexes as the organometallic complex is not supported by the solid itself, instead it is a solute in a supported liquid phase (Figure 1.23).[154] The thickness of SILP layers are often less than 10nm to minimize mass transfer limitations, as reactants and products must diffuse in and out of the SILP. For the

hydroformylation of propylene, $Rh(CO)_2(acac)$ in a particular SILP initially exhibited near perfect chemoselectivity to aldehydes, with 87% regioselectivity to n-butanal, and reasonable activity. The SILP also stabilized the formation of undesired aldol condensation products which would occupy catalytic sites and reduce activity over time. While these materials often exhibit high TOFs, low Rh loadings can limit the productivity of reactors when compared to liquid phase processes of the same volume. Despite this, the heterogeneous nature of these catalysts may still make them desirable for processes with expensive separations. The use of organometiallic complexes as active sites can allow researchers to leverage the vast body of literature on homogeneous hydroformylation catalysts to develop highly selective catalysts in heterogeneous systems. Additionally, the choice of ionic liquid can alter reaction rates and selectivities due to interactions between the ILs and the organometallic catalyst complex, analogous to solvent effects.

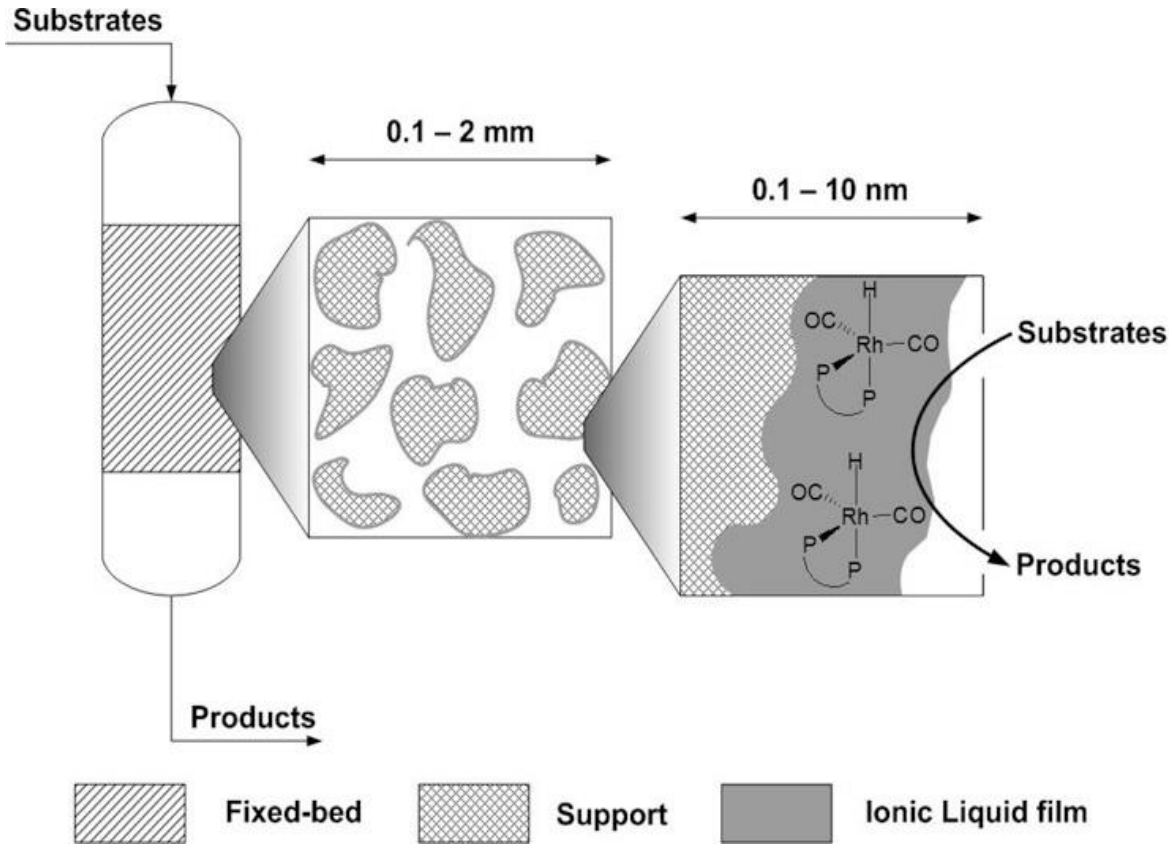

Figure 1.23: Schematic of a fixed-bed reactor using a SILP catalyst.[154]

1.4.4 Supported Metal Atoms

Supported metal atom catalysts (also known as single-atom catalysts or atomically dispersed catalysts) exhibit unique activity and selectivity compared to nanoparticles of the same metal.[162–178] For example, during NO reduction chemistry, atomically dispersed Rh was found to be highly selective towards ammonia, while Rh clusters were selective towards N_2.[178] These materials contain metal atoms coordinated to solid supports, and not to other metal atoms (hence "single-atom"). Unlike supported metal nanoparticles/clusters, these materials typically have 100% atom efficiency (all metal on the catalyst is accessible to adsorbates) which makes them ideal for expensive and rare metals (typically Pt group metals).

Additionally, atomically dispersed metal sites typically have enhanced uniformity relative to the nanoparticles or clusters of the same metal, with heterogeneity typically coming from the support the metal is coordinating to, rather than from local metal-metal coordination as observed for nanoparticles.

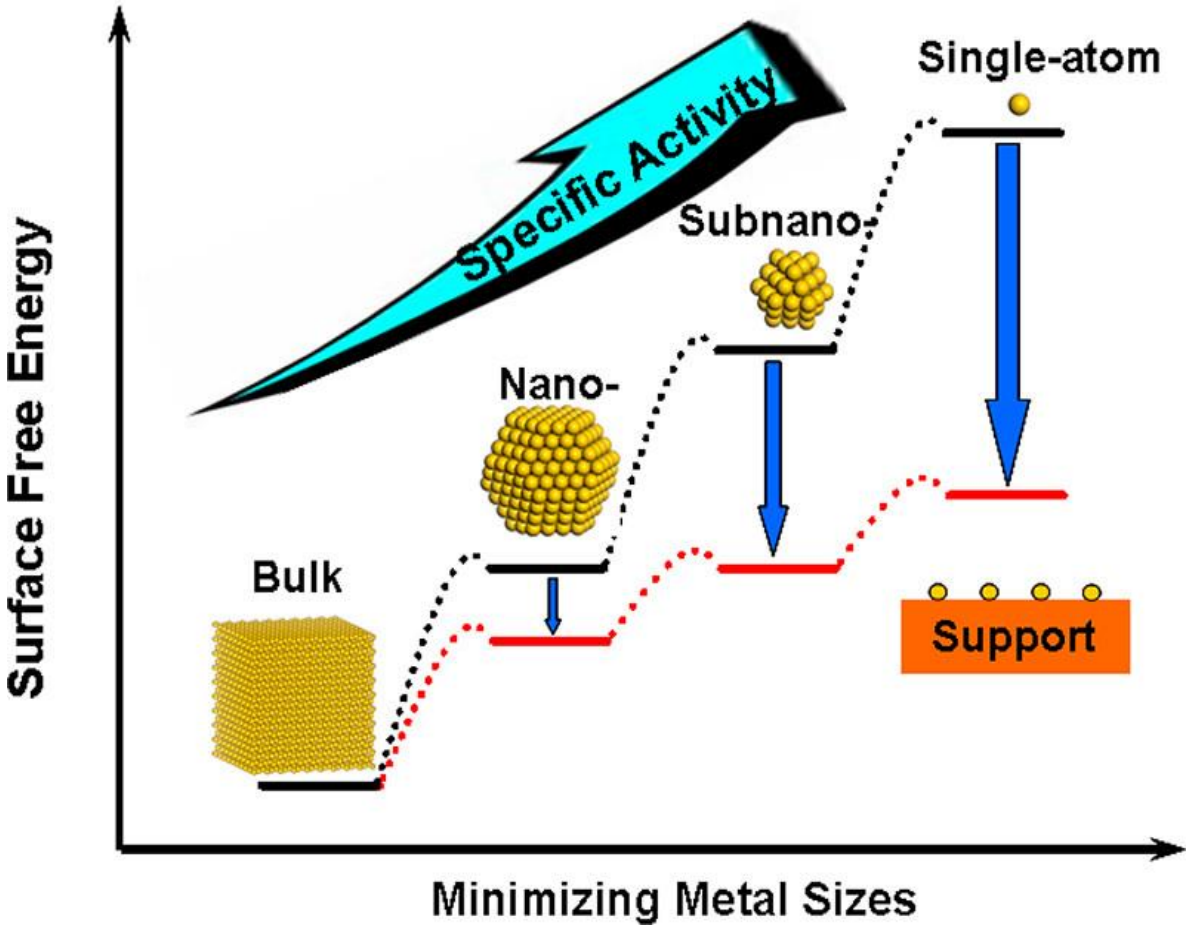

Figure 1.24: Relationship between metal structure size on surface free energy and specific activity.[179]

To some extent, the unique reactivity of these materials can be related to their high surface free energy relative to clusters of the same metals (Figure 1.24).[179] While contributing to the unique reactivity of these materials, the high surface free energy also results in instability, often resulting in sintering/agglomeration, and different strategies have been used to address this. Firstly, most atomically dispersed catalysts use low metal loadings on high surface area supports, reducing the likelihood of any two metal atoms encountering each other.

Another popular strategy is to use reducible or defective supports, such that metal atoms can interact more strongly with the support, lowering its surface free energy and preventing sintering. Unfortunately, metals that coordinate more strongly to the support often are less reactive, leading to a trade-off between activity and stability.[180] Another methodology is to introduce additives to the catalysts (S, N, ReO_x, and WO_x), increasing the stability of metal atoms and altering their electronic properties.[174,181,182]

The increased active site uniformity and ease of separation from products might allow atomically dispersed catalysts to bridge heterogeneous and homogeneous catalytic properties.[170] While supported atomically dispersed metals have not yet achieved parity with homogeneous hydroformylation catalysts,[183] recent works show promise. Several publications have demonstrated nearly 100% selectivity to aldehydes on atomically dispersed Rh catalysts for liquid-phase batch hydroformylation of propylene,[142,168,184] but few exhibit the desired regioselectivity towards n-butanal.[168] Gas phase continuous processes have failed to achieve similar selectivities, and often exhibit lower rates, suggesting that solvent effects may be relevant in this reaction.[185]

Ultimately, these atomically dispersed catalysts are promising for their relatively high stability and ease of synthesis compared to methods using organometallic complexes. The previous examples of atomically dispersed catalysts exploited different supports or promoters to alter the electronic structure of Rh, but few have aimed to exploit non-covalent interactions to alter reactivity. The body of this thesis will focus on atomically dispersed catalysts for ethylene hydroformylation. These catalysts consist of atomically dispersed Rh supported on γ-Al_2O_3, in which the support has been modified with phosphonic acid self-assembled monolayers (SAMs).

1.5 SUMMARY OF CHAPTERS

In Chapter 2, we discuss temperature programmed desorption (TPD), a technique by which the rate of desorption of adsorbed species is measured, from which the kinetics of desorption and energy of adsorption can be extracted. The different orders of desorption, and the starting equations for the analysis of different situations are discussed. Readsorption of desorbed species is noted as a particular problem, and parameters are established to qualify whether readsorption is of concern for a system. Specifically, TPDs in which adsorbed species are monitored via Fourier-Transform Infrared Spectroscopy (FTIR) are described, and arguments are made for why readsorption should not be an issue for TPDs performed this way on the catalysts examined in subsequent chapters.

In Chapter 3, the influence of phosphonic acid (PAs) SAMs formed around atomically dispersed Rh on γ-Al_2O_3 on ethylene hydroformylation (EHF) was examined. Specifically, octylphosphonic acid (OPA) and 1H,1H,2H,2H-Perfluorooctanephosphonic acid (FOPA) were examined. It was observed that the activity and selectivity towards propanal was improved by the presence of PAs, and that improvements are a function of coverage. Differences in the reactivity of OPA and FOPA modified catalysts were negligible, suggested that the electronegativity of the SAM is unimportant to its influence on EHF behavior. TPD experiments using CO as a probe molecule demonstrated decreased temperatures for desorption, which were attributed to statistically significant changes in activation entropies of desorption, with non-significant changes to desorption energetics. This, in combination with Eyring analysis, led us to hypothesize that PA SAMs modify the mobility of $Rh(CO)_2$ (the most abundant surface intermediate for both TPDs and EHF), such that the entropic kinetic barriers for both TPDs and EHF decrease.

In Chapter 4, the influence of PAs is further explored. Specifically, the influence of PA tail length on TPD and EHF behavior is examined. 1, 4, 8, 12, and 16 C linear alkane SAMs were formed on atomically dispersed Rh/γ-Al_2O_3. The desorption behavior and EHF activity both are a strong function of PA tail length, in which the 16 C PA exhibited the highest activity and lowest desorption temperature. Changes in the relative behavior between different length PAs at different temperatures leads us to hypothesize that interactions between PA tails far from $Rh(CO)_2$ dictate the rigidity of the formed SAM. We hypothesize that more rigid SAMs are better able to hinder the mobility of $Rh(CO)_2$, decreasing the entropic barrier for CO desorption and propanal formation via EHF. Calculated activation entropies for CO desorption and propanal formation via EHF were found to be highly correlated, suggesting that the main influence of PAs is the facilitation of CO desorption, a kinetically relevant step in EHF. This study demonstrates a rare situation in heterogeneous catalysis, in which the mobility/entropy of an active site is relevant to the kinetics of catalytic turnovers.

In Chapter 5, methodologies for improving the productivity and stability of atomically dispersed Rh/γ-Al_2O_3 catalysts in EHF was explored. It was found that by using highly porous Al_2O_3 as a support, and carefully controlling synthesis and pretreatment conditions, the loading of Rh was increased from 0.25 % wt/wt to up to 20% wt/wt Rh. Unfortunately, these catalysts were unstable at elevated pressures, resulting in sintering and the formation of undesired products. The stability and activity of these catalysts were promoted by functionalizing the catalysts with PAs. It was observed that catalysts were stable up to 10 bar, allowing for increases in catalyst productivity and improved selectivity.

Finally, in Chapter 6, the role of PAs in improving the catalytic performance of atomically dispersed Rh/γ-Al_2O_3 is summarized. Specifically, that PAs inhibit the mobility of

atomically dispersed $Rh(CO)_2$ supported on γ-Al_2O_3. This results in significant decreases to the activation entropy for CO desorption, increasing catalytic activity for EHF. This technique can also be used to improve the stability of atomically dispersed species, allowing for increased metal loading to improve catalyst productivity. Exploring methodologies by which to combine the benefits of PA functionalization with modifications of Rh electronic structure would be a promising avenue for further improvements in heterogeneous catalysts for EHF.

1.6 REFERENCES

[1] R. Schlögl, Heterogeneous Catalysis, Angew. Chemie Int. Ed. 54 (2015) 3465–3520. https://doi.org/10.1002/ANIE.201410738.

[2] G. Rothenberg, Catalysis : Concepts and Green Applications, 2nd ed., WIley VCH, 2017. https://www.wiley.com/en-sg/Catalysis%3A+Concepts+and+Green+Applications%2C+2nd+Edition-p-9783527343058 (accessed January 27, 2023).

[3] Z. Ma, F. Zaera, Heterogeneous Catalysis by Metals, in: Encycl. Inorg. Chem., John Wiley & Sons, Ltd, Chichester, UK, 2006. https://doi.org/10.1002/0470862106.ia084.

[4] P. Mehta, P. Barboun, F.A. Herrera, J. Kim, P. Rumbach, D.B. Go, J.C. Hicks, W.F. Schneider, Overcoming ammonia synthesis scaling relations with plasma-enabled catalysis, Nat. Catal. (2018). https://doi.org/10.1038/s41929-018-0045-1.

[5] F. Huang, Y. Deng, Y. Chen, X. Cai, M. Peng, Z. Jia, P. Ren, D. Xiao, X. Wen, N. Wang, H. Liu, D. Ma, Atomically Dispersed Pd on Nanodiamond/Graphene Hybrid for Selective Hydrogenation of Acetylene, J. Am. Chem. Soc. 140 (2018) 13142–13146. https://doi.org/10.1021/jacs.8b07476.

[6] M.P. McDaniel, A Review of the Phillips Supported Chromium Catalyst and Its Commercial Use for Ethylene Polymerization, in: Adv. Catal., 2010. https://doi.org/10.1016/S0360-0564(10)53003-7.

[7] V.C. Gibson, S.K. Spitzmesser, Advances in non-metallocene olefin polymerization catalysis, Chem. Rev. 103 (2003) 283–315. https://doi.org/10.1021/CR980461R/ASSET/IMAGES/LARGE/CR980461RF00034.JPEG.

[8] S. Sá, H. Silva, L. Brandão, J.M. Sousa, A. Mendes, Catalysts for methanol steam reforming-A review, Appl. Catal. B Environ. 99 (2010) 43–57. https://doi.org/10.1016/j.apcatb.2010.06.015.

[9] J.P. Van Hook, J.P. Van Hook, Methane-Steam Reforming, Catal. Rev. 21 (1980) 1–51. https://doi.org/10.1080/03602458008068059.

[10] M.A. Barteau, Linear free energy relationships for C1-oxygenate decomposition on transition metal surfaces, Catal. Letters. 8 (1991) 175–183. https://doi.org/10.1007/BF00764114.

[11] R.J. Madix, Reaction Kinetics and Mechanism on Metal Single Crystal Surfaces, Adv. Catal. 29 (1980) 1–53. https://doi.org/10.1016/S0360-0564(08)60119-4.

[12] J.K. Nørskov, T. Bligaard, A. Logadottir, S. Bahn, L.B. Hansen, M. Bollinger, H. Bengaard, B. Hammer, Z. Sljivancanin, M. Mavrikakis, Y. Xu, S. Dahl, C.J.H. Jacobsen, Universality in heterogeneous catalysis, J. Catal. 209 (2002) 275–278. https://doi.org/10.1006/jcat.2002.3615.
[13] F. Abild-Pedersen, J. Greeley, F. Studt, J. Rossmeisl, T.R. Munter, P.G. Moses, E. Skúlason, T. Bligaard, J.K. Nørskov, Scaling properties of adsorption energies for hydrogen-containing molecules on transition-metal surfaces, Phys. Rev. Lett. 99 (2007) 016105. https://doi.org/10.1103/PhysRevLett.99.016105.
[14] J. Hulva, M. Meier, R. Bliem, Z. Jakub, F. Kraushofer, M. Schmid, U. Diebold, C. Franchini, G.S. Parkinson, Unraveling CO adsorption on model single-atom catalysts, Science. 371 (2021) 375–379. https://doi.org/10.1126/science.abe5757.
[15] H. Xu, C.Q. Xu, D. Cheng, J. Li, Identification of activity trends for CO oxidation on supported transition-metal single-atom catalysts, Catal. Sci. Technol. 7 (2017) 5860–5871. https://doi.org/10.1039/c7cy00464h.
[16] T. Bligaard, J.K. Nørskov, S. Dahl, J. Matthiesen, C.H. Christensen, J. Sehested, The Brønsted-Evans-Polanyi relation and the volcano curve in heterogeneous catalysis, J. Catal. 224 (2004) 206–217. https://doi.org/10.1016/j.jcat.2004.02.034.
[17] B. Hammer, J.K. Nørskov, Theoretical surface science and catalysis—calculations and concepts, Adv. Catal. 45 (2000) 71–129. https://doi.org/10.1016/S0360-0564(02)45013-4.
[18] S. Wang, V. Petzold, V. Tripkovic, J. Kleis, J.G. Howalt, E. Skúlason, E.M. Fernández, B. Hvolbæk, G. Jones, A. Toftelund, H. Falsig, M. Björketun, F. Studt, F. Abild-Pedersen, J. Rossmeisl, J.K. Nørskov, T. Bligaard, Universal transition state scaling relations for (de)hydrogenation over transition metals, Phys. Chem. Chem. Phys. 13 (2011) 20760–20765. https://doi.org/10.1039/c1cp20547a.
[19] M. Boudart, Handbook of Heterogeneous Catalysis, Wiley-VCH Verlag, 1997. https://doi.org/10.1002/9783527619474.
[20] M. Boudart, Kinetics of Heterogeneous Catalytic, Princeton University Press, 1984.
[21] and A.A.T. James A. Dumesic, Dale F. Rudd, Luis M. Aparicio, James E. Rekoske, The Microkinetics of Heterogeneous Catalysis, American Chemical Society, 1993.
[22] M. Boudart, Pauling's theory of metals in catalysis, J. Am. Chem. Soc. 72 (1950) 1040. https://doi.org/10.1021/ja01158a522.
[23] B. Hammer, J.K. Norskov, Why gold is the noblest of all the metals, Nature. (1995). https://doi.org/10.1038/376238a0.
[24] M. Andersen, A.J. Medford, J.K. Nørskov, K. Reuter, Scaling-Relation-Based Analysis of Bifunctional Catalysis: The Case for Homogeneous Bimetallic Alloys, ACS Catal. (2017). https://doi.org/10.1021/acscatal.7b00482.
[25] M.T. Darby, M. Stamatakis, A. Michaelides, E.C.H. Sykes, Lonely Atoms with Special Gifts: Breaking Linear Scaling Relationships in Heterogeneous Catalysis with Single-Atom Alloys, J. Phys. Chem. Lett. (2018). https://doi.org/10.1021/acs.jpclett.8b01888.
[26] G. Kumar, E. Nikolla, S. Linic, J.W. Medlin, M.J. Janik, Multicomponent Catalysts: Limitations and Prospects, ACS Catal. 8 (2018) 3202–3208. https://doi.org/10.1021/acscatal.8b00145.
[27] A. Khorshidi, J. Violet, J. Hashemi, A.A. Peterson, How strain can break the scaling relations of catalysis, Nat. Catal. (2018). https://doi.org/10.1038/s41929-018-0054-0.

[28] S.S.C. Chuang, S.I. Pien, Role of silver promoter in carbon monoxide hydrogenation and ethylene hydroformylation over Rh/SiO2 catalysts, J. Catal. (1992). https://doi.org/10.1016/0021-9517(92)90305-2.
[29] J. Qi, J. Resasco, H. Robatjazi, I.B. Alvarez, O. Abdelrahman, P. Dauenhauer, P. Christopher, Dynamic Control of Elementary Step Energetics via Pulsed Illumination Enhances Photocatalysis on Metal Nanoparticles, ACS Energy Lett. 18 (2020) 3518–3525. https://doi.org/10.1021/acsenergylett.0c01978.
[30] M.A. Ardagh, O.A. Abdelrahman, P.J. Dauenhauer, Principles of Dynamic Heterogeneous Catalysis: Surface Resonance and Turnover Frequency Response, ACS Catal. (2019). https://doi.org/10.1021/acscatal.9b01606.
[31] Moshoeshoe Mohau, Misael Silas Nadiye-Tabbiruka, Veronica Obuseng, M. Moshoeshoe, M. Silas Nadiye-Tabbiruka, V. Obuseng, A Review of the Chemistry, Structure, Properties and Applications of Zeolites, Am. J. Mater. Sci. 7 (2017) 196–221. http://article.sapub.org/10.5923.j.materials.20170705.12.html (accessed October 27, 2020).
[32] J.E. Šponer, Z. Sobalík, J. Leszczynski, B. Wichterlová, Effect of metal coordination on the charge distribution over the cation binding sites of zeolites. A combined experimental and theoretical study, J. Phys. Chem. B. 105 (2001) 8285–8290. https://doi.org/10.1021/jp010098j.
[33] N. Widiastuti, H. Wu, H.M. Ang, D. Zhang, Removal of ammonium from greywater using natural zeolite, Desalination. 277 (2011) 15–23. https://doi.org/10.1016/J.DESAL.2011.03.030.
[34] A. Farkaš, M. Rožić, Ž. Barbarić-Mikočević, Ammonium exchange in leakage waters of waste dumps using natural zeolite from the Krapina region, Croatia, J. Hazard. Mater. 117 (2005) 25–33. https://doi.org/10.1016/J.JHAZMAT.2004.05.035.
[35] D.L. Bish, D.W. Ming, Mineralogical Society of America - Natural Zeolites: Occurrence, Properties, Applications, Mineral. Soc. Am. 45 (2001) 654. http://www.minsocam.org/msa/rim/rim45.html (accessed April 22, 2022).
[36] P. Castaldi, L. Santona, S. Enzo, P. Melis, Sorption processes and XRD analysis of a natural zeolite exchanged with Pb(2+), Cd(2+) and Zn(2+) cations, J. Hazard. Mater. 156 (2008) 428–434. https://doi.org/10.1016/J.JHAZMAT.2007.12.040.
[37] M.W. Ackley, S.U. Rege, H. Saxena, Application of natural zeolites in the purification and separation of gases, Microporous Mesoporous Mater. 61 (2003) 25–42. https://doi.org/10.1016/S1387-1811(03)00353-6.
[38] N. Kosinov, J. Gascon, F. Kapteijn, E.J.M. Hensen, Recent developments in zeolite membranes for gas separation, J. Memb. Sci. 499 (2016) 65–79. https://doi.org/10.1016/J.MEMSCI.2015.10.049.
[39] A.M. Cardoso, M.B. Horn, L.S. Ferret, C.M.N. Azevedo, M. Pires, Integrated synthesis of zeolites 4A and Na-P1 using coal fly ash for application in the formulation of detergents and swine wastewater treatment, J. Hazard. Mater. 287 (2015) 69–77. https://doi.org/10.1016/J.JHAZMAT.2015.01.042.
[40] M. Rožić, Š. Cerjan-Stefanović, S. Kurajica, V. Vančina, E. Hodžić, Ammoniacal nitrogen removal from water by treatment with clays and zeolites, Water Res. 34 (2000) 3675–3681. https://doi.org/10.1016/S0043-1354(00)00113-5.
[41] M. Kithome, J.W. Paul, L.M. Lavkulich, A.A. Bomke, Effect of pH on ammonium adsorption by natural Zeolite clinoptilolite,

Http://Dx.Doi.Org/10.1080/00103629909370296. 30 (2008) 1417–1430. https://doi.org/10.1080/00103629909370296.
[42] K. Pavelić, M. Hadžija, L. Bedrica, J. Pavelić, I. Crossed D signikić, M. Katić, M. Kralj, M.H. Bosnar, S. Kapitanović, M. Poljak-Blaži, Š. Križanac, R. Stojković, M. Jurin, B. Subotić, M. Čolić, Natural zeolite clinoptilolite: new adjuvant in anticancer therapy, J. Mol. Med. (Berl). 78 (2001) 708–720. https://doi.org/10.1007/S001090000176.
[43] H. Heinemann, Technological Applications of Zeolites in Catalysis, Https://Doi.Org/10.1080/03602458108068081. 23 (2006) 315–328. https://doi.org/10.1080/03602458108068081.
[44] M.E. Davis, Zeolite-based catalysts for chemicals synthesis, Microporous Mesoporous Mater. 21 (1998) 173–182. https://doi.org/10.1016/S1387-1811(98)00007-9.
[45] W.E. Farneth, R.J. Gorte, Methods for Characterizing Zeolite Acidity, Chem. Rev. 95 (1995) 615–635. https://doi.org/10.1021/cr00035a007.
[46] D.W. Flaherty, E. Iglesia, Transition-state enthalpy and entropy effects on reactivity and selectivity in hydrogenolysis of n -alkanes, J. Am. Chem. Soc. 135 (2013) 18586–18599. https://doi.org/10.1021/ja4093743.
[47] A. Bhan, R. Gounder, J. Macht, E. Iglesia, Entropy considerations in monomolecular cracking of alkanes on acidic zeolites, J. Catal. 253 (2008) 221–224. https://doi.org/10.1016/j.jcat.2007.11.003.
[48] R. Gounder, E. Iglesia, The Roles of Entropy and Enthalpy in Stabilizing Ion-Pairs at Transition States in Zeolite Acid Catalysis, Acc. Chem. Res. 45 (2012) 229–238. https://doi.org/10.1021/ar200138n.
[49] M. Guisnet, P. Magnoux, Coking and deactivation of zeolites: Influence of the Pore Structure, Appl. Catal. 54 (1989) 1–27. https://doi.org/10.1016/S0166-9834(00)82350-7.
[50] E.G. Derouane, Zeolites as solid solvents, J. Mol. Catal. A Chem. 134 (1998) 29–45. https://doi.org/10.1016/S1381-1169(98)00021-1.
[51] X. Zhu, S. Liu, Y. Song, L. Xu, Catalytic cracking of C4 alkenes to propene and ethene: Influences of zeolites pore structures and Si/Al2 ratios, Appl. Catal. A Gen. 288 (2005) 134–142. https://doi.org/10.1016/J.APCATA.2005.04.050.
[52] P. Fenter, P. Eisenberger, J. Li, N. Camillone, S. Bernasek, G. Scoles, T.A. Ramanarayanan, K.S. Liang, Structure of CH3(CH2)17SH Self-Assembled on the Ag(111) Surface: An Incommensurate Monolayer, Langmuir. 7 (1991) 2013–2016. https://doi.org/10.1021/la00058a008.
[53] F.R. Ribeiro, F. Alvarez, C. Henriques, F. Lemos, J.M. Lopes, M.F. Ribeiro, Structure-activity relationship in zeolites, J. Mol. Catal. A. Chem. 96 (1995) 245–270. https://doi.org/10.1016/1381-1169(94)00058-1.
[54] M.L. Poutsma, Zeolite Chemistry and Catalysis, ACS Monogr. 171 (1976) 437.
[55] M. Stöcker, Gas phase catalysis by zeolites, Microporous Mesoporous Mater. 82 (2005) 257–292. https://doi.org/10.1016/J.MICROMESO.2005.01.039.
[56] T. Odedairo, R.J. Balasamy, S. Al-Khattaf, Toluene disproportionation and methylation over zeolites TNU-9, SSZ-33, ZSM-5, and mordenite using different reactor systems, Ind. Eng. Chem. Res. 50 (2011) 3169–3183. https://doi.org/10.1021/ie1018904.
[57] N. Kosinov, C. Liu, E.J.M. Hensen, E.A. Pidko, Engineering of Transition Metal

Catalysts Confined in Zeolites, Chem. Mater. 30 (2018) 3177–3198. https://doi.org/10.1021/acs.chemmater.8b01311.
[58] D. Yang, P. Xu, N.D. Browning, B.C. Gates, Tracking Rh Atoms in Zeolite HY: First Steps of Metal Cluster Formation and Influence of Metal Nuclearity on Catalysis of Ethylene Hydrogenation and Ethylene Dimerization, J. Phys. Chem. Lett. (2016). https://doi.org/10.1021/acs.jpclett.6b01153.
[59] V. Ortalan, A. Uzun, B.C. Gates, N.D. Browning, Direct imaging of single metal atoms and clusters in the pores of dealuminated HY zeolite, Nat. Nanotechnol. (2010). https://doi.org/10.1038/nnano.2010.92.
[60] C.A. Schoenbaum, D.K. Schwartz, J.W. Medlin, Controlling the surface environment of heterogeneous catalysts using self-assembled monolayers, Acc. Chem. Res. 47 (2014) 1438–1445. https://doi.org/10.1021/ar500029y.
[61] A.W. Adamson, A.P. Gast, Physical Chemistry of Surfaces, 6th ed., John Wiley & Sons, Inc., New York, 1997.
[62] A. Ulman, Formation and structure of self-assembled monolayers, Chem. Rev. 96 (1996) 1533–1554. https://doi.org/10.1021/cr9502357.
[63] J.C. Love, L.A. Estroff, J.K. Kriebel, R.G. Nuzzo, G.M. Whitesides, Self-assembled monolayers of thiolates on metals as a form of nanotechnology, Chem. Rev. 105 (2005) 1103–1169. https://doi.org/10.1021/cr0300789.
[64] W.C. Bigelow, D.L. Picket, W.A. Zisman, No Title, J. Colloid Interface Sci. 1 (1946).
[65] P. Fenter, P. Eisenberger, J. Li, N. Camillone, S. Bernasek, G. Scoles, T.A. Ramanarayanan, K.S. Liang, Structure of CH3(CH2)17SH Self-Assembled on the Ag(111) Surface: An Incommensurate Monolayer, Langmuir. 7 (1991) 2013–2016. https://doi.org/10.1021/la00058a008.
[66] M.D. Porter, T.B. Bright, D.L. Allara, C.E. Chidsey, Spontaneously Organized Molecular Assemblies. 4. Structural Characterization of n-Alkyl Thiol Monolayers on Gold by Optical Ellipsometry, Infrared Spectroscopy, and Electrochemistry, J. Am. Chem. Soc. 109 (1987) 3559–3568. https://doi.org/10.1021/ja00246a011.
[67] R.G. Nuzzo, D.L. Allara, Adsorption of Bifunctional Organic Disulfides on Gold Surfaces, J. Am. Chem. Soc. 105 (1983) 4481–4483. https://doi.org/10.1021/ja00351a063.
[68] S.T. Marshall, M. O'Brien, B. Oetter, A. Corpuz, R.M. Richards, D.K. Schwartz, J.W. Medlin, Controlled selectivity for palladium catalysts using self-assembled monolayers, 9 (2010) 853–858. http://www.nature.com/articles/nmat2849 (accessed December 16, 2019).
[69] S.T. Marshall, D.K. Schwartz, J.W. Medlin, Adsorption of oxygenates on alkanethiol-functionalized Pd(111) surfaces: Mechanistic insights into the role of self-assembled monolayers on catalysis, Langmuir. 27 (2011) 6731–6737. https://doi.org/10.1021/la104921p.
[70] S.H. Pang, A.M. Román, J.W. Medlin, Adsorption orientation-induced selectivity control of reactions of benzyl alcohol on pd(111), J. Phys. Chem. C. 116 (2012) 13654–13660. https://doi.org/10.1021/jp303147c.
[71] S.H. Pang, J.W. Medlin, Adsorption and reaction of furfural and furfuryl alcohol on Pd(111): Unique reaction pathways for multifunctional reagents, ACS Catal. 1 (2011) 1272–1283. https://doi.org/10.1021/cs200226h.

[72] S.H. Pang, C.A. Schoenbaum, D.K. Schwartz, J.W. Medlin, Directing reaction pathways by catalyst active-site selection using self-assembled monolayers, Nat. Commun. 4 (2013). https://doi.org/10.1038/NCOMMS3448.
[73] K.R. Kahsar, D.K. Schwartz, J.W. Medlin, Control of metal catalyst selectivity through specific noncovalent molecular interactions, J. Am. Chem. Soc. 136 (2014) 520–526. https://doi.org/10.1021/ja411973p.
[74] B.R. Moser, M.J. Haas, J.K. Winkler, M.A. Jackson, S.Z. Erhan, G.R. List, Evaluation of partially hydrogenated methyl esters of soybean oil as biodiesel, Eur. J. Lipid Sci. Technol. 109 (2007) 17–24. https://doi.org/10.1002/EJLT.200600215.
[75] G. Corthey, A.A. Rubert, A.L. Picone, G. Casillas, L.J. Giovanetti, J.M. Ramallo-López, E. Zelaya, G.A. Benitez, F.G. Requejo, M. José-Yacamán, R.C. Salvarezza, M.H. Fonticelli, New insights into the chemistry of thiolate-protected palladium nanoparticles, J. Phys. Chem. C. 116 (2012) 9830–9837. https://doi.org/10.1021/jp301531n.
[76] Y.B. Zheng, J.L. Payton, T. Bin Song, B.K. Pathem, Y. Zhao, H. Ma, Y. Yang, L. Jensen, A.K.Y. Jen, P.S. Weiss, Surface-enhanced Raman spectroscopy to probe photoreaction pathways and kinetics of isolated reactants on surfaces: Flat versus curved substrates, Nano Lett. 12 (2012) 5362–5368. https://doi.org/10.1021/nl302750d.
[77] A. Jiménez, A. Sarsa, M. Blázquez, T. Pineda, A molecular dynamics study of the surfactant surface density of alkanethiol self-assembled monolayers on gold nanoparticles as a function of the radius, J. Phys. Chem. C. 114 (2010) 21309–21314. https://doi.org/10.1021/jp1088977.
[78] C. Paolucci, I. Khurana, A.A. Parekh, S. Li, A.J. Shih, H. Li, J.R. Di Iorio, J.D. Albarracin-Caballero, A. Yezerets, J.T. Miller, W.N. Delgass, F.H. Ribeiro, W.F. Schneider, R. Gounder, Dynamic multinuclear sites formed by mobilized copper ions in NOx selective catalytic reduction, Science. 357 (2017) 898–903. https://doi.org/10.1126/science.aan5630.
[79] S.H. Krishna, C.B. Jones, R. Gounder, Temperature dependence of Cu(I) oxidation and Cu(II) reduction kinetics in the selective catalytic reduction of NOx with NH3 on Cu-chabazite zeolites, J. Catal. 404 (2021) 873–882. https://doi.org/10.1016/J.JCAT.2021.08.042.
[80] A. Suzuki, Y. Inada, A. Yamaguchi, T. Chihara, M. Yuasa, M. Nomura, Y. Iwasawa, Time Scale and Elementary Steps of CO-Induced Disintegration of Surface Rhodium Clusters, Angew. Chemie - Int. Ed. 115 (2003) 4943–4947. https://doi.org/10.1002/anie.200352318.
[81] E.K. Schroeder, J. Finzel, P. Christopher, Photolysis of Atomically Dispersed Rh/Al2O3 Catalysts: Controlling CO Coverage in Situ and Promoting Reaction Rates, J. Phys. Chem. C. (2022). https://doi.org/10.1021/ACS.JPCC.2C04642.
[82] B.R. Goldsmith, E.D. Sanderson, R. Ouyang, W.X. Li, CO- and NO-induced disintegration and redispersion of three-way catalysts rhodium, palladium, and platinum: An ab initio thermodynamics study, J. Phys. Chem. C. (2014). https://doi.org/10.1021/jp502201f.
[83] O. Roelen, German Patent DE 849,548, 1938/1952, 1944. https://patents.google.com/patent/DE849548C/es (accessed April 19, 2022).
[84] H. Adkins, G. Kresk, Catalytic Dehydrogenation of Hydroaromatic Compounds in

Benzene, J. Am. Chem. Soc. 71 (1949).
[85] R. Franke, D. Selent, A. Börner, Applied hydroformylation, 2012.
[86] M. Lenarda, L. Storaro, R. Ganzerla, Hydroformylation of simple olefins catalyzed by metals and clusters supported on unfunctionalized inorganic carriers, Elsevier, 1996. https://doi.org/10.1016/1381-1169(96)00211-7.
[87] G.G. Stanley, Hydroformylation (OXO) Catalysis, in: Kirk-Othmer Encycl. Chem. Technol., John Wiley & Sons, Inc., Hoboken, NJ, USA, 2017: pp. 1–19. https://doi.org/10.1002/0471238961.1524150209121.a01.pub2.
[88] S. Hanf, L.A. Rupflin, R. Gläser, S.A. Schunk, L. Alvarado Rupflin, R. Gläser, S.A. Schunk, L.A. Rupflin, R. Gläser, S.A. Schunk, Current State of the Art of the Solid Rh-Based Catalyzed Hydroformylation of Short-Chain Olefins, 10 (2020) 510. https://doi.org/10.3390/catal10050510.
[89] H. Bahrmann, H. Bach, G.D. Frey, Oxo Synthesis, Ullmann's Encycl. Ind. Chem. (2009) 1–8. https://doi.org/10.1002/14356007.a18_321.pub2.
[90] R. Tudor, M. Ashley, Enhancement of industrial hydroformylation processes by the adoption of rhodium-based catalyst: Part II, Platin. Met. Rev. 51 (2007) 164–171. https://doi.org/10.1595/147106707X238211.
[91] F.J. Smith, NEW TECHNOLOGY FOR INDUSTRIAL HYDROFORMYLATION., Platin. Met. Rev. 19 (1975) 93–95. https://www.ingentaconnect.com/content/matthey/pmr/1975/00000019/00000003/art00004 (accessed July 17, 2019).
[92] J.B. Conn, G. Kistiakowsky, § Smith, E.A. Turner, R.B. Meador, W.R. Winkler, R.E. Turner, R.B. Skinner, H.A. Snelson, A. Rogers, D.W. Dejroongruang, K. Roth, W.R. Lennartz, H.W. Wiberg, K.B. Wasserman, D.J. Wiberg, K.B. Squires, R.R. Wiberg, K.B. Cunningham, W.C. Jr, K.B. Wiberg, R.R. Squires, E.J. Martin, Thermochemical Studies of Carbonyl Compounds. 5. Enthalpies of Reduction of Carbonyl Groups, Trans. Faraday Soc. 113 (1991) 487. https://pubs.acs.org/sharingguidelines (accessed April 20, 2022).
[93] Y. Jiao, M.S. Torne, J. Gracia, J.W. Niemantsverdriet, P.W.N.M. Van Leeuwen, Ligand effects in rhodium-catalyzed hydroformylation with bisphosphines: steric or electronic?, Catal. Sci. Technol. 7 (2017) 1404–1414. https://doi.org/10.1039/C6CY01990K.
[94] H.W. Bohnen, B. Cornils, Hydroformylation of alkenes: An industrial view of the status and importance, Adv. Catal. 47 (2002) 1–64. https://doi.org/10.1016/S0360-0564(02)47005-8.
[95] J. Falbe, New Syntheses with Carbon Monoxide, Springer Berlin Heidelberg, Berlin, Heidelberg, 1980. https://doi.org/10.1007/978-3-642-67452-5.
[96] London Fix Historical rhodium - result, (n.d.). https://www.kitco.com/scripts/hist_charts/yearly_graphs.plx?rd72-79=on&rd80-89=on&rd90-99=on&rd00-09=on&submitrdB=View+Charts+and+Data (accessed April 21, 2022).
[97] Cobalt Price 2022 [Updated Daily] - Metalary, (n.d.). https://www.metalary.com/cobalt-price/ (accessed April 21, 2022).
[98] Statista, Cobalt - 2022 Data - 2010-2021 Historical - 2023 Forecast - Price - Quote - Chart, Trading Econ. (2022). https://www.kitco.com/scripts/hist_charts/yearly_graphs.plx?rd72-79=on&rd80-

89=on&rd90-99=on&rd00-09=on&submitrdB=View+Charts+and+Data (accessed April 21, 2022).
[99] D.J. Cole-Hamilton, R.P. Tooze, eds., Catalyst Separation, Recovery and Recycling, Springer Netherlands, Dordrecht, 2006. https://doi.org/10.1007/1-4020-4087-3.
[100] F.P. Pruchnik, S.A. Duraj, Organometallic Chemistry of the Transition Elements, Organomet. Chem. Transit. Elem. (1990). https://doi.org/10.1007/978-1-4899-2076-8.
[101] C. Li, L. Chen, M. Garland, Synchronicity of mononuclear and dinuclear events in homogeneous catalysis. Hydroformylation of cyclopentene using Rh 4(CO) 12 and HRe(CO) 5 as precursors, J. Am. Chem. Soc. 129 (2007) 13327–13334. https://doi.org/10.1021/ja073339v.
[102] T. Senthamarai, K. Murugesan, J. Schneidewind, N. V. Kalevaru, W. Baumann, H. Neumann, P.C.J. Kamer, M. Beller, R. V. Jagadeesh, Simple ruthenium-catalyzed reductive amination enables the synthesis of a broad range of primary amines, Nat. Commun. 2018 91. 9 (2018) 1–12. https://doi.org/10.1038/s41467-018-06416-6.
[103] S. Priyarega, M.M. Tamizh, R. Karvembu, R. Prabhakaran, K. Natarajan, Synthesis, spectroscopic characterization and catalytic oxidation properties of ONO/ONS donor Schiff base ruthenium(III) complexes containing PPh3/AsPh3, J. Chem. Sci. 2011 1233. 123 (2011) 319–325. https://doi.org/10.1007/S12039-011-0087-2.
[104] A. Börner, R. Franke, Hydroformylation : fundamentals, processes, and applications in organic systhesis, 2017.
[105] F. Kirk, G. Whitfield, D. Miles, WO Patent 2002072520A2 Process for production of oxygenated organic compounds, 2002. https://patents.google.com/patent/WO2002072520A2/zh (accessed April 20, 2022).
[106] M. Beller, B. Cornils, C.D. Frohning, C.W. Kohlpaintner, Progress in hydroformylation and carbonylation, J. Mol. Catal. A. Chem. 104 (1995) 17–85. https://doi.org/10.1016/1381-1169(95)00130-1.
[107] T. Mizoroki, M. Kioka, M. Suzuki, S. Sakatani, A. Okumura, K. ichi Maruya, Behavior of Amine in Rhodium Complex–Tertiary Amine Catalyst System Active for Hydrogenation of Aldehyde under Oxo Reaction Conditions, Http://Dx.Doi.Org/10.1246/Bcsj.57.577. 57 (2006) 577–578. https://doi.org/10.1246/BCSJ.57.577.
[108] L.A.D. Van Der Veen, P.K. Keeven, P.C.J. Kamer, P.W.N.M. Van Leeuwen, Novel arsine ligands for selective hydroformylation of alk-1-enes employing platinum/tin catalysts, Chem. Commun. (2000) 333–334. https://doi.org/10.1039/A906903H.
[109] J.T. Carlock, A comparative study of triphenylamine, triphenylphosphine, triphenylarsine, triphenylantimony and triphenylbismuth as ligands in the rhodium-catal yzed hydroformylation of 1-dodecene, Tetrahedron. 40 (1984) 185–187. https://doi.org/10.1016/0040-4020(84)85118-2.
[110] B.F. Straub, Organotransition Metal Chemistry. From Bonding to Catalysis. Edited by John F. Hartwig., John Wiley & Sons, Ltd, 2010. https://doi.org/10.1002/ANIE.201004890.
[111] D. Evans, G. Yagupsky, G. Wilkinson, The reaction of hydridocarbonyltris(triphenylphosphine)rhodium with carbon monoxide, and of the reaction products, hydridodicarbonylbis(triphenylphosphine)rhodium and dimeric species, with hydrogen, J. Chem. Soc. A Inorganic, Phys. Theor. . 0 (1968) 2660–2665. https://doi.org/10.1039/J19680002660.

[112] G. Kiss, E.J. Mozeleski, K.C. Nadler, E. VanDriessche, C. DeRoover, Hydroformylation of ethene with triphenylphosphine modified rhodium catalyst: Kinetic and mechanistic studies, J. Mol. Catal. A Chem. 138 (1999) 155–176. https://doi.org/10.1016/S1381-1169(98)00166-6.
[113] T. Kégl, Computational aspects of hydroformylation, RSC Adv. 5 (2014) 4304–4327. https://doi.org/10.1039/C4RA13121E.
[114] R. Lazzaroni, R. Settambolo, G. Alagona, C. Ghio, Investigation of alkyl metal intermediate formation in the rhodium-catalyzed hydroformylation: Experimental and theoretical approaches, Coord. Chem. Rev. 254 (2010) 696–706. https://doi.org/10.1016/j.ccr.2009.09.032.
[115] C. Li, W. Wang, L. Yan, Y. Ding, A mini review on strategies for heterogenization of rhodium-based hydroformylation catalysts, Front. Chem. Sci. Eng. 12 (2018) 113–123. https://doi.org/10.1007/s11705-017-1672-9.
[116] H. Arai, Hydroformylation, hydrogenation, and isomerization of olefins over polymer-immobilized rhodium complexes, J. Catal. 51 (1978) 135–142. https://doi.org/10.1016/0021-9517(78)90286-5.
[117] Â.C.B. Neves, M.J.F. Calvete, T.M.V.D. Pinho E Melo, M.M. Pereira, Immobilized Catalysts for Hydroformylation Reactions: A Versatile Tool for Aldehyde Synthesis, European J. Org. Chem. 2012 (2012) 6309–6320. https://doi.org/10.1002/EJOC.201200709.
[118] R.H. Grubbs, L.R.C. Kroll, Catalytic Reduction of Olefins with a Polymer-Supported Rhodium(I) Catalyst, American Chemical Society, 1971. https://pubs.acs.org/doi/abs/10.1021/ja00741a050 (accessed April 19, 2021).
[119] M. Ichikawa, Bimetallic cluster-derived heterogeneous catalysts-heteronuclear two-site activation of CO in syngas conversion to oxygenates, Polyhedron. 7 (1988) 2351–2367. https://doi.org/10.1016/S0277-5387(00)86353-6.
[120] C. Dossi, A. Fusi, L. Garlaschelli, R. Psaro, R. Ugo, Heterogeneous Ethylene Hydroformylation Catalyzed by Oxide-Supported [Rh12(CO)30]2- Anion: Influence of the Nature of the Support, Stud. Surf. Sci. Catal. 75 (1993) 2345–2348. https://doi.org/10.1016/S0167-2991(08)64296-2.
[121] N. Sudheesh, S.K. Sharma, R.S. Shukla, R. V. Jasra, HRh(CO)(PPh3)3 encapsulated mesopores of hexagonal mesoporous silica (HMS) acting as nanophase reactors for effective catalytic hydroformylation of olefins, J. Mol. Catal. A Chem. 296 (2008) 61–70. https://doi.org/10.1016/J.MOLCATA.2008.08.019.
[122] V.I. Zapirtan, B.L. Mojet, J.G. Van Ommen, J. Spitzer, L. Lefferts, Gas phase hydroformylation of ethylene using organometalic Rh-complexes as heterogeneous catalysts, Catal. Letters. 101 (2005) 43–47. https://doi.org/10.1007/s10562-004-3747-8.
[123] Q. Sun, Z. Dai, X. Liu, N. Sheng, F. Deng, X. Meng, F.S. Xiao, Highly efficient heterogeneous hydroformylation over rh-metalated porous organic polymers: Synergistic effect of high ligand concentration and flexible framework, J. Am. Chem. Soc. 137 (2015) 5204–5209. https://doi.org/10.1021/jacs.5b02122.
[124] S.S.C. Chuang, S.I. Pien, Infrared study of the CO insertion reaction on reduced, oxidized, and sulfided Rh/SiO2 catalysts, J. Catal. 135 (1992) 618–634. https://doi.org/10.1016/0021-9517(92)90058-P.
[125] M.W. Balakos, S.S.C. Chuang, Transient response of propionaldehyde formation

during CO/H2/C2H4 reaction on Rh/SiO2, J. Catal. 151 (1995) 253–265. https://doi.org/10.1006/jcat.1995.1026.
[126] S.I. Pien, S.S.C. Chuang, An in situ infrared study of ethylene hydroformylation and CO hydrogenation on Ru/SiO2 and sulfided Ru/SiO2, J. Mol. Catal. 68 (1991) 313–330. https://doi.org/10.1016/0304-5102(91)80090-P.
[127] M.A. Brundage, M.W. Balakos, S.S.C. Chuang, LHHW and PSSA kinetic analysis of rates and adsorbate coverages in CO/H2/C2H4 reactions on Mn-Rh/SiO2, J. Catal. 173 (1998) 122–133. https://doi.org/10.1006/jcat.1997.1923.
[128] S.S.C. Chuang, R.W. Stevens, R. Khatri, Mechanism of C2+ oxygenate synthesis on Rh catalysts, Top. Catal. 32 (2005) 225–232. https://doi.org/10.1007/s11244-005-2897-2.
[129] M.W. Balakos, S.S.C. Chuang, Dynamic and LHHW kinetic analysis of heterogeneous catalytic hydroformylation, J. Catal. 151 (1995) 266–278. https://doi.org/10.1006/jcat.1995.1027.
[130] S.S.C. Chuang, Sulfided group VIII metals for hydroformylation, Appl. Catal. 66 (1990) L1–L6. https://doi.org/10.1016/S0166-9834(00)81619-X.
[131] S.M. McClure, M.J. Lundwall, D.W. Goodman, Planar oxide supported rhodium nanoparticles as model catalysts, Proc. Natl. Acad. Sci. (2011). https://doi.org/10.1073/pnas.1006635107.
[132] Z. Mao, Z. Xie, J.G. Chen, Comparison of Heterogeneous Hydroformylation of Ethylene and Propylene over RhCo3/MCM-41 Catalysts, ACS Catal. 11 (2021) 14575–14585. https://doi.org/10.1021/acscatal.1c04359.
[133] N. Takahashi, M. Kobayashi, Comparison of ethylene with propylene hydroformylation over a Rh-Y zeolite catalyst under atmospheric pressure, J. Catal. (1984). https://doi.org/10.1016/0021-9517(84)90112-X.
[134] S.S.C. Chuang, S.I. Pien, Enhancement of ethylene hydroformylation over Ni/SiO2 through sulfur promotion, Catal. Letters. 6 (1990) 389–393. https://doi.org/10.1007/BF00764006.
[135] S.A. Hedrick, S.S.C. Chuang, A. Pant, A.G. Dastidar, Activity and selectivity of Group VIII, alkali-promoted Mn-Ni, and Mo-based catalysts for C2+ oxygenate synthesis from the CO hydrogenation and CO/H2/C2H4 reactions, Catal. Today. 55 (2000) 247–257. https://doi.org/10.1016/S0920-5861(99)00245-X.
[136] L. Storaro, R. Ganzerla, M. Lenarda, R. Zanoni, G. Righini, Highly selective vapor phase propene hydroformylation catalyzed by Rh/B and Rh-Co/B systems on silica, J. Mol. Catal. A Chem. 112 (1996) 43–54. https://doi.org/10.1016/1381-1169(96)00243-9.
[137] M. Lenarda, R. Ganzerla, L. Storaro, R. Zanoni, Catalysis by the Rh/B system Part 1. Vapour-phase hydroformylation of ethylene at atmospheric pressure on Rh/B on silica, J. Mol. Catal. 78 (1993) 339–350. https://doi.org/10.1016/0304-5102(93)87063-E.
[138] L. Huang, Y. Xu, Synergy of ruthenium and cobalt in SiO2-supported catalysts on ethylene hydroformylation, Appl. Catal. A Gen. 205 (2001) 183–193. https://doi.org/10.1016/S0926-860X(00)00573-1.
[139] N. Navidi, J.W. Thybaut, G.B. Marin, Experimental investigation of ethylene hydroformylation to propanal on Rh and Co based catalysts, Appl. Catal. A Gen. (2014). https://doi.org/10.1016/j.apcata.2013.10.019.
[140] A. Fukuoka, M. Ichikawa, J.A. Hriljac, D.F. Shriver, Promoter Effect of Iron on

Olefin Hydroformylation Catalyzed By SiO2-Supported Rhodium-Iron Bimetallic Carbonyl Clusters: Rh-Fe3+Bimetallic Activation of Catalytic CO Insertion, Inorg. Chem. 26 (1987) 3643–3645. https://doi.org/10.1021/ic00269a001.
[141] Y. Izumi, K. Asakura, Y. Iwasawa, Promoting effects of Se on Rh/ZrO2 catalysis for ethene hydroformylation, J. Catal. (1991). https://doi.org/10.1016/0021-9517(91)90188-A.
[142] J. Zhang, P. Sun, G. Gao, J. Wang, Z. Zhao, Y. Muhammad, F. Li, Enhancing regioselectivity via tuning the microenvironment in heterogeneous hydroformylation of olefins, J. Catal. 387 (2020) 196–206. https://doi.org/10.1016/j.jcat.2020.03.032.
[143] L. Yan, Y.J. Ding, H.J. Zhu, J.M. Xiong, T. Wang, Z.D. Pan, L.W. Lin, Ligand modified real heterogeneous catalysts for fixed-bed hydroformylation of propylene, J. Mol. Catal. A Chem. 234 (2005) 1–7. https://doi.org/10.1016/J.MOLCATA.2005.01.047.
[144] L. Yan, Y. Ding, J. Liu, H. Zhu, L. Lin, Influence of Phosphine Concentration on Propylene Hydroformylation over the PPh3-Rh/SiO2 Catalyst, Chinese J. Catal. 32 (2011) 31–35. https://doi.org/10.1016/S1872-2067(10)60156-8.
[145] S. Shylesh, D. Hanna, A. Mlinar, X.Q. Kŏng, J.A. Reimer, A.T. Bell, In situ formation of Wilkinson-type hydroformylation catalysts: Insights into the structure, stability, and kinetics of triphenylphosphine- and xantphos-modified Rh/SiO2, ACS Catal. 3 (2013) 348–357. https://doi.org/10.1021/cs3007445.
[146] T. Kim, F.E. Celik, D.G. Hanna, S. Shylesh, S. Werner, A.T. Bell, Gas-phase hydroformylation of propene over silica-supported PPh 3-modified rhodium catalysts, Top. Catal. 54 (2011) 299–307. https://doi.org/10.1007/S11244-011-9664-3/SCHEMES/2.
[147] X. Li, Y. Ding, G. Jiao, J. Li, R. Lin, L. Gong, L. Yan, H. Zhu, A new concept of tethered ligand-modified Rh/SiO2 catalyst for hydroformylation with high stability, Appl. Catal. A Gen. 353 (2009) 266–270. https://doi.org/10.1016/J.APCATA.2008.10.052.
[148] J. Liu, L. Yan, M. Jiang, C. Li, Y. Ding, Effect of lengthening alkyl spacer on hydroformylation performance of tethered-phosphine modified Rh/SiO2 catalyst, Chinese J. Catal. 37 (2016) 268–272. https://doi.org/10.1016/S1872-2067(15)61019-1.
[149] J. Liu, L. Yan, Y. Ding, M. Jiang, W. Dong, X. Song, T. Liu, H. Zhu, Promoting effect of Al on tethered ligand-modified Rh/SiO2 catalysts for ethylene hydroformylation, Appl. Catal. A Gen. 492 (2015) 127–132. https://doi.org/10.1016/J.APCATA.2014.12.011.
[150] M. Tan, Y. Ishikuro, Y. Hosoi, N. Yamane, P. Ai, P. Zhang, G. Yang, M. Wu, R. Yang, N. Tsubaki, PPh3 functionalized Rh/rGO catalyst for heterogeneous hydroformylation: Bifunctional reduction of graphene oxide by organic ligand, Chem. Eng. J. 330 (2017) 863–869. https://doi.org/10.1016/J.CEJ.2017.08.023.
[151] D.P. Zhuchkov, M. V. Nenasheva, M. V. Terenina, Y.S. Kardasheva, D.N. Gorbunov, E.A. Karakhanov, Polymeric Heterogeneous Catalysts in the Hydroformylation of Unsaturated Compounds, Pet. Chem. 61 (2021) 5–20. https://doi.org/10.1134/S0965544121010011.
[152] J. Feldman, M. Orchin, Membrane-supported rhodium hydroformylation catalysts, J. Mol. Catal. 63 (1990) 213–221. https://doi.org/10.1016/0304-5102(90)85145-8.
[153] T.A. Zeelie, A. Root, A.O.I. Krause, Rh/fibre catalyst for ethene hydroformylation:

Catalytic activity and characterisation, Appl. Catal. A Gen. 285 (2005) 96–109. https://doi.org/10.1016/j.apcata.2005.02.010.
[154] A. Riisager, R. Fehrmann, M. Haumann, P. Wasserscheid, Supported Ionic Liquid Phase (SILP) Catalysis: An Innovative Concept for Homogeneous Catalysis in Continuous Fixed-Bed Reactors, Eur. J. Inorg. Chem. 2006 (2006) 695–706. https://doi.org/10.1002/EJIC.200500872.
[155] C. Van Doorslaer, J. Wahlen, P. Mertens, K. Binnemans, D. De Vos, Immobilization of molecular catalysts in supported ionic liquid phases, Dalt. Trans. 39 (2010) 8377–8390. https://doi.org/10.1039/c001285h.
[156] A. Riisager, R. Fehrmann, M. Haumann, B.S.K. Gorle, P. Wasserscheid, Stability and kinetic studies of supported ionic liquid phase catalysts for hydroformylation of propene, Ind. Eng. Chem. Res. 44 (2005) 9853–9859. https://doi.org/10.1021/ie050629g.
[157] T. Welton, Room-Temperature Ionic Liquids. Solvents for Synthesis and Catalysis, Chem. Rev. 99 (1999) 2071–2083. https://doi.org/10.1021/cr980032t.
[158] J.P. Hallett, T. Welton, Room-Temperature Ionic Liquids: Solvents for Synthesis and Catalysis. 2, Chem. Rev. 111 (2011) 3508–3576. https://doi.org/10.1021/CR1003248.
[159] H.P. Steinrück, J. Libuda, P. Wasserscheid, T. Cremer, C. Kolbeck, M. Laurin, F. Maier, M. Sobota, P.S. Schulz, M. Stark, Surface Science and Model Catalysis with Ionic Liquid-Modified Materials, Adv. Mater. 23 (2011) 2571–2587. https://doi.org/10.1002/ADMA.201100211.
[160] M. Haumann, A. Riisager, Hydroformylation in room temperature ionic liquids (RTILs): Catalyst and process developments, Chem. Rev. 108 (2008) 1474–1497. https://doi.org/10.1021/cr078374z.
[161] A. Riisager, R. Fehrmann, M. Haumann, P. Wasserscheid, Supported ionic liquids: versatile reaction and separation media, Top. Catal. 2006 401. 40 (2006) 91–102. https://doi.org/10.1007/S11244-006-0111-9.
[162] J. Resasco, F. Yang, T. Mou, B. Wang, P. Christopher, D.E. Resasco, Relationship between Atomic Scale Structure and Reactivity of Pt Catalysts: Hydrodeoxygenation of m-Cresol over Isolated Pt Cations and Clusters, ACS Catal. 10 (2020) 595–603. https://doi.org/10.1021/acscatal.9b04330.
[163] L. DeRita, S. Dai, K. Lopez-Zepeda, N. Pham, G.W. Graham, X. Pan, P. Christopher, Catalyst Architecture for Stable Single Atom Dispersion Enables Site-Specific Spectroscopic and Reactivity Measurements of CO Adsorbed to Pt Atoms, Oxidized Pt Clusters, and Metallic Pt Clusters on TiO2, J. Am. Chem. Soc. 139 (2017) 14150–14165. https://doi.org/10.1021/jacs.7b07093.
[164] J. Zhang, C. Asokan, G. Zakem, P. Christopher, J.W. Medlin, Enhancing Sintering Resistance of Atomically Dispersed Catalysts in Reducing Environments with Organic Monolayers, Green Energy Environ. (2021). https://doi.org/10.1016/j.gee.2021.01.022.
[165] H. Jeong, G. Lee, B.S. Kim, J. Bae, J.W. Han, H. Lee, Fully Dispersed Rh Ensemble Catalyst to Enhance Low-Temperature Activity, J. Am. Chem. Soc. (2018). https://doi.org/10.1021/jacs.8b04613.
[166] H. Guan, J. Lin, B. Qiao, S. Miao, A. Wang, X. Wang, T. Zhang, Enhanced performance of Rh $_1$ /TiO $_2$ catalyst without methanation in water-gas shift reaction, AIChE J. 63 (2017) 2081–2088. https://doi.org/10.1002/aic.15585.

[167] J. Resasco, P. Christopher, Atomically Dispersed Pt-group Catalysts: Reactivity, Uniformity, Structural Evolution, and Paths to Increased Functionality, J. Phys. Chem. Lett. 11 (2020) 10114–10123. https://doi.org/10.1021/acs.jpclett.0c02904.
[168] L. Wang, W.W. Zhang, S. Wang, Z. Gao, Z. Luo, X. Wang, R. Zeng, A. Li, H. Li, M. Wang, X. Zheng, J. Zhu, W.W. Zhang, C. Ma, R. Si, J. Zeng, Atomic-level insights in optimizing reaction paths for hydroformylation reaction over Rh/CoO single-atom catalyst, Nat. Commun. 7 (2016) 1–8. https://doi.org/10.1038/ncomms14036.
[169] J. Liu, Catalysis by Supported Single Metal Atoms, ACS Catal. (2017). https://doi.org/10.1021/acscatal.6b01534.
[170] F. Chen, X. Jiang, L. Zhang, R. Lang, B. Qiao, Single-atom catalysis: Bridging the homo- and heterogeneous catalysis, Chinese J. Catal. 39 (2018) 893–898. https://doi.org/10.1016/S1872-2067(18)63047-5.
[171] M. Babucci, C.-Y. Fang, A.S. Hoffman, S.R. Bare, B.C. Gates, A. Uzun, Tuning the Selectivity of Single-Site Supported Metal Catalysts with Ionic Liquids, 16 (2020) 0. https://doi.org/10.1021/acscatal.7b02429.
[172] J.C. Matsubu, V.N. Yang, P. Christopher, Isolated metal active site concentration and stability control catalytic CO2 reduction selectivity, J. Am. Chem. Soc. 137 (2015) 3076–3084. https://doi.org/10.1021/ja5128133.
[173] M. Babucci, C.-Y. Fang, J.E. Perez-Aguilar, A.S. Hoffman, A. Boubnov, E. Guan, S.R. Bare, B.C. Gates, A. Uzun, Controlling catalytic activity and selectivity for partial hydrogenation by tuning the environment around active sites in iridium complexes bonded to supports, Chem. Sci. 10 (2019) 2623–2632. https://doi.org/10.1039/C8SC05287E.
[174] I. Ro, M. Xu, G.W. Graham, X. Pan, P. Christopher, Synthesis of Heteroatom Rh–ReO_x Atomically Dispersed Species on Al_2O_3 and Their Tunable Catalytic Reactivity in Ethylene Hydroformylation, ACS Catal. 9 (2019) 10899–10912. https://doi.org/10.1021/acscatal.9b02111.
[175] E.J. Peterson, A.T. DeLaRiva, S. Lin, R.S. Johnson, H. Guo, J.T. Miller, J.H. Kwak, C.H.F. Peden, B. Kiefer, L.F. Allard, F.H. Ribeiro, A.K. Datye, Low-temperature carbon monoxide oxidation catalysed by regenerable atomically dispersed palladium on alumina, Nat. Commun. (2014). https://doi.org/10.1038/ncomms5885.
[176] S. Lee, A. Patra, P. Christopher, D.G. Vlachos, S. Caratzoulas, Theoretical study of ethylene hydroformylation on atomically dispersed Rh/Al2O3 catalysts: Reaction mechanism and influence of ReOx promoter, ACS Catal. (2021) 9506–9518. https://doi.org/10.1021/acscatal.1c00705.
[177] C. Asokan, H.V. Thang, G. Pacchioni, P. Christopher, Reductant composition influences the coordination of atomically dispersed Rh on anatase TiO2, Catal. Sci. Technol. 10 (2020) 1597–1601. https://doi.org/10.1039/d0cy00146e.
[178] C. Asokan, Y. Yang, A. Dang, A. Getsoian, P. Christopher, Low-Temperature Ammonia Production during NO Reduction by CO Is Due to Atomically Dispersed Rhodium Active Sites, ACS Catal. 10 (2020) 5217–5222. https://doi.org/10.1021/acscatal.0c01249.
[179] X.F. Yang, A. Wang, B. Qiao, J. Li, J. Liu, T. Zhang, Single-atom catalysts: A new frontier in heterogeneous catalysis, Acc. Chem. Res. 46 (2013) 1740–1748. https://doi.org/10.1021/ar300361m.
[180] J. Resasco, L. Derita, S. Dai, J.P. Chada, M. Xu, X. Yan, J. Finzel, S. Hanukovich,

A.S. Hoffman, G.W. Graham, S.R. Bare, X. Pan, P. Christopher, Uniformity Is Key in Defining Structure-Function Relationships for Atomically Dispersed Metal Catalysts: The Case of Pt/CeO2, J. Am. Chem. Soc. 142 (2020) 169–184. https://doi.org/10.1021/jacs.9b09156.

[181] C.H. Choi, M. Kim, H.C. Kwon, S.J. Cho, S. Yun, H.T. Kim, K.J.J. Mayrhofer, H. Kim, M. Choi, Tuning selectivity of electrochemical reactions by atomically dispersed platinum catalyst, Nat. Commun. 2016 71. 7 (2016) 1–9. https://doi.org/10.1038/ncomms10922.

[182] I. Ro, J. Qi, S. Lee, M. Xu, X. Yan, Z. Xie, G. Zakem, A. Morales, J.G. Chen, X. Pan, D.G. Vlachos, S. Caratzoulas, P. Christopher, Bifunctional hydroformylation on heterogeneous Rh-WOx pair site catalysts, Nat. 2022 6097926. 609 (2022) 287–292. https://doi.org/10.1038/s41586-022-05075-4.

[183] F. Zaera, Designing Sites in Heterogeneous Catalysis: Are We Reaching Selectivities Competitive with Those of Homogeneous Catalysts?, Chem. Rev. (2021). https://doi.org/10.1021/acs.chemrev.1c00905.

[184] R. Lang, T. Li, D. Matsumura, S. Miao, Y. Ren, Y.T. Cui, Y. Tan, B. Qiao, L. Li, A. Wang, X. Wang, T. Zhang, Hydroformylation of Olefins by a Rhodium Single-Atom Catalyst with Activity Comparable to RhCl(PPh3)3, Angew. Chemie - Int. Ed. 55 (2016) 16054–16058. https://doi.org/10.1002/anie.201607885.

[185] B. Liu, Y. Wang, N. Huang, X. Lan, Z. Xie, J.G. Chen, T. Wang, Heterogeneous hydroformylation of alkenes by Rh-based catalysts, Chem. (2022). https://doi.org/10.1016/J.CHEMPR.2022.07.020.

Chapter 2: Temperature Programmed Desorption Spectroscopy to Probe Kinetics

In part adapted from article submitted to ACS Catalysis:

Gregory Zakem and Phillip Christopher
"Active Site Entropy of Atomically Dispersed Rh/Al2O3 Catalysts Dictates Activity for Ethylene Hydroformylation", ACS Catalysis (Submitted)

2.1 TEMPERATURE PROGRAMMED DESORPTION FUNDAMENTALS

Temperature programmed desorption (TPD) is a class of experimental techniques in which an event (desorption) on a solid surface is monitored during heating ($\beta(t) = \frac{dT}{dt}$). Usually, a linear heating rate is chosen to simplify the mathematics. In general, the goal of TPD experiments is to probe surface-adsorbate desorption kinetics. Some common parameters extracted include activation barriers (energies, enthalpies, and entropies), reaction orders, and the coverage dependencies of these parameters.

To discuss desorption, an understanding of the reverse process, adsorption, is important. Adsorption is a phenomenon in which a gas or liquid interacts strongly enough with a solid surface to overcome the entropic favorability of the fluid phase. Adsorption sites, also known as binding sites or active sites, are points on the solid surface in which adsorbates can strongly interact with the surface.[1,2] In general, a distinction is made between physisorption, in which interactions between the adsorbate and surface are due to weak intermolecular forces, and chemisorption, in which electrons are transferred between the surface and the adsorbate, resulting in covalent bonds. Physisorption usually only takes place at low temperatures due to Van Der Waals interactions and can form multilayers if the adsorbent can interact with itself. Importantly, the adsorbent is not altered chemically during physisorption, and the heats of adsorption are quite low (< 50 kJ/mol).[3] Conversely, chemisorption can take place over a wider range of temperatures and is limited to a single monolayer on the surface. Chemisorbed molecules are chemically altered, and typically have higher heats of adsorption (> 50 kJ/mol). For polyatomic molecules, strong interactions with the surface can weaken intramolecular bonds, resulting in dissociation. Physisorption is nearly energetically barrierless, while chemisorption, and especially dissociative chemisorption can have activation barriers.[1,2]

2.1.1 Thermodynamic Principles

All adsorption processes are inherently exothermic, as the entropy of adsorption (ΔS_{ads}) must be negative as any molecule will lose degrees of freedom when transferring from a fluid phase to a solid phase. Thus, for adsorption to happen spontaneously ($\Delta G_{ads} < 0$), the adsorption enthalpy (ΔH_{ads}) must also be negative as $\Delta G_{ads} = \Delta H_{ads} - T\Delta S_{ads}$. The ΔH_{ads} is a direct quantification of the interaction strength between a surface and adsorbate. Estimating these values is important in catalysis as the binding strength of adsorbates influences the rates and mechanisms of chemical reactions. The heats of adsorption can be determined from the kinetics of TPD experiments, such that a discussion of adsorption and desorption kinetics is warranted.[3]

2.1.2 Kinetic Principles

Adsorption of gas-phase species is often modeled using Langmuir isotherms which is developed using the following assumptions: (1) each active site can only interact with a single adsorbate, (2) adsorption stops when a full monolayer of adsorbates is formed, and (3) adsorbed species do not interact with each other.[1] While these assumptions are not always true, they form a basis from which we can describe many adsorption process. Adsorption and desorption rates (r_{ads} and r_{des}, respectively) are proportional to the fraction of empty sites (1-θ) and the fraction of occupied sites (θ), respectively (Equations 2.1 and 2.2).

$$r_{ads}(\theta) = k_{ads}P(1-\theta)^n \tag{2.1}$$

Where: $r_{ads}(\theta)$=Rate of adsorption (mol/s)
k_{ads} =Rate constant of adsorption (mol/(Pa·s))
P =Pressure of adsorbate species in the gas phase (Pa)
θ =Fraction of adsorption sites occupied (unitless)
n = Order of surface reaction (unitless)

$$r_{des}(\theta) = k_{des}\theta^n \tag{2.2}$$

Where: $r_{des}(\theta)$=Rate of adsorption (mol/s)

k_{des} =Rate constant of desorption (mol/s)

At equilibrium, r_{ads} and r_{des} are equal, and the equilibrium surface coverage can be calculated as Equation 2.3. k_{ads} and k_{des} are generally functions of temperature, such that θ is a function of temperature and pressure.

$$\theta = \frac{\left(\frac{k_{ads}}{k_{des}}P\right)^{\frac{1}{n}}}{1 + \left(\frac{k_{ads}}{k_{des}}P\right)^{\frac{1}{n}}} \tag{2.3}$$

This information is useful for experimental design (to determine the temperatures and pressure of gas is required to achieve a certain coverage of an adsorbate), but ultimately the TPD experiment are performed without the adsorbate in the gas phase, such that only Equation 2.2 is relevant. Unlike adsorption, which is not always an activated process, desorption is always activated, such that the rate constant can be well described in an Arrhenius form (Equation 2.4).

$$k_{des} = A(\theta)\exp\left(\frac{E_a}{RT}\right) \tag{2.4}$$

Where: $A(\theta)$= the coverage dependent preexponential factor (1/s)
E_a = the activation energy of desorption (J/mol)
R = the molar gas constant (J/(mol·K))
T = temperature (K)

Knowing this, we can write the rate of desorption as Equation (2.5).

$$r_{des} = -\frac{d\theta}{dt} = \theta^n A(\theta)\exp\left(\frac{E_a}{RT}\right) \tag{2.5}$$

Dividing both sides by $\beta(t) = \frac{dT}{dt}$ yields Equation 2.6.

$$-\frac{d\theta}{dT} = \frac{\theta^n}{\beta}A(\theta)\exp\left(\frac{E_a}{RT}\right) \tag{2.6}$$

Equation 2.6 is known as the Polanyi-Wigner Equation, and is used to describe any activated, non-reversible (no readsorption) desorption process. Derivations and applications of this equation will later be used to extract information from TPD experiments.[4]

2.1.3 Experimental Design

To understand the experimental design of TPDs, we will first discuss the workflow for TPD experiments: (1) If necessary, samples are pretreated (usually by heating the sample to remove non-probe molecule surface species), (2) samples is exposed to the adsorbate gas, (3) physisorbed adsorbates are removed via vacuum or an inert purge, (4) sample is heated in the desired atmosphere and evolved gases are measured.

While a variety of experimental setups have been developed to more closely mimic specific conditions, all TPD experiments share three common features: (1). A method of introducing the desired amount of adsorbate gas to the sample, (2) a method to heat the sample in a programmed manner, and (3) a method to measure gases after desorption.

Adsorbate gases are generally introduced isothermally, and many apparatuses allow for known amounts of the adsorbate to be introduced. This allows for sub-monolayer coverages to be formed by manipulating the temperature of the sample or the pressure/amount of the adsorbate gas. In general, polar, strongly interacting adsorbates are used (CO, CO_2, and NH_3 are particularly common), but larger non-polar molecules have also been used. These adsorbates are often referred to as probe molecules, and the choice of probe is dependent on the type of adsorption site that one is interested in.

Samples are placed in a heated area (usually a sample holder or a furnace) which allows for the introduction of the adsorbate gas at controlled temperatures. In surface science experiments, the most common apparatus for TPDs (Figure 2.1a) uses a sample holder, on

which a sample is deposited (usually a monolayer or single crystal) and is connected to a temperature controller. These experiments are generally performed under high vacuum and allow for well-controlled experiments (uniform known surfaces, known amounts of gas introduced/adsorbed).[5] In catalysis, the most common experimental apparatus involves and system in which a sample is packed into a quartz tube inside of a furnace, and gases are flowed through the sample. (Figure 2.1b) During TPD experiments, an inert is flown through the tube, such that desorbed gases are carried downstream for measurement.[6]

A variety of detectors have been used for detecting gases evolved from TPDs, but among the most common are thermal conductivity detectors (TCDs), flame ionization

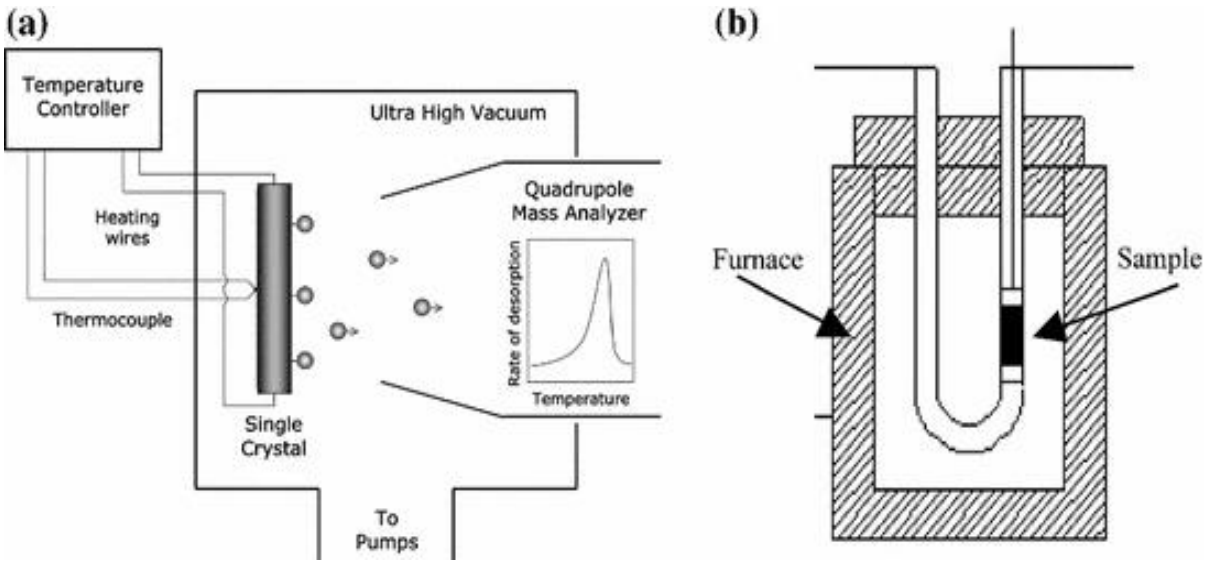

Figure 2.1: (a) Experimental apparatus for vacuum TPD experiments. Samples are placed on a sample holder which can be heated, while desorbed species are detected via mass spectrometry. The inset shows an example of data obtained by a TPD experiment. (b) Experimental apparatus for a flow TPD system. Samples are placed in a quartz tube, and the tube is placed in a furnace. Desorbed species are carried by an inert downstream for detection. [6]

detectors (FIDs), and mass spectrometers (MS).

- TCDs work based on the difference in thermal conductivity between the sample gas stream and a reference gas stream (TCDs can only be used in flow systems). Desorbed species change the thermal conductivity of the sample gas stream, resulting in a signal.

TCDs are useful when only a single species of gas is expected to evolve but cannot discriminate between different species.

- FIDs work by burning desorbed species in a hydrogen and air flame, and trapping formed ions between two electrodes with different potentials, generating a signal. FIDs can only detect organic species, as such they are useful for TPDs in which inorganic species may desorb at the same time as organic species of interest. This detector can also only be used in flow systems.
- MS is often used for its high sensitivity, and its ability to discriminate between different desorbed species. The species evolved are discriminated based on the atomic mass of the gases involved in the desorption process. It can be used for both flow and vacuum systems, but is most often used in vacuum systems for model systems.

Generally, in modern experiments, only TCD and MS are used for detection. TCDs are relatively inexpensive and easy to use for simple TPD experiments, while MS can be used for more complex experiments in which there are multiple desorbed species.

2.1.4 Extracting Kinetic Data from TPDs

TPDs are often used to learn information on adsorption strengths (for a non-activated adsorption process, the E_a of desorption is equal to the adsorption energy) and less commonly the attempt frequency (the preexponential factor). The analyses and experiments required to extract information from TPDs is different depending on the order of desorption. As such, this section will introduce 0^{th}, 1^{st}, and 2^{nd} order desorption processes, idealized spectra for each, and how to extract information from that data. This section is not exhaustive in its coverage of different TPD analyses but is meant to introduce the reader to the different types of TPDs and how they are approached. Simulated data is used to introduce these concepts.

The rate of a 0th order desorption is independent of adsorbate coverage and will increase exponentially until the surface is fully desorbed (at which point the rate drops precipitously, T_P in Figure 2.2). 0th order desorption typically only occurs from multilayers of adsorbed species, but 0th order monolayer desorption has been observed for some hydrocarbon species as well.[7] It is well described by Equation 2.7, and simulated TPD spectra for different initial adsorbate coverages is presented in Figure 2.2.

$$-\frac{d\theta}{dT} = \frac{A}{\beta}\exp\left(\frac{E_a}{RT}\right) \tag{2.7}$$

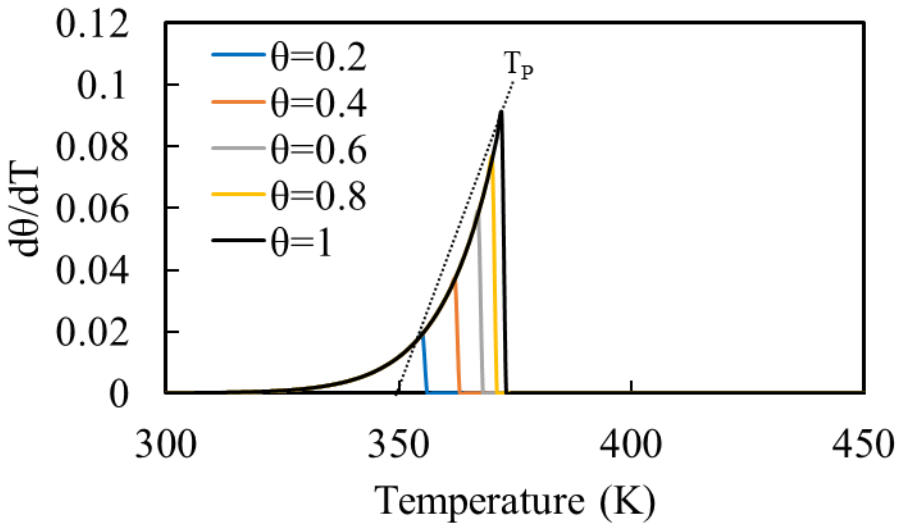

Figure 2.2: Simulated TPD spectra of a 0th order TPD for different initial adsorbate coverages. The spectra for each coverage overlap since rates are independent of initial coverage. The dashed line represents the change in the maximum temperature of desorption (T_P) with increased initial coverage. Parameters for simulation: E_a=100 kJ/mol, A=10^{13} s^{-1}, β= 1 K/s. It was assumed that E_a and A are constant at all coverages.

Since 0th order TPD spectra have different widths and temperatures of maximum desorption (T_P) for different initial coverages, the position of T_P is less useful than for 1st and 2nd order processes (described later in this chapter). Instead, most analyses of 0th order TPDs use a technique known as line shape analysis. This analysis involves fitting the TPD spectra to Equation 2.7 and extracting A and E_d from that fit. Usually, data is fit only near the onset of desorption to minimize the effects of coverage on A and E_d.

The rate of 1st order TPDs is linear with coverage and will increase with temperature until coverages are small enough that rates start to drop. Most TPD processes examined will be 1st order, as most molecular probes will adsorb and desorb without dissociation. It is well described by Equation 2.8, and simulated spectra for different initial adsorbate coverages is presented in figure 2.3.

$$-\frac{d\theta}{dT} = \frac{\theta}{\beta} A \exp\left(\frac{E_a}{RT}\right) \tag{2.8}$$

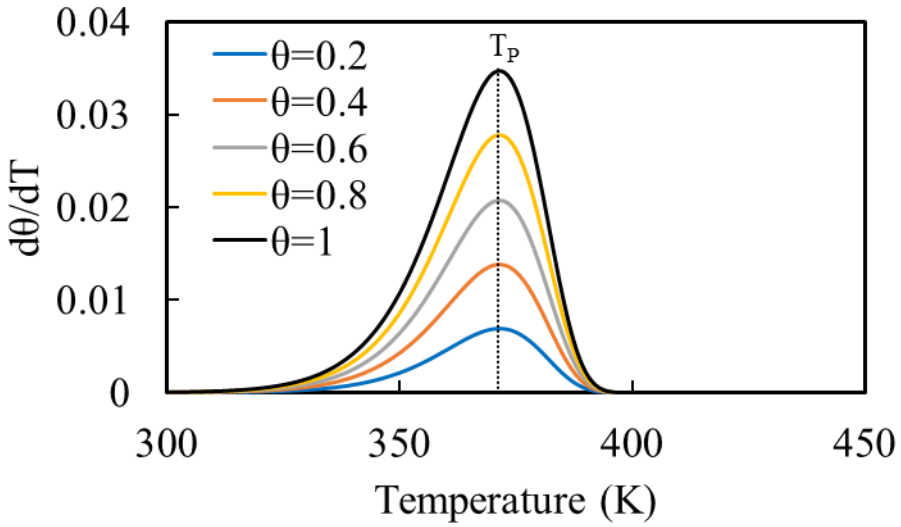

Figure 2.3: Simulated TPD spectra of a 1st order TPD for different initial adsorbate coverages. The dashed line represents the change in the maximum temperature of desorption (T_P) with increased initial coverage. Parameters for simulation: E_a=100 kJ/mol, A=10^{13} s^{-1}, β= 1 K/s. It was assumed that E_a and A are constant at all coverages.

1st order TPDs result in asymmetric desorption spectra, but T_P is constant with different initial coverages. These spectra are usually interpreted in one of three ways. Like with the 0th order spectra, line shape analysis can be used by fitting the initial desorption behavior to the form of Equation 2.8. This is useful for determining kinetic parameters at the onset of desorption, but significant changes in kinetics can occur at different coverages, such that this

information is limited to initial desorption behavior. This can, to some extent, be compensated for by repeating this analysis for a variety of different initial coverages.

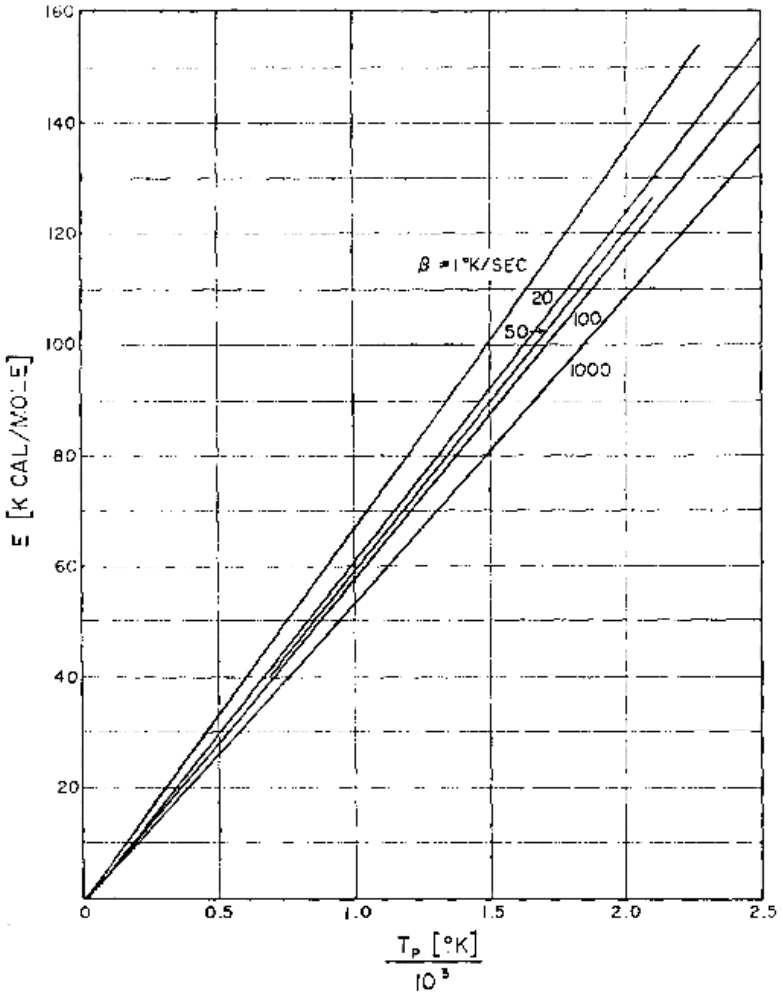

Figure 2.4: E_a as a function of T_P for a first order desorption event and a linear temperature ramp rate. $A=10^{13}\ s^{-1}$[8]

Another common approach is called Redhead analysis, which uses T_p and an assumed preexponential factor to calculate E_a. At T_p, $\frac{d^2\theta}{dT^2} = 0$, therefore the derivative of Equation 2.6 at T_P can be expressed as Equation 2.9.[8]

$$\frac{E_a}{RT_P^2} = \frac{A}{\beta} n\theta^{n-1} \exp\left(-\frac{E_a}{RT_P}\right) \tag{2.9}$$

Therefore, for a 1st order desorption event, one can simplify this Equation 2.9 to Equation 2.10.

$$\frac{E_a}{RT_P^2} = \frac{A}{\beta}\exp\left(-\frac{E_a}{RT_P}\right) \tag{2.10}$$

By taking the natural log of both sides and solving for the E_a in the exponential, one can obtain equation 2.11.

$$E_a = RT_P\left(\ln\left(\frac{AT_P}{\beta}\right) - \ln\left(\frac{E_a}{RT_P}\right)\right) \tag{2.11}$$

The term containing the natural log of E_a is relatively small compared to the first term, and E_a is linear with T_P (Figure 2.4).[8]

As such, we can simplify Equation 2.11 to Equation 2.12.

$$E_a = RT_P\left(\ln\left(\frac{AT_P}{\beta}\right) - 3.46\right) \tag{2.12}$$

Equation 2.12 is quick method to estimate E_a from a single TPD spectrum, but it is not very precise due to the assumptions that A and E_a are coverage independent, and A is usually assumed to be 10^{13} s^{-1}.[8]

A more rigorous method involves performing several TPDs at different β and plotting the data in the form of Equation 2.13 (a rearrangement of Equation 2.11).

$$\ln\left(\frac{\beta}{RT_P^2}\right) = \frac{-E_a}{RT_P} + \ln\left(\frac{\mathrm{A}}{\mathrm{E_a}}\right) \tag{2.13}$$

Different β results in different T_P, and based on these changes, one can determine E_a from the slope, and A from the intercept. This method is more accurate than Redhead analysis because it does not assume a value for A. The extracted parameters are ultimately the average parameter during desorption, and does not describe the coverage dependent changes in E_a or A. In order to examine changes in E_a and A as a function of coverage, the same experiments would need to be performed at a variety of initial coverages. Ultimately, many TPD spectra are required to fully describe the coverage dependent desorption of an adsorbate from a surface.[9]

The rate of 2nd order TPDs is 2nd order with coverage and will increase with temperature until coverages are small enough that rates start to drop. It is well described by Equation 2.14, and simulated spectra for different initial adsorbate coverages is presented in figure 2.5.

$$-\frac{d\theta}{dT} = \frac{\theta^2}{\beta} A \exp\left(\frac{E_a}{RT}\right) \tag{2.14}$$

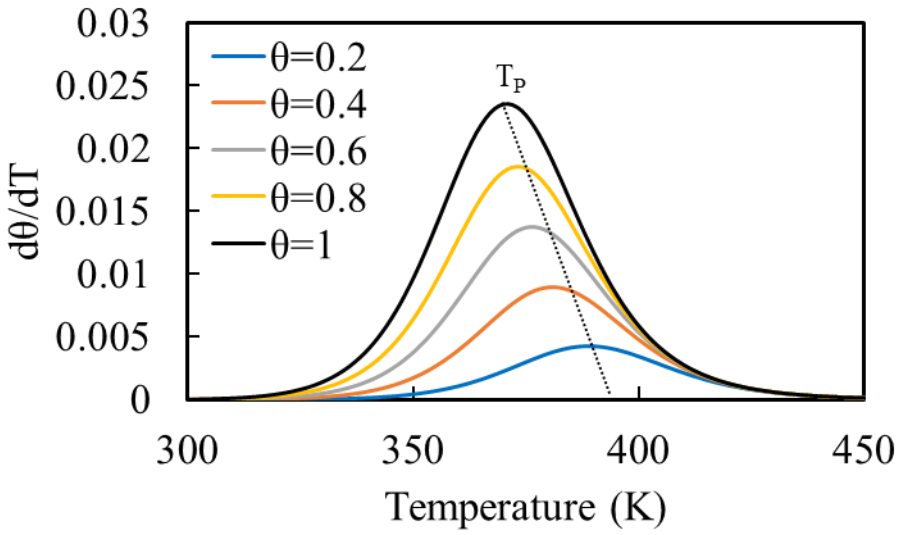

Figure 2.5: Simulated TPD spectra of a 2nd order TPD for different initial adsorbate coverages. The dashed line represents the change in the maximum temperature of desorption (T_P) with increased initial coverage. Parameters for simulation: E_a=100 kJ/mol, A=10^{13} s^{-1}, β= 1 K/s. It was assumed that E_a and A are constant at all coverages.

2nd order TPDs result in symmetric desorption spectra, but T_P shifts to higher temperatures at lower initial coverages. These spectra are usually interpreted in one of two ways. Like with the other orders of TPD spectra, line shape analysis can be used by fitting the initial desorption behavior to the form of Equation 2.14. This is again useful for determining kinetic parameters at the onset of desorption, but significant changes in kinetics can occur at different coverages, such that this information is limited to initial desorption behavior. This can, to some extent, be compensated for by repeating this analysis for a variety of different initial coverages.

Alternatively, by once again assuming that $\frac{d^2\theta}{dT^2} = 0$ at T_P and using Equation 2.9, we can get Equation 2.15

$$\frac{E_a}{RT_P^2} = \frac{A}{\beta} 2\theta \exp\left(-\frac{E_a}{RT_P}\right) \tag{2.15}$$

Unfortunately, since T_P changes with coverage, θ is a function of T_P which makes the same analysis that is used for the 1st order TPDs impossible. Fortunately, one can exploit the symmetry of 2nd order TPD spectra to assert that $\theta(T_P) = \frac{1}{2}\theta_i$, yielding Equation 2.16.[10]

$$\frac{E_a}{RT_P^2} = \frac{A}{\beta} \theta_i \exp\left(-\frac{E_a}{RT_P}\right) \tag{2.16}$$

Rearranging and taking the natural log yields Equation 2.17

$$ln\left(\frac{\beta}{k_B T_P^2}\right) = \frac{-E_a}{k_B T_P} + ln\left(\frac{A\theta_i}{E_a}\right) \tag{2.17}$$

Different β results in different T_P, and based on the slope of these changes, one can determine E_a from the slope, and A from the intercept. Again, the extracted parameters are ultimately the average parameter during desorption, and does not describe the coverage dependent changes in E_a or A. Further, E_a and A can defined in terms of activation enthalpies ($\Delta H^{\ddagger}$) and entropies ($\Delta S^{\ddagger}$). To examine changes in these parameters as a function of coverage, the same experiments would need to be performed at a variety of initial coverages.

2.2 TEMPERATURE PROGRAMMED DESORPTION OF NON-MODEL SURFACES

The previous section examined simulated data which might be comparable to some model systems, but non-model systems (generally catalyst surfaces) are often more complex. While there are myriad complications that can occur during these experiments, this section will

focus on two specific aspects: (i) heterogeneity in adsorption sites, and (ii) readsorption of desorbed species in diffusion limited systems.

2.2.1 Heterogeneity in Adsorption Sites

Real heterogeneous catalysts typically consist of supported metals or solid acids, of which, the support, and supported metals can exhibit heterogeneity in the strength/type and abundance of adsorption sites. Additionally, catalysts may contain adsorbed species that cannot be removed before TPDs without irreversibly changing the examined material. As such various analytical/experimental methods have been developed to separate the influence of heterogeneity.

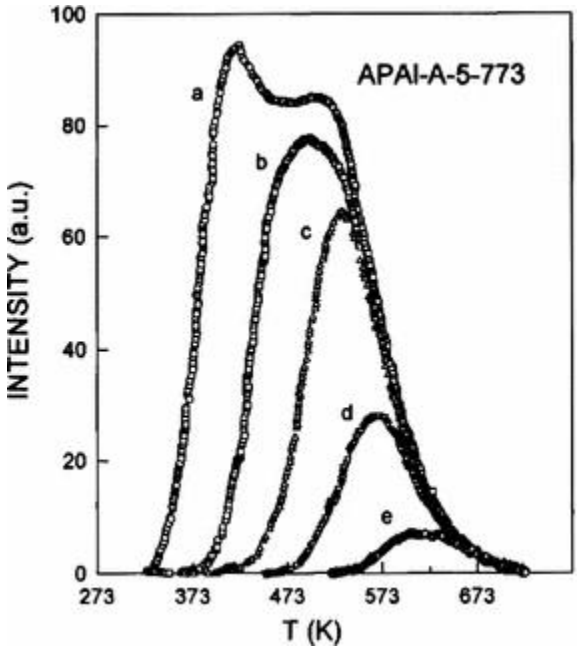

Figure 2.6: TPD spectra of pyridine adsorbed on $AlPO_4$-Al_2O_3. Pyridine was adsorbed at different temperatures, to selectively fill only stronger acids sites. The adsorption temperatures are as follows: (a) 50°C (b)100°C (c) 150°C (d) 200°C (e) 300°C. [11]

Solid acids are useful for demonstrating these phenomena, as they often exhibit a distribution of acid sites with different strengths. This results in TPD spectra without well-defined peaks, and therefore defining a T_P becomes challenging. One method frequently used to differentiate adsorption sites of different strength, is to perform several TPD experiments,

introducing the probe species at incrementally higher temperatures, such that weaker adsorption sites will desorb the probe molecule at adsorption temperature, and won't be observed during the TPD itself. This is well demonstrated by Figure 2.6, in which TPD spectra are shown for pyridine adsorbed at different temperatures, and subsequently desorbed on a $AlPO_4$-Al_2O_3 solid acid.[11] By subtracting out the areas associated with stronger acids sites, one can quantify the abundance of acid sites of different strength.

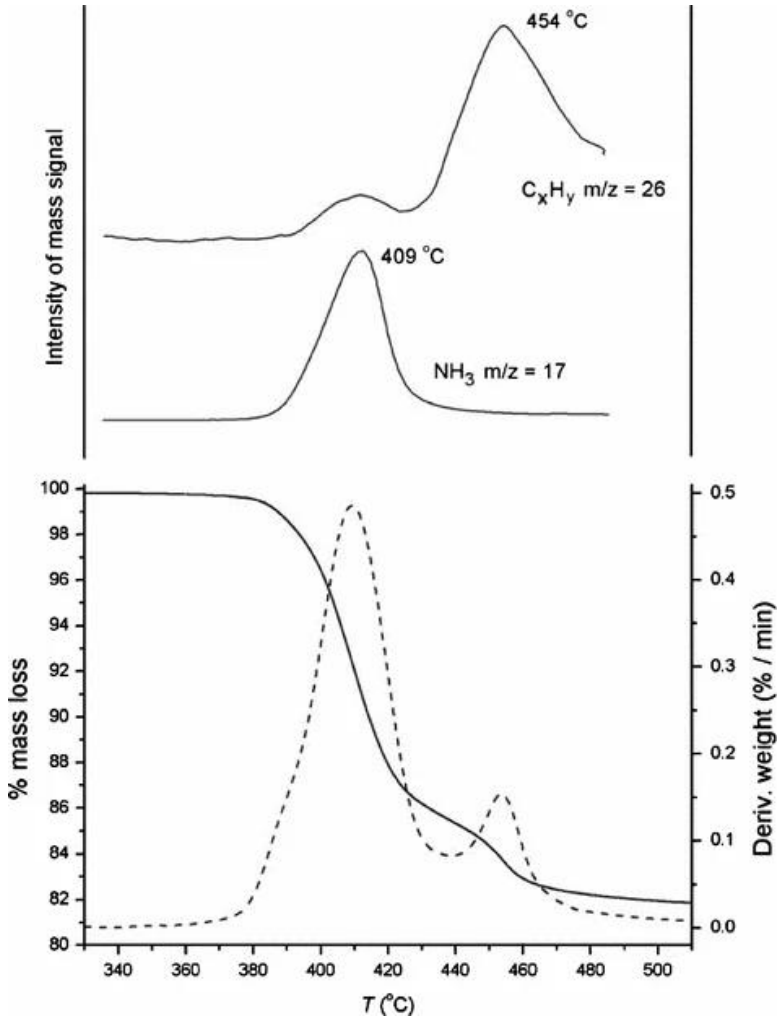

Figure 2.7: (Top) TPD spectra of (1,2-diaminopropane) decomposed inside of $(ZnPO_4)_2$. MS was used to differentiate NH_3 and hydrocarbon desorption. (Bottom) TGA during the TPD experiment.[12]

Another situation that may occur is that more complex surface events may occur during TPD experiments, resulting in more than one desorption feature and different species desorbing.[12] Figure 2.7 presents a TPD spectra, in which the probe molecule (1,2-

diaminopropane) decomposed inside of $(ZnPO_4)_2$, then desorbed as two separate species (NH_3 and hydrocarbons). Interestingly, the TPD experiment was performed using a thermogravimetric analysis (TGA) instrument, which allowed for the change in sample mass to be observed during desorption, while the desorbed species were tracked and identified using MS, allowing for differentiation of NH_3 and hydrocarbon desorption.

2.2.2 Readsorption in Flow Systems

The methods presented above rely on the assumption that desorption is the only kinetically relevant step, such that extrapolated parameters represent only the desorption processes. In UHV systems, this assumption is almost always valid, as samples are usually thin layers, such that mass transfer (diffusion) is negligible, and readsorption can be avoided by maintaining a sufficiently high pumping efficiency. Conversely, in flow systems, samples will have significant volumes, and can have significant mass transfer limitations. This can result in situations where desorbed species can readsorb, resulting in shifts in T_P to significantly higher temperatures. Interpreting this data in the traditional manner would result in overestimates of the binding energy of adsorbates. Porous samples can significantly reduce the effective diffusion coefficients of desorbed species inside of support particles. This occurs when the mean path length of diffusion of an unconstrained gas is on the order of sample pore diameter. In such a case, models for Fickian diffusion no longer accurately describe the mass transfer inside of the pores, and models for Knudsen diffusion should be used instead. As a rough approximation, the Knudsen diffusion coefficient inside of a sample with pore diameters smaller than the mean path length of diffusion is the Fickian diffusion coefficient multiplied by the ratio of the pore diameter to the mean path length.[3,6] The mean path length is a function of temperature, but for small probe molecules, is usually on the order of ~70 nm at

100°C. In such a scenario, desorbed species can accumulate inside of the pores faster than they can exit the sample, such that readsorption will occur.

Significant efforts have been made to define parameters to determine if readsorption will occur in flow systems.[13] In particular, four parameters have been identified as particularly relevant to the quality of kinetic parameters extracted via TPDs. Firstly, the average residence time of a gas in the sample cell determines the lag time between desorption events and detection of adsorbate gases from a non-diffusion limited sample (Equation 2.18)

$$\frac{V\beta}{Q\left(T_f - T_0\right)} \tag{2.18}$$

Where: V= Sample cell volume (cm^3)
Q= Carrier gas flow rate (cm^3/s)
T_f= Final Temperature of TPD experiment (K)
T_0= Initial Temperature of TPD experiment (K)

The parameter defined by Equation 2.18 should be less than 0.01 in order for the cell concentration of desorbed species to follow the net rate of desorption. This parameter can easily be adjusted into an acceptable regime by lower temperature ramp rates or increasing inert flow rates.

The second parameter, (Equation 2.19) describes the effect of carrier gas flow rates on concentration gradients inside of the catalyst pellet.

$$\frac{rQ}{DA} \tag{2.19}$$

Where: r= Catalyst pellet radius or length of catalyst bed (cm)
D=Effective diffusivity of the gas (cm^2/s)
A=External surface area of catalyst pellets (cm^2)

The parameter defined by Equation 2.19 should be less than 0.1 in order for the cell concentration of desorbed species to follow the net rate of desorption, such that the difference in concentration of desorbed species only varies by ~5% from the center of the particle to the

edge. In such a case, the rates of adsorption and desorption should not depend on the position within the catalyst particle. This limit is usually the case for vacuum systems but can be difficult to achieve in flow systems due to the low flow rates required. At flow rates above this limit, the shape and temperature of desorption features is a strong function of carrier flow rates. Fortunately, there is another limit at which the parameter is greater than 20, for which the shape and temperature are no longer functions of carrier gas flow rates.

The third parameter (Equation 2.20) describes the accumulation of desorbed species inside of catalyst pores. This should be minimized to reduce concentration gradients.

$$\frac{\beta r^2 \epsilon}{(T_f - T_0)D} \tag{2.20}$$

Where: ϵ= catalyst pellet void fraction

The parameter defined by Equation 2.20 should be maintained below 0.01 to ensure that the bulk cell concentration is not significantly different than the concentration inside of the pores. This can be difficult for large catalyst particles with small pores but can be mitigated to some extent by choosing low temperature ramp rates.

Finally, the fourth parameter (Equation 2.21) describes the ratio of adsorption rates to diffusion rates in the infinite carrier gas flow rate regime (when Equation 2.19 >20), and ultimately informs on whether readsorption is significant. This parameter should only be evaluated after the other three parameters have been satisfied.

$$\frac{\alpha \rho S F r^2}{\pi^2 D} \tag{2.21}$$

Where: α=active surface area of sample (cm^2/g)
ρ=bulk catalyst density (g/cm^3)
S=sticking coefficient
F=The velocity of a molecule at a given temperature (cm/s)

The sticking coefficient, S, represents the probability that a molecule at a surface will adsorb (as such it is always a number between 0 and 1). For a barrierless adsorption, S is assumed to be a constant with temperature, while the sticking coefficient for an activated adsorption can be described by Equation 2.22.

$$S = S_0 \exp\left(-\frac{E_a^{ads}}{RT}\right) \tag{2.22}$$

Where: S_0= Sticking coefficient for a barrierless adsorption
E_a^{ads}=Activation energy for desorption (J/mol)

The gas velocity (F) can be determined via Equation 2.23.

$$F = \left(\frac{RT}{2\pi M}\right)^{\frac{1}{2}} \tag{2.23}$$

Where: M= The molecular weight of the adsorbing/desorbing species (g/mol)

For readsorption to be important, the parameter defined in Equation 2.21 must be $\geq$1 such that readsorption rates are higher than diffusion rates. Unfortunately, for a specific sample, few of the parameters can be easily altered to decrease readsorption rates or increase diffusion rates. Diluting the sample can reduce the active surface area of a catalyst per gram of bed, but this subsequently can increase the total sample volume while simultaneously decreasing the number of active sites in a sample. Too little active surface in a sample can make detection of desorbed species difficult. The other term that can be altered is the particle radius (or bed length for larger chunks of porous solids). Breaking porous particles into smaller particles can drastically improve diffusion rates, but it is challenging to reduce particles to sub-micron sizes. In the case of a large solid sample, decreasing the bed length may result in insufficient sample for characterization.

Ultimately, for many porous materials, the length scales at which readsorption becomes relevant is <100 microns. It is difficult to prepare samples in flow systems that are below this threshold, such that alternative methods of detection may be required to perform TPD experiments.

2.3 DIFFUSE REFLECTANCE FOURIER-TRANSFORM SPECTROSCOPY MONITORED TPDS FROM ATOMICALLY DISPERSED RH

In the following chapters of this dissertation, TPDs are used to probe the activation entropies and energies of desorption from $Rh(CO)_2$ supported on γ-Al_2O_3. Unlike traditional TPD methods, the coverage of adsorbed species was tracked by monitoring the area of the Fourier-transform infrared spectroscopy (FTIR) stretches associated with CO adsorbed on Rh collected in a diffuse reflectance infrared Fourier-transform spectroscopy (DRIFTS) apparatus. During this technique. the top of a packed catalyst bed is probed with IR light. This technique provides several advantages and some disadvantages compared to traditional detection methods.

2.3.1 Advantages and Disadvantages Compared to Traditional Temperature Programmed Desorption

The most significant advantage of monitoring TPDs via FTIR is that the coverage of an adsorbate on different kinds of sites can be distinguished, meaning that desorption features that may be indistinguishable from each other using traditional methods, can be attributed to specific adsorption sites. For example, CO adsorbed on Rh/Al_2O_3 can exhibits multiple stretches that depend on the structure of Rh. Figure 2.8 presents an FTIR spectra of CO adsorbed on atomically dispersed Rh species, as well as on Rh nanoparticles.[14] $Rh(CO)_2$

exhibits unique CO stretches in FTIR spectra that are differentiable from linear and bridge-bound CO on Rh clusters.[14–21] $Rh(CO)_2$ supported on γ-Al_2O_3 presents symmetric and asymmetric CO stretches at ~2090 cm^{-1} and ~2020 cm^{-1}, respectively, while CO adsorbed to Rh clusters exhibits a linear bound CO stretch at ~2050 cm^{-1}, and a wide bridge bound CO stretch at ~1800 cm^{-1}.[17,22] During a TPD, these FTIR features can be individually monitored to distinguish the relative abundances of different adsorbed species.

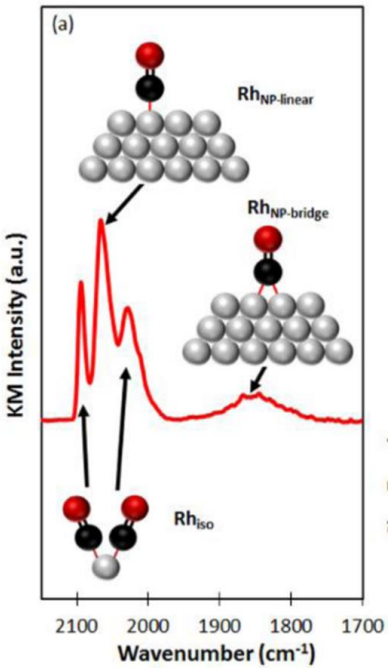

Figure 2.8: FTIR spectra of CO adsorbed on Rh/γ-Al_2O_3. CO on different Rh structures exhibit different stretching frequencies. Atomically dispersed $Rh(CO)_2$ exhibits two stretches (a symmetric and asymmetric stretch), while CO on nanoparticles exhibit a sharp linear stretch if CO is adsorbed in an atop configuration, or a broad bridgebound feature if CO is adsorbed to two Rh atoms.[14]

While FTIR detected TPD experiments are useful for discriminating the active site structures that adsorbates bind to, there are some disadvantages to this technique. For adsorbates on nanoparticles, stretch areas may not decrease linearly with coverage as the extinction coefficient of the adsorbate may change with coverage. Additionally, the total amount of sample being probed is poorly defined due to unknown path lengths inherent to these experiments (discussed more in section 2.3.3). Fortunately, the atomically dispersed

species examined in this dissertation should be non-interacting, such that extinction coefficients are constant as a function of CO coverage.

2.3.2 Readsorption of CO during TPDs from Atomically Dispersed $Rh(CO)_2$

Kinetic parameters extracted from TPDs using DRIFTS experiments are central to the arguments presented in the following chapters. As such, it is important to demonstrate that readsorption is unlikely to be significantly influencing desorption temperatures. The catalyst of interest is atomically dispersed Rh (0.25% W/W) on non-porous, 5 nm diameter spherical γ-Al_2O_3. Although the support material is non-porous, a bed of 5nm particles may be best modeled as a slab of catalyst, with pore diameters on the order of 5nm.This material is packed into a ¼ inch ID tube, typically with a thickness of ~0.3 cm. For such a system, we can calculate the parameters introduced in section 2.2.2.

Equation 2.18 describes how well the cell concentration of desorbed species corresponds with the net rate of desorption. This parameter is likely unimportant when using FTIR to monitor adsorbed species but will be relevant if a second detector was downstream of the DRIFTS cell. For the sake of exercise, we will calculate the parameter for this system. For nearly all experiments, β=0.33 K/s, V≈0.03 cm^3, T_F=723 K, T_0=323 K, and Q=1.7 cm^3/s. Plugging those parameters into Equation 2.18, results in a value of ~$4.7 \cdot 10^{-5}$, which is below the recommended maximum of 0.01.

Equation 2.19 describes the concentration gradient within a porous material. To calculate this parameter, both the external catalyst surface area and the effective diffusivity must be calculated. Since we are treating the catalyst bed as a slab of porous material, the external surface area is just the outside surfaces of the bed (top and bottom). The external surface area, A≈0.63 cm^2. As for the effective diffusivity, we will approximate that by

assuming that the mean path length of gases inside of the porous bed is 5nm, and that diffusivity decreases linearly with path length,[23] and scaling a known diffusivity value down to the value inside of the pores using Equation 2.24

$$D = D_{bulk} * \frac{\lambda_{pore}}{\lambda_{bulk}} \tag{2.24}$$

Where: D_{bulk}= Unrestricted gas phase diffusivity (cm^2/s)
λ_{pore}=Average path length of gas inside of porous medium (cm)
λ_{bulk}=Average path length of unrestricted gas (cm)

An experimentally determined D_{Bulk} for a mixture of CO and Ar at 300°C (near the temperature of maximum desorption occurs in these samples) is 0.615 cm^2/s.[24] Now we must calculate the mean free path of CO in an unconstrained system using Equation 2.25. This equation assumes that CO is dilute in Ar.

$$\lambda_{bulk} = \frac{RT}{\sqrt{2} * \pi d_{CO-Ar}^2 N_A P} \tag{2.25}$$

Where: d_{CO-Ar}=Average diameter of CO and Ar molecules (cm)
N_A= Avogadros Number (molecules/mol)
P= Pressure (J/cm^3)

d_{CO-Ar} can be calculated using Equation 2.26 from the known kinetic diameters of Ar and CO of 340 and 376 pm, respectively.

$$d_{CO-Ar} = \frac{d_{Ar} + d_{CO}}{2} \tag{2.26}$$

Where: d_{Ar}=Diameter of Ar (cm)
d_{CO}=Diameter of CO (cm)

This results in a collision diameter of 358 pm. Plugging the values into Equation 2.25 results in an unconstrained mean free path of 137 nm. From Equation 2.24, we obtain an effective diffusivity of 0.02 cm^2/s. Calculating the parameter defined by Equation 2.19, we obtain a value of ~23. This suggests that TPD spectra will not be a function of total flow rate.

Next, using Equation 2.20 we can calculate if desorbed species accumulation is significant inside of the catalyst bed. In this case, we are assuming a void volume of 0.5. From equation 2.20, we get a value of 0.002, which is below the maximum recommended value of 0.01.

Finally, with all other parameters satisfied, we can use Equation 2.21 to determine the bed length at which readsorption becomes relevant. First, we will examine the base case, in which we have the 0.3 cm long bed. We must assume a sticking coefficient; to represent the worst-case scenario (the case in which readsorption is most likely), we will set S to 1. F for CO at 300°C is approximately 5.2 cm/s. The bulk density of this support is ~0.4 g/cm^3. The active surface area requires knowledge of the structure and dispersion of your active metal. Fortunately, as all Rh in these samples are atomically dispersed, we can calculate it relatively easily using Equation 2.27. This assumes that half of all Rh atom surface is available.

$$\alpha = \frac{x_{Rh}}{8M_{Rh}} N_A \pi d_{Rh}^2 \tag{2.27}$$

Where: x_{Rh}=mass fraction of Rh in sample (g_{Rh}/g)
M_{Rh}=Molecular Weight of Rh (mol/g)
d_{Rh}=Atomic diameter of Rh (cm)

This yields an active surface area of ~34000 cm^2/g. Evaluating Equation 2.21, a value of ~3 million is obtained, suggesting that readsorption is a significant issue when the catalyst bed is 0.3 cm. To evaluate at which length of bed readsorption becomes significant, we can set Eq 2.21 to unity, and solve for the bed length (Equation 2.28).

$$r = \sqrt{\frac{D\pi^2}{\alpha \rho S F}} \tag{2.28}$$

This yields a value of 0.0018 cm, or 18 microns in length. This suggests that using traditional TPD detection methods, our bed would need to be extremely thin. This means to validate the

kinetic parameters obtained via TPDs using DRIFTS, we must establish the bed depth that is being probed.

2.3.3 Evaluation of Sampling Depth in DRIFTS Measurements

To evaluate the sampling depth, we must first discuss the mechanisms by which the light interacts with the catalyst bed. DRIFTS experiments have poorly defined path lengths due to the variety of pathways that the incident IR light can travel upon contact within a sample. Figure 2.9 presents an illustration of the behavior of incident IR light on a bed of packed particles.[25] Ultimately, there are four pathways for incident light: (1) specular reflectance (an initial reflectance off of the bed surface with no subsequent reflections), (2) diffuse reflectance (reflects off of the outside of particles in such a way that the light travels deeper into the bed), (3) transmission (the light travels through the particle), and (4) absorption (the light is extinguished by a strong absorber (the adsorbate of interest) or via weak absorption from the support particles). Ultimately, the incident light takes a variety of paths, the relative abundance of which is dependent on the optical properties of the sample material.

A particularly relevant parameter in evaluating the sampling depth for DRIFTS experiments is the size of the individual catalyst particles relative to the wavelength of light (Equation 2.29).[26,27] In the FTIR region of interest (~2000 cm^{-1}), the wavelength of light is ~5 microns.

$$x = \frac{2\pi r_p}{L} \tag{2.29}$$

Where: x=dimensionless parameter to characterize light-matter interactions
r_p=radius of particle (cm)
L=wavelength of incident light (cm).

The scattering behavior of light will fall into three mechanisms depending on the value of x. When x>>1, light will scatter off geometric shapes in the manners expected and described by the Fresnel equations. In DRIFTS experiments, we would expect significant diffuse reflectance contributions to the spectra, as light should be able to enter and leave the bed with relative

ease. Unfortunately, a complete analytical mathematical description of diffuse reflectance is not available, but various computational methods have been developed to model this behavior, called Lambertian reflectance.

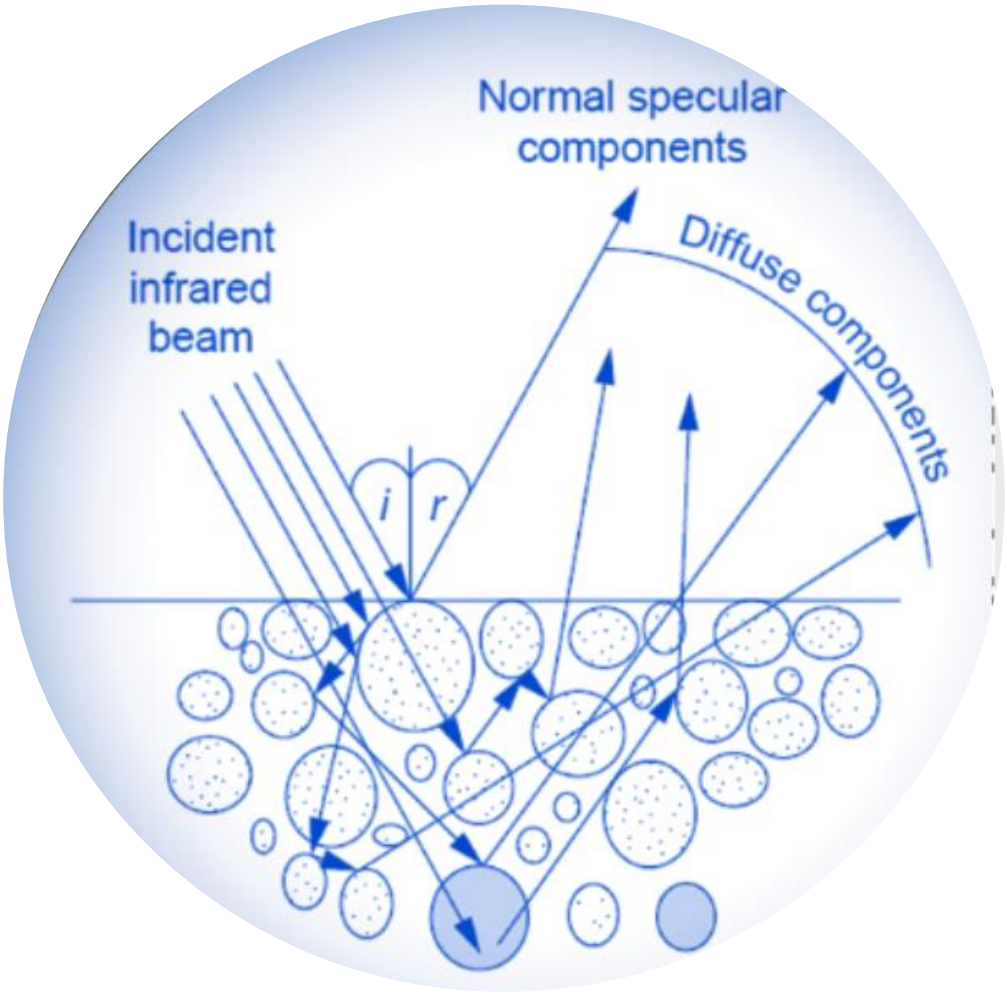

Figure 2.9: Illustration of the variety of pathways an incident IR beam may take during DRIFTS experiments. Due to the distribution of path lengths, resulting FTIR spectra cannot be used to quantitatively describe the absolute concentration of adsorbates in a sample.[25]

When x≈1, Mie scattering mechanisms are dominant. In Mie scattering, light reflects in a probabilistic manner in many directions. Due to the significant likelihood of scattering events deeper into the bed, we would expect IR light to probe non-negligible depths. There are analytical solutions to these scattering problems, but each solution only describes the behavior

of light at specific distances from the scattering particle. As such, these problems are generally modeled computationally.

When x<<1 (usually less than 1/10th), Rayleigh scattering mechanisms dominate. As x decreases, the probability that light will scatter off a particular particle drastically decreases. The scattering probability of light scattering off of small particles is described by Equation 2.30.

$$\sigma = \frac{2\pi^5}{3}\frac{\left(2r_p\right)^6}{L^4}\left(\frac{n^2-1}{n^2+2}\right) \tag{2.30}$$

Where: σ=Rayleigh scattering cross-section (cm^2)
n=Refractive index of the particle

For the samples probed via TPD in this dissertation, the incident light is ~5 microns, while the support particles are ~5 nm. As such, it should be appropriate to model the light-particle interactions as Rayleigh scattering. In such a scenario, the catalyst bed can be treated as a homogeneous medium for light transmission, in which there is an initial specular reflection off the top of the bed, with secondary reflections from Rayleigh scattering. Assuming a refractive index of 1.728 for Alumina,[28] the Rayleigh scattering cross section is ~8·10^{-32} cm^2. The fraction of light scattered via Rayleigh scattering per unit distance traveled is described by Equation 2.31.

$$\sigma_L = \sigma n \tag{2.31}$$

Where: σ_L= probability of light scattering per distance traveled (1/cm)
n= number density of scattering particles per unit volume (1/cm^3)

This results in a value of 0.0001 cm^{-1}, suggesting that essentially no light is scattered inside of the catalyst bed.

The previous calculations establish that negligible scattering will occur inside the catalyst bed during DRIFTS experiments, meaning that diffuse reflectance should be

negligible. This suggests that incident light will reflect off the bed surface, with some fraction transmitting into the bed. To account for the light that transmits into the bed, we can model the attenuation of the IR light in a "solid" bed of alumina using Equation 2.32.

$$\frac{I}{I_0} = \exp(-k_{abs}z) \tag{2.32}$$

Where: I=Final intensity of light after attenuation (J/(cm^2 s))
I_0=Initial intensity of light before attenuation (J/(cm^2 s))
k_{abs}= the absorption coefficient (cm^{-1})
z= distance transmitted (cm)

Assuming an absorption coefficient of 804 cm^{-1}, we would expect less than 10% of the light intensity to remain after traveling 30 microns. This means that any IR light that is not initially reflected at the surface of the bed is unlikely to ever leave the catalyst bed. From these calculations, we can conclude that DRIFTS of very small particles (5nm in this case) is likely only probing the very surface of the bed, such that readsorption should not be an issue.

2.4 CONCLUSION

In this chapter we have briefly discussed the theory and application of TPDs in extracting kinetic and thermodynamic parameters of adsorption/desorption processes. Additionally, we discussed common issues encountered in TPD experiments and some strategies to overcome these issues. After discussing these traditional TPD methods, we introduced FTIR monitored TPD techniques that will be used in the following chapters to investigate adsorbate behavior. We demonstrated calculations that support the validity of this methodology, such that parameters extracted via this method should be accurate. This chapter is a contribution to this thesis to introduce this approach that is useful for characterizing atomically dispersed metals on small support particles.

2.5 REFERENCES

[1] J. Rouquerol, F. Rouquerol, P. Llewelly, G. Maurin, K. Sing, Adsorption by Powders and Porous Solids, Elsevier, 2014. https://books.google.com/books?hl=en&lr=&id=UOE-ZscCYncC&oi=fnd&pg=PP1&ots=0T__KyrolA&sig=MF9qgJS49MZdATUO6vTz_WxHtPU#v=onepage&q&f=false (accessed November 16, 2022).

[2] D. Ruthven, Principles of Adsorption and Adsorption Processes , John Wile and Sons, 1984. https://books.google.com/books?hl=en&lr=&id=u7wq21njR3UC&oi=fnd&pg=PR17&ots=wcYvQnCiuT&sig=_kaYTm0smtRpLgC8hCd5eNIJ8bE#v=onepage&q&f=false (accessed November 16, 2022).

[3] V. Rakić, L. Damjanović, Temperature-Programmed Desorption (TPD) Methods, Springer Ser. Mater. Sci. 154 (2013) 131–174. https://doi.org/10.1007/978-3-642-11954-5_4/FIGURES/20.

[4] M. Doronin, M. Bertin, X. Michaut, L. Philippe, J.H. Fillion, Adsorption energies and prefactor determination for CH3OH adsorption on graphite, J. Chem. Phys. 143 (2015) 084703. https://doi.org/10.1063/1.4929376.

[5] I. Chorkendorff, J. Niemantsverdriet, Concepts of Modern Catalysis and Kinetics, 3rd ed., Wiley-VCH Verlag GmbH & Co. KGaA, Weinheim, 2017. https://books.google.com/books?hl=en&lr=&id=OE0nDwAAQBAJ&oi=fnd&pg=PP2&ots=jQ9bfThtSX&sig=Ul2wYcX27kpa5elsf6jjbdchUwo#v=onepage&q&f=false (accessed December 12, 2022).

[6] J.M. Kanervo, T.J. Keskitalo, R.I. Slioor, A.O.I. Krause, Temperature-programmed desorption as a tool to extract quantitative kinetic or energetic information for porous catalysts, J. Catal. 238 (2006) 382–393. https://doi.org/10.1016/J.JCAT.2005.12.026.

[7] R.S. Smith, J. Matthiesen, B.D. Kay, Desorption kinetics of methanol, ethanol, and water from graphene, J. Phys. Chem. A. 118 (2014) 8242–8250. https://doi.org/10.1021/jp501038z.

[8] P.A. Redhead, Thermal desorption of gases, Vacuum. (1962). https://doi.org/10.1016/0042-207X(62)90978-8.

[9] J.L. Falconer, R.J. Madix, Flash desorption activation energies: DCOOH decomposition and CO desorption from Ni (110), Surf. Sci. 48 (1975) 393–405. https://doi.org/10.1016/0039-6028(75)90414-8.

[10] J.A. Konvalinka, J.J.F. Scholten, J.C. Rasser, Analysis of second-order desorption kinetics in temperature-programmed desorption, J. Catal. 48 (1977) 365–373. https://doi.org/10.1016/0021-9517(77)90110-5.

[11] J.M. Campelo, A. Garcia, D. Luna, J.M. Marinas, A.A. Romero, Characterization of acidity in AlPO4□Al2O3 (5–15 wt% Al2O3) catalysts using pyridine temperature programmed desorption, Thermochim. Acta. 265 (1995) 103–110. https://doi.org/10.1016/0040-6031(95)02379-G.

[12] D. Stojakovic, N. Rajic, V. Rakic, N.Z. Logar, V. Kaucic, Structure and thermal behavior of the layered zincophosphate [NH3–CH2–CH(NH3)–CH3](ZnPO4)2, Inorganica Chim. Acta. 362 (2009) 1991–1995. https://doi.org/10.1016/J.ICA.2008.09.020.

[13] R.J. Gorte, Design parameters for temperature programmed desorption from porous

catalysts, J. Catal. 75 (1982) 164–174. https://doi.org/10.1016/0021-9517(82)90131-2.
[14] J.C. Matsubu, V.N. Yang, P. Christopher, Isolated metal active site concentration and stability control catalytic CO2 reduction selectivity, J. Am. Chem. Soc. 137 (2015) 3076–3084. https://doi.org/10.1021/ja5128133.
[15] Y. Kwon, T.Y. Kim, G. Kwon, J. Yi, H. Lee, Selective Activation of Methane on Single-Atom Catalyst of Rhodium Dispersed on Zirconia for Direct Conversion, J. Am. Chem. Soc. (2017). https://doi.org/10.1021/jacs.7b11010.
[16] J.T. Yates, K. Kolasinski, Infrared spectroscopic investigation of the rhodium gem-dicarbonyl surface species, J. Chem. Phys. (1983). https://doi.org/10.1063/1.445844.
[17] J.T. Yates, T.M. Duncan, S.D. Worley, R.W. Vaughan, Infrared spectra of chemisorbed CO on Rh, J. Chem. Phys. (1979). https://doi.org/10.1063/1.437603.
[18] T.M. Duncan, J.T. Yates, R.W. Vaughan, A 13C NMR study of the adsorbed states of CO on Rh dispersed on Al203, J. Chem. Phys. (1980). https://doi.org/10.1063/1.440746.
[19] C. Asokan, L. Derita, P. Christopher, Using probe molecule FTIR spectroscopy to identify and characterize Pt - group metal based single atom catalysts, Chinese J. Catal. 38 (2017) 1473–1480. https://doi.org/10.1016/S1872-2067(17)62882-1.
[20] C. Asokan, Y. Yang, A. Dang, A. Getsoian, P. Christopher, Low-Temperature Ammonia Production during NO Reduction by CO Is Due to Atomically Dispersed Rhodium Active Sites, ACS Catal. 10 (2020) 5217–5222. https://doi.org/10.1021/acscatal.0c01249.
[21] C. Asokan, M. Xu, S. Dai, X. Pan, P. Christopher, Synthesis of Atomically Dispersed Rh Catalysts on Oxide Supports via Strong Electrostatic Adsorption and Characterization by Cryogenic Infrared Spectroscopy, J. Phys. Chem. C. (2022). https://doi.org/10.1021/ACS.JPCC.2C05426.
[22] R.R. Cavanagh, J.T. Yates, Site distribution studies of Rh supported on Al2O3 - An infrared study of chemisorbed CO, J. Chem. Phys. (1981). https://doi.org/10.1063/1.441544.
[23] C. Satterfield, Mass transfer in heterogeneous catalysis, MIT, Cambridge, 1969. https://www.worldcat.org/title/67597 (accessed January 9, 2023).
[24] T.R. Marrero, E.A. Mason, Gaseous Diffusion Coefficients, J. Phys. Chem. Ref. Data. 1 (1972) 3–118. https://doi.org/10.1063/1.3253094.
[25] C. Henry, DRIFTS Apparatus Diffuse Reflectance Infrared Fourier Transform Spectroscopy (DRIFTS), Southwest Res. Inst. 236 (2004). https://www.swri.org/sites/default/files/brochures/drifts.pdf (accessed January 9, 2023).
[26] A.J. Cox, A.J. DeWeerd, J. Linden, An experiment to measure Mie and Rayleigh total scattering cross sections, Am. J. Phys. 70 (2002) 620–625. https://doi.org/10.1119/1.1466815.
[27] C.F. Bohren, D.R. Huffman, Absorption and scattering of light by small particles, Wiley-VCH Verlag, 1983. https://doi.org/10.1088/0031-9112/35/3/025.
[28] M.R. (University of K. Querry, Optical Constants, (n.d.). https://apps.dtic.mil/docs/citations/ADA158623 (accessed December 11, 2020).

Chapter 3: Support Functionalization as an Approach for Modifying Activation Entropies of Catalytic Reactions on Atomically Dispersed Metal Sites

Adapted From Journal of Catalysis:

Gregory Zakem, Insoo Ro, Jordan Finzel, and Phillip Christopher
"Support Functionalization as an Approach for Modifying Activation Entropies of Catalytic Reactions on Atomically Dispersed Metal Sites", Journal of Catalysis ,404, 883-896, 2021

3.1 INTRODUCTION

The catalytic reactivity of extended metal surfaces,[1,2] supported metal nanoparticles,[3,4] and atomically dispersed metal catalysts[5,6] can be correlated to descriptors, such as elementary step reaction enthalpies.[7–12] These correlations leverage linear relationships between the adsorption enthalpies of similar reaction intermediates (scaling relations) and between elementary step reaction enthalpies and transition state enthalpies (Bronsted-Evans-Polanyi (BEP) relations), and can be further related to variations in the metal site electronic structure.[13] While this conceptual framework is useful for developing intuition and predicting compositions for catalyst optimization, it also imposes inherent limitations on how active or selective a catalyst can be.[14]

This has motivated a focus on creating active sites that deviate from the relationships described above. A variety of means have been used in attempts to "break" scaling relations, such as creating bifunctional sites with varying BEP or scaling relations,[15–17] introducing electronic promoters,[18] straining active sites,[19] or dynamically controlling active site characteristics,[20,21] among others.[22] These modifications attempt to decouple reaction enthalpies of similar adsorbates or reaction enthalpies and transition state enthalpies.

Another approach for enabling catalytic properties outside the bounds of predictions based on linear correlations of reaction and transition state enthalpies is selectively modifying activation entropies without influencing enthalpies. This requires breaking of another well-known correlation – the compensation effect between activation enthalpies and entropies.[23–25] The modification of apparent activation entropies has been observed in zeolites due to confinement effects, when pores that contain active sites are of a similar size to transition states.[25–28] As an example, for alkane cracking, the activation entropy can vary greatly with

carbon chain length, with minimal changes in activation enthalpies.[26] It remains less clear if activation enthalpies and entropies can be influenced in a decoupled manner by varying zeolite structure for a particular reaction.[26] The development of site selective placement of acid and metal sites in zeolites may allow such control over reaction kinetics, but this is still synthetically challenging.[26,29–34]

Apart from the use of inorganic micropores, supported metal active sites have also been confined using organic modifiers. Recent approaches have used thiols or other adsorbed modifiers on metal surfaces to influence the reactivity of vicinal unoccupied metal sites,[35–38] organic functionalization of oxide supports surrounding metal particles to modify the reactivity of interfacial sites,[39,40] or the placement of metal sites in organic frameworks.[41,42] However, it has remained challenging to elucidate the distinct influence of the modified local environment on reaction enthalpies and entropies due to the existence of a range of active site characteristics in each sample and interplay of the rates of apparent kinetics and diffusion.[43–46]

Here, we demonstrate that the functionalization of γ-Al_2O_3 with octylphosphonic acid (OPA) ligands (Figure 3.1) surrounding atomically dispersed Rh sites influences activation entropies of elementary steps (CO desorption) and catalytic cycles (ethylene hydroformylation) with minimal influence on reaction enthalpies. Support functionalization was observed to induce more facile desorption of adsorbed CO from Rh sites, and increases in turn over frequencies (TOF) for ethylene hydroformylation, which resulted in an improvement of selectivity towards the desired product, propanal. Changes in reactivity were correlated to changes in activation entropies through Eyring analysis of kinetic and temperature programmed desorption (TPD) measurements, suggesting that support functionalization

constrained the initial state (hindered the mobility of the active site) of kinetically relevant elementary steps. These results demonstrate that organic functionalization of supports surrounding atomically dispersed metal sites enables breaking of compensation relationships, suggesting this may be an effective strategy for the design of selective catalysts.

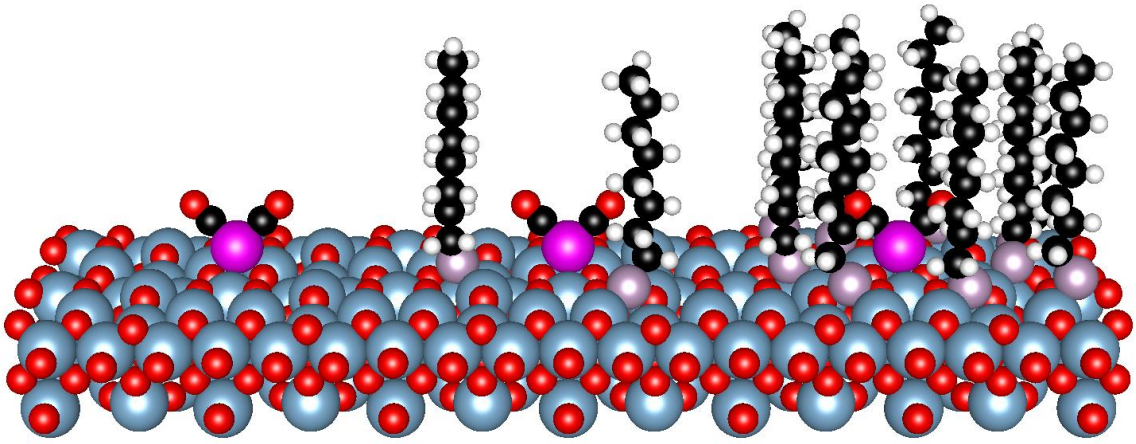

Figure 3.1: Illustration of atomically dispersed $Rh(CO)_2$ species on γ-Al_2O_3 with no OPA ligands (left), $Rh(CO)_2$ on a partially OPA covered γ-Al_2O_3 surface (center), and $Rh(CO)_2$ on γ-Al_2O_3 with a high OPA coverage (right). The color scheme for this schematic is: oxygen (red), aluminum (blue), rhodium (purple), carbon (black), hydrogen (white), and phosphorous (grey).

3.2 EXPERIMENTAL

3.2.1 Catalyst Preparation

Catalysts consisting of atomically dispersed Rh on γ-Al_2O_3 were prepared via a modified strong electrostatic adsorption (SEA) approach using rhodium (III) chloride hydrate (Sigma Aldrich, 206261) as a precursor.[47–49] 5 nm diameter γ-Al_2O_3 nanoparticles (US Research Nanomaterials, US3007) were used as the support to minimize the propensity for Rh cluster formation.[47,49,50] Catalysts were prepared in 1.5 g batches. A surface loading of 1200 m^2/L was used for Rh deposition (see Equation. 3.1). Rh precursor was dissolved in 40 mL of high-performance liquid chromatography (HPLC) grade water (JT4218-3, J.T. Baker) and the pH of the precursor solution was adjusted to a pH slightly over 10 by the addition of NH_4OH. 1.5 g of support was added in 110 mL of HPLC grade water and the suspension was

stirred well in a round-bottomed porcelain dish. The pH of the support suspension was adjusted to slightly over a pH of 10 using NH_4OH and allowed to equilibrate for 1.0 hour. Additional NH_4OH was added at the end of the equilibration to bring the pH back to slightly above 10. The 40 mL precursor solution was added via syringe pump to the support solution at a rate of 8.0 mL/hour. Additional NH_4OH was added as needed throughout injection to ensure that a pH of above 10 was maintained. After injection was complete, the catalyst suspension was heated to 80°C and allowed to evaporate while maintaining stirring. Dried catalyst was calcined at 623 K for 6 hours and stored in a sealed vial.

$$Surface\ Loading\ \left(\frac{m^2}{L}\right) = \frac{Surface\ Area\ of\ Support\left(\frac{m^2}{g}\right) * support\ mass\ (g)}{Total\ Volume\ of\ Solution\ (L)} \qquad (3.1)$$

Phosphonic acid functionalization of the oxide support was achieved via liquid phase condensation onto pre-prepared $Rh/\gamma\text{-}Al_2O_3$ catalysts.[40] An appropriate amount (see Equation 3.2) of either octylphosphonic acid (Sigma Aldrich, 735914) or 1H,1H,2H,2H-Perfluorooctanephosphonic acid (FOPA; Sigma Aldrich, 737461) was dissolved in a well stirred beaker of an appropriate volume (see Figure 3.4) of tetrahydrofuran (THF) (Sigma Aldrich, 401757). Catalyst was added to the THF solution and the suspension was stirred for 24 hours. The suspension was centrifuged to separate the solid catalyst and was washed with THF several times to remove physically bound phosphonic acids from the catalyst. The dried catalyst was then annealed at 120°C in air for at least 6 hours.

Following the synthesis procedures outlined by previous works,[40] we attempted to estimate the required loading for 1 monolayer of OPA by matching anchoring group cross-sectional areas with support area.

$$\text{Monolayer Mass} \approx \frac{\eta M m A}{N_A \pi R_{PO4}^2} \quad (3.2)$$

Where: η = Packing factor (dimensionless)
M= Molar Mass of the Phosphonic Acid (g/mol)
m= Mass of support (g)
A= Surface Area of Support (m^2/g)
N_A= Avogadro Number (molecules/mol)
R_{PO4}= Radius of a phosphate ion (m^2/mol)

Ultimately, the actual maximum coverage was less than the than the theoretical monolayer. The synthesis volumes were designed such that 1mM is equal to 1 theoretical monolayer mass. The coverages examined in this work (0,0.8, 2.1, and 3.2 P/nm^2) corresponded to 0, 0.1, 0.5, and 5 mM of OPA or FOPA respectively. This is in turn corresponds to 0, 0.1, 0.5, and 5 theoretical monolayers, respectively.

3.2.2 Catalyst Characterization

3.2.2.1 Fourier-Transform Infrared Spectroscopy (FTIR)

Catalysts were loaded into a Harrick Praying Mantis low temperature reaction chamber with ZnSe windows mounted inside of a Thermo Scientific Praying Mantis diffuse reflectance adapter set inside of a Thermo Scientific Nicolet iS10 FT-IR spectrometer with a mercury cadmium telluride (MCT) detector cooled by liquid nitrogen. All samples were measured in a diffuse reflectance infrared Fourier-transform spectroscopy (DRIFTS) configuration. All gases were passed across an isopropyl alcohol/liquid nitrogen cold trap and a glass trap filled with Drierite desiccant to remove trace moisture. Before characterization, catalysts were reduced at 250°C in 10% CO in Ar for 2.5 hours, then cooled to room temperature. The reaction cell was purged with Ar for 10 minutes before spectra were taken. In all measurements, spectra were obtained by averaging 32 scans at a resolution of 4 cm^{-1}. The interaction strength between CO and Rh was probed via temperature programmed desorption (TPD) experiments. Temperature

was increased from 50°C to 450°C at rates ranging from 5°C per minute to 60°C per minute in Ar. The number of scans per spectrum was varied from 8 to 32 based on the temperature ramp rate such that a spectrum was taken at least once per 10°C. Spectra at each temperature were baselined and fit using gaussian curves. A central finite difference method was used to calculate the numerical derivative of the peak area versus temperature.[51] The numerical derivative curve was fit to a bifurcated gaussian to determine the temperature of maximum desorption. Kinetic parameters were calculated using Equation 2. A derivation of this equation can be found in the appendix as Equation 3.6.1

3.2.2.2 Brunauer-Emmett-Teller (BET)

Support surface area was measured via nitrogen physisorption in a Micromeritics 3Flex Porosimeter. Supports were degassed at 350°C in vacuum before BET measurements.

3.2.2.3 Thermogravimetric Analysis (TGA)

A Discovery TGA 5500 was used to approximately determine the coverage of phosphonic acids and their stability in both oxidative and inert environments. OPA and FOPA functionalized catalysts were examined in both air and argon from 50°C to 900°C at a ramp rate of 5 °C /min.

3.2.2.4 Inductively Coupled Plasma Optical Emission Spectroscopy (ICP-OES)

To ensure no Rh leeching occurred during surface functionalization, a Thermo iCap 6300 ICP Emission Spectrometer was used to determine Rh loadings before and after functionalization. Additionally, ICP was used to determine OPA coverages. Samples were digested in aqua regia by reflux boiling or microwave digestion. Samples were filtered using 0.45 μm syringe filters PTFE membrane (Corning, 431231).

3.2.2.5 Dispersion Estimates

Rh dispersion on all Rh/Al_2O_3 samples was estimated using a Micromeritics AutoChem 2920 instrument. Approximately 200mg of each sample was purged with He (50cc/min) at room temperature. Samples were purged with He (50cc/min) at 200°C for 5 minutes and then reduced in H_2 (50cc/min) for 1 hour. Samples were then cooled to 50°C and purged in He (25cc/min) for 5 minutes. 10% CO in He (25cc/min) was flown through an injection loop. At 3-minute intervals, the injection valve was turned to introduce fixed volumes of CO to the sample. CO that was not adsorbed was detected using a thermal conductivity detector (TCD). Knowing the concentration of injected CO, the weight loading of Rh from ICP measurements, the mass of catalyst, and the data from the TCD allows for dispersion estimates. It was assumed that CO would bond to Rh in a 2:1 ratio because FTIR measurements indicated entirely atomically dispersed Rh species, which selectively form $Rh(CO)_2$ species.

3.2.3 Reactivity Measurements

Catalytic rates and selectivity for ethylene hydroformylation were evaluated in a fixed-bed quartz reactor (0.3025 Inch ID) in the temperature range of 140-170°C at atmospheric pressure. An ultra-high purity (UHP) grade reactant gas mixture of C_2H_4, H_2, and CO at a molar ratio of 1:1:1 was used with a total flow rate of 30 cc/min for all experiments. The CO gas was housed in an aluminum-lined cylinder to avoid potential contamination by iron and nickel carbonyls. Catalysts (50-300mg) were diluted in 0.5-3.0g of purified sand (SiO_2, Sigma Aldrich, 84878) to ensure that internal heat and mass transfer limitations were absent. Measurements of the influence of reaction rate on total flow rate, with constant partial pressures, evidenced no external mass transfer limitations.[50] Prior to reactivity measurements, catalysts were reduced in-situ in 10 cc/min CO at 250°C for 2.5 hours, and the

reaction was allowed to proceed for approximately 24 hours to allow for surface bound propanal species to saturate, as previously noted for this reaction.[52] Partial pressure dependence studies were conducted with flow rates of the gas of interest ranging from 3-10cc/min while balanced by helium to maintain partial pressure of other species and a total flow rate of 30c/min. All kinetic experiments were performed at least three times on catalysts synthesized at different times, and these repeat measurements were used to assess the uncertainties of extracted kinetic parameters. Products were quantified using an SRI Multiple Gas Analyzer #5 gas chromatographer equipped with a HayeSep-D packed column and FID detector.

3.3 RESULTS

3.3.1 Synthesis of Phosphonic Acid Modified Atomically Dispersed Rh/γ-Al_2O_3 Catalysts

With the motivation of designing heterogeneous, oxide supported hydroformylation catalysts we focused on atomically dispersed Rh active sites on γ-Al_2O_3. In industrial practice, hydroformylation reactions for short chain alkenes are performed using homogeneous Rh catalysts that have similar cationic oxidation state as oxide supported atomically dispersed $Rh(CO)_2$, but with sterically hindered active sites. Both steric and electronic characteristics of the ligands on homogeneous Rh complexes have been tuned to promote chemoselectivity (CO insertion into the alkene over hydrogenation) and regioselectivity (the location of CO insertion for alkenes longer than 2 carbons) in alkene hydroformylation reactions.[53] Recent efforts toward the design of heterogeneous hydroformylation catalysts have analyzed the influence of oxide support composition and promoters on the reactivity of oxide supported atomically dispersed Rh catalysts in liquid phase reaction conditions.[50,54–58] Here, we instead focus on the influence of support functionalization by phosphonic acids on atomically dispersed Rh

active sites for gas phase hydroformylation. This approach is akin to analyzing the steric influence of ligands on homogeneous Rh active sites and our focus on gas phase processes exploits the primary benefits of heterogeneous catalysis, mitigating metal leaching and challenging separation processes.

Atomically dispersed Rh/γ-Al_2O_3 catalysts were synthesized using a modified SEA method. 5 nm diameter γ-Al_2O_3 nanoparticles were used as a support, along with low Rh weight loadings (0.25 wt%) to decrease the likelihood of Rh cluster formation due to the small number of Rh atoms on each support particle.[47] Structural characterization of the Rh species is discussed in the following section. Rh/γ-Al_2O_3 samples were functionalized through the liquid phase condensation of phosphonic acids on support hydroxyls. Phosphonic acids were chosen as an anchoring group, as they have been shown to be stable at elevated temperatures in inert and reductive environments.[59] OPA was chosen as a modifier because it was hypothesized that an 8-carbon tail should provide sufficient steric interactions to affect adsorbates on atomically dispersed Rh active sites.[60] Further, FOPA was chosen for the differing tail electronegativity, with OPA having a hydrogen saturated tail while FOPA has a predominately fluorine saturated tail. Varying phosphonic acid coverage and tail electronegativity allowed for differentiation of electronic and steric (confinement) effects of functionalization on the reactivity of atomically dispersed Rh active sites.

The presence, stability, and coverage of phosphonic acids on the γ-Al_2O_3 were determined via FTIR, TGA, and ICP-OES, respectively. The FTIR spectrum of γ-Al_2O_3 was compared to OPA and FOPA functionalized γ-Al_2O_3 samples at saturation coverage. The appearance of strong C-H stretches in the region of 2800 to 3000 cm^{-1} for OPA functionalized samples, and the appearance of a strong C-F stretch around 1250 cm^{-1} for FOPA functionalized samples (Figure 3.2), evidence the successful functionalization of γ-Al_2O_3. The stability of phosphonic acid ligands in inert and oxidative environments was monitored via TGA. In an inert environment, OPA decomposition began to occur at ~525°C, while FOPA decomposition occurred at ~400°C (Figure 3.3). In air, OPA began to decompose (burn) at ~250°C while FOPA still decomposed at ~400°C. The similar stability of FOPA in both oxidative and inert

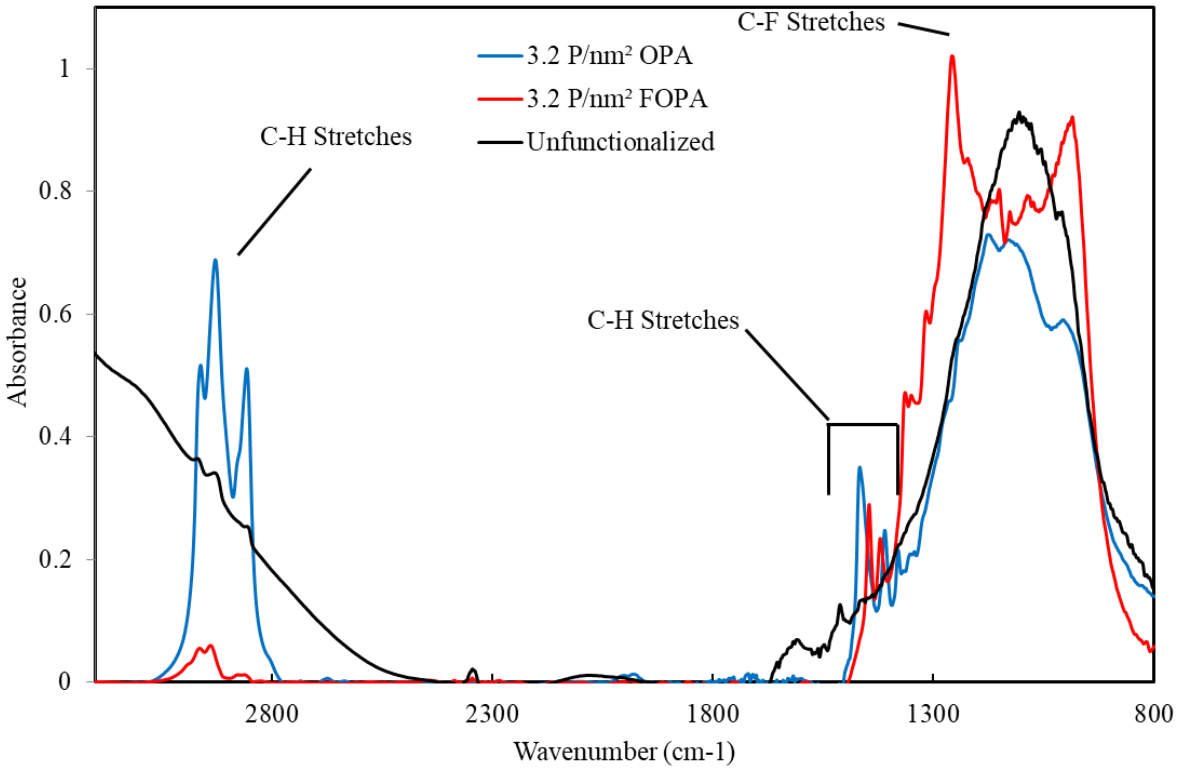

Figure 3.2: FTIR of 3.2 P/nm^2 OPA, 3.2 P/nm^2 FOPA, and unfunctionalized γ-Al_2O_3. A mirror background was used to see all IR active features. Upon functionalization, strong C-H stretches became apparent for OPA functionalized catalysts, and a strong C-F stretch appeared on FOPA functionalized catalysts.

environments was expected due to the incombustible nature of halocarbon species in air.[61] Previous work has shown the stability of similar phosphonic acids on metal oxides in H_2 at comparable temperatures to those used in this study.[45,62]

The Rh and P loadings for OPA functionalized samples were measured by reflux boiling samples in concentrated aqua regia, filtering and diluting the supernatant solution, and measuring analyte concentrations via ICP-OES (Figure 3.4). Surface concentrations were calculated using a support surface area of 128 m^2/g, determined via N_2 physisorption BET analysis. The uptake of phosphonic acids onto γ-Al_2O_3 as a function of phosphonic acid concentration in solution was fit to a Langmuir isotherm with a maximum of 3.5 P/nm^2 for infinite liquid phase concentration (Equation 3.3). The amount of Rh leached by aqua regia treatment was nearly identical for both functionalized and unfunctionalized samples, suggesting that no measurable Rh was leached into the solution during phosphonic acid

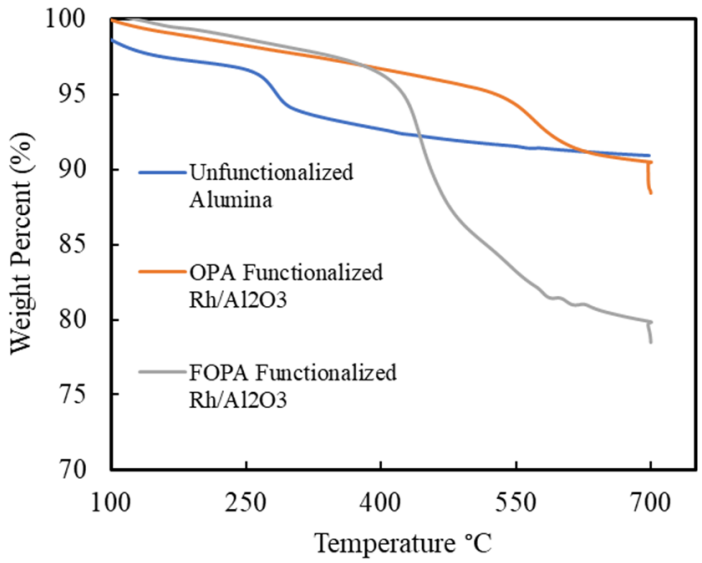

Figure 3.3: TGA of unfunctionalized γ-Al_2O_3 (blue), 3.2 P/nm^2 OPA functionalized Rh/γ-Al_2O_3 (orange), and 3.2 P/nm^2 FOPA functionalized Rh/γ-Al_2O_3 (grey). Samples were heated in an Argon atmosphere at 50°C/min. Upon reaching 700°C, functionalized samples were isothermally exposed to air for 5 minutes to burn remaining surface carbon. Around 200°C, the unfunctionalized samples lost surface hydroxyls. This loss is not observed in the functionalized samples because those samples had already been exposed to that temperature during synthesis. OPA pyrolysis was observed around 500°C, while FOPA pyrolysis occurred at approximately 400°C.

functionalization. FOPA condensed onto γ-Al_2O_3 was resistant to dissolution by aqua regia and could not be directly quantified. Given their similar molecular size and geometry, it was assumed that OPA and FOPA shared similar surface coverages. This assumption is supported by the mass loss from phosphonic acids in TGA for both OPA and FOPA functionalized γ-Al_2O_3, in which FOPA mass loss was approximately twice that of OPA. This is logical for similar coverages because OPA has a molar mass that is approximately half of the molar mass of FOPA (194.21 g/mol and 428.08 g/mol, respectively). Thus, we successfully controlled the coverages of OPA and FOPA functional groups on Rh loaded γ-Al_2O_3 without influencing the Rh loading.

$$Surface\ Coverage\ \left(\frac{P}{nm^2}\right) = 3.5\ \left(\frac{P}{nm^2}\right)\left(\frac{(2.9C)}{1+2.9C}\right) \tag{3.3}$$

Where: C = Synthesis concentration of octlyphosphonic acid (mM)

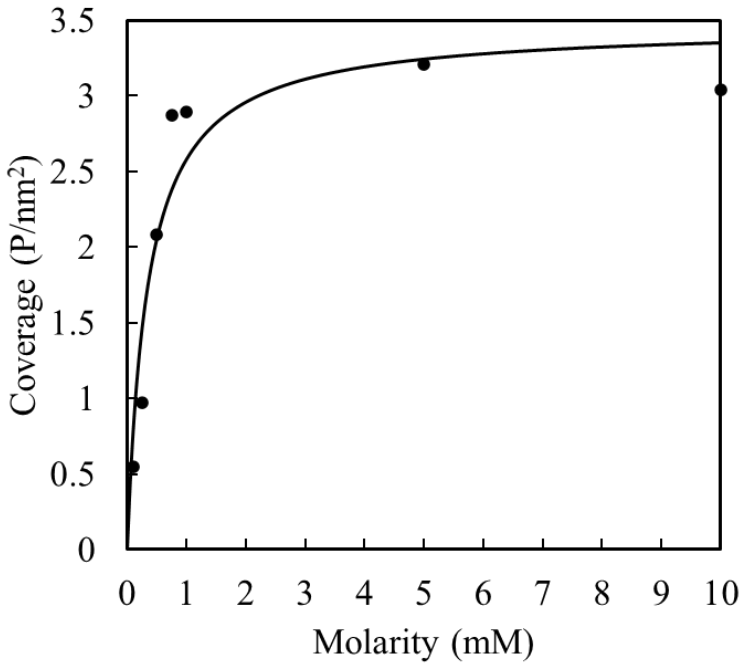

Figure 3.4: Coverage of octlyphosphonic acid on γ-Al_2O_3 as a function of synthesis concentration. Coverages were determined using ICP-OES on a digested catalyst solution. Support surface areas were determined by nitrogen physisorption. This data was fit to a Langmuir isotherm presented as Equation S3

3.3.2 Characterization of $Rh(CO)_2$ Interactions with Phosphonic Acids.

Atomically dispersed Rh species on oxide supports uniquely adsorb two CO molecules to form gem-dicarbonyl species, $Rh(CO)_2$.[63–69] $Rh(CO)_2$ exhibits CO stretches in FTIR spectra that are distinct from linear and bridge-bound CO on Rh clusters. γ-Al_2O_3 supported $Rh(CO)_2$ exhibits symmetric and asymmetric CO stretches at ~2090 cm^{-1} and 2020 cm^{-1}, respectively, while CO adsorbed to Rh clusters exhibit a linear bound CO stretch at ~2050 cm^{-1}, and a broad bridge bound CO stretch at ~1800 cm^{-1}.[66,70] These assignments have been

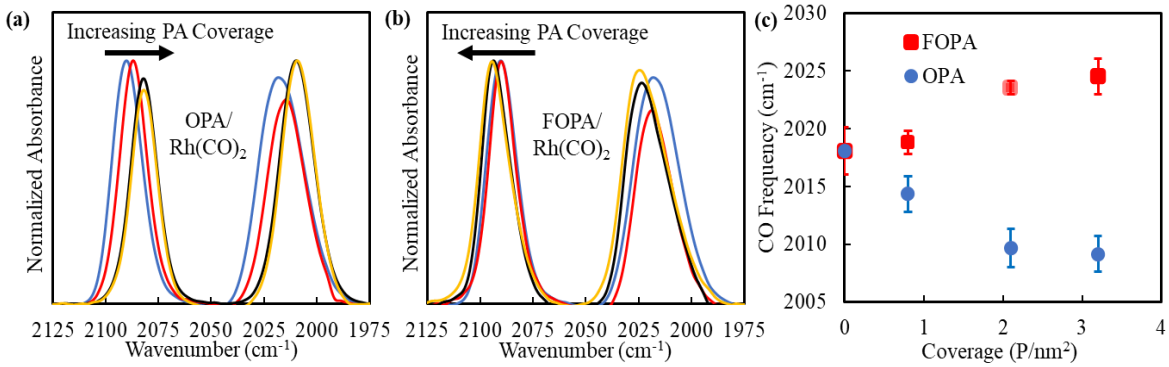

Figure 3.5: FTIR analysis of the influence of phosphonic acid support functionalization on $Rh(CO)_2$. (a) CO probe molecule FTIR spectra of atomically dispersed Rh/Al_2O_3 with 0, 0.8, 2.1, and 3.2 P/nm^2 coverages of octylphosphonic acid (OPA) corresponding to blue, red, black, and yellow, respectively. (b) CO probe molecule FTIR spectra of atomically dispersed Rh/Al_2O_3 with 0, 0.8, 2.1, and 3.2 P/nm^2 coverages of 1*H*,1*H*,2*H*,2*H*-perfluorooctanephosphonic acid (FOPA) corresponding to blue, red, black, and yellow, respectively. (c) Asymmetric $Rh(CO)_2$ stretch position as a function of OPA and FOPA coverage. The standard error of the stretch position of three different samples at the same coverage was used as the uncertainty. All samples were reduced in 10% H_2 at 200°C for one hour, cooled to 25°C in Ar, saturated with 1000ppm of CO for 15 minutes, then purged with Ar prior to measurements.

supported by our group and many others using a battery of techniques, including nuclear magnetic resonance, X-ray photoelectron spectroscopy (XPS), X-ray absorption spectroscopy, and high-angle annular dark-field scanning transmission electron microscopy imaging.[71–75] Thus, CO probe molecule FTIR spectroscopy, combined with the volumetric CO pulse chemisorption measurements described below, provides a sufficient approach for demonstrating the predominant existence of atomically dispersed Rh species in the samples we studied.[76]

Full atomic dispersion of the deposited Rh species was verified through CO probe molecule FTIR and CO pulse chemisorption. CO probe molecule FTIR measurements for unfunctionalized Rh/γ-Al_2O_3 following either H_2 or CO reduction showed only evidence of CO stretches associated with $Rh(CO)_2$ species, again consistent with the complete dispersion of Rh in these samples. CO stretches associated with linear Rh-CO and bridge bound Rh_2-CO species on Rh clusters were not observed in any FTIR measurements (Figure 3.5a and b).[66,77] CO pulse chemisorption measurements for unfunctionalized Rh/γ-Al_2O_3 provided a 2:1 CO:Rh ratio (Rh content was determined by ICP), consistent with the exclusive observation of $Rh(CO)_2$ species in IR measurements. Assuming a 2:1 CO:Rh ratio, the CO chemisorption measurements resulted in dispersion estimates of 93%-108%, which, in combination with the FTIR spectra presented in Figure 5, demonstrate that Rh species were atomically dispersed.

To verify that Rh remained atomically dispersed after γ-Al_2O_3 functionalization and characterize interactions between adsorbates bound to Rh and phosphonic acid ligands, CO probe molecule FTIR was performed at 4 different coverages of both OPA and FOPA (0, 0.8, 2.1, and 3.2 P/nm^2). Large batches of Rh/γ-Al_2O_3 were prepared, from which smaller batches of functionalized samples were made. This was repeated 3 times to provide statistical differentiation of CO probe molecule FTIR spectra and reactivity. For all coverages of FOPA and OPA, γ-Al_2O_3 functionalization resulted in wavenumber shifts of the $Rh(CO)_2$ stretches as compared to the unfunctionalized sample. OPA functionalization resulted in a redshift of the CO stretches bound to Rh of up to 9 cm^{-1}, while FOPA functionalization resulted in a blueshift of up to 6 cm^{-1} (Figure 3.5a,b,c). These shifts in CO stretching frequencies are larger than previously reported by our group for the influence of colocalization of Rh near ReO_x, but smaller than those associated with changes in support composition.[50,78]

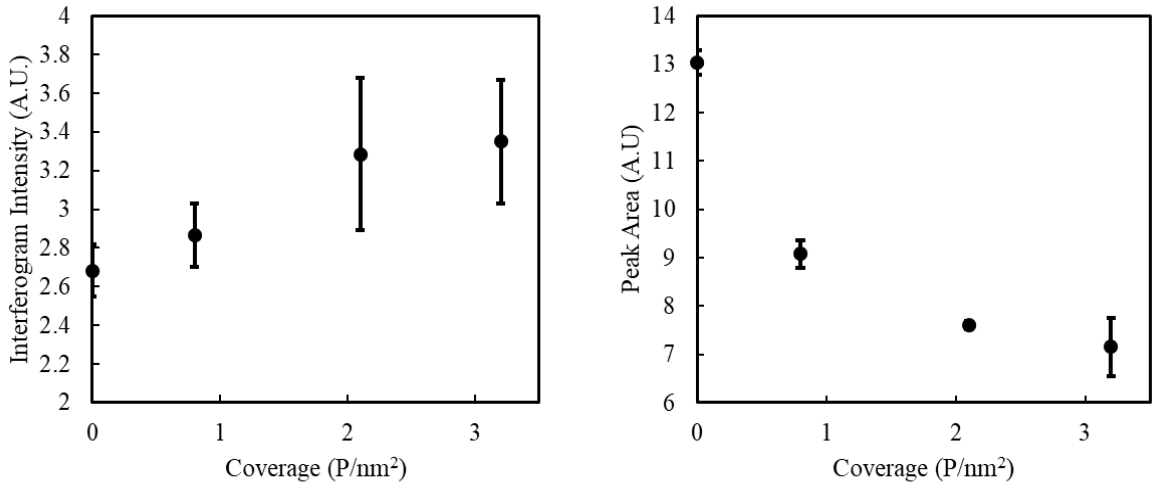

Figure 3.6: FTIR Interferogram intensity (left) and total $Rh(CO)_2$ stretch areas (right) as a function of OPA coverage. Interferogram intensity increased with coverage, while total stretch area decreased. This suggested that OPA was blocking Rh sites, and that the available sites are less than the stretch areas suggest.

Traditional interpretations of metal-carbonyl bonding would suggest that shifts in CO stretch position indicate a decrease in electron density on the CO molecule for FOPA functionalization, and an increase in the electron density on CO for OPA functionalization.[78–80] Hammett substituent analysis suggests that OPA and FOPA should have nearly identical electron density at the phosphonic acid anchoring groups.[81] Furthermore, γ-Al_2O_3 is a strongly insulating support. This suggests that the observed shifts in CO stretching frequencies from support functionalization are due to through-space interactions between adsorbed CO and the phosphonic acid tails, not changes in the charge on Rh. This is further supported and discussed in the context of reactivity results presented later. Attempts to measure the electronic structure of Rh using XPS were unsuccessful for the functionalized samples due to the influence of the long carbon tails on photoelectron emission from the sample.

The area of the $Rh(CO)_2$ stretches decreased significantly with increasing phosphonic acid coverages on γ-Al_2O_3, suggesting that either the extinction coefficients of CO were decreasing, the optical properties of the catalysts were changing, or that functionalization was blocking CO adsorption sites (Figure 3.6). The rather small shifts in IR frequency of CO bound

to Rh with variation in phosphonic acid coverage suggest that the CO dipole moments were relatively consistent and that variations in CO stretch extinction coefficients could not cause the significant decrease in CO stretch area. The measured interferogram intensity by the FTIR was observed to increase with phosphonic acid coverage. So despite the consistency in stretch areas between the samples of the same OPA coverage, the stretch areas could not be compared between samples to directly interpret $Rh(CO)_2$ concentrations. At a constant extinction coefficient and $Rh(CO)_2$ concentration, one would expect a sample with a higher interferogram intensity to have a greater stretch area. This suggests that the inherent concentration of $Rh(CO)_2$ species probed in FTIR measurements was decreasing due to support functionalization.

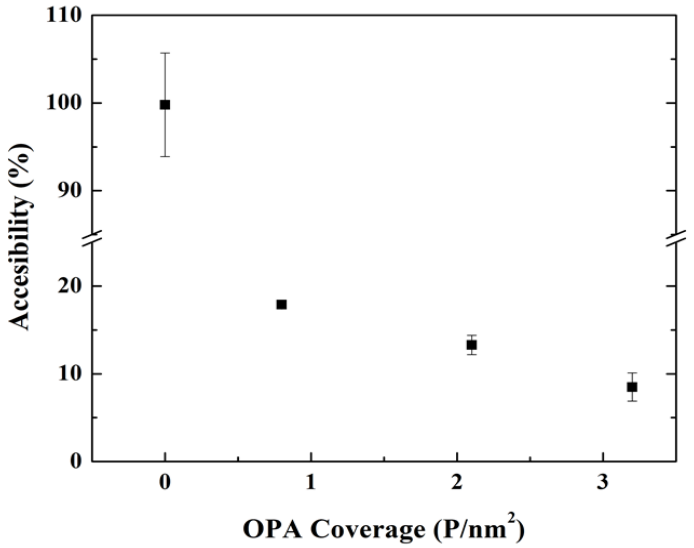

Figure 3.7: Fraction of Rh accessible by CO as a function of OPA coverage. These values were determined via CO pulse chemisorption assuming a 2:1 CO:Rh stoichiometry. Atomic dispersion of these samples under these pretreatments was supported by the FTIR in Figure 5a. These values were used in calculating the TOF for the reactivity data presented later in this chapter.

CO pulse chemisorption measurements showed that the accessibility of Rh sites decreased with increased coverage of phosphonic acids (Figure 3.7). Despite the decrease in accessible Rh indicated by CO pulse chemisorption, CO FTIR still displayed exclusively

$Rh(CO)_2$ stretches for all OPA and FOPA coverages, suggesting that the loss in adsorption sites is due to blockage by phosphonic acids, and not Rh sintering. As such, we will refer to the fraction of Rh available to CO as the catalyst accessibility, rather than dispersion. The accessible Rh sites measured by CO chemisorption will be used in the calculation of turn over frequencies. This is justified despite different pretreatments for CO chemisorption and reactions (H_2 versus CO reduction), because FTIR measurements indicated complete atomic dispersion for both pretreatments. Furthermore, the functionalized catalysts exhibited minimal time to reach steady-state in reactivity measurements, with no significant increase in reactivity with time on stream that could be attributed to an increase in Rh site exposure.

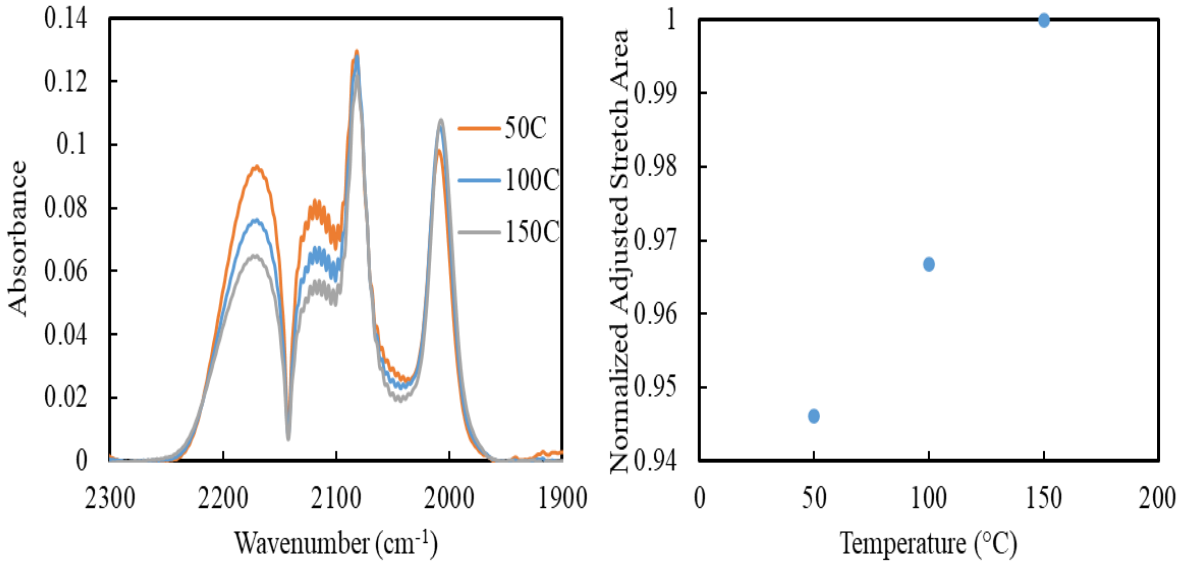

Figure 3.8: FTIR spectra of 3.2 P/nm^2 OPA functionalized Rh/Al_2O_3 exposed to CO at 50°C, 100°C, and 150°C, sequentially, after reduction in H_2 at 225°C (left). The normalized and adjusted CO stretch areas for 3.2 P/nm^2 OPA functionalized Rh/Al_2O_3 reduced at 225°C are shown (right). The stretch areas were adjusted linearly with interferogram intensity to account for changes in surface reflectivity with temperature. The nearly constant CO stretch area versus temperature demonstrates that Rh active site accessibility on functionalized catalysts does not significantly change between the temperature of CO chemisorption measurements and reactivity measurements.

It has been previously reported that the orientation of the tails of self-assembled monolayers can change with temperature.[82,83] This is of important note in this work because Rh active site accessibility was measured at 50°C by volumetric CO chemisorption, while

reactivity was evaluated at ~150°C. To examine potential changes in Rh accessibility with temperature, a 3.2 P/nm^2 OPA functionalized catalyst was reduced in H_2 and exposed to CO at 50°C, 100°C, and 150°C, sequentially (Figure 3.8A). Minimal changes in CO stretch areas were observed as a function of temperature, after adjusting for changes in interferogram intensity due to changes in material reflectivity (Figure 3.8B). As such, the Rh accessibilities measured at 50°C are justified for calculation of turn over frequencies for reactivity measurements at 150°C.

3.3.3 Changes in Ethylene Hydroformylation Reactivity Due to Functionalization

Ethylene hydroformylation was used as a probe reaction to explore the influence of γ-Al_2O_3 functionalization on the reactivity of atomically dispersed Rh species. This is an excellent probe reaction as adsorbed CO is the most abundant surface intermediate (MASI) in this reaction and thus we can relate changes in the reactivity to changes in characteristics of Rh-CO interactions. Ethylene hydroformylation serves as a simpler probe reaction as compared to propylene, due to the lack of regioselective CO insertion. Further, recent DFT based microkinetic modeling[84] of ethylene hydroformylation on atomically dispersed Rh/ γ-Al_2O_3, and comparison to our previous kinetic measurements, has provided insights into rate-determining steps (RDS).[50,84] For propanal formation, the RDS is CO insertion into adsorbed ethyl on a Rh site that contains additional CO and H ligands ($Rh(CO)_2(C_2H_5)(H)$ → $Rh(CO)(H)(COC_2H_5)$). For ethane formation the RDS is hydrogenation of adsorbed ethylene on a Rh site with a single CO adsorbed ($Rh(CO)(H)_2(C_2H_4)$ → $Rh(CO)(H)(C_2H_5)$). Although, there were 2 different geometric isomers of this surface reaction that compete to enable ethane formation, which will be discussed later. Furthermore, both ethane and propanal formation are

kinetically limited by CO desorption from $Rh(CO)_2$ to start the catalytic cycle. Thus, it was expected that γ-Al_2O_3 functionalization would have different influences on the two competing steps, due to differences in the Rh site occupancy, transition state sizes for the kinetically relevant steps, and the existence of multiple pathways toward ethane formation. Further mechanistic details will be discussed below in the context of the kinetic results.

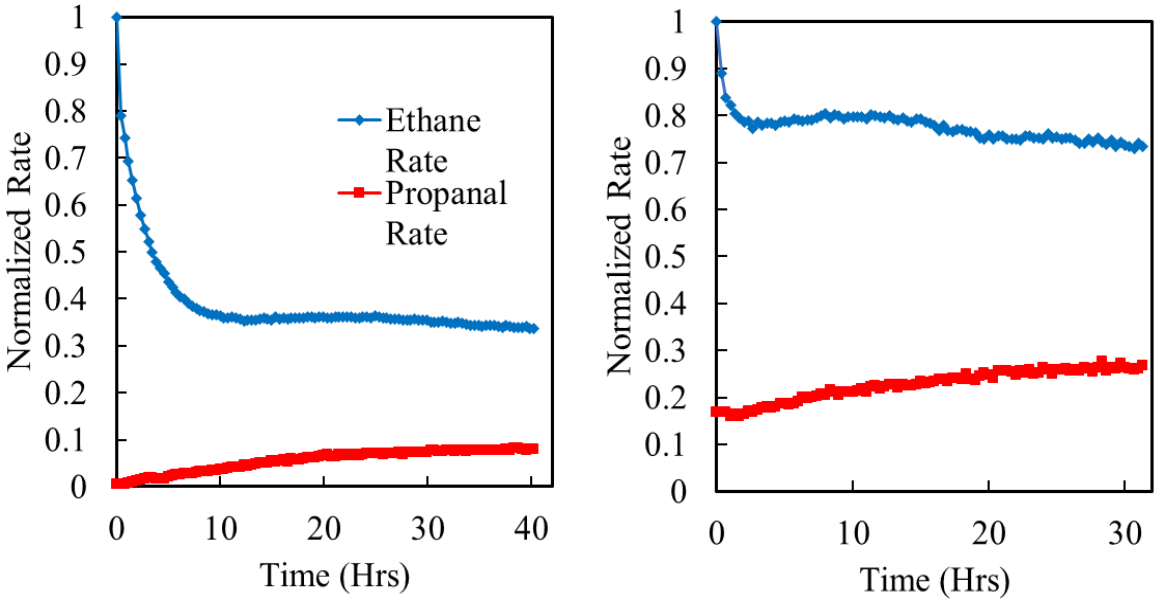

Figure 3.9: Rate vs time on stream for unfunctionalized (left) and 3.2 P/nm^2 OPA catalyst (right). Rates were normalized to the highest observed rate over time on stream. Catalysts were at 170°C during this activation period, so selectivities do not match those listed in Table S1, which were recorded for 150°C. 30cc/min flow rate of 1:1:1 CO:H_2:C_2H_4 at ambient pressure.

Hydroformylation reactivity measurements were performed on catalysts of similar Rh loadings (0.25%-0.3%). The catalysts were reduced in-situ in pure CO at 200°C for 2.5 hours. Catalysts were reduced in CO rather than H_2, as CO is known to stabilize Rh as atomically dispersed Rh species.[71] Catalysts were exposed to an equimolar gas mixture of C_2H_4, H_2, and CO at temperatures between 140 and 170°C. Reactant conversion was less than 0.2% in all experiments. TOF and selectivity were measured under steady-state conditions, following a transient period ranging between 12 and 24 hours (Figure 3.9). This transient period is likely due to the formation of surface species on the support.[85] The transient period was shorter for

functionalized samples, due to a combination of phosphonic acids reducing available support surface sites, and increased reaction rates on functionalized samples. Similar transient periods were observed previously for ethylene hydroformylation, in which the catalysts with enhanced rates had shorter transient periods.[50]

At all times, the only detectable products were ethane from hydrogenation and propanal from hydroformylation. Rh clusters make a variety of products, including methane, ethane, propanal, propanol, and propane, while for the atomically dispersed Rh species we only observed the formation of ethane and propanal at steady-state.[86–88] The TOF for propanal formation and selectivity towards propanal increased with increasing phosphonic acid coverage on γ-Al_2O_3 (Figure 3.10). Comparable increases in TOFs and propanal selectivity were observed for both FOPA and OPA at all coverages. Even the lowest coverage of OPA and FOPA enhanced propanal formation TOF by 15x at 150°C. For the highest phosphonic acid coverages, propanal TOFs were enhanced 51x and 41x for 3.2 P/nm^2 OPA and FOPA functionalized catalysts, respectively, while ethane TOFs were enhanced by 27x and 21x, respectively (Figure 3.11). The greater increase in TOF for propanal formation than for ethane formation resulted in an increase in selectivity towards propanal, from 31±2% for the unfunctionalized case to 49±3% for 3.2P/nm^2 OPA and FOPA. All reactivity data can be found in (Table 3.1).

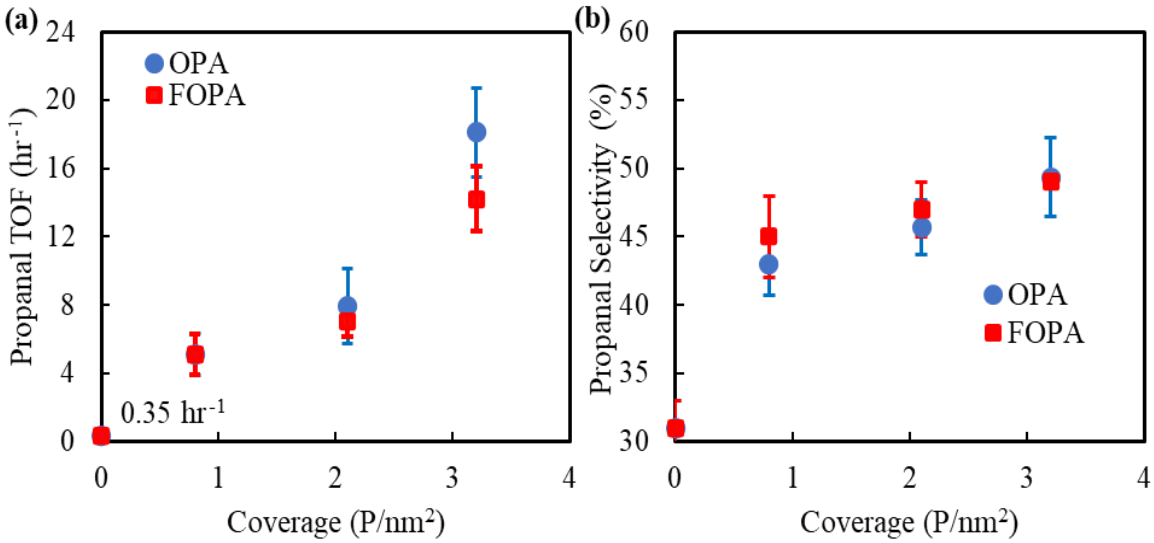

Figure 3.10: The influence of phosphonic acid functionalization on TOF and selectivity for ethylene hydroformylation. (a) Turn over frequency (TOF) for propanal formation as a function of OPA and FOPA coverage. The standard error of the TOF for at least three samples was used as the uncertainty. (b) The selectivity towards propanal formation as a function of phosphonic acid coverage. The standard error of the selectivity towards propanal for at least three samples was used as the uncertainty. TOF were defined based on repeated CO chemisorption estimates of each sample. Ethylene hydroformylation reactivity measurements were recorded at 150°C with a 30cc/min flow rate of 1:1:1 $CO:H_2:C_2H_4$ at ambient pressure at steady state (usually after 24 hours on stream).

The similar changes in reactivity for both OPA and FOPA functionalized samples suggest that the shifts in CO stretching frequencies observed by FTIR (red vs blue shift in frequency for OPA and FOPA, respectively) were not predominantly responsible for changes in observed catalytic reactivity. TOF enhancements observed on functionalized samples were significantly larger than decreases in Rh site accessibility caused by functionalization. The observed product formation rates on a per g Rh basis were enhanced by 3-5x by functionalization, even with the poisoning of Rh sites by phosphonic acids. Thus, the exposed

active sites were significantly modified in their catalytic reactivity by support functionalization.

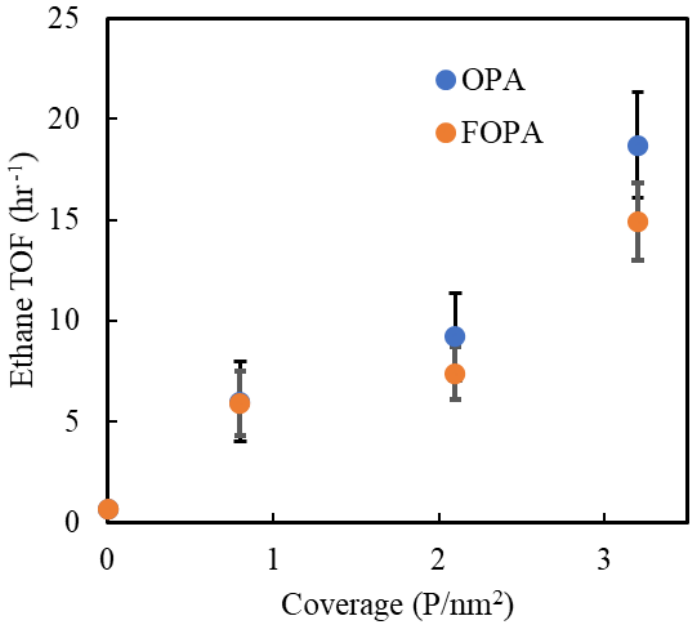

Figure 3.11: Ethane TOF vs coverage at 150°C. Hydroformylation reactivity measurements were recorded at 150°C with a 30cc/min flow rate of 1:1:1 $CO:H_2:C_2H_4$ at ambient pressure at steady state (usually after 24 hours on stream). The standard error of the TOF for at least three samples was used as the uncertainty.

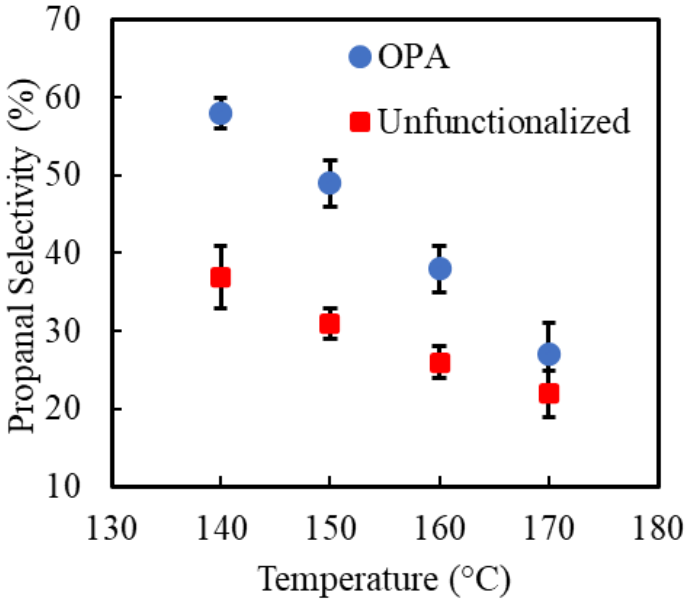

Figure 3.12: Selectivity towards propanal for 3.2 P/nm^2 OPA functionalized Rh/Al_2O_3 (blue) and unfunctionalized Rh/Al_2O_3 (red). Hydroformylation reactivity measurements were recorded between 130°C and 170°C with a 30cc/min flow rate of 1:1:1 $CO:H_2:C_2H_4$ at ambient pressure at steady state (usually after 24 hours on stream). Error bars represent the standard error for the results of at least three repeat experiments at each temperature.

Table 3.1: Ethylene hydroformylation rates, selectivities, activation enthalpies, and activation entropies for all coverages of OPA and FOPA at 150°C in 30 cc/min of equimolar reactants. Error bars for TOF and selectivity represent the standard error of at least 3 repeat experiments with different catalysts. A 68% confidence interval was used as the uncertainty of all activation enthalpies and entropies.

Sample	Ethane Activity (hr^{-1})	Propanal Activity (hr^{-1})	Selectivity (%)	Ethane $\Delta H^{\ddagger}$ (kJ/mol)	Propanal $\Delta H^{\ddagger}$ (kJ/mol)	Ethane $\Delta S^{\ddagger}$ (J/(mol*K))	Propanal $\Delta S^{\ddagger}$ (J/(mol*K))
Unfunctionalized	0.7±0.1	0.35±0.05	31±2	67±6	34±4	-115±17	-184±16
0.8 P/nm^2 OPA	6.0±2.0	5.1±1.2	43±2	78±5	33±3	-73±15	-174±17
0.8 P/nm^2 FOPA	5.9±1.6	5.1±1.2	45±2	81±7	31±3	-61±14	-173±15
2.1 P/nm^2 OPA	9.2±2.2	7.9±2.2	46±2	81±5	32±5	-38±12	-170±17
2.1 P/nm^2 FOPA	7.4±1.3	7.0±0.9	47±3	73±7	33±3	-87±13	-168±18
3.2 P/nm^2 OPA	18.7±2.6	18.1±2.6	49±3	86±6	33±3	-38±9	-152±17
3.2 P/nm^2 FOPA	14.9±1.9	14.2±1.9	49±2	77±3	33±4	-66±14	-159±16

The propanal selectivity observed in these experiments is comparable or better than those observed for ethylene hydroformylation on oxide supported Rh clusters doped with other metals or sulfides.[85–89] Further, due to the more negative reaction order in CO for the formation of ethane (-1.4) compared to that for the formation of propanal (-0.7) observed for our samples (Table 3.2), we would expect improvements in hydroformylation selectivity towards propanal by raising total pressure at a constant 1:1:1 reactant feed ratio. Additionally, the increased rates at higher pressures would allow for similar rates at reduced temperatures,

which would further favor hydroformylation over hydrogenation. Figure 3.12 demonstrates that selectivity towards propanal increases with decreasing temperature.

Table 3.2: Ethylene hydroformylation reaction orders for the unfunctionalized and highest coverages of each phosphonic acid species. Hydroformylation reactivity measurements were recorded at 150°C with a 30cc/min flow rate of 1:1:1 $CO:H_2:C_2H_4$ at ambient pressure at steady state (usually after 24 hours on stream). The standard error of the linear regression for each experiment was used as the uncertainty.

Sample	CO Reaction Order (Ethane)	CO Reaction Order (Propanal)	H2 Reaction Order (Ethane)	H2 Reaction Order (Propanal)	C2H4 Reaction Order (Ethane)	C2H4 Reaction Order (Propanal)
Unfunctionalized	-1.3±0.1	-0.6±0.1	0.9±0.1	0.8±0.1	0.6±0.1	0.8±0.1
3.2 P/nm^2 OPA	-1.4±0.1	-0.7±0.1	1.0±0.1	1.0±0.1	0.9±0.1	1.0±0.1
3.2 P/nm^2 FOPA	-1.4±0.2	-0.7±0.1	1.0±0.2	0.8±0.1	0.9±0.2	0.9±0.1

3.3.4 Understanding the Influence of Phosphonic Acids on Rh Reactivity

We performed an Eyring analysis (Equation 3.4) of the temperature-dependent ethylene hydroformylation kinetic data to understand the influence of phosphonic acid functionalization on apparent activation enthalpies and entropies. The reaction orders in ethylene, CO, and H_2 did not change significantly with functionalization (Table 3.2), suggesting that changes in steady-state adsorbate coverages on Rh were minimal and did not control variations in TOFs. There were no measurable changes in the apparent activation enthalpies for propanal formation comparing unfunctionalized and functionalized samples with values consistently around 35 kJ/mol, even though the TOF varied by up to 50x (Figure 3.13). Alternatively, the apparent activation entropies for propanal formation decreased from -184±16 J/(mol·K) for the unfunctionalized sample to -152±17 J/(mol·K) and -159±16 J/(mol·K) for the 3.2 P/nm^2 OPA and FOPA samples, respectively (Figure 3.13B). An unpaired two-tailed t test for kinetic parameters on unfunctionalized and 3.2 P/nm^2 OPA functionalized catalysts results in P-values

of 0.077 and 0.747 for activation entropies and activation enthalpies, respectively. This implies that the activation entropies are statistically different at a 90% confidence level, while the activation enthalpies are not statistically different at any reasonable confidence. The activation entropy for propanal formation was observed to be dependent on phosphonic acid coverage, with less negative values at increasing coverage and a similar dependence for both OPA and FOPA. The data in Figure 3.13 and B shows direct evidence that phosphonic acid functionalization of the support surrounding atomically dispersed Rh sites causes the breaking of compensation relationships in the apparent kinetics of propanal formation.

$$\ln\left(\frac{k}{T}\right) = \frac{-\Delta H^{\ddagger}}{RT} + \ln\left(\frac{\kappa k_B}{\mathrm{h}}\right) + \frac{\Delta S^{\ddagger}}{R} \tag{3.4}$$

Where: k = rate constant (units are dependent on reaction order)
T= temperature (K)
$\Delta H^{\ddagger}$ = Activation Enthalpy (J/mol)
$\Delta S^{\ddagger}$ = Activation Entropy (J/(mol*K))
R= Molar gas constant (J/(mol*K))
κ= Transmission Coefficient (assumed to be unity)
k_B= Boltzmann Constant (J/K)
h = Planck Constant (J*s)

The influence of support functionalization on the kinetics of ethane formation was less straightforward. The apparent activation enthalpy for ethane formation increased from 67±6 kJ/mol for the unfunctionalized samples to 86±6 kJ/mol and 77±3 kJ/mol for the 3.2 P/nm^2 OPA and FOPA functionalized samples, respectively. For OPA, the ethane activation enthalpy increased with coverage. For FOPA, the 2.1 P/nm^2 sample demonstrated a lower activation enthalpy than the 0.8 P/nm^2. Despite this, the overall trend is that the activation enthalpy for ethane formation increases with coverage for FOPA as well. The apparent activation entropy for ethane formation became less negative with increase phosphonic acid coverage, which caused the overall observation of increased TOF for ethane formation with increasing

coverage. But again, the trend between the apparent activation entropy and phosphonic acid coverage is less clear for FOPA as compared to OPA. Representative Eyring plots can be found as Figure 3.14

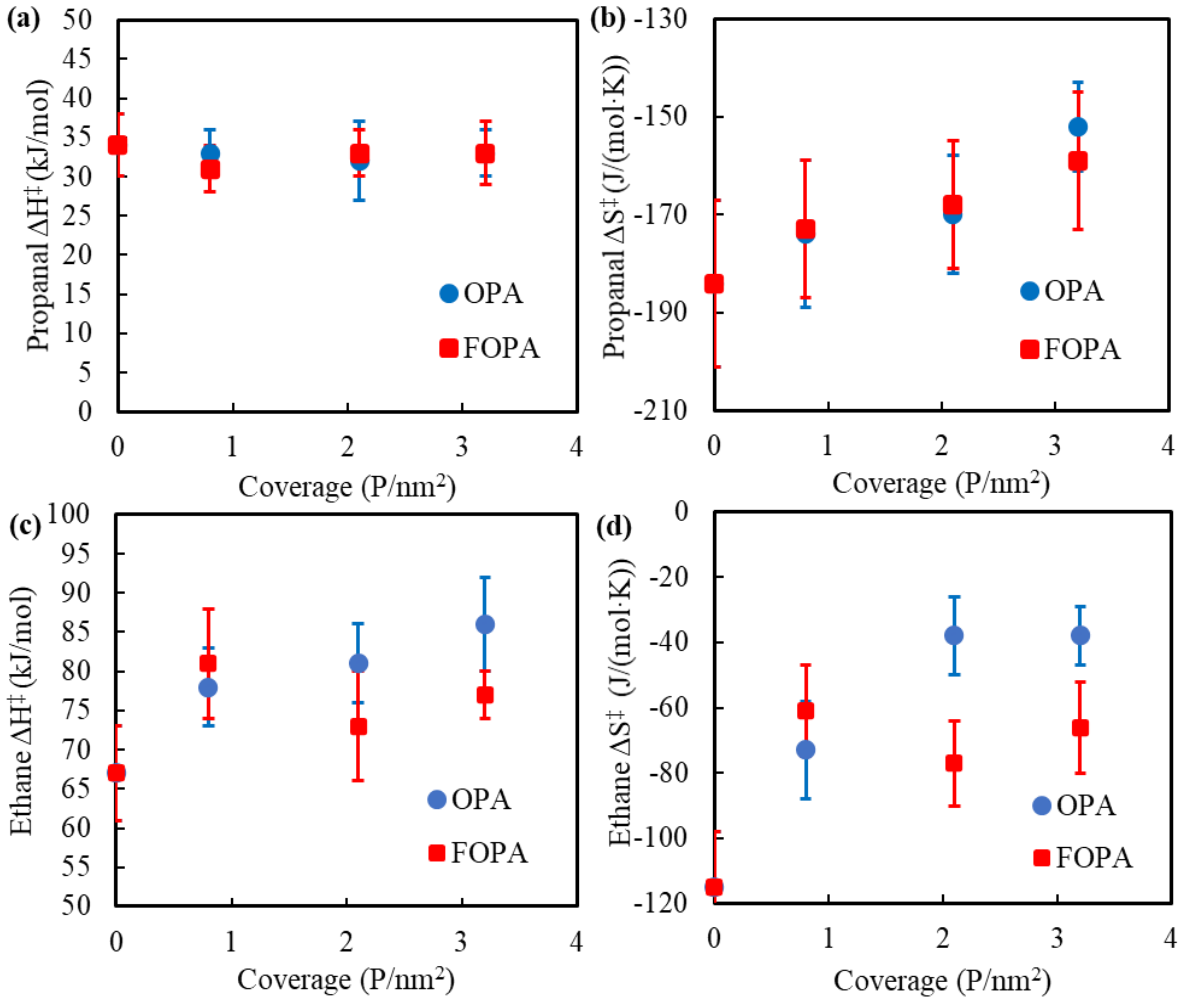

Figure 3.13: Eyring analysis of hydroformylation kinetics. (a) The activation enthalpy and (b) entropy for propanal formation as a function of OPA and FOPA coverage. (c) The activation enthalpy and (d) entropy for ethane formation as a function of OPA and FOPA coverage. Reactivity measurements for Eyring analysis were recorded between 130°C and 170°C with a 30cc/min flow rate of 1:1:1 $CO:H_2:C_2H_4$ at ambient pressure. A 68% confidence interval of the linear regression was used as the uncertainty for all activation enthalpies and entropies for the data from three different samples at each coverage. The Eyring plots for ethane and propanal formation for all coverages can be found in Figure (3.14).

The apparent deviation from the compensation effect for propanal formation kinetics and the simultaneous existence of a relationship between apparent activation enthalpy and entropy for ethane formation seems to be in disagreement. Recent DFT-based microkinetic

modeling for these reaction pathways on atomically dispersed Rh/γ-Al_2O_3 showed that propanal forms through a single reaction pathway.[84] Thus, our analysis is examining the influence of phosphonic acid modification on the kinetics of a single reaction pathway for propanal formation. Alternatively, DFT calculations showed that ethane formation occurred through two competing reaction pathways with different stereochemistry associated with the adsorbate arrangement during the final hydrogenation step (Rh(CO)(H)(C_2H_5) → Rh(CO)(C_2H_6)). These two steps exhibited competitive rates for Rh/γ-Al_2O_3, but with distinct apparent activation enthalpies and entropies. Therefore, it is likely that phosphonic acid functionalization of the support surrounding Rh sites modified the relative reaction flux through the two pathways toward ethane formation. As a result, it is hypothesized that the impact of support functionalization on ethane formation kinetics was a confluence of changes in the predominant reaction pathway, which would change both apparent activation enthalpies and entropies, and a specific influence on the apparent activation entropy of the predominant reaction pathway.

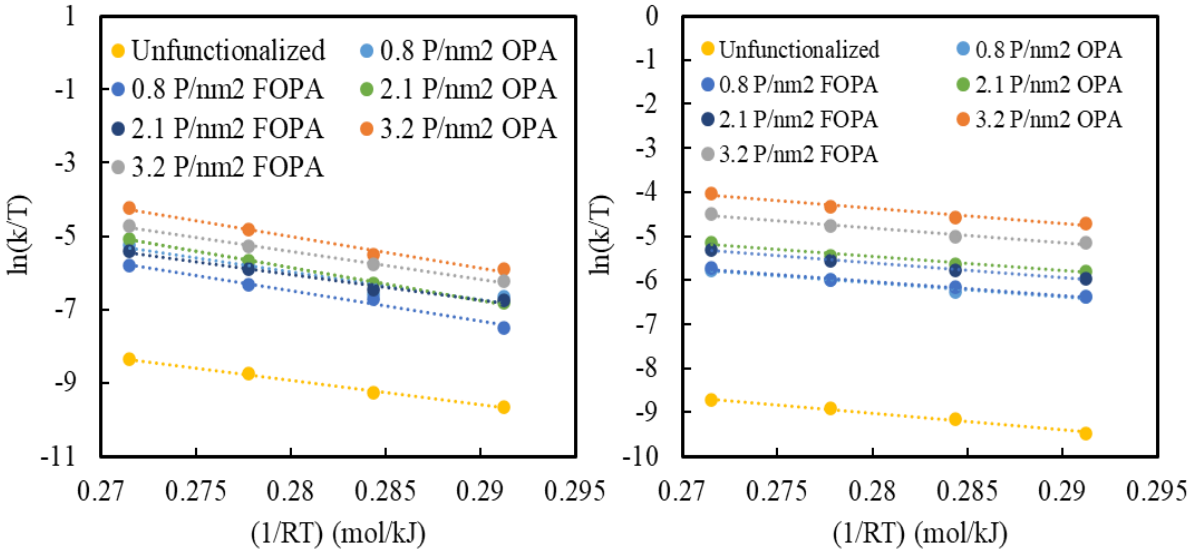

Figure 3.14: Representative Eyring plots for ethane formation (left) and propanal formation (right). Reactivity measurements for Eyring analysis were recorded between 130°C and 170°C with a 30cc/min flow rate of 1:1:1 CO:H_2:C_2H_4 at ambient pressure.

As described above, apparent activation enthalpies and activation entropies obtained using Eyring analysis of hydroformylation kinetics derive from a convolution of several elementary steps and potentially multiple reaction pathways. Therefore, it is difficult to make direct inferences about how physical changes in the catalyst system influenced elementary step kinetics at a level that allows direct relationships between catalyst functionalization and activation enthalpies and entropies. To better understand how phosphonic acid functionalization of γ-Al_2O_3 influenced the kinetics of elementary steps on atomically dispersed Rh sites, we performed kinetic analyses of CO desorption from $Rh(CO)_2$ using TPD measurements. CO desorption is a kinetically relevant elementary step in both ethylene hydroformylation and hydrogenation.[50,84] Thus, information gleaned from CO desorption kinetics should be directly relatable to changes in catalytic reactivity.

For TPDs of adsorbates from porous materials, re-adsorption of desorbed species is often a concern and can significantly influence the extracted desorption kinetic parameters.[90] Rather than using mass spectrometry to monitor desorbing species that pass through the porous catalyst bed before being detected, CO coverages on Rh sites during TPDs were monitored *in-situ* via DRIFTS. In our case, re-adsorption is not a significant issue for the active sites probed by the DRIFTS measurements due to the primary reflection plane being the top of the catalyst bed and the downward flow direction of the sweep gas. The wavelength of IR light at frequencies of interest (2080 cm^{-1} and 2020 cm^{-1}) is ~5 μm, which is significantly larger than the length scale of the support particles used in this study, ~ 5 nm diameter. Due to this length scale discrepancy, the catalyst bed in our experiments "appears" to the IR light as a continuous phase, with a Lambertian reflection at the surface, and minimal scattering below the surface.[91,92] IR photon scattering off of the top of the bed is significantly more likely (orders of magnitude) than reflections from the inside of the bed. As a result, the effective depth being probed by the DRIFTS measurements of CO coverage on Rh in our experiments is differential. Additionally, given the absorption coefficient of alumina,[93] the light was likely extinguished inside of the bed before it could reflect off of the bottom or sides of the catalyst bed. Thus, we argue that the desorption kinetics of CO from atomically dispersed Rh on our samples is not influenced by re-adsorption and can be modeled as an irreversible desorption process. A more

detailed explanation with calculations can be found in the appendix. (Equation. 3.6.2)

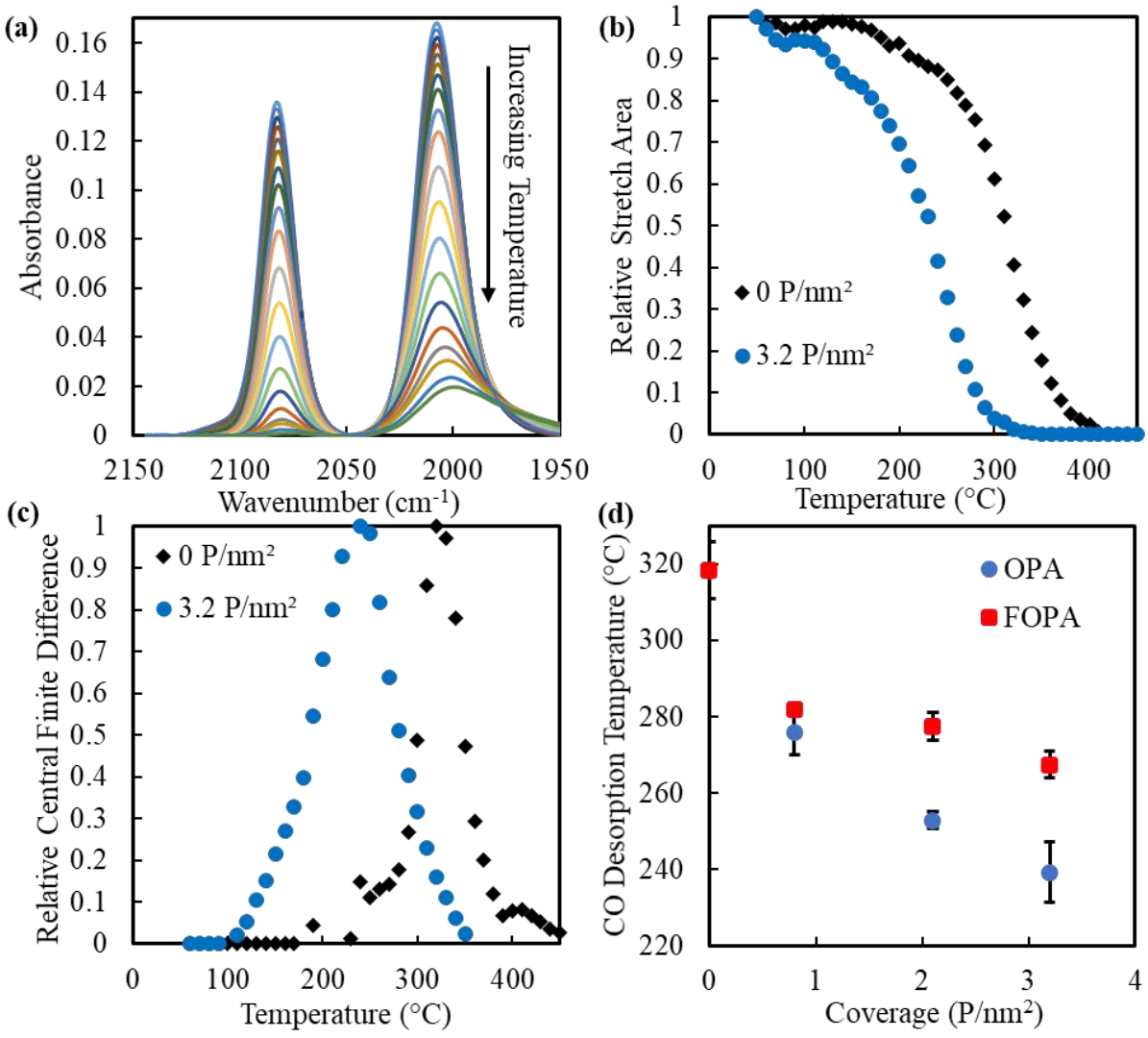

Figure 3.15: (a) Temperature programmed desorption (TPD) of CO from $Rh(CO)_2$ on 3.2 P/nm^2 OPA functionalized Al_2O_3. Samples were heated from 50°C to 450°C at 6°C per minute in 100 cc/min Ar. Spectra were taken once every 10°C. (b) Normalized symmetric $Rh(CO)_2$ stretch areas for 0 and 3.2 P/nm^2 OPA functionalized Rh/Al_2O_3 as a function of sample temperature. The area was determined by fitting the symmetric stretch to a Gaussian function. (c) Normalized numerical derivative of the $Rh(CO)_2$ symmetric stretch area of 0 and 3.2 P/nm^2 OPA functionalized Rh/Al_2O_3 as a function of temperature. A central finite difference method was used to approximate the derivative. (d) The temperature of maximum rate of loss of the symmetric $Rh(CO)_2$ stretch area as a function of OPA and FOPA coverage. The standard error of the CO desorption temperature of at least three different samples was used as the uncertainty.

In TPD experiments, catalysts were first reduced in CO at 250°C, consistent with the pre-treatment during catalytic reactivity measurements, and then were cooled to 50°C and purged with Ar. Samples were then heated at a constant ramp rate of 10°C/min and spectra

were taken at least once per 10°C (Figure 3.15a). The area of the symmetric stretch of the $Rh(CO)_2$ species at each temperature was calculated (Figure 3.15b) and a numerical derivative was taken to determine the rate of CO desorption at each temperature (Figure 3.15c). The temperature at which rate of maximum CO desorption occurred was then labeled as the desorption temperature (Figure 5d). It was assumed that CO desorption on atomically dispersed Rh is a first-order process. The numerical derivative curves (Figure 3.15C) generally appear to be first-order, and both COs from $Rh(CO)_2$ appear to desorb simultaneously, suggesting that the second CO is bound with the same strength or more weakly than the first CO.[71] We rule out the potential of CO dissociation causing a loss of the CO stretch, due to the lack of methane formation under hydroformylation conditions, which is seen at elevated temperature on Rh nanoparticles.

The formation of a small stretch at ~1980 cm^{-1} at higher temperatures in Figure 5a is noted. This stretch has previously been observed during CO desorption from $Rh(CO)_2$ species and was attributed to the formation of Rh monocarbonyl species, Rh(CO), that are stabilized by surface hydroxyls.[51] This species is a significant contributor to the CO desorption process from $Rh(CO)_2$ only when H_2 is used as an initial reductant, which presumably results in the production of vicinal hydroxyl species. As observed here, this species is a minor contributor to the CO desorption process when CO is used as the initial reductant. The primary CO desorption pathway involves the simultaneous (within the time resolution of our IR measurements) loss of both COs as indicated by the simultaneous loss of the symmetric and asymmetric CO stretches without the formation of other bands for a majority of the desorption process.

For both OPA and FOPA functionalized catalysts, the temperature of the maximum rate of CO desorption decreased with increasing phosphonic acid coverage. The temperature of the maximum desorption rate decreased from 318°C for the unfunctionalized sample, to 268°C and 239°C for the 3.2 P/nm^2 FOPA and OPA samples, respectively. The decrease in desorption temperature, despite opposite shifts in CO stretch wavenumber (Figure 3.5), further suggests that electronic changes to CO due to OPA and FOPA have a smaller influence on CO desorption kinetics compared to steric (confinement) effects. If one were to follow the classical metal carbonyl interpretation of the shifts in CO stretch positions due to the presence of phosphonic acids near Rh, one would expect the FOPA functionalized catalyst to have the lowest desorption temperature, but instead we see the OPA functionalized catalyst having the lowest desorption temperature. From these experiments, we can conclude that support functionalization is modifying the free energy of desorption for CO, but these experiments do not tell us anything specific about how the activation entropies and enthalpies of desorption change.

To probe the activation entropy and enthalpy of CO desorption, TPDs were performed at ~10 different temperature ramp rates for the unfunctionalized, 3.2 P/nm^2 OPA functionalized, and the 3.2 P/nm^2 FOPA functionalized samples. The ramp rate-dependent TPD data were plotted in the form of Equation 3.5 in order to extract activation enthalpies and entropies.[94,95] Equation 3.5 was derived from the Polanyi-Wigner equation, which describes a kinetically limited, irreversible desorption process. It was assumed that desorption from $Rh(CO)_2$ was first-order and that the second CO had the same desorption energy as the first, as justified earlier. A full derivation can be found in the appendix as Equation 3.6.1. The data is shown in Figure 3.16. Using these measurements, we determine the desorption energy

from the slope of the lines, and the activation entropy can be calculated from Equation 3.6 using the preexponential factor determined from the intercept. It should be noted that E_d is roughly equivalent to the activation enthalpy, varying only by a multiple of k_BT.[96] A derivation of Equation 3.6 can be found in the appendix as Equation 3.6.3.

$$\ln\left(\frac{\beta}{k_B T_P^2}\right) = \frac{-E_d}{k_B T_P} + \ln\left(\frac{\mathrm{A}}{\mathrm{E_d}}\right) \tag{3.5}$$

Where: β = The Temperature ramp rate (K/s)
k_B= Boltzmann constant (eV/K)
T_P= Temperature of maximum desorption (K)
E_d= Desorption energy (eV)
A = Preexponential factor (1/s)

$$\Delta S^{\ddagger} = R\,(\ln\left(\frac{Ah}{k_B T}\right) - 1) \tag{3.6}$$

Where: $\Delta S^{\ddagger}$=Activation Entropy (J/(mol·K))
R =Molar Gas Constant (J/(mol·K))
h = Planck's Consta

$$\Delta S^{\ddagger} = R\,(\ln\left(\frac{Ah}{k_B T}\right) - 1)$$

nt (eV·s)

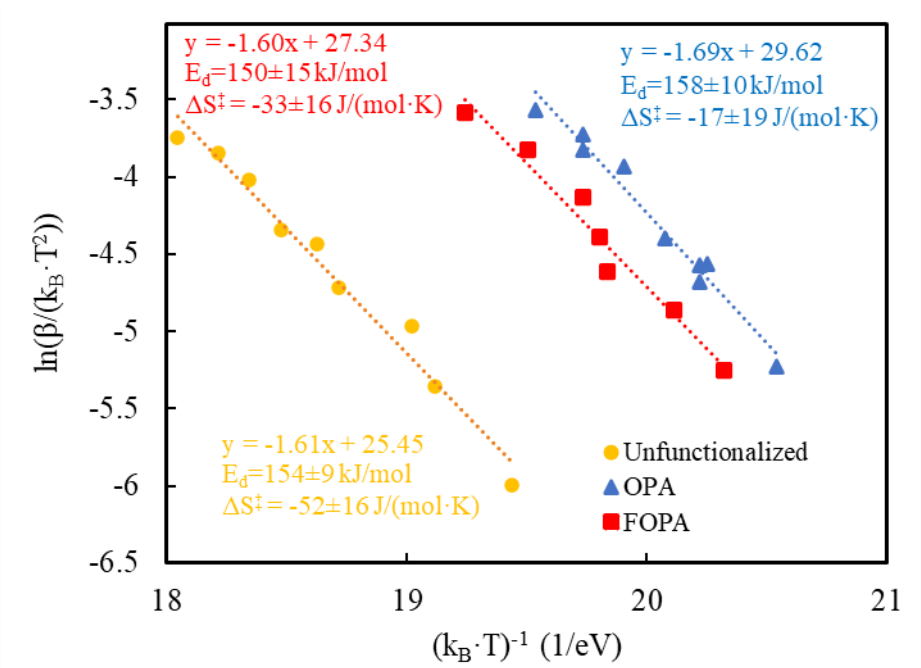

Figure 3.16: Variable ramp rate CO TPDs from Rh/Al_2O_3 (unfunctionalized), 3.2 P/nm^2 OPA (OPA), and 3.2 P/nm^2 FOPA (FOPA) samples plotted in the form of Equation 2. Samples were heated from 50°C to 450°C at rates ranging from 5°C per minute to 60°C per minute in 100 cc/min Ar. Desorption energies were calculated from the slopes, while activation entropies were calculated using both the slopes and intercepts. A 68% confidence interval was used as the uncertainty for the intercepts and slopes.

The activation enthalpy of CO desorption for all samples was ~150 kJ/mol and did not differ significantly due to functionalization. Conversely, we saw statistically significant differences between the activation entropy of CO desorption for the unfunctionalized case versus the OPA and FOPA functionalized samples. For the unfunctionalized, 3.2 P/nm^2 OPA, and 3.2 P/nm^2 FOPA samples the entropy of activation for CO desorption was calculated to be -52±16 J/(mol·K), -17±19 J/(mol·K), and -33±16 J/(mol·K), respectively. These activation entropies approximately correspond to preexponential factors of $7 \cdot 10^{10}$ s^{-1}, $4 \cdot 10^{12}$ s^{-1}, and $6 \cdot 10^{11}$ s^{-1}, respectively. An unpaired two-tailed t test for the unfunctionalized and 3.2 P/nm^2 OPA functionalized catalysts results in P-values 0.0006 and 0.3856 for desorption activation entropies and energies, respectively. This implies that the differences in activation entropies of desorption for functionalized and unfunctionalized catalysts are statistically significant at all

reasonable confidence levels, while the activation energies are not statistically different at any reasonable confidence. P-values comparing all E_a and all $\Delta S^{\ddagger}$ for the unfunctionalized, 3.2 P/nm^2 OPA functionalized, and 3.2 P/nm^2 FOPA functionalized samples can be found as Tables 3.3 and 3.4.

These results evidence that phosphonic acids are changing the activation entropy of CO desorption without changing the activation enthalpy, resulting in a smaller Gibbs free activation energy for desorption. This evidences that phosphonic acid functionalization of Al_2O_3 surrounding atomically dispersed Rh active sites is a modification that allows for deviation from the entropy-enthalpy compensation effect; at least for the CO desorption elementary step.

Table 3.3: P-values from an unpaired two-tailed t tests comparing E_a values between the unfunctionalized, 3.2 P/nm^2 OPA functionalized, and 3.2 P/nm^2 FOPA functionalized samples.

	Unfun E_a	FOPA E_a	OPA E_a
Unfun E_a	1	0.52	0.39
FOPA E_a	0.52	1	0.22
OPA E_a	0.39	0.22	1

Table 3.4: P-values from an unpaired two-tailed t tests comparing $\Delta S^{\ddagger}$ values between the unfunctionalized, 3.2 P/nm^2 OPA functionalized, and 3.2 P/nm^2 FOPA functionalized samples.

	Unfun $\Delta S^{\ddagger}$	FOPA $\Delta S^{\ddagger}$	OPA $\Delta S^{\ddagger}$
Unfun $\Delta S^{\ddagger}$	1	0.03	0.0006
FOPA $\Delta S^{\ddagger}$	0.03	1	0.096
OPA $\Delta S^{\ddagger}$	0.0006	0.096	1

3.4. DISCUSSION

Our results raise some interesting questions that are worth discussing further: (1) Why is the activation entropy for CO desorption from $Rh(CO)_2$ negative? (2) How does phosphonic acid functionalization of the support make the activation entropy of CO desorption from $Rh(CO)_2$ less negative? (3) How does phosphonic acid functionalization of the support

promote TOF and increase selectivity for ethylene hydroformylation by Rh? (4) Is this a step toward imparting properties of homogeneous catalysts onto solid surfaces?

The activation entropy for CO desorption represents the difference in entropy between the initial state, $Rh(CO)_2$, and the transition state for desorption. The negative values observed in our experiments are interesting because late transition states for desorption typically have more entropy than the bound initial state due to the increase in degrees of freedom associated with transitioning to the gas phase. However, there is a precedent for multi-carbonyl desorption from organometallic complexes in zeolites exhibiting negative activation entropies.[28]

We hypothesize an origin for the negative activation entropy of CO desorption in our studies by first examining adsorption. Both COs in $Rh(CO)_2$ adsorb with equal binding energy,[71] but the second CO must approach at a particular orientation to enable $Rh(CO)_2$ formation. This results in a constrained transition state for adsorption of the second CO which, by microscopic reversibility, must be the same transition state for desorption. Thus, in the process of desorption, the transition state likely involves a constrained motion of the first CO leaving, while the second CO is still intact. This makes the transition appear much more similar to the initial state, $Rh(CO)_2$, as compared to the final state where both COs have desorbed. The higher entropy of the initial state compared to the desorption transition state suggests that $Rh(CO)_2$ has configurational entropy (e.g., rotational or translation degrees of freedom on the Al_2O_3 support) that is lost in forming the desorption transition state, resulting in a negative entropy of activation for desorption. It is known that $Rh(CO)_2$ complexes are mobile on supports such as Al_2O_3.[72,97,98] Further, COs bound to atomically dispersed metals have been observed by scanning tunneling microscopy to rotate, suggesting that the initial state has entropy beyond the C-O stretching modes.[99] The formation of the desorption transition state

may require a translationally or rotationally immobile $Rh(CO)_2$, effectively reducing the transition state entropy with respect to the initial state entropy.

The entropy of supported $Rh(CO)_2$ is hypothesized to be dominated by its translation on the support surface.[100] We have previously shown that the addition of phosphonic acid groups reduces the sintering of Rh species on Al_2O_3, presumably by hindering their translation on the support surface.[45] Therefore, $Rh(CO)_2$ species on Al_2O_3 surfaces are likely to possess between 0 to 2 degrees of translational freedom, which is decreased or hindered by the introduction of phosphonic acid groups. Estimates for a single translational degree of freedom for mobile species on surfaces are on the order of ~60-80 J/(mol K), as experimentally measured for adsorbates confined to 1D versus 2D arrangements on surfaces.[101] This estimate is in line with our measured entropy of activation (e.g., $\Delta S^{\ddagger}$ = -52±16 J/mol K for the unfunctionalized sample) for CO desorption from $Rh(CO)_2$/Al2O3. This suggests that $Rh(CO)_2$ species lose entropy equal to ~1 translational degree of freedom in the transition state for desorption. The induced change in activation entropy for CO desorption caused by OPA or FOPA functionalization (~ $\Delta\Delta S^{\ddagger}$ = 20-35 J/mol K) suggests that phosphonic acid functionalization significantly hinders the translation of $Rh(CO)_2$ species, in agreement with the diminished sintering we previously observed.

We note that rigorous assessments of the contribution of translational degrees of freedom to the entropy of $Rh(CO)_2$ would require accurate assessments of their diffusion barrier. Further, it has previously been hypothesized that rotations of molecular complexes can have unexpectedly large contributions to the entropy of species bound to surfaces.[102] While we expect translational degrees of freedom will dominate the entropy of bound $Rh(CO)_2$ species, given their small moment of inertia for rotation and known fast diffusion, future efforts

will address this specifically. It is also important to consider why the process of $Rh(CO)_2$ surface diffusion, which presumably is not barrierless, would not contribute to the enthalpy of desorption. Assuming that diffusion occurs between identical sites on the support, and that the process is equilibrated in the context of CO desorption, there would be no net ΔH_{rxn} for $Rh(CO)_2$ diffusion and thus no contribution to the activation enthalpy of CO desorption, thereby only influencing the activation entropy of CO desorption.

The less negative activation entropies for functionalized samples suggest that the entropy associated with the initial state, $Rh(CO)_2$, is reduced to the extent of being almost as constrained as the transition state, resulting in a nearly isentropic process (Figure 3.17). This modifies the free energy of desorption, such that CO desorbs at lower temperatures for phosphonic acid-functionalized samples. This suggests that these systems do not obey enthalpy-entropy compensation for at least some elementary steps, specifically those with mobile initial states and stationary transition states, as the activation entropies can be significantly modified without changes to the activation enthalpy. We hypothesize that deviation from enthalpy-entropy compensation is uniquely allowed in this system due to the mobile nature of the active site, and an apparent requirement of a stationary state for particular elementary steps to occur. By breaking enthalpy-entropy compensation, atomically dispersed catalysts with support functionalization provide a framework for exploring new reactivities that break linear free energy relationships.

As in the case with CO desorption, less negative activation entropies are observed for ethylene hydroformylation and hydrogenation. We would expect this, since CO desorption is a requisite elementary step in both hydroformylation and hydrogenation pathways, such that the apparent activation entropies obtained from Eyring analysis of the catalytic processes

include the changes in the kinetics of CO desorption.[84] This results in the promotion of the turn over frequency for both ethane and propanal formation, as CO desorption is a kinetically relevant step. The change in apparent activation entropy due to functionalization is almost identical for propanal formation and CO desorption, suggesting that the primary role of functionalization in propanal formation is the modification of CO desorption activation entropies. Due to the complexity of the apparent kinetics, this hypothesis cannot be verified experimentally. There is a more significant change in the apparent activation entropy for hydrogenation than hydroformylation as a result of support functionalization. This could be rationalized based on the more negative reaction order in CO for hydrogenation, which would cause changes in the kinetics of CO desorption to more significantly influence the kinetics of ethylene hydrogenation. Although, the confluence of the likely change in reaction flux through the competing reaction pathways for ethane formation makes it challenging to justify this assertion.

The less negative activation entropy is accompanied by an activation enthalpy that does not change with phosphonic acid coverage for ethylene hydroformylation, but does increase with phosphonic acid coverage for hydrogenation. Based on recent DFT-based microkinetic modeling for this system,[84] it is likely that changes in activation enthalpy for ethylene hydrogenation are due to changes in the relative flux of product formation through two possible hydrogenation pathways. The two pathways proceed through isomers of the $Rh(CO)(H)(C_2H_5)$ species and exhibit distinct apparent activation enthalpies and entropies. Thus, steric hindrance caused by phosphonic acid functionalization around the active site may cause a change in the relative flux through these pathways, and as a result cause changes to the apparent activation enthalpy and entropy. It is therefore reasonable that changes in enthalpic and entropic barriers

are observed for hydrogenation, but only changes in entropic barriers are observed for propanal formation. For these reasons, it is likely that entropy-enthalpy compensation is broken by support functionalization for all reactions examined here, despite the change in the apparent enthalpy of activation for ethane formation. The increase in activation enthalpy for hydrogenation, but not hydroformylation, results in greater increases in the rate for hydroformylation and increased selectivity towards propanal.

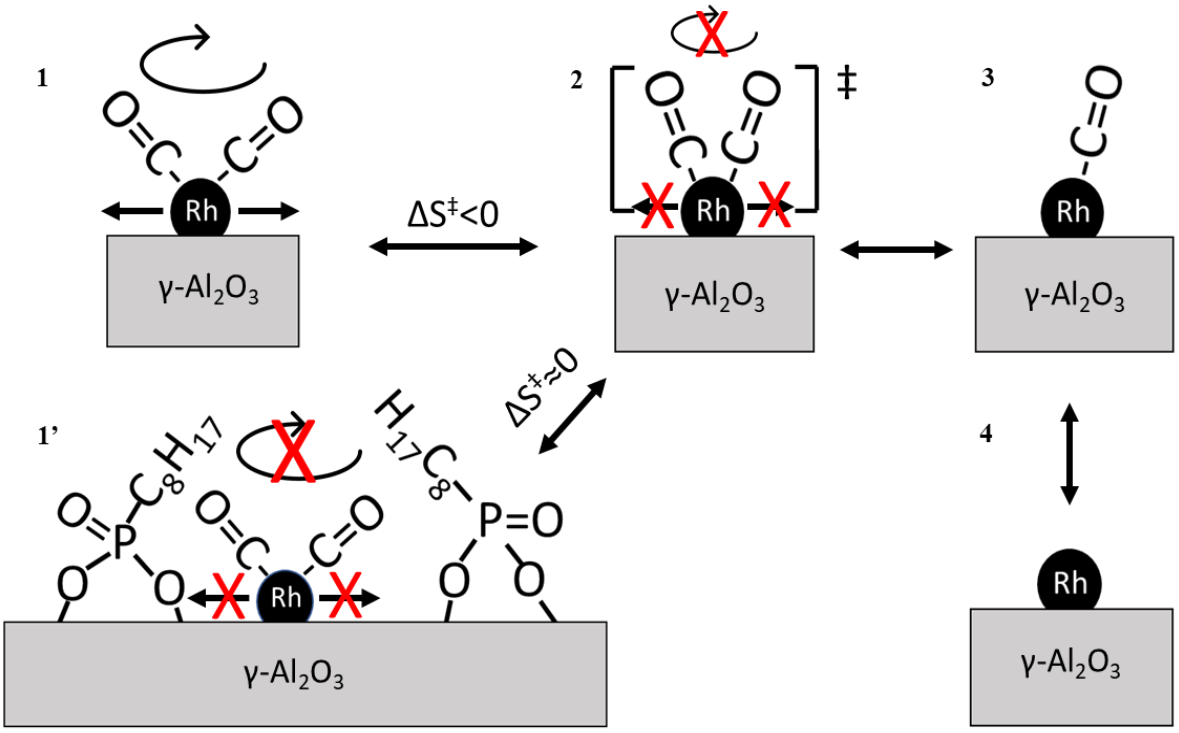

Figure 3.17: Proposed mechanism by which CO desorption from $Rh(CO)_2$ has a negative activation entropy, and how PA functionalization results in a less negative activation entropy. (1) Initial state of $Rh(CO)_2$ on γ-Al_2O_3. (1') Initial state of $Rh(CO)_2$ on PA functionalized γ-Al_2O_3. (2) Transition state for desorption/adsorption of the second CO. (3) Rh on γ-Al_2O_3 with single CO adsorbed. (4) Rh on γ-Al_2O_3 with no adsorbates. In (1), $Rh(CO)_2$ has translational and rotational degrees of freedom. In (2), these degrees of freedom are constrained to allow for desorption of the first CO. This results in an entropic barrier to go from (1) to (2). In (1'), rotational and translational degrees of freedom are already constrained by PA functionalization, resulting in a smaller entropic barrier to go from (1') to (2). (3) goes to (4) facilely since both COs in $Rh(CO)_2$ have the same binding energy.

The preceding discussion suggests that the primary influence of support functionalization is to reduce the configurational entropy of the $Rh(CO)_2$ species. However,

the opposite shifts in vibrational frequency of CO bound to Rh upon OPA and FOPA functionalization of the support and the apparent influence of support functionalization on the ethylene hydrogenation reaction pathway also suggests interactions between the phosphonic acid monolayer and adsorbates bound to Rh. It appears as if interactions between adsorbates and phosphonic acid tails are entirely through space, such that the electronic state of Rh remains approximately constant. This is evidenced by the constant activation enthalpy for propanal formation, along with the constant activation enthalpy of CO desorption. This suggests that the shifts in stretch frequencies observed for adsorbed CO upon support functionalization are due to through-space interactions between the phosphonic acid tails and adsorbed CO. For example, it has previously been demonstrated that non-covalent interactions between nearby chemical species can shift CO stretching frequencies in $Rh(CO)_2$ via nonspecific inductive and dispersive interactions. [103] Additionally, C-H and C-F may be altering the local electric fields at the support surface, resulting in Stark shifts in CO vibrational frequencies, as has been previously reported for changes in local electric fields around IR active species.[104,105] Further, the similar coverage of OPA and FOPA inferred from TGA measurements suggests that they should have a similar influence on the activation entropy of CO desorption from Rh, if the only influence of support functionalization was on decreasing the translational mobility of $Rh(CO)_2$. This suggests that intermolecular interactions between phosphonic acid tails may also control activation entropies of elementary steps on atomically dispersed metal sites. The higher desorption temperature of CO for the FOPA functionalized catalyst than the OPA functionalized catalyst may be attributed to the increased rigidity of fluorocarbon species compared to hydrocarbons, resulting in less interactions between phosphonic acid ligands and adsorbed CO.[106] In the future, it will be interesting to consider

how intermolecular interactions within the phosphonic acid monolayer control the resulting influence on chemistry occurring at atomically dispersed active sites.[82,83]

This method of catalyst modification is of particular interest for systems in which regioselectivity is important. The evidence that adsorbates bound to atomically dispersed Rh sites are significantly constrained by phosphonic acid ligands suggests that for larger molecules, these effects might be amplified. Controlling adsorbate orientation is essential for dictating regioselectivity in reactions where bond breaking or formation can occur in different positions on reactant molecules. For these types of reactions, such as Reppe carbonylation[107] and longer chain olefin hydroformylation,[53] homogeneous catalysts that can control adsorbate geometry are the industrial standard. Mimicking the local environment of these molecular catalysts in heterogenous catalysts could allow for less energy-intensive industrial processes.

3.5. CONCLUSION

In conclusion, we have demonstrated an approach for modifying the activation entropy of elementary steps and catalytic reactions on atomically dispersed Rh active sites on oxide supports. This was achieved by confining adsorbed species via the functionalization of the oxide support with phosphonic acid ligands, resulting in fewer degrees of freedom for the active site and the introduction of a constrained active site environment. This reduces the difference in entropy between the initial adsorbed states and transition states, while not affecting activation enthalpies. Evidence was provided that phosphonic acid functionalization enabled tuning of catalytic functionality in a way that breaks enthalpy-entropy compensation, reducing the activation Gibbs free energy, and increasing reaction rates. This approach is unique in that changes in reactivity are due to changes in the steric environment, while most

approaches for modifying atomically dispersed metal active sites seek to alter the active metal coordination to the support, resulting in changes in the electronic structure and thus reaction enthalpies. As a result, this catalyst system shows increased activity and selectivity in ethylene hydroformylation and shows promise for use in systems that require adsorbate confinement to control regioselectivity.

3.6 APPENDIX

Derivation of Equation 3.5 (Equation 3.6.1)

The Polanyi-Wigner equation describes a kinetically limited desorption process[95]:

$$-\frac{d\theta}{dT} = \frac{A}{\beta}\theta^m \exp\left(-\frac{E_d}{k_B T}\right) \qquad (3.6.1A)$$

Where: θ=Coverage of adsorbate
T=Temperature (K)
A=Preexponential Factor (1/s)
β=Temperature Ramp Rate (K/s)
E_d=Desorption Energy (eV)
k_B=Boltzmann Constant (eV/K)
m= the desorption order.

At the maximum desorption rate, $-\frac{d\theta^2}{dT^2} = 0$. Taking the second derivative and setting it to zero:

$$\frac{E_d}{k_B T_P^2} = \frac{A}{\beta} m\theta^{m-1} \exp\left(-\frac{E_d}{k_B T_P}\right) \qquad (3.6.1B)$$

Where: T_P=temperature at which there is maximum desorption (K)

Further, CO desorption on atomically dispersed Rh is first order, therefore m=1

$$\frac{E_d}{k_B T_P^2} = \frac{A}{\beta} \exp\left(-\frac{E_d}{k_B T_P}\right) \qquad (3.6.1C)$$

Rearranging:

$$\ln\left(\frac{\beta}{k_B T_P^2}\right) = \frac{-E_d}{k_B T_P} + \ln\left(\frac{\mathrm{A}}{\mathrm{E_d}}\right) \qquad (3.6.1D)$$

Performing experiments at different β will result in different T_P. Plotting $\ln\left(\frac{\beta}{k_B T_P^2}\right)$ vs $\frac{1}{k_B T_P}$ and fitting a line to the data yields $-E_d$ as the coefficient and $\ln(A/E_d)$ as the intercept

Readsorption Calculations for TPDs (Equation 3.6.2)

For a porous bed packed bed, the ratio of adsorption to diffusion can be defined as:[90]

$$\frac{\alpha \rho F l^2}{\pi^2 D} \qquad (3.6.2A)$$

Where: α= active surface area (cm^2/g)
ρ= bulk density (cm^3/g)
F= Flux of gas to the catalyst surface (cm/s)
l= Length of bed probed (cm)
D= Diffusivity of adsorbate (cm^2/s)

For readsorption to be significant, $\frac{\alpha \rho F l^2}{\pi^2 D} \geq 1$

Although our particles are not porous, we are treating the packing of the 5 nm particles as if it was a slab of γ-Al_2O_3 with pores on the scale of 5nm.

For these calculations, the sticking coefficient was assumed to be one to represent the worst-case scenario for readsorption.

This results in readsorption being significant at a depth of ~17 microns.

The question is how deep the IR light is probing? Traditionally, DRIFTS exhibits behavior such that light scatters and reflects off of the initial interface between the bed and the gas phase, while the light scatters continuously off of the particles below the surface. In our case, our particles are only 5nm while the wavelength of our IR light of interest is ~5 microns. This results in negligible scattering from individual support particles as calculated via Equation 3.6.2B.[91] σ_s, known as the Rayleigh scattering cross section, represents the fraction of light scattered off of particles much smaller than the wavelength of the light.

$$\sigma_s = \frac{2\pi^5}{3} \frac{d^6}{\lambda^4} \left(\frac{n^2 - 1}{n^2 + 2}\right)^2 \qquad (3.6.2B)$$

Where: σ_s=Rayleigh scattering cross section (m^2)
d=Diameter of the sphere (m)
λ=Wavelength of incident light (m)
n=index of refraction of alumina

Using an index of refraction of 1.728 for alumina[93],

$$\sigma_s \approx 8 * 10^{-28}\, m^2$$

Given that our bed of catalytic material is less than 1 mm thick, this results in negligible scattering of the IR light after the initial reflection at the surface.

Calculating the Activation Entropy From the Preexponential Factor (Equation 3.6.3)

In order to calculate the activation entropy from the preexponential factor, the preexponential factor in the Arrhenius equation (Equation 3.6.3A) must be defined in the context of the Eyring-Polanyi equation (Equation 3.6.3B).

$$k = A \exp\left(\frac{-E_a}{RT}\right) \qquad (3.6.3A)$$

Where: k = rate constant (units are dependent on the reaction order)
T= temperature (K)
E_a= Activation Energy (J/mol)
R= Molar gas constant (J/(mol*K))

$$k = \frac{\kappa k_B T}{h} \exp\left(\frac{\Delta S^{\ddagger}}{\mathrm{R}}\right) \exp\left(-\frac{\Delta H^{\ddagger}}{RT}\right) \qquad (3.6.3B)$$

Where:
$\Delta H^{\ddagger}$ = Activation Enthalpy (J/mol)
$\Delta S^{\ddagger}$ = Activation Entropy (J/(mol*K))
κ= Transmission Coefficient (assumed to be unity)
k_B= Boltzmann Constant (J/K)
h = Planck Constant (J*s)

For a unimolecular, single step reaction, the activation energy can be related to the activation enthalpy by Equation 3.6.3C.[96,108]

$$E_a = \Delta H^{\ddagger} + RT \qquad (S.6.3C)$$

Substituting Equation 3.6.3C into Equation 3.6.3B results in Equation 3.6.3D

$$k = \frac{\kappa k_B T}{h} \exp\left(\frac{\Delta S^{\ddagger}}{\mathrm{R}}\right) \exp\left(\frac{-E_a + RT}{RT}\right) \qquad (3.6.3D)$$

Setting Equation 3.6.3A equal to Equation 3.6.3D yields Equation 3.6.3E

$$A \exp\left(\frac{-E_a}{RT}\right) = \frac{\kappa k_B T}{h} \exp\left(\frac{\Delta S^{\ddagger}}{\mathrm{R}}\right) \exp\left(\frac{-E_a + RT}{RT}\right) \quad (3.6.3E)$$

Dividing both sides of the equation by $\exp\left(\frac{-E_a}{RT}\right)$ yields Equation 3.6.3F.

$$A = \frac{\kappa k_B T}{h} \exp\left(\frac{\Delta S^{\ddagger}}{\mathrm{R}}\right) \exp(1) \quad (3.6.3F)$$

Solving for the activation entropy and setting the transmission coefficient to one yields Equation 3.6.3G

$$\Delta S^{\ddagger} = R\left(\ln\left(\frac{Ah}{k_B T}\right) - 1\right) \quad (3.6.3G)$$

3.7 REFERENCES

[1] M.A. Barteau, Linear free energy relationships for C1-oxygenate decomposition on transition metal surfaces, Catal. Letters. 8 (1991) 175–183. https://doi.org/10.1007/BF00764114.

[2] R.J. Madix, Reaction Kinetics and Mechanism on Metal Single Crystal Surfaces, Adv. Catal. 29 (1980) 1–53. https://doi.org/10.1016/S0360-0564(08)60119-4.

[3] J.K. Nørskov, T. Bligaard, A. Logadottir, S. Bahn, L.B. Hansen, M. Bollinger, H. Bengaard, B. Hammer, Z. Sljivancanin, M. Mavrikakis, Y. Xu, S. Dahl, C.J.H. Jacobsen, Universality in heterogeneous catalysis, J. Catal. 209 (2002) 275–278. https://doi.org/10.1006/jcat.2002.3615.

[4] F. Abild-Pedersen, J. Greeley, F. Studt, J. Rossmeisl, T.R. Munter, P.G. Moses, E. Skúlason, T. Bligaard, J.K. Nørskov, Scaling properties of adsorption energies for hydrogen-containing molecules on transition-metal surfaces, Phys. Rev. Lett. 99 (2007) 016105. https://doi.org/10.1103/PhysRevLett.99.016105.

[5] J. Hulva, M. Meier, R. Bliem, Z. Jakub, F. Kraushofer, M. Schmid, U. Diebold, C. Franchini, G.S. Parkinson, Unraveling CO adsorption on model single-atom catalysts, Science. 371 (2021) 375–379. https://doi.org/10.1126/science.abe5757.

[6] H. Xu, C.Q. Xu, D. Cheng, J. Li, Identification of activity trends for CO oxidation on supported transition-metal single-atom catalysts, Catal. Sci. Technol. 7 (2017) 5860–5871. https://doi.org/10.1039/c7cy00464h.

[7] T. Bligaard, J.K. Nørskov, S. Dahl, J. Matthiesen, C.H. Christensen, J. Sehested, The Brønsted-Evans-Polanyi relation and the volcano curve in heterogeneous catalysis, J. Catal. 224 (2004) 206–217. https://doi.org/10.1016/j.jcat.2004.02.034.

[8] B. Hammer, J.K. Nørskov, Theoretical surface science and catalysis—calculations and concepts, Adv. Catal. 45 (2000) 71–129. https://doi.org/10.1016/S0360-0564(02)45013-4.

[9] S. Wang, V. Petzold, V. Tripkovic, J. Kleis, J.G. Howalt, E. Skúlason, E.M. Fernández, B. Hvolbæk, G. Jones, A. Toftelund, H. Falsig, M. Björketun, F. Studt, F. Abild-Pedersen, J. Rossmeisl, J.K. Nørskov, T. Bligaard, Universal transition state scaling relations for (de)hydrogenation over transition metals, Phys. Chem. Chem. Phys. 13 (2011) 20760–20765. https://doi.org/10.1039/c1cp20547a.

[10] M. Boudart, Handbook of Heterogeneous Catalysis, Wiley-VCH Verlag, 1997. https://doi.org/10.1002/9783527619474.

[11] M. Boudart, Kinetics of Heterogeneous Catalytic, Princeton University Press, 1984.

[12] and A.A.T. James A. Dumesic, Dale F. Rudd, Luis M. Aparicio, James E. Rekoske, The Microkinetics of Heterogeneous Catalysis, American Chemical Society, 1993.

[13] M. Boudart, Pauling's theory of metals in catalysis, J. Am. Chem. Soc. 72 (1950) 1040. https://doi.org/10.1021/ja01158a522.

[14] B. Hammer, J.K. Norskov, Why gold is the noblest of all the metals, Nature. (1995). https://doi.org/10.1038/376238a0.

[15] M. Andersen, A.J. Medford, J.K. Nørskov, K. Reuter, Scaling-Relation-Based Analysis of Bifunctional Catalysis: The Case for Homogeneous Bimetallic Alloys, ACS Catal. (2017). https://doi.org/10.1021/acscatal.7b00482.

[16] M.T. Darby, M. Stamatakis, A. Michaelides, E.C.H. Sykes, Lonely Atoms with Special Gifts: Breaking Linear Scaling Relationships in Heterogeneous Catalysis with

Single-Atom Alloys, J. Phys. Chem. Lett. (2018). https://doi.org/10.1021/acs.jpclett.8b01888.
[17] G. Kumar, E. Nikolla, S. Linic, J.W. Medlin, M.J. Janik, Multicomponent Catalysts: Limitations and Prospects, ACS Catal. 8 (2018) 3202–3208. https://doi.org/10.1021/acscatal.8b00145.
[18] J. Pérez-Ramírez, N. López, Strategies to break linear scaling relationships, Nat. Catal. (2019). https://doi.org/10.1038/s41929-019-0376-6.
[19] A. Khorshidi, J. Violet, J. Hashemi, A.A. Peterson, How strain can break the scaling relations of catalysis, Nat. Catal. (2018). https://doi.org/10.1038/s41929-018-0054-0.
[20] J. Qi, J. Resasco, H. Robatjazi, I.B. Alvarez, O. Abdelrahman, P. Dauenhauer, P. Christopher, Dynamic Control of Elementary Step Energetics via Pulsed Illumination Enhances Photocatalysis on Metal Nanoparticles, ACS Energy Lett. 18 (2020) 3518–3525. https://doi.org/10.1021/acsenergylett.0c01978.
[21] M.A. Ardagh, O.A. Abdelrahman, P.J. Dauenhauer, Principles of Dynamic Heterogeneous Catalysis: Surface Resonance and Turnover Frequency Response, ACS Catal. (2019). https://doi.org/10.1021/acscatal.9b01606.
[22] P. Mehta, P. Barboun, F.A. Herrera, J. Kim, P. Rumbach, D.B. Go, J.C. Hicks, W.F. Schneider, Overcoming ammonia synthesis scaling relations with plasma-enabled catalysis, Nat. Catal. (2018). https://doi.org/10.1038/s41929-018-0045-1.
[23] R. Hercigonja, V. Rac, V. Rakic, A. Auroux, Enthalpy-entropy compensation for n-hexane adsorption on HZSM-5 containing transition metal ions, J. Chem. Thermodyn. 48 (2012) 112–117. https://doi.org/10.1016/j.jct.2011.12.016.
[24] R. Hercigonja, V. Rakić, Enthalpy-entropy compensation for n-hexane adsorption on Y zeolite containing transition metal cations, Sci. Sinter. 47 (2015) 83–88. https://doi.org/10.2298/SOS1501091H.
[25] D.W. Flaherty, E. Iglesia, Transition-state enthalpy and entropy effects on reactivity and selectivity in hydrogenolysis of n -alkanes, J. Am. Chem. Soc. 135 (2013) 18586–18599. https://doi.org/10.1021/ja4093743.
[26] A. Bhan, R. Gounder, J. Macht, E. Iglesia, Entropy considerations in monomolecular cracking of alkanes on acidic zeolites, J. Catal. 253 (2008) 221–224. https://doi.org/10.1016/j.jcat.2007.11.003.
[27] R. Gounder, E. Iglesia, The Roles of Entropy and Enthalpy in Stabilizing Ion-Pairs at Transition States in Zeolite Acid Catalysis, Acc. Chem. Res. 45 (2012) 229–238. https://doi.org/10.1021/ar200138n.
[28] A.L. Fernandez, J. Hao, R.L. Parkes, A.J. Poë, E.J.S. Vichi, Zeolite activation of organometallics: Anchoring and decarbonylation kinetics of Mo(CO) 6 in dehydrated Na 56Y zeolite, Organometallics. 23 (2004) 2715–2723. https://doi.org/10.1021/om040005v.
[29] N. Kosinov, C. Liu, E.J.M. Hensen, E.A. Pidko, Engineering of Transition Metal Catalysts Confined in Zeolites, Chem. Mater. 30 (2018) 3177–3198. https://doi.org/10.1021/acs.chemmater.8b01311.
[30] D. Yang, P. Xu, N.D. Browning, B.C. Gates, Tracking Rh Atoms in Zeolite HY: First Steps of Metal Cluster Formation and Influence of Metal Nuclearity on Catalysis of Ethylene Hydrogenation and Ethylene Dimerization, J. Phys. Chem. Lett. (2016). https://doi.org/10.1021/acs.jpclett.6b01153.

[31] V. Ortalan, A. Uzun, B.C. Gates, N.D. Browning, Direct imaging of single metal atoms and clusters in the pores of dealuminated HY zeolite, Nat. Nanotechnol. (2010). https://doi.org/10.1038/nnano.2010.92.
[32] G.A. Ozin, S. Ozkart, Zeolates: A Coordination Chemistry View of Metal-Ligand Bonding in Zeolite Guest-Host Inclusion Compounds, Chem. Mater. 4 (1992) 511–521. https://doi.org/10.1021/cm00021a008.
[33] L. Liu, M. Lopez-Haro, C.W. Lopes, C. Li, P. Concepcion, L. Simonelli, J.J. Calvino, A. Corma, Regioselective generation and reactivity control of subnanometric platinum clusters in zeolites for high-temperature catalysis, Nat. Mater. (2019). https://doi.org/10.1038/s41563-019-0412-6.
[34] L. Liu, A. Corma, Metal Catalysts for Heterogeneous Catalysis: From Single Atoms to Nanoclusters and Nanoparticles, Chem. Rev. 118 (2018) 4981–5079. https://doi.org/10.1021/acs.chemrev.7b00776.
[35] C.A. Schoenbaum, D.K. Schwartz, J.W. Medlin, Controlling surface crowding on a Pd catalyst with thiolate self-assembled monolayers, J. Catal. (2013). https://doi.org/10.1016/j.jcat.2013.03.012.
[36] M. Siemer, G. Tomaschun, T. Klüner, P. Christopher, P. Christopher, K. Al-Shamery, Insights into Spectator-Directed Catalysis: CO Adsorption on Amine-Capped Platinum Nanoparticles on Oxide Supports, ACS Appl. Mater. Interfaces. 12 (2020) 27765–27776. https://doi.org/10.1021/acsami.0c06086.
[37] S. Schauermann, J. Hoffmann, V. Johánek, J. Hartmann, J. Libuda, H.J. Freund, Catalytic activity and poisoning of specific sites on supported metal nanoparticles, Angew. Chemie - Int. Ed. 41 (2002) 2532–2535. https://doi.org/10.1002/1521-3773(20020715)41:14<2532::AID-ANIE2532>3.0.CO;2-3.
[38] H.U. Blaser, M. Studer, Cinchona-modified platinum catalysts: From ligand acceleration to technical processes, Acc. Chem. Res. 40 (2007) 1348–1356. https://doi.org/10.1021/ar700088f.
[39] C.A. Schoenbaum, D.K. Schwartz, J.W. Medlin, Controlling the surface environment of heterogeneous catalysts using self-assembled monolayers, Acc. Chem. Res. 47 (2014) 1438–1445. https://doi.org/10.1021/ar500029y.
[40] J. Zhang, L.D. Ellis, B. Wang, M.J. Dzara, C. Sievers, S. Pylypenko, E. Nikolla, J.W. Medlin, Control of interfacial acid–metal catalysis with organic monolayers, Nat. Catal. 1 (2018). https://doi.org/10.1038/s41929-017-0019-8.
[41] A.R. Riscoe, C.J. Wrasman, A.A. Herzing, A.S. Hoffman, A. Menon, A. Boubnov, M. Vargas, S.R. Bare, M. Cargnello, Transition state and product diffusion control by polymer–nanocrystal hybrid catalysts, Nat. Catal. 2 (2019) 852–863. https://doi.org/10.1038/s41929-019-0322-7.
[42] Q. Sun, Z. Dai, X. Liu, N. Sheng, F. Deng, X. Meng, F.S. Xiao, Highly efficient heterogeneous hydroformylation over rh-metalated porous organic polymers: Synergistic effect of high ligand concentration and flexible framework, J. Am. Chem. Soc. 137 (2015) 5204–5209. https://doi.org/10.1021/jacs.5b02122.
[43] T.K. Slot, N. Riley, N.R. Shiju, J.W. Medlin, G. Rothenberg, An experimental approach for controlling confinement effects at catalyst interfaces, Chem. Sci. 11 (2020) 11024–11029. https://doi.org/10.1039/d0sc04118a.

[44] L.O. Mark, C. Zhu, J.W. Medlin, H. Heinz, Understanding the Surface Reactivity of Ligand-Protected Metal Nanoparticles for Biomass Upgrading, ACS Catal. 10 (2020) 5462–5474. https://doi.org/10.1021/acscatal.9b04772.
[45] J. Zhang, C. Asokan, G. Zakem, P. Christopher, J.W. Medlin, Enhancing Sintering Resistance of Atomically Dispersed Catalysts in Reducing Environments with Organic Monolayers, Green Energy Environ. (2021). https://doi.org/10.1016/j.gee.2021.01.022.
[46] L. Chen, G.E. Sterbinsky, S.L. Tait, Synthesis of platinum single-site centers through metal-ligand self-assembly on powdered metal oxide supports, J. Catal. 365 (2018) 303–312. https://doi.org/10.1016/j.jcat.2018.07.004.
[47] L. DeRita, S. Dai, K. Lopez-Zepeda, N. Pham, G.W. Graham, X. Pan, P. Christopher, Catalyst Architecture for Stable Single Atom Dispersion Enables Site-Specific Spectroscopic and Reactivity Measurements of CO Adsorbed to Pt Atoms, Oxidized Pt Clusters, and Metallic Pt Clusters on TiO2, J. Am. Chem. Soc. 139 (2017) 14150–14165. https://doi.org/10.1021/jacs.7b07093.
[48] L. DeRita, J. Resasco, S. Dai, A. Boubnov, H.V. Thang, A.S. Hoffman, I. Ro, G.W. Graham, S.R. Bare, G. Pacchioni, X. Pan, P. Christopher, Structural evolution of atomically dispersed Pt catalysts dictates reactivity, Nat. Mater. (2019). https://doi.org/10.1038/s41563-019-0349-9.
[49] J. Resasco, L. Derita, S. Dai, J.P. Chada, M. Xu, X. Yan, J. Finzel, S. Hanukovich, A.S. Hoffman, G.W. Graham, S.R. Bare, X. Pan, P. Christopher, Uniformity Is Key in Defining Structure-Function Relationships for Atomically Dispersed Metal Catalysts: The Case of Pt/CeO2, J. Am. Chem. Soc. 142 (2020) 169–184. https://doi.org/10.1021/jacs.9b09156.
[50] I. Ro, M. Xu, G.W. Graham, X. Pan, P. Christopher, Synthesis of Heteroatom Rh–ReO_x Atomically Dispersed Species on Al_2O_3 and Their Tunable Catalytic Reactivity in Ethylene Hydroformylation, ACS Catal. 9 (2019) 10899–10912. https://doi.org/10.1021/acscatal.9b02111.
[51] C. Asokan, H.V. Thang, G. Pacchioni, P. Christopher, Reductant composition influences the coordination of atomically dispersed Rh on anatase TiO2, Catal. Sci. Technol. 10 (2020) 1597–1601. https://doi.org/10.1039/d0cy00146e.
[52] Y. Izumi, K. Asakura, Y. Iwasawa, Promoting effects of Se on Rh/ZrO2 catalysis for ethene hydroformylation, J. Catal. (1991). https://doi.org/10.1016/0021-9517(91)90188-A.
[53] R. Tudor, M. Ashley, Enhancement of industrial hydroformylation processes by the adoption of rhodium-based catalyst: Part II, Platin. Met. Rev. 51 (2007) 164–171. https://doi.org/10.1595/147106707X238211.
[54] R. Lang, T. Li, D. Matsumura, S. Miao, Y. Ren, Y.T. Cui, Y. Tan, B. Qiao, L. Li, A. Wang, X. Wang, T. Zhang, Hydroformylation of Olefins by a Rhodium Single-Atom Catalyst with Activity Comparable to RhCl(PPh3)3, Angew. Chemie - Int. Ed. 55 (2016) 16054–16058. https://doi.org/10.1002/anie.201607885.
[55] L. Wang, W.W. Zhang, S. Wang, Z. Gao, Z. Luo, X. Wang, R. Zeng, A. Li, H. Li, M. Wang, X. Zheng, J. Zhu, W.W. Zhang, C. Ma, R. Si, J. Zeng, Atomic-level insights in optimizing reaction paths for hydroformylation reaction over Rh/CoO single-atom catalyst, Nat. Commun. 7 (2016) 1–8. https://doi.org/10.1038/ncomms14036.

[56] J. Zhang, P. Sun, G. Gao, J. Wang, Z. Zhao, Y. Muhammad, F. Li, Enhancing regioselectivity via tuning the microenvironment in heterogeneous hydroformylation of olefins, J. Catal. 387 (2020) 196–206. https://doi.org/10.1016/j.jcat.2020.03.032.
[57] C. Li, W. Wang, L. Yan, Y. Ding, A mini review on strategies for heterogenization of rhodium-based hydroformylation catalysts, Front. Chem. Sci. Eng. 12 (2018) 113–123. https://doi.org/10.1007/s11705-017-1672-9.
[58] S. Hanf, L.A. Rupflin, R. Gläser, S.A. Schunk, L. Alvarado Rupflin, R. Gläser, S.A. Schunk, L.A. Rupflin, R. Gläser, S.A. Schunk, Current State of the Art of the Solid Rh-Based Catalyzed Hydroformylation of Short-Chain Olefins, 10 (2020) 510. https://www.mdpi.com/2073-4344/10/5/510/htm (accessed February 23, 2021).
[59] X. Wan, I. Lieberman, A. Asyuda, S. Resch, H. Seim, P. Kirsch, M. Zharnikov, Thermal Stability of Phosphonic Acid Self-Assembled Monolayers on Alumina Substrates, J. Phys. Chem. C. 124 (2020) 2531–2542. https://doi.org/10.1021/acs.jpcc.9b10628.
[60] K.R. Kahsar, D.K. Schwartz, J.W. Medlin, Control of metal catalyst selectivity through specific noncovalent molecular interactions, J. Am. Chem. Soc. 136 (2014) 520–526. https://doi.org/10.1021/ja411973p.
[61] E. Larsen, Fluorine Compounds in Anesthesiology: VI Flammability, Fluor. Chem. Rev. (1969) 22–27.
[62] A.H. Jenkins, C.B. Musgrave, J.W. Medlin, Enhancing Au/TiO2 Catalyst Thermostability and Coking Resistance with Alkyl Phosphonic-Acid Self-Assembled Monolayers, ACS Appl. Mater. Interfaces. 11 (2019) 41289–41296. https://doi.org/10.1021/acsami.9b13170.
[63] J.C. Matsubu, V.N. Yang, P. Christopher, Isolated Metal Active Site Concentration and Stability Control Catalytic CO 2 Reduction Selectivity, (n.d.). https://doi.org/10.1021/ja5128133.
[64] Y. Kwon, T.Y. Kim, G. Kwon, J. Yi, H. Lee, Selective Activation of Methane on Single-Atom Catalyst of Rhodium Dispersed on Zirconia for Direct Conversion, J. Am. Chem. Soc. (2017). https://doi.org/10.1021/jacs.7b11010.
[65] J.T. Yates, K. Kolasinski, Infrared spectroscopic investigation of the rhodium gem-dicarbonyl surface species, J. Chem. Phys. (1983). https://doi.org/10.1063/1.445844.
[66] J.T. Yates, T.M. Duncan, S.D. Worley, R.W. Vaughan, Infrared spectra of chemisorbed CO on Rh, J. Chem. Phys. (1979). https://doi.org/10.1063/1.437603.
[67] T.M. Duncan, J.T. Yates, R.W. Vaughan, A 13C NMR study of the adsorbed states of CO on Rh dispersed on Al203, J. Chem. Phys. (1980). https://doi.org/10.1063/1.440746.
[68] C. Asokan, L. Derita, P. Christopher, Using probe molecule FTIR spectroscopy to identify and characterize Pt - group metal based single atom catalysts, Chinese J. Catal. 38 (2017) 1473–1480. https://doi.org/10.1016/S1872-2067(17)62882-1.
[69] C. Asokan, Y. Yang, A. Dang, A. Getsoian, P. Christopher, Low-Temperature Ammonia Production during NO Reduction by CO Is Due to Atomically Dispersed Rhodium Active Sites, ACS Catal. 10 (2020) 5217–5222. https://doi.org/10.1021/acscatal.0c01249.
[70] R.R. Cavanagh, J.T. Yates, Site distribution studies of Rh supported on Al2O3 - An infrared study of chemisorbed CO, J. Chem. Phys. (1981). https://doi.org/10.1063/1.441544.

[71] Y. Tang, C. Asokan, M. Xu, G.W. Graham, X. Pan, P. Christopher, J. Li, P. Sautet, Rh single atoms on TiO2 dynamically respond to reaction conditions by adapting their site, Nat. Commun. 10 (2019) 1–10. https://doi.org/10.1038/s41467-019-12461-6.
[72] H.F.J. van't Blik, T. Huizinga, J.B.A.D. van Zon, J.C. Vis, D.C. Koningsberger, R. Prins, Structure of Rhodium in an Ultradispersed Rh/Al2O3 Catalyst as Studied by EXAFS and Other Techniques, J. Am. Chem. Soc. 107 (1985) 3139–3147. https://doi.org/10.1021/ja00297a020.
[73] J.L. Robbins, Rhodium dicarbonyl sites on alumina surfaces. 1. Preparation and characterization of a model system, J. Phys. Chem. 90 (1986) 3381–3386. https://doi.org/10.1021/j100406a016.
[74] D.A. Buchanan, M.E. Hernandez, F. Solymosi, J.M. White, CO-induced structural changes of Rh on TiO2 Support, J. Catal. 125 (1990) 456–466. https://doi.org/10.1016/0021-9517(90)90318-E.
[75] H. Guan, J. Lin, B. Qiao, S. Miao, A. Wang, X. Wang, T. Zhang, Enhanced performance of Rh $_1$ /TiO $_2$ catalyst without methanation in water-gas shift reaction, AIChE J. 63 (2017) 2081–2088. https://doi.org/10.1002/aic.15585.
[76] J. Resasco, S. Dai, G. Graham, X. Pan, P. Christopher, Combining In-Situ Transmission Electron Microscopy and Infrared Spectroscopy for Understanding Dynamic and Atomic-Scale Features of Supported Metal Catalysts, J. Phys. Chem. C. 122 (2018) 25143–25157. https://doi.org/10.1021/acs.jpcc.8b03959.
[77] H.C. Yao, W.G. Rothschild, Infrared spectra of chemisorbed CO on Rh/γ-AI2O 3: Site distributions and molecular mobility, J. Chem. Phys. (1978). https://doi.org/10.1063/1.435657.
[78] A.S. Hoffman, C.Y. Fang, B.C. Gates, Homogeneity of Surface Sites in Supported Single-Site Metal Catalysts: Assessment with Band Widths of Metal Carbonyl Infrared Spectra, J. Phys. Chem. Lett. (2016). https://doi.org/10.1021/acs.jpclett.6b01825.
[79] M. Babucci, C.-Y. Fang, A.S. Hoffman, S.R. Bare, B.C. Gates, A. Uzun, Tuning the Selectivity of Single-Site Supported Metal Catalysts with Ionic Liquids, 16 (2020) 0. https://doi.org/10.1021/acscatal.7b02429.
[80] M. Babucci, C.-Y. Fang, J.E. Perez-Aguilar, A.S. Hoffman, A. Boubnov, E. Guan, S.R. Bare, B.C. Gates, A. Uzun, Controlling catalytic activity and selectivity for partial hydrogenation by tuning the environment around active sites in iridium complexes bonded to supports, Chem. Sci. 10 (2019) 2623–2632. https://doi.org/10.1039/C8SC05287E.
[81] C. Hansch, A. Leo, R.W. Taft, R.W. Hansch, Corwin; Leo, A; Taft, A Survey of Hammett Substituent Constants and Resonance and Field Parameters, Chem. Rev. 91 (1991) 165–195.
[82] B.W. Ewers, J.D. Batteas, Molecular dynamics simulations of alkylsilane monolayers on silica nanoasperities: Impact of surface curvature on monolayer structure and pathways for energy dissipation in tribological contacts, J. Phys. Chem. C. 116 (2012) 25165–25177. https://doi.org/10.1021/jp303097v.
[83] R.L. Jones, N.C. Pearsall, J.D. Batteas, Disorder in alkylsilane monolayers assembled on surfaces with nanoscopic curvature, J. Phys. Chem. C. 113 (2009) 4507–4514. https://doi.org/10.1021/jp8081358.
[84] S. Lee, A. Patra, P. Christopher, D.G. Vlachos, S. Caratzoulas, Theoretical study of ethylene hydroformylation on atomically dispersed Rh/Al2O3 catalysts: Reaction

mechanism and influence of ReOx promoter, ACS Catal. (2021) 9506–9518. https://doi.org/10.1021/acscatal.1c00705.
[85] M. Ichikawa, A.J. Lang, D.F. Shriver, W.M.H. Sachtler, Selective hydroformylation of ethylene on rhodium-zinc-silica. An apparent example of site isolation of rhodium and Lewis acid-promoted carbonyl insertion, J. Am. Chem. Soc. 107 (2005) 7216–7218. https://doi.org/10.1021/ja00310a098.
[86] S.S.C. Chuang, S.I. Pien, Role of silver promoter in carbon monoxide hydrogenation and ethylene hydroformylation over Rh/SiO2 catalysts, J. Catal. (1992). https://doi.org/10.1016/0021-9517(92)90305-2.
[87] Y. Konishi, M. Ichikawa, W.M.H. Sachtler, Hydrogenation and hydroformylation with supported rhodium catalysts. Effect of adsorbed sulfur, J. Phys. Chem. (1987). https://doi.org/10.1021/j100308a041.
[88] S.S.C. Chuang, S.I. Pien, Infrared study of the CO insertion reaction on reduced, oxidized, and sulfided Rh/SiO2 catalysts, J. Catal. 135 (1992) 618–634. https://doi.org/10.1016/0021-9517(92)90058-P.
[89] S.S.C. Chuang, R.W. Stevens, R. Khatri, Mechanism of C2+ oxygenate synthesis on Rh catalysts, Top. Catal. 32 (2005) 225–232. https://doi.org/10.1007/s11244-005-2897-2.
[90] R.J. Gorte, Design parameters for temperature programmed desorption from porous catalysts, J. Catal. 75 (1982) 164–174. https://doi.org/10.1016/0021-9517(82)90131-2.
[91] C.F. Bohren, D.R. Huffman, Absorption and scattering of light by small particles, Wiley-VCH Verlag, 1983. https://doi.org/10.1088/0031-9112/35/3/025.
[92] A.J. Cox, A.J. DeWeerd, J. Linden, An experiment to measure Mie and Rayleigh total scattering cross sections, Am. J. Phys. 70 (2002) 620–625. https://doi.org/10.1119/1.1466815.
[93] M.R. (University of K. Querry, Optical Constants, (n.d.). https://apps.dtic.mil/docs/citations/ADA158623 (accessed December 11, 2020).
[94] A.M. de Jong, J.W. Niemantsverdriet, Thermal desorption analysis: Comparative test of ten commonly applied procedures, Surf. Sci. 233 (1990) 355–365. https://doi.org/10.1016/0039-6028(90)90649-S.
[95] M. Doronin, M. Bertin, X. Michaut, L. Philippe, J.H. Fillion, Adsorption energies and prefactor determination for CH3OH adsorption on graphite, J. Chem. Phys. 143 (2015) 084703. https://doi.org/10.1063/1.4929376.
[96] B.K. Carpenter, Determination of Organic Reaction Mechanisms, Wiley, New York, 1984. https://www.worldcat.org/title/determination-of-organic-reaction-mechanisms/oclc/9894996 (accessed March 21, 2021).
[97] A. Suzuki, Y. Inada, A. Yamaguchi, T. Chihara, M. Yuasa, M. Nomura, Y. Iwasawa, Time Scale and Elementary Steps of CO-Induced Disintegration of Surface Rhodium Clusters, Angew. Chemie - Int. Ed. 115 (2003) 4943–4947. https://doi.org/10.1002/anie.200352318.
[98] P.B. Panayotov, J.T. Yates, Rhodium-Carbon Monoxide Surface Chemistry: The Involvement of Surface Hydroxyl Groups on A12O3 and SiO2Supports, J. Am. Chem. Soc. 110 (1988) 2074–2081. https://doi.org/10.1021/ja00215a010.
[99] R. Bliem, J.E.S. Van Der Hoeven, J. Hulva, J. Pavelec, O. Gamba, P.E. De Jongh, M. Schmid, P. Blaha, U. Diebold, G.S. Parkinson, Dual role of CO in the stability of

subnano Pt clusters at the Fe3 O4(001) surface, Proc. Natl. Acad. Sci. U. S. A. 113 (2016) 8921–8926. https://doi.org/10.1073/pnas.1605649113.
[100] C.T. Campbell, J.R.V. Sellers, The entropies of adsorbed molecules, J. Am. Chem. Soc. 134 (2012) 18109–18115. https://doi.org/10.1021/ja3080117.
[101] D.E. Starr, C.T. Campbell, Large entropy difference between terrace and step sites on surfaces, J. Am. Chem. Soc. 130 (2008) 7321–7327. https://doi.org/10.1021/ja077540h.
[102] R.T. Hannagan, K. Groden, A.M. Larson, A.J. Therrien, T. Thuening, A.C. Schilling, J.-S. McEwen, E. Charles, H. Sykes, E.C.H. Sykes, Visualizing the origin of rotational entropy effects in coadsorbed systems, Phys. Rev. Res. 2 (2020) 023326. https://journals.aps.org/prresearch/abstract/10.1103/PhysRevResearch.2.023326 (accessed November 9, 2020).
[103] J.T. Yates, G.L. Haller, Interaction of physisorbed species with chemisorbed species as studied by infrared spectroscopy, J. Phys. Chem. 88 (1984) 4660–4664. https://doi.org/10.1021/j150664a044.
[104] S.D. Dalosto, J.M. Vanderkooi, K.A. Sharp, Vibrational Stark Effects on Carbonyl, Nitrile, and Nitrosyl Compounds Including Heme Ligands, CO, CN, and NO, Studied with Density Functional Theory, (2004). https://doi.org/10.1021/jp0310697.
[105] S.H. Schneider, S.G. Boxer, Vibrational Stark Effects of Carbonyl Probes Applied to Reinterpret IR and Raman Data for Enzyme Inhibitors in Terms of Electric Fields at the Active Site, J. Phys. Chem. B. 120 (2016) 9672–9684. https://doi.org/10.1021/acs.jpcb.6b08133.
[106] L. Lu, M.L. Berkowitz, The effect of the rigidity of perfluoropolyether surfactant on its behavior at the water/ supercritical carbon dioxide interface, J. Phys. Chem. B. 109 (2005) 21725–21731. https://doi.org/10.1021/jp053384u.
[107] G. Kiss, Palladium-catalyzed reppe carbonylation, Chem. Rev. 101 (2001) 3435–3456. https://doi.org/10.1021/cr010328q.
[108] J. Steinfeld, J. Francisco, W. Hase, Chemical Kinetics and Dynamics, 2nd ed., Prentice Hall, Upper Saddle River, N.J., 1999. https://www.worldcat.org/title/chemical-kinetics-and-dynamics/oclc/39281966 (accessed March 23, 2021).

Chapter 4: Active Site Entropy of Atomically Dispersed Rh/Al_2O_3 Catalysts Dictates Activity for Ethylene Hydroformylation

Adapted from article submitted to ACS Catalysis:

Gregory Zakem and Phillip Christopher
"Active Site Entropy of Atomically Dispersed Rh/Al2O3 Catalysts Dictates Activity for Ethylene Hydroformylation", ACS Catalysis (Submitted)

4.1 INTRODUCTION

Efforts to improve supported metal catalyst activity and selectivity are typically motivated by relationships between the active site structure or composition and the activation or reaction enthalpies of kinetically relevent elementary steps.[1–7] While it is known that activation and reaction enthalpies are often correlated to activation and reaction entropies, it is less common for catalyst modifications to be motivated by expected changes in entropic barriers.[8–14] Recently, it has been proposed that certain atomically dispersed metal active sites (e.g. Cu/Chabazite zeolites and Rh/Al_2O_3) are mobile on support surfaces and that kinetically relevant elementary steps occur only when the active site reaches an immobile state, requiring a change in active site entropy.[15–19] In these circumstances, changes in active site enthalpy and entropy, as they go from mobile to stationary species, can be kinetically relevant and thus it is hypothesized that controlling active site entropy may be an effective design strategy for promoting catalytic rates.

Recently, we examined atomically dispersed $Rh(CO)_2$ active sites (a species previously proposed to be highly mobile) [20–23] on 5 nm diameter γ-Al_2O_3 support particles and focused on understanding the influence of γ-Al_2O_3 functionalization with octylphosphonic acid (OPA) on $Rh(CO)_2$ reactivity. It was observed that the deposition of OPA surrounding $Rh(CO)_2$ species resulted in decreased required temperatures for desorption of CO from $Rh(CO)_2$ during temperature programmed desorption (TPD) experiments and increased turn over frequencies (TOFs) for ethylene hydroformylation ($C_2H_4 + CO + H_2 \rightarrow CH_3CH_2CHO$, EHF), as compared to on the unfunctionalized γ-Al_2O_3.[18] EHF is an interesting model system, as $Rh(CO)_2$ is the most abundant reactive intermediate in this reaction and the desorption of CO from $Rh(CO)_2$ has been proposed to be kinetically relevant for product formation.[24–26]

Eyring analyses of the EHF reaction and CO desorption suggested that promoted rates of reaction and desorption, respectively, on the OPA modified sample were due reduced entropic barriers for kinetically relevant steps. Further, negative activation entropies for CO desorption from $Rh(CO)_2$ were observed, which suggested that $Rh(CO)_2$ is mobile and must lose entropy in the transition state for CO desorption. Based on these analyses, it was hypothesized that OPA confined $Rh(CO)_2$ species, limiting rotational and/or translational degrees of freedom, resulting in more favorable activation entropies for CO desorption. This resulted in more frequent CO desorption attempts, which is a kinetically relevant step in the EHF catalytic cycle.

Interestingly, the structure and interactions of straight-chain hydrocarbon self-assembled monolayers (SAMs) formed on small (less than 20nm) spherical particles have been theoretically and experimentally demonstrated to change with tail length and temperature.[27–29] The small radius of curvature of the supporting particles creates a situation where "fanning out" (SAM tails being normal to the surface to maximize degrees of freedom) of the SAM would be entropically favored, while the formation of more crystalline SAM layers (tilted and interacting hydrocarbon tails that maximize contact between SAM tails) would be favored due to Van der Waals interactions between the hydrocarbon tails. Based on this competition, lower temperatures or longer chain hydrocarbon tails favor the formation of crystalline SAMs, while higher temperatures or shorter tail lengths favor disordered SAM structures. Associated with this, it has been theoretically observed that increasing tail length resulted in decreased Gauche defect density in the SAM, decreased mean angles of C-C bonds with respect to the particle surface, increased rigidity of the SAM, and increased temperature required to induce disorder (fanning out) of the SAM. We hypothesized that interactions between chain tails in SAMs

consisting of phosphonic acids (PA) on γ-Al_2O_3 could be used to control the entropy of $Rh(CO)_2$ on γ-Al_2O_3 and thus modify $Rh(CO)_2$ reactivity for reactions requiring $Rh(CO)_2$ to be in a stationary state in kinetically relevant steps.

Here, we varied the tail length (1, 4, 8, 12, and 16 carbons) of straight chain alkyl PAs surrounding atomically dispersed $Rh(CO)_2$ on 5 nm diameter γ-Al_2O_3 support particles (Figure 4.1). It was observed that CO desorbed at a 120°C lower temperature from $Rh(CO)_2$/γ-Al_2O_3 functionalized by hexadecyl PA (HDPA) as compared to unfunctionalized Rh/γ-Al_2O_3 due to a 60 J/(mol·K) increase in the activation entropy (corresponding to an increase in attempt frequency). Additionally, the turn-over frequency and selectivity for propanal formation via EHF were observed to increase from 0.018±0.005 hr^{-1} and 42±2% for no PA, to 19±5 hr^{-1} and 89±4% for the HDPA at 100°C and 10 bar. A correlation between PA tail length and CO desorption temperature from $Rh(CO)_2$ was observed, while for EHF a tail length dependence of the TOF was observed that varied with reaction temperature. These observations were interpreted based on calculations of the entropy of mobile $Rh(CO)_2$ species confined to a surface (the most abundant species in both reactions) and interactions between the alkyl PA tails. Further, a quantitative correlation between changes in CO desorption and EHF activation entropies was observed. The alkyl chain tail length influence on entropies of elementary steps suggests that interactions between PAs far from the active site influence $Rh(CO)_2$ mobility and entropy, ultimately modifying the activation entropy and rates of CO desorption and EHF.

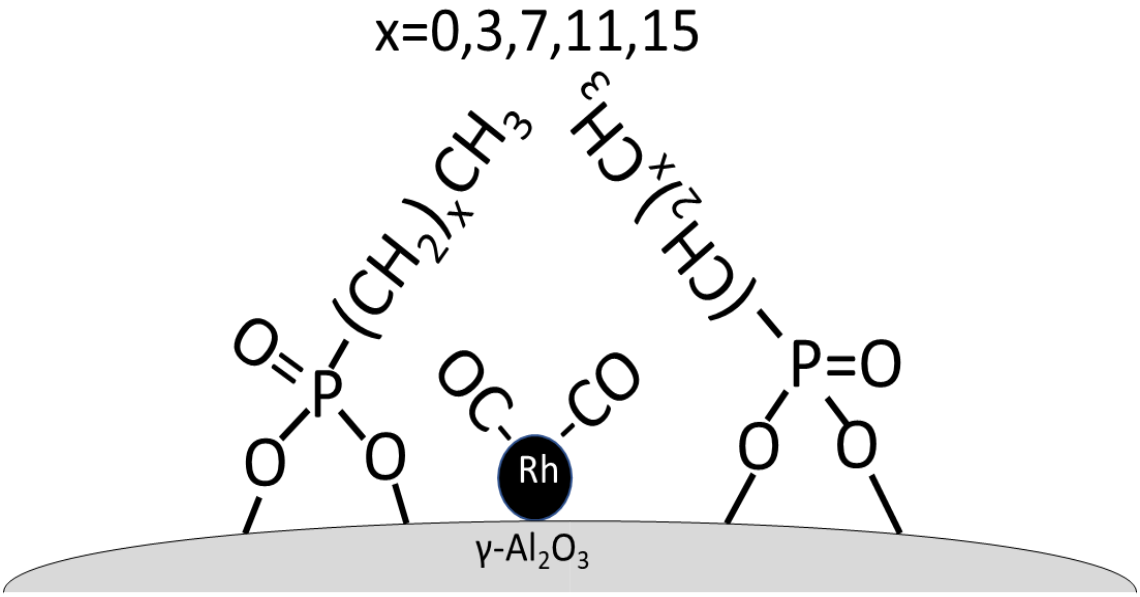

Figure 4.1: Illustration of atomically dispersed $Rh(CO)_2$ species on γ-Al_2O_3 functionalized by PAs with varying alkyl tail length. Methyl (x=0), butyl (x=3), octyl (x=7), dodecyl (x=11), and hexadecyl (x=15) PAs are examined. PAs with longer tails have stronger intermolecular interactions, resulting in more ordered monolayers.

4.2 EXPERIMENTAL

4.2.1 Catalyst Preparation

Catalysts consisting of atomically dispersed ~0.25% w/w Rh on γ-Al_2O_3 were prepared via a modified strong electrostatic adsorption (SEA) approach using rhodium (III) chloride hydrate (Sigma Aldrich, 206261) as a precursor.[30–32] 5 nm diameter γ-Al_2O_3 nanoparticles (US Research Nanomaterials, US3007) were used as the support to minimize the propensity for Rh cluster formation and to modulate interactions within PA SAMs of varying chain length (the large radius of curvature mediates SAM interactions).[24,30,32] Catalysts were prepared in 1.0 g batches. A surface loading of 1200 m^2/L was used for Rh deposition (see Equation 4.1). Rh precursor was dissolved in 40 mL of high-performance liquid chromatography (HPLC) grade water (JT4218-3, J.T. Baker) and the pH of the precursor solution was adjusted

to a pH slightly over 10 by the addition of NH_4OH. 1.0 g of support was added to 60 mL of HPLC grade water, and the suspension was stirred well in a round-bottomed porcelain dish. The pH of the support suspension was adjusted to slightly over a pH of 10 using NH_4OH and allowed to equilibrate for 1 hour. Additional NH_4OH was added at the end of the equilibration period to bring the pH back to slightly above 10. The 40 mL precursor solution was added via syringe pump to the support solution at a rate of 4.0 mL/hour. Additional NH_4OH was added as needed throughout injection to ensure that a pH of above 10 was maintained. After injection was complete, the catalyst suspension was heated to 60°C and allowed to evaporate while maintaining stirring. Dried catalyst was calcined at 623 K for 6 hours in dry air and stored in a sealed vial.

$$Surface\ Loading\ \left(\frac{m^2}{L}\right) = \frac{Surface\ Area\ of\ Support\ \left(\frac{m^2}{g}\right) * support\ mass\ (g)}{Total\ Volume\ of\ Solution\ (L)} \qquad (4.1)$$

PA functionalization was achieved via liquid phase condensation onto pre-prepared Rh/γ-Al_2O_3 catalysts.[33] An appropriate amount (as described in detail previously[18]) of methyl PA (MPA; Sigma Aldrich 289868), butyl PA (BPA; Sigma Aldrich 737933), OPA (Sigma Aldrich, 735914), dodecyl PA (DPA; Sigma Aldrich, 795755), or HDPA (Sigma Aldrich, 736244) was dissolved in a well stirred beaker of an appropriate volume of tetrahydrofuran (THF) (Sigma Aldrich, 401757). Catalyst was added to the THF solution, and the suspension was stirred for 24 hours. The suspension was centrifuged to separate the solid catalyst and was washed with THF several times to remove physically bound PAs. The dried catalyst was then treated at 120°C in air for at least 6 hours.

4.2.2 Catalyst Characterization

4.2.2.1 Fourier-Transform Infrared Spectroscopy (FTIR)

Catalysts were loaded into a Harrick Praying Mantis low temperature reaction chamber with ZnSe windows mounted inside of a Thermo Scientific Praying Mantis diffuse reflectance adapter set inside of a Thermo Scientific Nicolet iS10 FT-IR spectrometer with a mercury cadmium telluride (MCT) detector cooled by liquid nitrogen. All samples were measured in a diffuse reflectance infrared Fourier-transform spectroscopy (DRIFTS) configuration. Before characterization, catalysts were heated to 250°C at 20°C/min in 1000 PPM CO in Ar and held at 250°C for 3 hours, and then cooled to 50°C. The reaction cell was purged with Ar for 10 minutes before spectra were taken. In all measurements, spectra were obtained by averaging 8 to 32 scans at a resolution of 4 cm^{-1}. The interaction strength between CO and Rh was probed via TPD experiments. Temperature was increased from 50°C to 450°C at rates ranging from 5°C per minute to 60°C per minute in Ar. The number of scans per spectrum was varied from 8 to 32 based on the temperature ramp rate such that a spectrum was taken at least once per 10°C. Spectra at each temperature were baselined and fit using gaussian curves. The CO stretch area associated with $Rh(CO)_2$ as a function of temperature was fit to a sigmoidal function, and an analytical derivative was used to determine the temperature of maximum desorption (T_P). Kinetic parameters were extracted from desorption temperatures using Equations 4.2 and 4.3. The TPD experiments performed for all samples were single ramp rate TPD experiments and were performed at least three times for each sample on catalysts synthesized at different times, and these repeat measurements were used to assess the uncertainties of extracted kinetic parameters. The HDPA functionalized sample was examined in varied temperature ramp rate experiments. Experiments were repeated at least twice for each ramp rate, for a total of thirteen TPD experiments at different ramp rates. The standard error of parameters extracted this way was used as the uncertainty.

4.2.2.2 Brunauer-Emmett-Teller (BET)

Support surface area was measured via nitrogen physisorption in a Micromeritics 3Flex Porosimeter. Supports were degassed at 350°C in vacuum before BET measurements.

4.2.2.3 Inductively Coupled Plasma Optical Emission Spectroscopy (ICP-OES)

To ensure no Rh leeching occurred during PA functionalization of γ-Al_2O_3, a Thermo iCap 6300 ICP Emission Spectrometer was used to determine Rh loadings before and after functionalization. Additionally, ICP was used to determine PA coverages by analyzing amount of P in each sample. Samples were digested in aqua regia by reflux boiling or microwave digestion. Samples were filtered using 0.45 μm syringe filters PTFE membrane (Corning, 431231).

4.2.2.4 Dispersion Estimates

Rh dispersion (or accessibility) on all samples was estimated using a Micromeritics AutoChem 2920 instrument. Approximately 200mg of each sample was purged with He (50 SCCM) at room temperature. Samples were purged with He (50 SCCM) at 175°C for 5 minutes and then reduced in H_2 (50 SCCM) at 175°C for 1 hour. Samples were then cooled to 100°C and purged in He (25 SCCM) for 5 minutes. Pulses of 10% CO in He (25 SCCM) were introduced through an injection loop. At 3-minute intervals, the injection valve was turned to introduce fixed volumes of CO to the sample. CO that was not adsorbed was detected using a thermal conductivity detector (TCD). Knowing the concentration of injected CO, the weight loading of Rh from ICP measurements, the mass of catalyst, and the data from the TCD allows for dispersion estimates. It was assumed that CO would bond to Rh in a 2:1 ratio because FTIR measurements indicated entirely atomically dispersed Rh species, which selectively form $Rh(CO)_2$ species. It is noted that previous analysis of the influence of CO adsorption

temperature on PA modified Rh/γ-Al_2O_3 showed that increasing temperature did not influence Rh accessibility. Thus, temperature influences on reactivity are solely a result of kinetics, rather than changing number of active sites.

4.2.3 Reactivity Measurements

Catalytic rates and selectivity for EHF were evaluated in a fixed-bed 316 stainless steel tube (0.26 Inch ID) in the temperature range of 100-170°C at 10 bar pressure (absolute). An ultra-high purity (UHP) grade reactant gas mixture of C_2H_4, H_2, and CO at a molar ratio of 1:1:1 was used with a total flow rate of 30 SCCM for all experiments. The CO gas was housed in an aluminum-lined cylinder to avoid potential contamination by iron and nickel carbonyls. Catalysts (30-800 mg) were diluted in 0.5-4.0g of purified sand (SiO_2, Sigma Aldrich, 84878) to ensure that internal heat and mass transfer limitations were absent. Measurements of the influence of reaction rate on total flow rate, with constant partial pressures, evidenced no external mass transfer limitations.[24][25] Prior to reactivity measurements, catalysts were reduced in-situ in 10 SSCM CO at 200°C for 3 hours. Afterward, the reactor was cooled to 170°C and the reaction was allowed to proceed for approximately 24 hours at ambient pressure to allow for surface bound propanal species to saturate, as previously noted for this reaction.[34] All kinetic experiments were performed at least three times on catalysts synthesized at different times, and these repeat measurements were used to assess the uncertainties of extracted kinetic parameters. Products were quantified using an SRI Multiple Gas Analyzer #3 gas chromatographer equipped with a 3’ packed alumina column in series with a MXT wax capillary column and FID detector.

For total pressure dependent measurements at 130 and 170°C, catalysts were allowed to react for 2 hours at each pressure (1.0, 2.5, 5.0, 7.5, and 10 bar) following the initial 24-hour

induction period. For temperature dependent measurements, after the 24-hour induction period, the temperature was decreased to 130°C, and the total pressure was increased to 10 bar and allowed to react for 12 hours before kinetic measurements were recorded. Kinetic parameters were calculated for the range of 100 to 130°C. Partial pressure dependence studies were conducted at 130°C with flow rates of the gas of interest ranging from 3-10 SCCM while balanced by argon to maintain partial pressure of other species and a total flow rate of 30 SCCM.

4.3. RESULTS

4.3.1 Characterization of PA Modified/Rh/γ-Al_2O_3

As previously described, atomically dispersed Rh was deposited onto 5 nm diameter γ-Al_2O_3 at 0.25% w/w via a modified strong electrostatic adsorption approach. [18] [30] [35] Methyl, butyl, octyl, dodecyl, and hexadecyl phosphonic acid (MPA, BPA, OPA, DPA, and HDPA, respectively) were chosen to modify Rh/γ-Al_2O_3 to represent a range of tail lengths that have been shown to exhibit varying levels of interactions between PAs (resulting in varying SAM crystallinity) at temperatures relevant for hydroformylation.[27,29] This approach is analogous to changing the length of ligands on an organometallic complex, but in this case, PAs are not directly bonded to the Rh active site, and as a result the steric environment of Rh is modified without modifying the electronic structure of Rh. The lack of electronic structure modification of Rh by PAs is further enabled by the use of the insulating γ-Al_2O_3 support.[36]

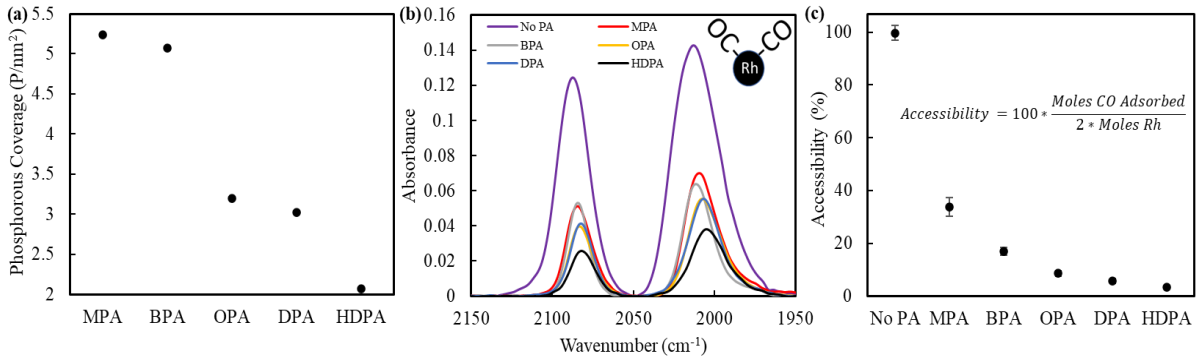

Figure 4.2: (a) Saturation surface coverage of PAs, reported as P/nm^2, for the different PA tails. (b) CO Probe Molecule FTIR of no PA Rh/Al_2O_3 and of MPA, BPA, OPA, DPA, and HDPA functionalized Rh/Al_2O_3. Before characterization, catalysts were heated to 250°C at 20°C/min in 1000 PPM CO in Ar and held at 250°C for 3 hours, and then cooled to 50°C. The reaction cell was purged with Ar for 10 minutes before spectra were collected. CO stretch frequencies associated with $Rh(CO)_2$ species redshift and decrease in area with increasing tail length. (c) Accessibility (fraction of Rh that adsorbs CO) for different PA lengths. FTIR only exhibits stretches associated with atomically dispersed $Rh(CO)_2$, indicating that accessible Rh is primarily atomically dispersed.

Functionalization was performed through liquid phase condensation of PAs on surface hydroxyls of Rh/γ-Al_2O_3 samples. PAs were chosen as a suitable anchoring group to γ-Al_2O_3 as they exhibit high stability at elevated temperatures in inert and reducing environments.[37] The coverage PAs was determined by utilizing microwave digestion in concentrated aqua regia to leach the PAs from PA functionalized catalysts and measuring the concentration of P in the filtered and diluted solution via ICP. The P coverages were 5.2, 5.1, 3.2, 3.0, and 2.1 P/nm^2 for MPA, BPA, OPA, DPA, HDPA functionalized catalysts, respectively, when condensing PAs at saturation coverage (Figure 4.2a). Additionally, to deconvolute the effects of PA coverage and tail length, a 2.1 P/nm^2 (the same coverage as HDPA) OPA functionalized sample was prepared.

A variety of techniques have been used to demonstrate the presence and predominance of atomically dispersed Rh in a catalyst sample.[38–42]. While transmission electron microscopy can be useful to directly evidence the existence of single Rh atoms, and X-ray absorption spectroscopy can provide support for atomically dispersed Rh being the most abundant Rh structure, CO probe molecule FTIR is a particularly discriminating technique that can differentiate the presence and relative abundance of different Rh structures (atomically dispersed vs small clusters). As will be described throughout, the combination of CO-FTIR, volumetric CO chemisorption, and analysis of the product distribution under EHF conditions will be used to assert the claim that Rh remains predominantly atomically dispersed throughout characterization and reactivity studies.

$Rh(CO)_2$ exhibits unique CO stretches in FTIR spectra that are differentiable from linear and bridge-bound CO on Rh clusters.[22,35,43–48] $Rh(CO)_2$ supported on γ-Al_2O_3 presents symmetric and asymmetric CO stretches at ~2090 cm^{-1} and ~2020 cm^{-1}, respectively,

while CO adsorbed to Rh clusters exhibits a linear bound CO stretch at ~2050 cm^{-1}, and a wide bridge bound CO stretch at ~1800 cm^{-1}.[21,22] CO probe molecule FTIR measurements of no PA and all PA functionalized ~0.25% Rh/γ-Al_2O_3 samples following reduction in 1000 PPM CO at 250°C only exhibited evidence of CO stretches associated with atomically dispersed $Rh(CO)_2$ species (Figure 4.2b). This is in agreement with CO pulse chemisorption measurements for Rh/γ-Al_2O_3 with no PA, which provided dispersion estimates of 93%-108% at 100°C when assuming a 2:1 CO:Rh stoichiometry, consistent with the formation of $Rh(CO)_2$. $Rh(CO)_2$ stretch frequencies were observed to redshift with increased PA tail length. This phenomena was previously attributed to a Stark shift due to through-space electric field interactions between PA tails and $Rh(CO)_2$.[18] The continued increase in stretch redshift with increased tail length further evidences that these interactions are through space, as Hammett substituent analysis suggests no difference in electronic structure at the PA anchoring group for tails beyond 3 carbons in length.[49]

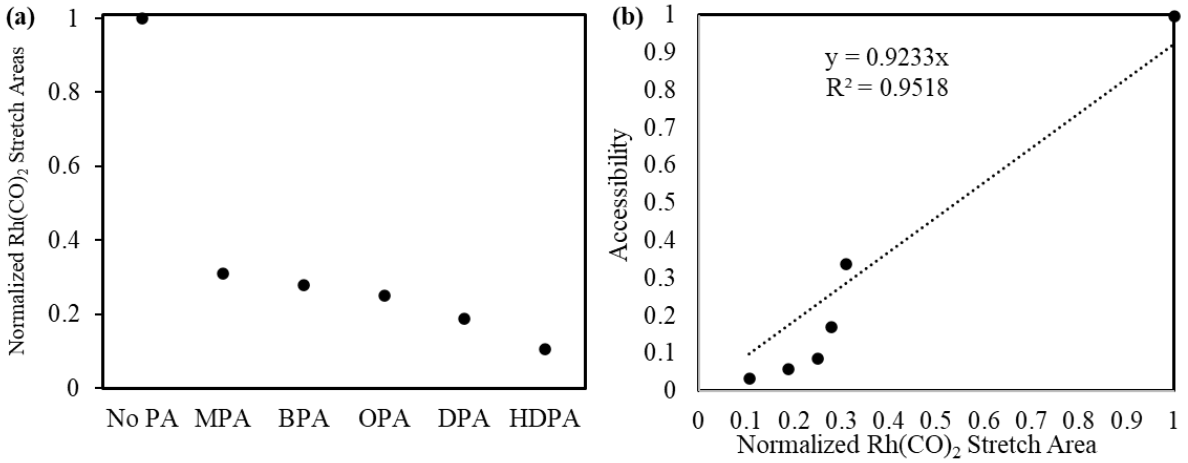

Figure 4.3: (a) CO stretch areas associated with the $Rh(CO)_2$ species for various samples, normalized to the $Rh(CO)_2$ stretch areas of the No PA Rh/Al_2O_3. Before characterization, catalysts were heated to 250°C at 20°C/min in 1000 PPM CO in Ar and held at 250°C for 3 hours, and then cooled to 50°C. The reaction cell was purged with Ar for 10 minutes before spectra were taken. (b) Correlation between Rh accessibility for different samples (as determined by CO pulse chemisorption experiments) and normalized $Rh(CO)_2$ stretch areas. Deviations from parity are likely due to changes in sample reflectivity with the addition of PAs.

Interestingly, it was observed that the absolute magnitude of the CO stretch absorbance observed in IR measurements decreased with increasing PA tail length. For example, the area under the symmetric CO stretch of $Rh(CO)_2$ decreased in magnitude by up to 90% compared to the unfunctionalized sample (Figure 4.3a). This suggests that PA functionalization blocks a fraction of Rh sites from being able to interact with adsorbates. We note that it is not expected that additional Rh sites would be exposed under EHF conditions as the reaction is run at significantly lower temperature than the pre-treatment used in the IR studies, and previously we observed minimal changes in $Rh(CO)_2$ stretch area on OPA modified catalysts while flowing CO and raising temperatures from 50°C to 150°C.[18]

To assess the blocking of Rh sites by PAs, the percentage of accessible Rh was measured by volumetric chemisorption, referred to as the accessibility, and is 100±3%, 34±3%, 17±1%, 13±1%, 9±1%, 6±1%, and 3±1% for no PA, MPA, BPA, OPA, DPA, and HDPA functionalized catalysts, respectively (Figure 4.2c). These values assume that only atomically dispersed Rh exists (substantiated by the FTIR measurements). There is a correlation between measured accessibility and $Rh(CO)_2$ stretch areas ($R^2 \approx 95$, Figure 4.3b), suggesting that in this case, DRIFTS measurements of $Rh(CO)_2$ concentrations based on CO stretch areas are predictive of Rh accessibility. Deviation from quantitative predictability is likely due to changes in sample reflectivity with PA functionalization. This is evidenced visibly (no PA Rh/Al_2O_3 appears grey, while functionalized samples are whiter in color) and by an increase in interferogram intensity for PA functionalized samples. It is observed that all $Rh(CO)_2$ derived CO stretches on PA functionalized samples fall within the envelope of the no PA $Rh(CO)_2$ stretches. This raises the question of whether changes in catalyst behavior are due to selective exposure of only certain sites, or whether PA inherently modify the reactivity of the

remaining accessible sites. CO TPD and EHF reactivity measurements presented later provide strong evidence that the remaining exposed Rh sites are inherently altered by PAs.

4.3.2 CO Desorption Kinetics from $Rh(CO)_2$

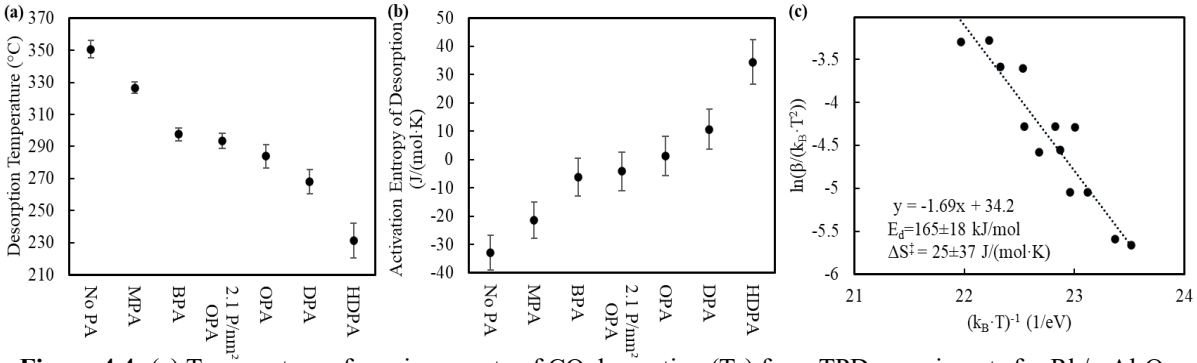

Figure 4.4: (a) Temperature of maximum rate of CO desorption (T_P) from TPD experiments for Rh/γ-Al_2O_3 functionalized by PAs with varying tail lengths. Before characterization, catalysts were heated to 250°C at 20°C/min in 1000 PPM CO in Ar and held at 250°C for 3 hours, and then cooled to 50°C. Samples were heated from 50°C to 450°C at 20°C per minute in 100 SCCM of Ar. The error bars represent the standard error from three duplicate experiments using different batches of catalysts. (b) Activation entropy of desorption, $\Delta S^{\ddagger}$, was calculated from the T_P and is plotted for the various samples. Error bars represent the propagated error from the T_P and the activation energy of desorption. (c) Variable ramp rate TPDs plotted in the form of Equation 4.3. HDPA samples were heated from 50°C to 450°C at rates ranging from 10 °C per minute to 60°C per minute in 100 cc/min Ar. Desorption energies were calculated from the slope, while activation entropies were calculated using both the slopes and intercepts. The uncertainty of each variable represents the standard error from the regression.

To explore the effect of PA tail length on CO desorption temperature from $Rh(CO)_2$, TPD experiments were performed by measuring relative CO coverage during a linear temperature ramp via FTIR. Due to the use of nonporous, small (~5 nm) support particles relative to the wavelength of the IR light (5 μm), the surface layer of catalyst was predominantly probed during diffuse reflectance measurements, such that we can assume that CO readsorption is negligible, and thus model the system as an irreversible desorption process.[18] The temperature where the rate of CO desorption is maximum (T_P) was determined for no PA Rh/γ-Al_2O_3 and Rh/γ-Al_2O_3 functionalized by PAs with varying tail lengths (Figure 4.4a). Example TPDs and example curve fittings for each sample, along with associated discussion, can be found as Figures 4.5 and 4.6.

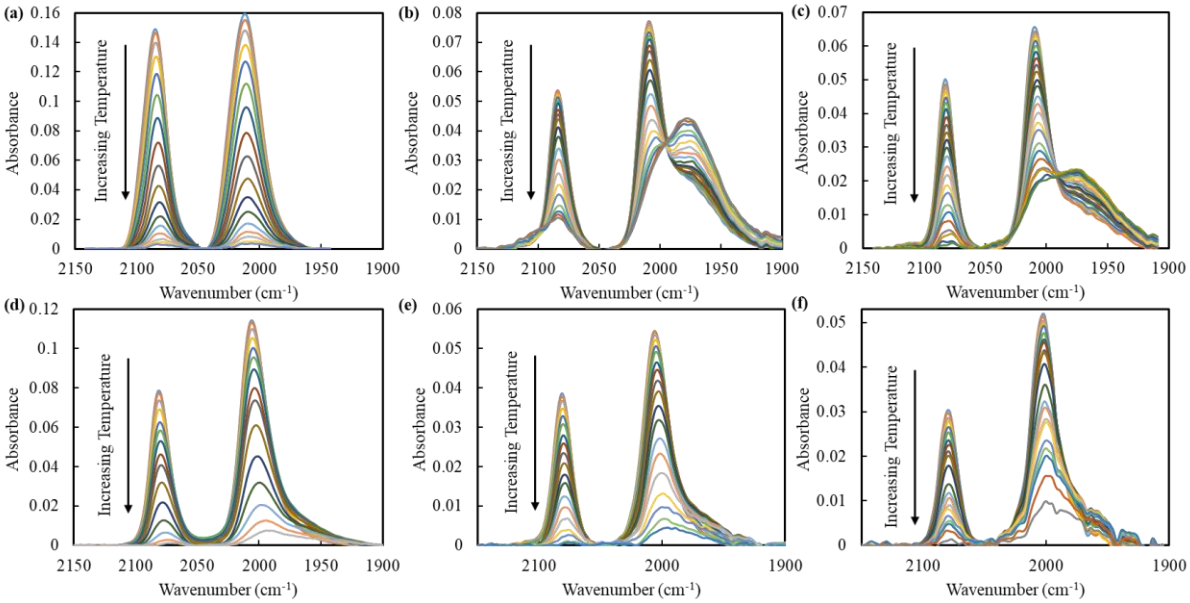

Figure 4.5: Example TPD spectra for each catalyst. Before characterization, catalysts were heated to 250°C at 20°C/min in 1000 PPM CO in Ar and held at 250°C for 3 hours, and then cooled to 50°C. During each TPD, samples were heated from 50°C to 450°C at 20°C per minute in 100 SCCM of Ar. (a) No PA Rh/Al_2O_3 (b) MPA modified Rh/Al_2O_3, (c) BPA modified Rh/Al_2O_3, (d) OPA modified Rh/Al_2O_3, (e) DPA modified Rh/Al_2O_3, (f) HDPA modified Rh/Al_2O_3. It should be noted that reduction in low concentrations of CO (1000 PPM in this case) results in simultaneous desorption of both COs from $Rh(CO)_2$; this is observed in all samples except for MPA and BPA. This suggests that MPA and BPA uniquely stabilize the monocarbonyl Rh species. Previously it has been demonstrated that the binding motif of PAs can change from tridentate, to bidentate at high PA coverage.[6] We hypothesize that the higher coverage of MPA and BPA species results in a higher abundance of bidentate-bound PAs, leaving P-OH bonds free near $Rh(CO)_2$ species. This allows Rh to coordinate to the free OH, stabilizing the monocarbonyl species.[7–9] This phenomena does not seem to influence the desorption behavior of the first CO (as tracked via the symmetric $Rh(CO)_2$ stretch), and is likely not relevant under reaction conditions as they are at much lower temperatures than the TPD experiments are performed.

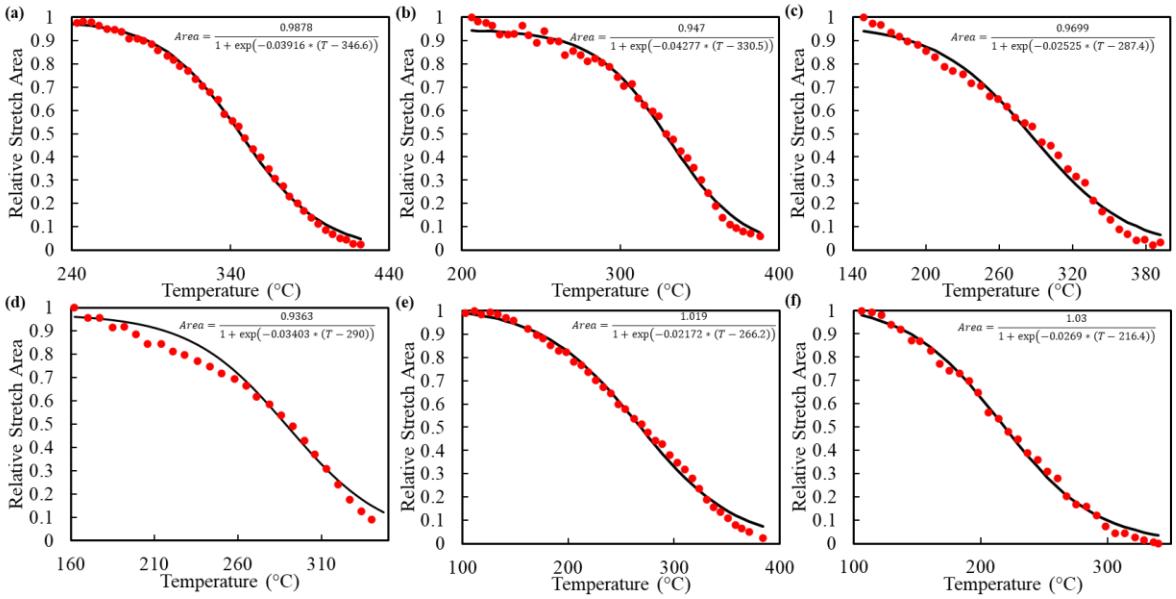

Figure 4.6: Example fits of normalized symmetric stretch area of $Rh(CO)_2$ vs temperature for each catalyst. Before characterization, catalysts were heated to 250°C at 20°C/min in 1000 PPM CO in Ar and held at 250°C for 3 hours, and then cooled to 50°C and purged with Ar. During each TPD, samples were heated from 50°C to 450°C at 20°C per minute in 100 SCCM of Ar. (a) No PA Rh/Al_2O_3 (b) MPA modified Rh/Al_2O_3, (c) BPA modified Rh/Al_2O_3, (d) OPA modified Rh/Al_2O_3, (e) DPA modified Rh/Al_2O_3, (f) HDPA modified Rh/Al_2O_3.

It was observed that T_P decreased with increasing PA tail length, from ~350°C for no PA $Rh/\gamma\text{-}Al_2O_3$ to 230°C for HDPA functionalized $Rh/\gamma\text{-}Al_2O_3$. Assuming that the activation energy of desorption (E_d) is not changing with PA functionalization, the activation entropy of desorption ($\Delta S^{\ddagger}$) was calculated using (Equation 4.2). A derivation of this equation can be found in the appendix as Equation 4.4. Following this analysis, $\Delta S^{\ddagger}$of CO desorption from $Rh(CO)_2$ was observed to increase from ~-30 J/(mol·K) for no PA to ~30 J/(mol·K)) for HDPA (Figure 4.4b). Interestingly, the 2.1 P/nm^2 OPA sample and the saturation coverage OPA sample exhibited a small change in T_P compared to differences between samples with different length PA tails but similar coverages (HDPA functionalized catalysts also had coverages of 2.1 P/nm^2 but exhibited significantly lower desorption temperatures (~70°C)). This suggests that PA tail length is more significant than PA coverage in modifying CO desorption behavior from $Rh(CO)_2$. It should be noted that estimates of apparent kinetic parameters (E_d and $\Delta S^{\ddagger}$)

from TPD measurements that follow relative CO coverage during the temperature ramp are agnostic to the total number of available Rh sites, as all calculations are based on initial $Rh(CO)_2$ stretch areas for a particular sample. Thus, $\Delta S^{\ddagger}$ estimates are not influenced by site counting as required for analysis of apparent kinetic parameters from steady state reactivity measurements (see below).

To test the assumption of constant E_d of CO desorption, TPD experiments were performed at different temperature ramp rates for the HDPA modified sample to extract the E_d and $\Delta S^{\ddagger}$ of desorption by plotting data in the form of Equation 4.3 (Figure 4.4c). It was observed that the E_d of desorption for CO from $Rh(CO)_2$ on HDPA functionalized $Rh/\gamma\text{-}Al_2O_3$ (165±18 kJ/mol) was not significantly different to that previously observed for no PA (154±9 kJ/mol) and OPA functionalized $Rh/\gamma\text{-}Al_2O_3$ using an identical analysis approach. (158±10 kJ/mol).[18] Therefore, it is reasonable to assume that all samples examined have negligibly different E_d for CO desorption from $Rh(CO)_2$. We note that at a fixed $\Delta S^{\ddagger}$, a ~35kJ/mol decrease in E_d would be required to cause a decrease in desorption temperature from ~350°C to ~230°C, which is larger than the errors bound on E_d from our measurements, and thus we conclude that PA modification promotes CO desorption from $Rh(CO)_2$ by changing $\Delta S^{\ddagger}$. This is clear evidence that PAs are modifying the inherent entropy of $Rh(CO)_2$ and further that the entropy of this species is relevant to the kinetics of CO desorption.

$$\Delta S^{\ddagger} = \mathrm{R}\ln\left(\frac{hE_d\beta}{k_B^2 T_P^3}\right) + \frac{E_d}{T_P} - R \tag{4.2}$$

Where: $\Delta S^{\ddagger}$=Activation Entropy of Desorption (J/(mol·K))
R = Molar Gas Constant (J/(mol·K)
h = Planck Constant (J·s)
E_d =Desorption Energy (J/mol)
β =Temperature Ramp Rate (K/s)

k_B =Boltzmann Constant (J/K)
T_P =Temperature of maximum desorption (K)

$$\ln\left(\frac{\beta}{k_B T_P^2}\right) = \frac{-E_d}{k_B T_P} + \ln\left(\frac{\mathrm{A}}{\mathrm{E_d}}\right) \tag{4.3}$$

Where: A=Preexponential Factor (1/s)

The change in $\Delta S^{\ddagger}$ of CO desorption from $Rh(CO)_2$ due to γ-Al_2O_3 functionalization by HDPA (~60 J/mol·K) can be compared to the translational, rotational, and vibrational degrees of freedom for a $Rh(CO)_2$ complex confined to a 2-dimensional surface. The approaches used to calculate the entropy of $Rh(CO)_2$ are shown in the appendix as Equations 4.5, 4.6, and 4.7. It was assumed that the maximum translational and rotational entropies for this complex on a surface would be two-thirds of the gas phase entropy, as one degree of freedom is lost for translation due to being bound to a surface, and half of two of the rotational modes are lost. This assumes that $Rh(CO)_2$ is highly mobile on γ-Al_2O_3; essentially it is quasi-equilibrated in all sites across the surface, which is justified based on previous measurements of the diffusion barrier of $Rh(CO)_2$ on γ-Al_2O_3.[20] At 290°C (the average T_P of for all samples), the maximum possible translational, rotational, and vibrational entropies associated with $Rh(CO)_2$ were calculated to be 123 J/(mol·K), 84 J/(mol·K), and 24 J/(mol·K), respectively. This suggests that changes to vibrational entropy alone cannot account for the observed changes in activation entropy of desorption (~60 J/(mol·K)), while changes to translation, rotational, or a combination of both modes could be responsible for the observed changes in CO desorption kinetics from $Rh(CO)_2$.

From this kinetic analysis, we hypothesize mechanisms for how PAs influence CO desorption from $Rh(CO)_2$. Based on the negative activation energy for desorption of CO from $Rh(CO)_2$ on unfunctionalized γ-Al_2O_3, there must be least one kinetically relevant step requires

$Rh(CO)_2$ to be more constrained than the most abundant state. Additionally, the FTIR spectra of $Rh(CO)_2$ exhibits simultaneous losses in both the symmetric and asymmetric CO stretches (except for the MPA and BPA functionalized catalysts, see Figure 4.5 for example spectra and further hypotheses), suggesting that the second CO desorbs quickly after the first CO, such that the Rh(CO) species is too short lived to detect with the temporal resolution of the FTIR. From this information, we hypothesize that CO desorption from $Rh(CO)_2$ proceeds via: (1) $Rh(CO)_2$ (mobile) → $Rh(CO)_2$ (constrained), (2) $Rh(CO)_2$ (constrained) → $Rh(CO)+CO_{(g)}$, and (3) $Rh(CO) \rightarrow Rh+CO_{(g)}$. In such a scenario, the kinetically relevant steps must include both steps 1 and 2 to explain the observed energetic and entropic barriers. The simultaneous desorption of the second CO suggests that this process is fast. Thus, $Rh(CO)_2$ is proposed to diffuse between stationary or constrained or stationary states (at which point CO desorption can proceed) on γ-Al_2O_3 and PAs are hypothesized to increase the proportion of $Rh(CO)_2$ existing in stationary states, thus increasing the attempt frequency for CO desorption.

We note that this proposed mechanism of CO desorption from $Rh(CO)_2$ is distinct from recent reports from our group, where initially oxidized RhO_x/γ-Al_2O_3 was reduced in H_2 prior to CO adsorption (in the current work oxidized RhO_x /γ-Al_2O_3 is reduced by a 1000 PPM CO stream). [15,16,50] When using H_2 as the initial reductant prior to CO adsorption, the desorption process was proposed to occur in two distinct steps where first, mobile $Rh(CO)_2$ species find "wet regions" of the support (produced from the H_2O generated during RhO_x reduction by H_2) and then CO desorbs to produce Rh monocarbonyl, Rh(CO), species that are stabilized through coordination to OH species. However, the use of CO as a reductant in the current study decreases the water content on γ-Al_2O_3 and results in the simultaneous CO desorption from $Rh(CO)_2$. In both cases clear evidence of $Rh(CO)_2$ mobility is observed.

However, in the case of an H_2 pre-treatment it is proposed that the initial CO desorption occurs in wet regions of the support, which enables a sequential CO desorption process. However, in the current study, the "drier" support caused by RhO_x reduction in a 1000 PPM CO stream seems to mitigate the involvement of adsorbed H_2O in the CO desorption process thus resulting in simultaneous CO desorption from $Rh(CO)_2$. Future studies will address in detail mechanistic distinctions between CO desorption from $Rh(CO)_2$/ γ-Al_2O_3 depending on initial reductant composition.

4.3.3 Ethylene Hydroformylation Reactivity

To explore the effects of PA tail length on Rh reactivity, EHF was used as a probe reaction, which has competing reaction pathways of ethylene hydrogenation to produce ethane and hydroformylation to produce propanal. EHF is an interesting model system for probing the reactivity of supported $Rh(CO)_2$ due to its similar cationic oxidation state to homogeneous Rh catalysts that are used industrially for hydroformylation reactions.[51] Under EHF reaction conditions, $Rh(CO)_2$ is the most abundant surface intermediate (MASI), as observed previously by in-situ FTIR measurements.[18,24–26] Furthermore, CO desorption from $Rh(CO)_2$ is a quasi-equilibrated, kinetically relevant step in both the desired pathway (hydroformylation to propanal) and the undesired pathway (hydrogenation to ethane).[26] Thus, changes in kinetics of CO desorption from $Rh(CO)_2$ are expected to be related to changes in EHF reactivity.

All catalysts contained Rh loadings between 0.18% and 0.25%, negating any influence of Rh loading on reactivity measurements. Catalysts were reduced in semiconductor grade pure CO at 200°C for 3 hours to form $Rh(CO)_2$ and stabilize atomically dispersed Rh.[38] After CO reduction, catalysts were cooled to 170°C and exposed to an equimolar mixture of CO, H_2, and C_2H_4 at 30 SCCM total flow rate and atmospheric pressure. Catalysts exhibited an induction

period ranging between 12 and 36 hours to reach steady state reactivity and selectivity. Previous studies have demonstrated that this induction period is due to the formation of surface species,[52] and that more active catalysts have shorter induction periods.[18,24,25] All reactivity measurements were recorded under conditions with less than 0.2% ethylene conversion to ensure differential reactivity.

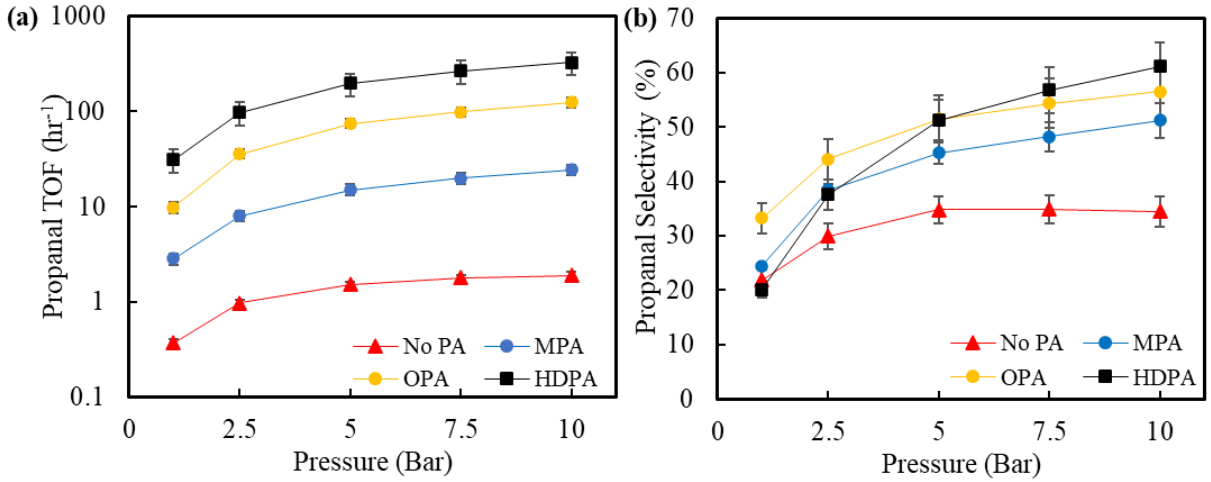

Figure 4.7: (a) Propanal formation turn over frequencies (TOF) for no PA, MPA, OPA, and HDPA functionalized Rh/Al_2O_3 measured at 170°C and 30 SCCM 1:1:1 H_2:CO:C_2H_4 and at 1, 2.5, 5, 7.5, and 10 bar. The error bars represent the propagated error from rate and site counting measurements. Lines between data points exist to guide the eye, not to represent measured data. (b) Selectivity towards propanal for no PA, MPA, OPA, and HDPA functionalized Rh/Al_2O_3 associated with the propanal TOF shown in (a). The error bars represent the standard error from three duplicate experiments using different batches of samples.

The only products detected at steady state were propanal (from hydroformylation) and ethane (from hydrogenation). This is suggestive that Rh remains atomically dispersed, as a variety of other products (methane, ethane, propanol, and propane) have been observed to form when Rh clusters are present; propanol is a particularly common byproduct when Rh clusters exist.[53–56] Motivated by previous studies that demonstrated increased total pressure enhances both the selectivity and rate of EHF on Rh,[25] catalysts were tested at 1.0, 2.5, 5.0, 7.5, and 10 bar total pressure and 170°C (Figure 4.7). It was observed that at all pressures, propanal formation TOFs increased with PA tail length, and that functionalized catalysts

exhibited greater enhancements in propanal TOF due to pressure than the no PA catalysts (Figure 4.7a), resulting in higher selectivities towards propanal (Figure 4.7b). At 1 bar and 170°C, the no PA, MPA, OPA, and HDPA functionalized samples exhibited propanal production rates of 0.37±0.03 hr^{-1}, 2.9±0.4 hr^{-1}, 10±1 hr^{-1}, and 31±9 hr^{-1}, respectively, corresponding to enhancements in TOF of 8x, 26x, and 84x for MPA, OPA, and HDPA, respectively, compared to no PA. At 10 bar and 170°C the no PA, MPA, OPA, and HDPA functionalized samples exhibited a propanal production rate of 1.9±0.2 hr^{-1}, 25±3 hr^{-1}, 130±20 hr^{-1}, and 330±90 hr^{-1}, respectively, corresponding to enhancements of 13x, 66x, and 172x for MPA, OPA, and HDPA, respectively, compared to no PA.

Table 4.1 Mass normalized rates for selected catalysts at 170°C and 10 bar, 30 SCCM 1:1:1 $CO:C_2H_4:H_2$. Functionalized catalysts exhibited increased mass normalized rates despite a large portion of surface Rh being blocked by the PA SAM. The uncertainty represents the standard error from at least three samples made in different batches.

Sample	Ethane Formation Rate ($\mu mol/(hr \cdot g_{cat})$)	Propanal Formation Rate ($\mu mol/(hr \cdot g_{cat})$)
No PA	93±10	46±6
MPA	153±18	161±12
OPA	159±15	207±21
HDPA	135±14	212±29

The uncertainty of reported turnover frequencies (TOFs) represent the standard error from at least three repeat experiments of samples synthesized at different times. TOFs were calculated accounting for accessibilities measured by CO chemisorption. The approach of using various batches of each catalyst to produce uncertainty estimates, along with the significant differences in observed TOFs, provides confidence in the observed PA tail length dependent trends and the quantitative values measured. The observed trend in reactivity as a

function of PA tail length is consistent with the changes in CO desorption temperature and activation entropy from the CO TPD measurements, suggesting that facilitation of CO desorption kinetics allows for greater catalytic activity, as samples modified by longer tail PAs exhibit higher TOFs and lower desorption temperatures. Since $Rh(CO)_2$ desorption is quasi-equilibrated under steady-state reaction conditions,[26] more facile CO desorption should result in more frequent attempts at initiating the catalytic cycle.

Despite PA functionalization blocking a significant fraction of Rh sites (~95% for HDPA), the enhancement in TOF is sufficient to increase per gram Rh propanal formation rates by 4x for MPA, and 5x for HDPA when compared to the no PA sample (Table 4.1). This, in combination with the differences in the temperature onset of CO desorption shown in Figure 4.6, demonstrate that PAs modify the inherent reactivity of accessible Rh active sites, rather than selectively blocking a subset of less active Rh sites. Additionally, the number of accessible Rh active sites is not likely significantly changing between site-counting conditions and

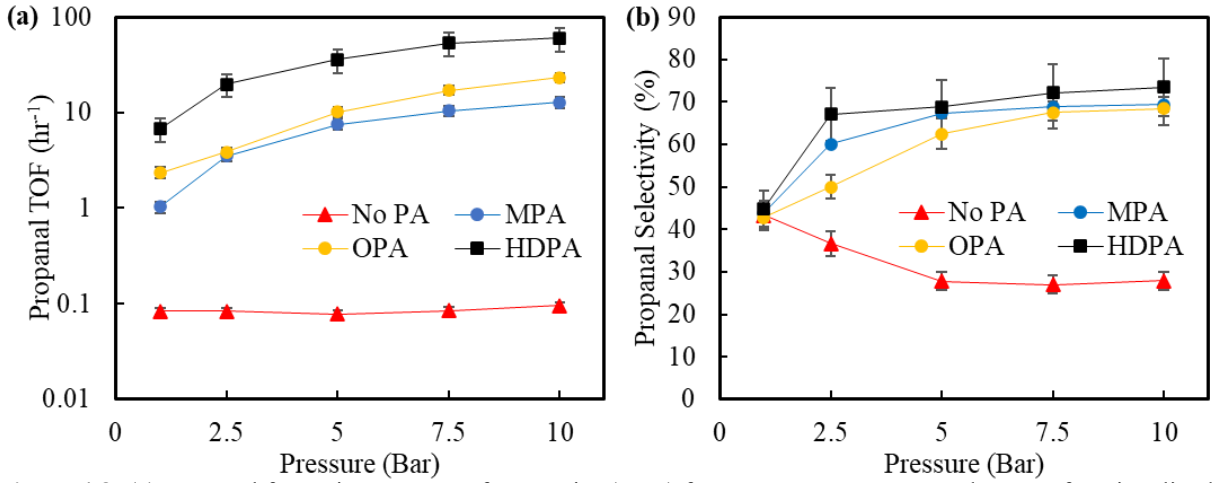

Figure 4.8: (a) Propanal formation turn over frequencies (TOF) for no PA, MPA, OPA, and HDPA functionalized Rh/Al_2O_3 measured at 130°C and 30 SCCM 1:1:1 H_2:CO:C_2H_4 and at 1, 2.5, 5, 7.5, and 10 bar. The error bars represent the propagated error from rate and site counting measurements. Lines between data points exist to guide the eye, not to represent measured data. (b) Selectivity towards propanal for no PA, MPA, OPA, and HDPA functionalized Rh/Al_2O_3 associated with the propanal TOF shown in (a). The error bars represent the standard error from three duplicate experiments using different batches of samples.

reaction conditions, as it was previously observed that CO FTIR stretch areas of OPA modified $Rh(CO)_2/\gamma\text{-}Al_2O_3$ catalysts changed by only 5% when changing temperatures from 50°C to 150°C in a CO atmosphere. Thus, it seems that PA functionalization modifies the inherent reactivity of the accessible Rh sites on each sample.

Table 4.2 Reaction orders of CO, C2H4, H2 for functionalized and unfunctionalized samples at different temperatures and pressures.

Sample	Product	CO Order	C2H4 Order	H2 Order
No PA (150°C 1 Bar)	Ethane	-1.3±0.1	0.6±0.1	0.9±0.1
	Propanal	-0.6±0.1	0.8±0.1	0.8±0.1
No PA (130°C 10 Bar)	Ethane	-1.8±0.1	0.7±0.1	1.1±0.1
	Propanal	-0.9±0.1	0.5±0.1	0.7±0.1
HDPA (130°C 10 Bar)	Ethane	-1.8±0.1	1.1±0.1	1.1±0.1
	Propanal	-0.9±0.1	0.9±0.1	1.0±0.1

The same set of experiments was conducted at 130°C (Figure 4.8). A similar trend was observed, in that the PA functionalized catalysts exhibited increased activity with longer alkyl chain tail length. However, while the enhancement in TOF from the no PA sample to any of the PA samples increased, the enhancement from MPA to HDPA decreased, as compared to at 170°C. Unlike experiments at 170°C, the no PA sample exhibited no enhancement in propanal formation rate (both on a per-site and per gram basis) from increased pressure at this temperature, while ethane formation did increase with pressure, resulting in decreasing selectivity with increasing pressure. Normally a decrease in selectivity might be attributed to the formation of Rh clusters, but the absence of propanol formation suggests that Rh remained

atomically dispersed.[53–56] This difference in selectivity trends is attributable to differences in reaction orders for no PA and PA functionalized samples at these conditions (Table 4.2).

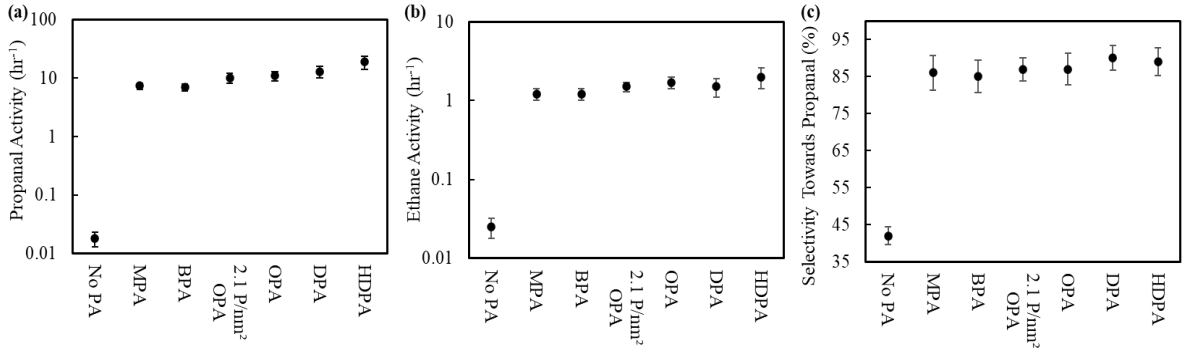

Figure 4.9: (a) Propanal formation turn over frequencies (TOF) for PA functionalized samples measured at 100°C and 30 SCCM total flow rate of 1:1:1 H_2:CO:C_2H_4 at 10 bar. The error bars represent the propagated error from rate and site counting measurements. (b) Ethane formation TOF for different PA functionalized samples. The error bars represent the propagated error from rate and site counting measurements. (c) Selectivity towards propanal for different PA functionalized samples. The error bars represent the standard error from three duplicate experiments using different batches of samples.

At 1 bar and 130°C, the no PA, MPA, OPA, and HDPA functionalized samples exhibited propanal TOFs of 0.084±0.007 hr^{-1}, 1.0±0.1 hr^{-1}, 2.3±0.3 hr^{-1}, and 7±2 hr^{-1}, respectively, corresponding to enhancements of 12x, 28x, and 80x for MPA, OPA, and HDPA, respectively, as compared to the no PA case. At 10 bar and 130°C the no PA, MPA, OPA, and HDPA functionalized samples exhibited a propanal production rate of 0.95±0.08 hr^{-1}, 13±2 hr^{-1}, 23±3 hr^{-1}, and 60±16 hr^{-1}, respectively, corresponding to enhancements of 133x, 244x, and 630x for MPA, OPA, and HDPA, respectively. Again, the 630x enhancement in TOF comparing the no PA and HDPA functionalized samples, in the context of the decrease in Rh accessibility from ~100% to ~3%, shows that PAs are inherently modifying the reactivity of exposed Rh sites.

Table 4.3 Rates, selectivities, apparent activation enthalpies, and apparent activation entropies for EHF performed at 100°C, 10 bar, and 30 SCCM 1:1:1 $CO:C_2H_4:H_2$. Barriers were obtained in the range of 100°C to 130°C. Uncertainty in TOF values represent the standard error from at least three replicate trials and the propagated error from site counting measurements. The uncertainty in selectivity represents the standard error from at least three replicate trials, while the uncertainty for apparent activation barriers either represents the standard error from at least three replicate trials, or the standard error of the regression used to obtain the values, whichever was greater.

Sample	Ethane Activity (hr^{-1})	Propanal Activity (hr^{-1})	Selectivity (%)	Ethane $\Delta H^{\ddagger}$ (kJ/mol)	Propanal $\Delta H^{\ddagger}$ (kJ/mol)	Ethane $\Delta S^{\ddagger}$ (J/(mol·K))	Propanal $\Delta S^{\ddagger}$ (J/(mol·K))
No PA	0.025±0.007	0.018±0.005	42±2	100±7	51±5	-71±16	-206±21
MPA	1.2±0.2	7.4±0.9	86±5	93±7	53±4	-70±13	-156±14
BPA	1.2±0.2	7±1	85±4	96±8	53±4	-58±11	-151±14
2.1 P/nm^2 OPA	1.5±0.2	10±2	87±3	91±6	52±4	-71±12	-150±16
OPA	1.7±0.3	11±2	87±4	95±5	54±4	-51±11	-147±15
DPA	1.5±0.3	13±2	90±3	89±5	53±5	-77±15	-142±16
HDPA	2.0±0.6	19±5	89±4	89±6	60±4	-74±14	-137±14

Interestingly, differences in TOF enhancement between different PAs became smaller at 130°C than at 170°C. This suggests that at lower temperatures, PAs of different tail lengths exhibit more similar influences on the reactivity of atomically dispersed Rh species. To further examine the behavior of PA modified samples with decreasing temperature, reactions were performed for all samples (no PA, MPA, BPA, 2.1 P/nm^2 OPA, OPA, DPA, and HDPA) at 10 bar between 100°C-130°C (Figure 4.9 for activities and selectivities, and Table 4.3 for apparent kinetic barriers). At 100°C and 10 bar, the propanal production rates were 0.018±0.005 hr^{-1}, 7.4±0.9 hr^{-1}, 7±1 hr^{-1}, 10±2 hr^{-1}, 11±2 hr^{-1}, 13±2 hr^{-1}, and 19±5 hr^{-1}, while selectivities were 42±2%, 86±5%, 85±4%, 87±3%, 87±4%, 90±3%, 89±4%, for the no PA, MPA, BPA, 2.1

P/nm^2 OPA, OPA, DPA, and HDPA functionalized catalysts respectively. This corresponds to enhancements in propanal TOF of 411x, 389, 563x, 611x, 722x, and 1056x for the MPA, BPA, 2.1 P/nm^2 OPA, OPA, DPA, and HDPA functionalized catalysts, respectively. At this condition the differences in TOFs for the various PA functionalized samples are not statistically significant, but the difference between the TOFs for no PA and PA functionalized samples are statistically significant. This suggests that at this temperature, all PAs, regardless of tail length, similarly influence the reactivity of exposed Rh sites.

To summarize the EHF results: (1) At all conditions, PA functionalization improved TOFs, per gram Rh rates of propanal formation, and selectivities to propanal, with longer tail PAs exhibiting the greatest enhancements. (2) PAs improved EHF TOF and selectivity even further at 10 bar than at 1 bar, likely due to more facile desorption of CO by PA modified catalysts. (3). PAs have greater impacts on EHF TOF and selectivity at lower temperatures, but the influence of PA tail length on TOF is minimized. (4) At 100°C, PAs significantly improved catalytic performance compared to the No PA catalyst, but the influence of tail length is no longer existent (all PAs resulted in similar catalytic reactivities).

4.3.4 Effects of SAM Rigidity on $Rh(CO)_2$ Reactivity

For EHF performed on atomically dispersed Rh/Al_2O_3, $Rh(CO)_2$ is the most abundant surface intermediate (MASI) under reaction conditions,[24,25] and CO desorption is a kinetically relevant elementary step.[26] The TPD experiments demonstrated that PA functionalization increased rate constants for CO desorption from $Rh(CO)_2$ by increasing the attempt frequency. These changes in CO desorption attempt frequency were attributed to changes in $Rh(CO)_2$ mobility (entropy). The apparent dependence of CO desorption rate and EHF activity at temperatures of 130°C or higher on PA tail length, despite a decrease in PA coverage, and the lack of dependence of EHF activity on PA tail length at 100°C merits further

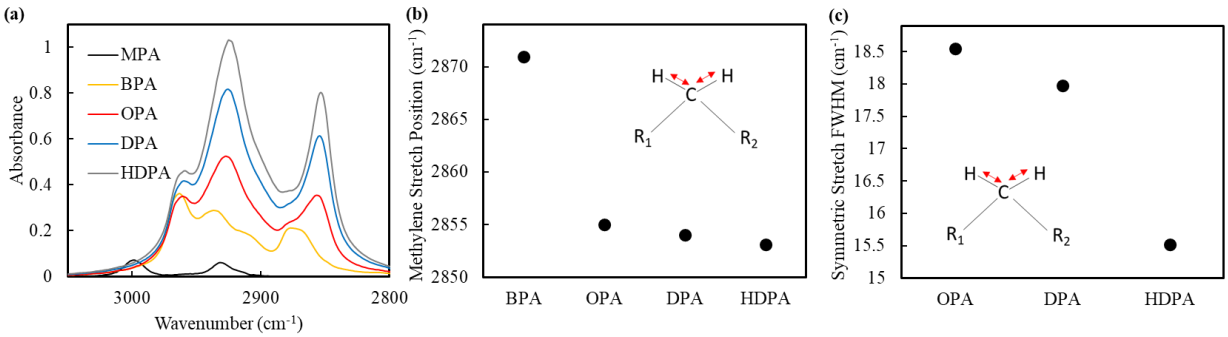

Figure 4.10: (a) FTIR spectra of the C-H stretch region of MPA (black), BPA (yellow), OPA (red), DPA (blue), and HDPA (grey) functionalized $Rh/\gamma\text{-}Al_2O_3$ at 100°C (b) Symmetric methylene stretch position for different PA species. Lower wavenumber stretches are indicative of more rigid and ordered monolayers. (c) Full width at half of maximum (FWHM) for OPA, DPA, and HDPA. Decreased FWHM is indicative or a more well-ordered CH_2 environment, suggesting a more well-ordered monolayer.

discussion.

Previous reports of SAMs on surfaces correlated increased length of the tail group with increased "crystal-like" (rigid) nature of the SAM along with more complete occlusion of the surface from other molecules (consistent with the decreased accessibility observed in this work).[27–29,57] Molecular dynamics studies suggest that the radius of curvature of very small support particles minimizes SAM tail to tail interactions for shorter tail groups, while longer tail groups will assume orientations non-orthogonal to the particle surface in order to

maximize interactions with other tails. To qualitatively examine the rigidity of the PA monolayers here, FTIR spectra were collected of the symmetric methylene stretch for each of the PA functionalized samples at 100°C (Figure 4.10a). Decreases in the full width at half of maximum (FWHM) and shifts in stretch position to lower wavenumbers are associated with increased uniformity and rigidity in SAMs.[28,58–60]

It was observed that for BPA functionalized catalysts, there was a broad feature centered around ~2875 cm^{-1}, likely a convolution of methylene stretches in different environments, that was approximately 20 cm^{-1} blueshifted relative to OPA functionalized catalysts, while OPA, DPA, and HDPA functionalized catalysts exhibited narrower stretches at ~2855 cm^{-1}, 2854 cm^{-1}, and 2853 cm^{-1}, respectively (Figure 4.10b). The FWHM of OPA, DPA, and HDPA were ~18.5 cm^{-1}, 18 cm^{-1}, and 15.5 cm^{-1}, respectively (Figure 4.10c). MPA functionalized catalysts were not included in this analysis as they do not exhibit methylene stretches, while methyl stretches are poorer indicators of uniformity as they exist at the end of PA tails.[28,58–60] The narrowing and redshifting of the methylene stretches indicates that longer tail PAs form more rigid SAMS.

We hypothesize that the SAM rigidity plays a key role in determining the mobility of $Rh(CO)_2$. Specifically, strong interactions between SAM tails can minimize rotation or translation of $Rh(CO)_2$ species on γ-Al_2O_3. The more pronounced effect of HDPA on CO desorption and EHF TOF than MPA, despite MPA functionalized samples exhibiting twice the PA surface density (5.2 P/nm^2 for MPA, 2.1 P/nm^2 for HDPA), suggests that the interactions between PA tails play an important role in blocking $Rh(CO)_2$ mobility. Specifically, shorter tailed, less rigid SAMs are more likely to have defects, and the alkyl tails will have more rotational mobility.[29] These factors may provide opportunities for $Rh(CO)_2$ to move, while

the less defective and more rigid SAM from longer tailed PAs may present fewer opportunities for $Rh(CO)_2$ mobility.

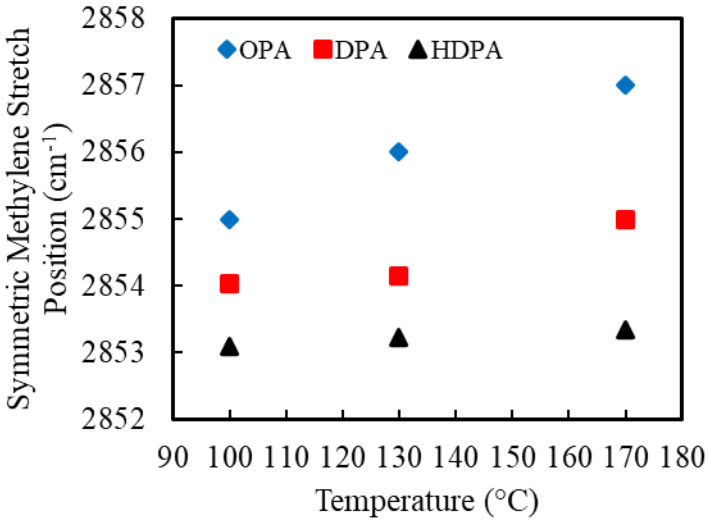

Figure 4.11: (a) Symmetric methylene stretch position for OPA, DPA, and HDPA functionalized Rh/Al_2O_3 at 100°C, 130 °C, and 170 °C.

To examine how SAM characteristics of different PA tails change with temperature, the position and FWHM of the symmetric methylene stretch were examined at three different temperatures (100°C, 130°C, and 170°C) for all PAs, corresponding to temperatures of reactivity measurements. Figure 4.11 presents the stretch positions of OPA, DPA, and HDPA as a function of temperature.The spectra at each temperature for each PA tail can be found in Figure 4.12. MPA and BPA were not included in this analysis for the same reasons as mentioned above. It was observed that the symmetric methylene stretch position of HDPA functionalized catalysts was nearly constant when examined at 100°C, 130°C, and 170°C, while the OPA and DPA functionalized catalysts exhibited a symmetric methylene stretch that blueshifted 2 cm^{-1} and 1 cm^{-1}, respectively, when the temperature was raised from 100°C to 170°C. While these shifts are small, they were repeatably observed. This suggests that longer tailed PAs form more rigid SAMs, and that the rigidity is maintained at higher temperatures for SAMs formed from longer tailed PAs. While there is some shift in the FWHM for all

samples when increasing temperature, the HDPA sample stretches remain narrower than the other samples (Figure 4.13).

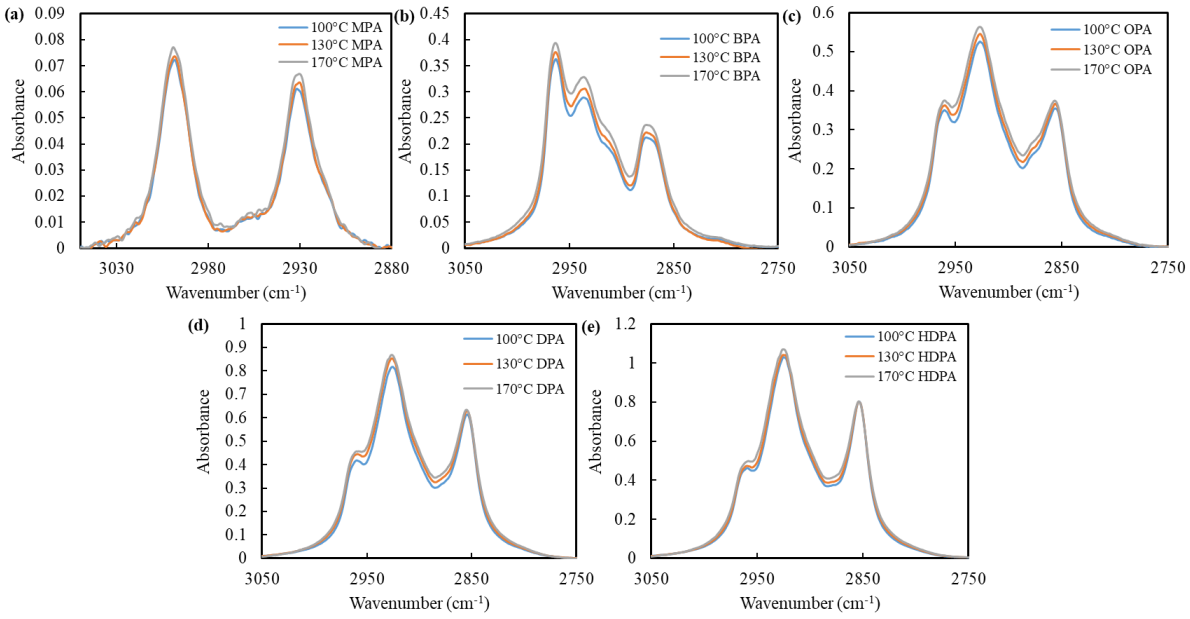

Figure 4.12: C-H stretching region for MPA (a), BPA (b), OPA (c), DPA (d), and HDPA (e) functionalized Rh/Al_2O_3 catalysts at various temperatures. Samples were heated in Ar to the desired temperature and allowed to sit for 10 minutes before the spectra were taken. Spectra were recorded using the high-resolution aperture setting and represent the average of 256 scans with a data spacing of 0.241 cm^{-1}.

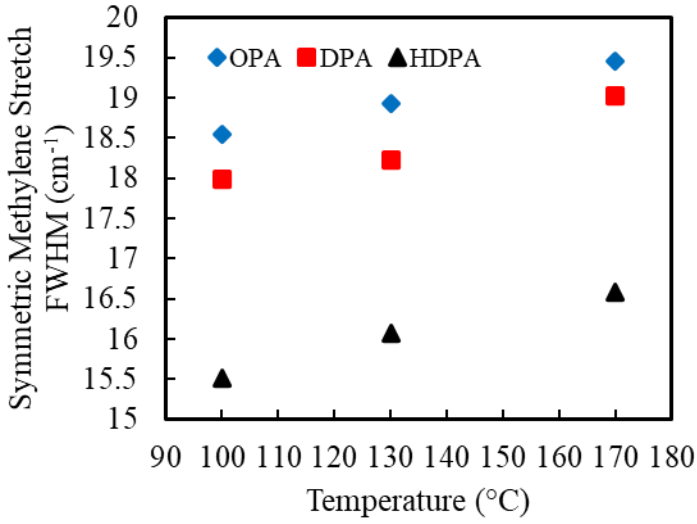

Figure 4.13: FHWM of the symmetric methylene stretch for OPA, DPA, and HDPA functionalized Rh/Al_2O_3 at 100°C, 130°C, and 170°C.

The differences in PA SAM behavior with temperature may explain the changes in $Rh(CO)_2$ reactivity seen with variation in temperature. If longer PAs retain SAM rigidity at higher temperatures, restricting the mobility of $Rh(CO)_2$, then greater influence on $Rh(CO)_2$ reactivity would be expected with longer PAs at the elevated temperatures. Additionally, at lower temperatures, all PA SAMs will be more rigid, similarly restricting $Rh(CO)_2$, resulting in the smaller differences between reactivity of PA functionalized samples at lower temperatures. It is important to note that MPA should not exhibit "crystallinity" at any condition as MPA tails should have little to no interactions with each other. This suggests that at lower temperatures, $Rh(CO)_2$ may lack the requisite thermal energy to move through SAMs on functionalized surfaces (regardless of SAM crystallinity), such that MPA and HDPA are similarly able to restrict $Rh(CO)_2$ mobility, while $Rh(CO)_2$ on the no PA catalyst still exhibits mobility.[20] A schematic illustration of this hypothesis can be found in Figure 4.14.

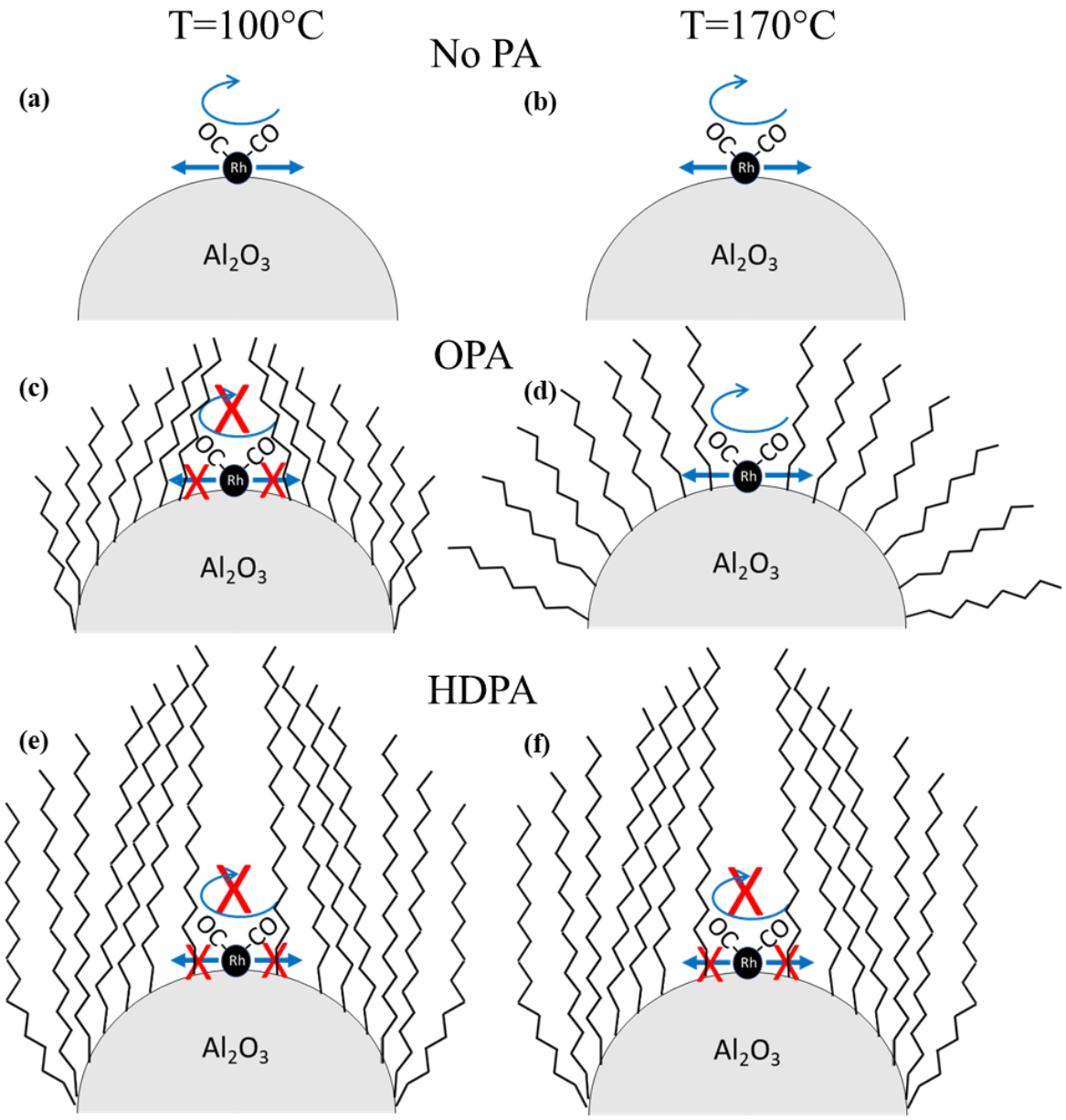

Figure 4.14: Illustration of the proposed behavior of $Rh(CO)_2$ at different temperatures on no PA, OPA, and HDPA modified Rh/Al_2O_3. (a) At 100°C, $Rh(CO)_2$ is unconstrained and has sufficient energy for facile translation. (b) At 170°C, $Rh(CO)_2$ is unconstrained and has sufficient energy for facile translation. (c) At 100°C, $Rh(CO)_2$ is constrained by OPA. OPA tails assume conformations to maximize tail-tail interactions. (d) At 170°C, OPA tails are more "fanned out", resulting in less rigid SAMs that are worse at constraining $Rh(CO)_2$. (e) At 100°C $Rh(CO)_2$ is constrained by HDPA. HDPA tails assume conformations to maximize tail-tail interactions. (f) At 170°C, HDPA tails are able to maintain rigidity in the SAM, constraining $Rh(CO)_2$.

4.3.5 Desorption from $Rh(CO)_2$ is Kinetically Relevant for EHF

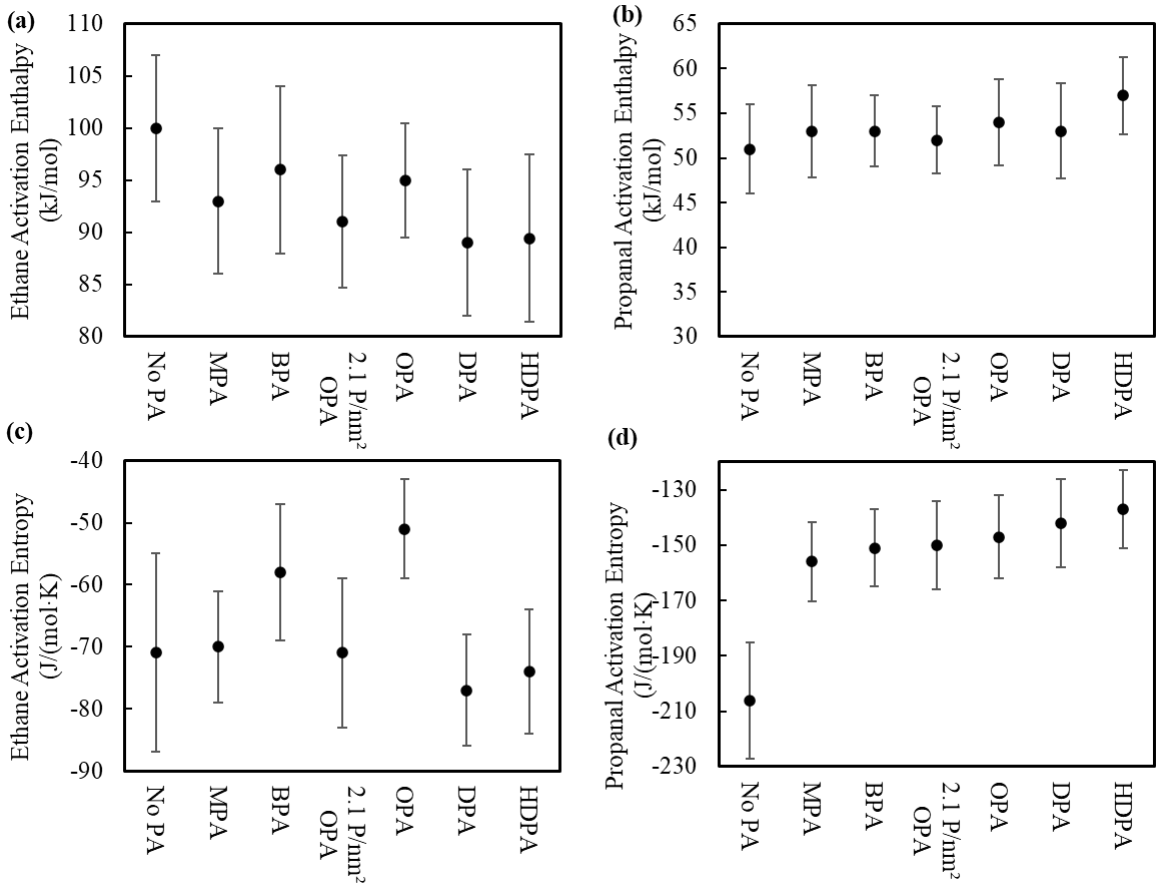

Figure 4.15: Apparent activation entropies and enthalpies for propanal and ethane formation via EHF at 10 bar and 30 SCCM 1:1:1 $CO:C_2H_4:H_2$. Kinetic parameters were obtained in the range of 100°C to 130°C. The uncertainty for apparent activation barriers either represents the standard error from at least three replicate trials, or the standard error of the regression used to obtain the values, whichever was greater.

With a proposed mechanism by which PA interactions affect CO desorption and EHF reactivity on $Rh(CO)_2$, CO desorption and EHF kinetic parameters can be correlated. At 10 bar, between 100°C and 130°C, the apparent activation enthalpies and entropies for propanal and ethane formation during EHF were calculated using the Eyring-Polanyi Equation (Equation S1F). Consistent with our previous study of OPA functionalized $Rh/\gamma\text{-}Al_2O_3$,[18] all samples exhibited statistically insignificant differences ($P\approx0.2$, $n=4$) apparent enthalpic activation barriers (51±5 to 60±4 kJ/mol) for propanal formation, despite orders of magnitude changes in TOFs between samples. Alternatively, the PA functionalized samples exhibited statistically

significant differences (P≈0.04, n=4) in apparent activation entropies from the no PA sample (from -206±21 (J/(mol·K)), to -137±14 (J/(mol·K)) for HDPA (Figure 4.15)). At a fixed apparent activation entropy, the observed difference in TOF for no PA and HDPA at 100°C and 10 bar would correspond to a ~20 kJ/mol difference in activation enthalpy, much larger than the uncertainty of the observed enthalpic barriers. This demonstrates that activation enthalpy changes within the error bounds of the parameter estimation could not explain observed changes in TOF, and thus supports the conclusion that changes in activation entropy are the primary cause of changes in TOF.

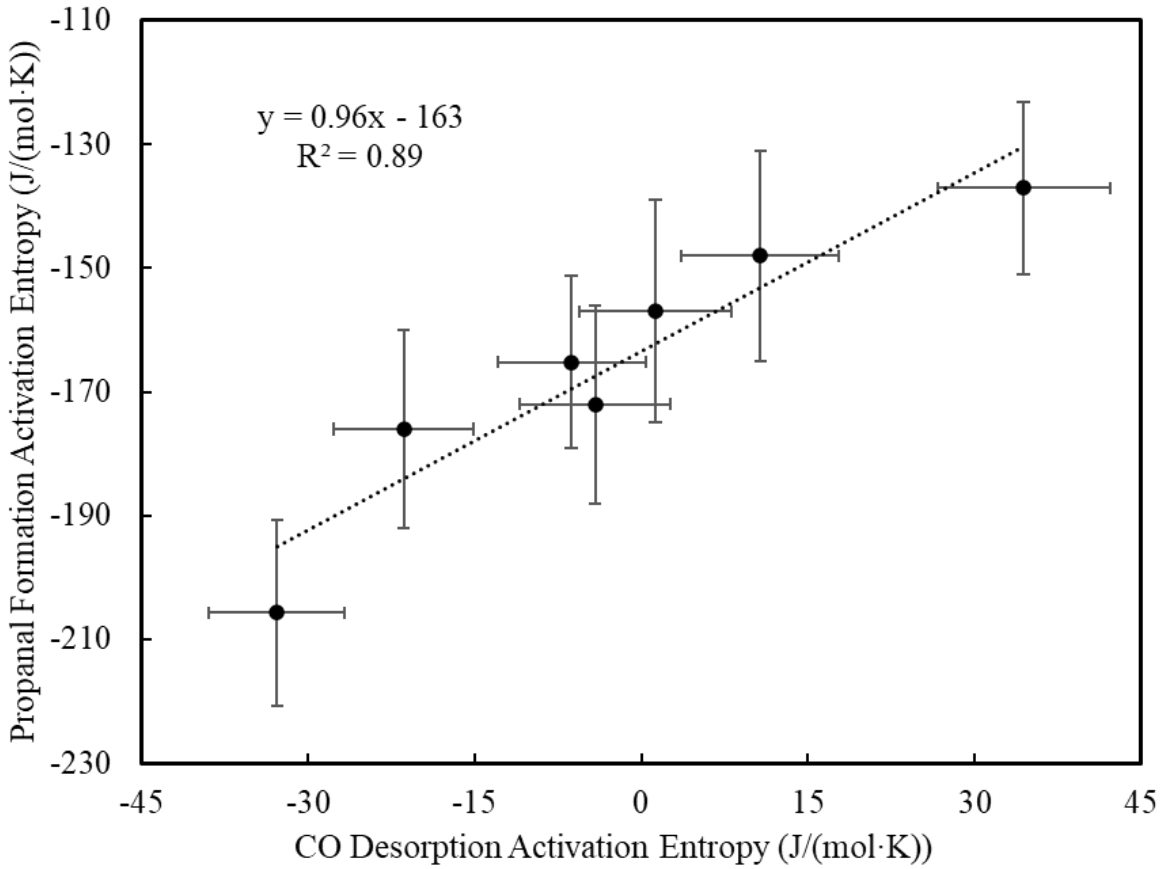

Figure 4.16: Parity plot of EHF activation entropy calculated via Eyring analysis (100°C-130°C, 30 SCCM 1:1:1 H_2:CO:C_2H_4 at 10 bar) versus the activation entropy of CO desorption for each sample. The high correlation between EHF activation entropy and CO desorption suggests that improvements in EHF activity are almost entirely due to decreased barriers for CO desorption.

With the activation entropies of EHF and of CO desorption from $Rh(CO)_2$ for a variety of PA tails estimated, trends can be drawn between the two processes. A parity plot of propanal formation apparent activation entropies and CO desorption activation entropies (Figure 4.16) shows a strong correlation between the two barriers. This is suggestive that more facile desorption of CO from $Rh(CO)_2$ caused by increased attempt frequency is the main contribution of PAs to improving propanal formation TOFs. We hypothesize that PAs enable the promoted CO desorption rates by restricting the mobility of the $Rh(CO)_2$ active site. In this case, the mobility of the active site is likely relevant to catalytic turnovers as the timescales of individual catalytic turnovers are much larger than of $Rh(CO)_2$ motion.[20] Thus, in the case

of mobile active sites that must find stationary states to react, there is a potential for controlling reactivity by specifically influencing the entropy (mobility) of the active site.

4.3.6 Comparison of Catalyst Performance to Other Heterogeneous EHF Catalysts

A brief discussion is warranted of the catalytic performance of these samples compared to other catalytic materials previously reported for EHF. A recent review compared and categorized the catalytic performance of Rh-based heterogeneous hydroformylation catalysts.[61] Broadly, these catalysts were categorized into oxide supported Rh, second metal modified supported Rh, inorganic phosphide supported Rh, and organic phosphine supported Rh. In general, organic phosphine supported Rh exhibit the greatest activity (>100 hr^{-1}) and selectivity to propanal (>85%), but are air and moisture sensitive, resulting in difficult syntheses and poorer stability than oxide-supported analogs. Oxide supported Rh catalysts have exhibited a wide range of TOFs (<10 to 2000 hr^{-1}) and selectivities (20 to 95%); typically the catalysts exhibiting higher TOF also exhibit lower selectivity.[25] The catalyst presented in this work exhibit comparable selectivity to organic phosphine catalysts and the most selective oxide supported catalysts (~85-90%), but lower activity (~20 hr^{-1}) at 100°C and 10 bar. Further work is merited for exploring previously established methodologies for enhancing hydroformylation activity (specifically second metal modification) in combination with the methodologies presented in this work to create highly active and selective EHF catalysts that do not require organic phosphine supports.

4.4 CONCLUSION

In conclusion, we have demonstrated a methodology for systematically modifying the mobility (entropy) of atomically dispersed $Rh(CO)_2$ supported on γ-Al_2O_3, through functionalization of the support with straight-chain alkyl-PAs of different tail lengths. By restricting the mobility of $Rh(CO)_2$ with PAs, desorption temperatures for CO were decreased by up to 120°C, and turn over frequencies for propanal formation via EHF were increased by up to 1000x compared to the unmodified $Rh(CO)_2/\gamma$-Al_2O_3. Kinetic analyses of TPD experiments and EHF evidence statistically significant differences in activation entropies, with insignificant changes to activation enthalpies. The observed dependence of CO desorption temperature and EHF TOFs with the length of PAs tails suggests that interactions between PAs tails, far from $Rh(CO)_2$, dictated active site mobility via changes to the SAM rigidity. Additionally, longer tail PAs retain SAM rigidity at higher temperatures, thus more effectively restricting $Rh(CO)_2$ mobility, and therefore promoting CO desorption and EHF rates. This methodology of controlling active site entropy seems promising to control the activity and selectivity of mobile active sites beyond the limits of scaling relations.

4.5 APPENDIX

Derivation of Equation 4.2 (Equation 4.4)

The Polanyi-Wigner equation describes a kinetically limited desorption process[1]:

$$-\frac{d\theta}{dT} = \frac{A}{\beta}\theta^m \exp\left(-\frac{E_d}{k_B T}\right) \quad (4.4A)$$

Where: θ=Coverage of adsorbate
T=Temperature (K)
A=Preexponential Factor (1/s)
β=Temperature Ramp Rate (K/s)
E_d=Desorption Energy (J)
k_B=Boltzmann Constant (J/K)
m= the desorption order.

At the maximum desorption rate, $-\frac{d\theta^2}{dT^2} = 0$. Taking the second derivative and setting it to zero yields:

$$\frac{E_d}{k_B T_P^2} = \frac{A}{\beta} m\theta^{m-1} \exp\left(-\frac{E_d}{k_B T_P}\right) \quad (4.4B)$$

Where: T_P=temperature at which there is maximum desorption (K)
Further, CO desorption on atomically dispersed Rh is first order, therefore m=1

$$\frac{E_d}{k_B T_P^2} = \frac{A}{\beta} \exp\left(-\frac{E_d}{k_B T_P}\right) \quad (4.4C)$$

For a known, T_P and E_d, one can calculate A directly.

$$A = \frac{E_d \beta}{k_B T_P^2} \exp\left(\frac{E_d}{k_B T_P}\right) \quad (4.4D)$$

In order to calculate the activation entropy from the preexponential factor, the preexponential factor in the Arrhenius equation (Equation 4.4E) must be defined in the context of the Eyring-Polanyi equation (Equation 4.4F).

$$k = A \exp\left(\frac{-E_a}{RT}\right) \quad (4.4E)$$

Where: k = rate constant (1/s)
E_a= Activation Energy (J/mol)
R= Molar gas constant (J/(mol*K))

$$k = \frac{\kappa k_B T}{h} \exp\left(\frac{\Delta S^{\ddagger}}{\mathrm{R}}\right) \exp\left(-\frac{\Delta H^{\ddagger}}{RT}\right) \quad (4.4F)$$

Where:

$\Delta H^{\ddagger}$ = Activation Enthalpy (J/mol)
$\Delta S^{\ddagger}$ = Activation Entropy (J/(mol*K))
κ= Transmission Coefficient (assumed to be unity)
h = Planck Constant (J*s)
T= Temperature (K)

For a unimolecular, single step reaction, the activation energy can be related to the activation enthalpy by Equation 4.4G.[2,3]

$$E_a = \Delta H^{\ddagger} + RT \tag{4.4G}$$

Substituting Equation 4.4G into Equation 4.4F results in Equation 4.4H

$$k = \frac{\kappa k_B T}{h} \exp\left(\frac{\Delta S^{\ddagger}}{\mathrm{R}}\right) \exp\left(\frac{-E_a + RT}{RT}\right) \tag{4.4H}$$

Setting Equation 4.4E equal to Equation 4.4H yields Equation 4.4I

$$A \exp\left(\frac{-E_a}{RT}\right) = \frac{\kappa k_B T}{h} \exp\left(\frac{\Delta S^{\ddagger}}{\mathrm{R}}\right) \exp\left(\frac{-E_a + RT}{RT}\right) \tag{4.4I}$$

Dividing both sides of the equation by $\exp\left(\frac{-E_a}{RT}\right)$ yields Equation 4.4J.

$$A = \frac{\kappa k_B T}{h} \exp\left(\frac{\Delta S^{\ddagger}}{\mathrm{R}}\right) \exp(1) \tag{4.4J}$$

Setting Equation 4.4J equal to Equation 4.4D yields Equation 4.4K

$$\frac{E_d \beta}{k_B T_P^2} \exp\left(\frac{E_d}{k_B T_P}\right) = \frac{\kappa k_B T}{h} \exp\left(\frac{\Delta S^{\ddagger}}{\mathrm{R}}\right) \exp(1) \tag{4.4K}$$

Setting $T_P = T$, dividing both sides by $\frac{\kappa k_B T}{h}$, assuming κ to unity, and taking the natural log of both sides yields Equation 4.4L

$$\ln\left(\frac{h E_d \beta}{k_B^2 T_P^3}\right) + \frac{E_d}{k_B T_P} = \frac{\Delta S^{\ddagger}}{\mathrm{R}} + 1 \tag{4.4L}$$

Making the necessary adjustment of units such that $k_B = R$, and solving for $\Delta S^{\ddagger}$ yields Equation 4.4M

$$\Delta S^{\ddagger} = \mathrm{R}\ln\left(\frac{h E_d \beta}{k_B^2 T_P^3}\right) + \frac{E_d}{T_P} - R \tag{4.4M}$$

Calculation of Maximum Translational, Rotational, and Vibrational Entropic Contributions

Translational Entropy (Equation 4.5)

The gas phase translational entropy of a $Rh(CO)_2$ complex can be calculated using Equation 4.5A. [4]

$$S^0_{trans} = S^0_{Ar,298K} + Rln\left[\left(\frac{m}{m_{Ar}}\right)^{\frac{3}{2}}\left(\frac{T}{298}\right)^{\frac{5}{2}}\right] \quad (4.5A)$$

Where:

S^0_{trans}= Translational entropy of the molecule of interest (J/mol·K)
$S^0_{Ar,298K}$= Translational entropy of Ar at 298K (J/mol·K)
m = mass of the molecule of interest (kg)
m_{Ar}= mass of Ar (kg)

Assuming that one translational degree of freedom is lost when $Rh(CO)_2$ is on a surface (it can only move in two dimensions instead of three), then we can approximate the maximum possible entropy of a molecule on a surface as Equation 4.5B.

$$S^0_{trans-2D} = \frac{2S^0_{trans}}{3} \quad (4.5B)$$

Where:

$S^0_{trans-2D}$= Translational entropy of the molecule of interest constrained to two dimensions (J/mol·K).

Rotational Entropy (Equation 4.6)

The gas phase rotational entropy of a $Rh(CO)_2$ complex can be calculated using Equation 4.6A. [4]

$$S_{rot} = R\left\{\ln\left[\frac{\sqrt{\pi I_A I_B I_C}}{\sigma}\left(\frac{8\pi^2 k_B T}{h^2}\right)^{\frac{3}{2}}\right] + \frac{3}{2}\right\} \quad (4.6A)$$

Where:

S_{rot}= The rotational entropy of the molecule of interest (J/mol·K)
I_A= The principal moment of inertia along axis A (kg·m^2)
I_B= The principal moment of inertia along axis B (kg·m^2)
I_C= The principal moment of inertia along axis C (kg·m^2)
σ= The external symmetry number for the molecule of interest

Assuming that two rotational degrees of freedom is are hindered when $Rh(CO)_2$ is on a surface (two of the rotational modes lose half of their available rotation), then we can approximate the maximum possible entropy of a molecule on a surface as Equation 4.6B.

$$S_{rot-2D} = \frac{2S_{rot}}{3} \tag{4.6B}$$

Where:

S_{rot-2D}= Rotational entropy of the molecule of interest constrained to two dimensions (J/mol·K).

Vibrational Entropy (Equation 4.7)

The gas phase vibrational entropy of a $Rh(CO)_2$ complex is the sum of the vibrational entropies for the individual bonds. Therefore the total vibrational entropy of the complex can be written as Equation 4.7A.[5]

$$S_v = \sum S_{v_i} \tag{4.7A}$$

Where:

S_v= the total vibrational entropy of the molecule (J/mol·K)

S_{v_i}= the vibrational entropy of a specific bond (J/mol·K)

The vibrational entropy of a specific bond can be calculated using Equation 4.7B.

$$S_{v_i} = \frac{Rhcv_i}{k_B T\left(e^{\frac{hcv_i}{k_B T}} - 1\right)} - Rln\left(1 - e^{-\frac{hcv_i}{k_B T}}\right) \tag{4.7B}$$

Where: c= the speed of light in a vacuum (m/s)

v_i= the vibrational wavenumber of the bond (m^{-1})

4.6 REFERENCES

[1] M.A. Barteau, Linear free energy relationships for C1-oxygenate decomposition on transition metal surfaces, Catal. Letters. 8 (1991) 175–183. https://doi.org/10.1007/BF00764114.

[2] R.J. Madix, Reaction Kinetics and Mechanism on Metal Single Crystal Surfaces, Adv. Catal. 29 (1980) 1–53. https://doi.org/10.1016/S0360-0564(08)60119-4.

[3] J.K. Nørskov, T. Bligaard, A. Logadottir, S. Bahn, L.B. Hansen, M. Bollinger, H. Bengaard, B. Hammer, Z. Sljivancanin, M. Mavrikakis, Y. Xu, S. Dahl, C.J.H. Jacobsen, Universality in heterogeneous catalysis, J. Catal. 209 (2002) 275–278. https://doi.org/10.1006/jcat.2002.3615.

[4] F. Abild-Pedersen, J. Greeley, F. Studt, J. Rossmeisl, T.R. Munter, P.G. Moses, E. Skúlason, T. Bligaard, J.K. Nørskov, Scaling properties of adsorption energies for hydrogen-containing molecules on transition-metal surfaces, Phys. Rev. Lett. 99 (2007) 016105. https://doi.org/10.1103/PhysRevLett.99.016105.

[5] J. Hulva, M. Meier, R. Bliem, Z. Jakub, F. Kraushofer, M. Schmid, U. Diebold, C. Franchini, G.S. Parkinson, Unraveling CO adsorption on model single-atom catalysts, Science. 371 (2021) 375–379. https://doi.org/10.1126/science.abe5757.

[6] H. Xu, C.Q. Xu, D. Cheng, J. Li, Identification of activity trends for CO oxidation on supported transition-metal single-atom catalysts, Catal. Sci. Technol. 7 (2017) 5860–5871. https://doi.org/10.1039/c7cy00464h.

[7] M. Boudart, Pauling's theory of metals in catalysis, J. Am. Chem. Soc. 72 (1950) 1040. https://doi.org/10.1021/ja01158a522.

[8] R. Hercigonja, V. Rac, V. Rakic, A. Auroux, Enthalpy-entropy compensation for n-hexane adsorption on HZSM-5 containing transition metal ions, J. Chem. Thermodyn. 48 (2012) 112–117. https://doi.org/10.1016/j.jct.2011.12.016.

[9] R. Hercigonja, V. Rakić, Enthalpy-entropy compensation for n-hexane adsorption on Y zeolite containing transition metal cations, Sci. Sinter. 47 (2015) 83–88. https://doi.org/10.2298/SOS1501091H.

[10] D.W. Flaherty, E. Iglesia, Transition-state enthalpy and entropy effects on reactivity and selectivity in hydrogenolysis of n -alkanes, J. Am. Chem. Soc. 135 (2013) 18586–18599. https://doi.org/10.1021/ja4093743.

[11] A.L. Fernandez, J. Hao, R.L. Parkes, A.J. Poë, E.J.S. Vichi, Zeolite activation of organometallics: Anchoring and decarbonylation kinetics of Mo(CO) 6 in dehydrated Na 56Y zeolite, Organometallics. 23 (2004) 2715–2723. https://doi.org/10.1021/om040005v.

[12] P.J. Dauenhauer, O.A. Abdelrahman, A Universal Descriptor for the Entropy of Adsorbed Molecules in Confined Spaces, ACS Cent. Sci. 4 (2018) 1235–1243. https://doi.org/10.1021/ACSCENTSCI.8B00419.

[13] D.T. Bregante, M.C. Chan, J.Z. Tan, E.Z. Ayla, C.P. Nicholas, D. Shukla, D.W. Flaherty, The shape of water in zeolites and its impact on epoxidation catalysis, Nat. Catal. 2021 49. 4 (2021) 797–808. https://doi.org/10.1038/s41929-021-00672-4.

[14] R. Gounder, E. Iglesia, The catalytic diversity of zeolites: Confinement and solvation effects within voids of molecular dimensions, Chem. Commun. 49 (2013) 3491–3509. https://doi.org/10.1039/c3cc40731d.

[15] A.J. Hoffman, C. Asokan, N. Gadinas, E. Schroeder, G. Zakem, S. V. Nystrom, A.B. Getsoian, P. Christopher, D. Hibbitts, Experimental and Theoretical Characterization

of Rh Single Atoms Supported on γ-Al2O3with Varying Hydroxyl Contents during NO Reduction by CO, ACS Catal. 12 (2022) 11697–11715. https://doi.org/10.1021/acscatal.2c02813.
[16] E.K. Schroeder, J. Finzel, P. Christopher, Photolysis of Atomically Dispersed Rh/Al2O3 Catalysts: Controlling CO Coverage in Situ and Promoting Reaction Rates, J. Phys. Chem. C. (2022). https://doi.org/10.1021/ACS.JPCC.2C04642.
[17] S.H. Krishna, C.B. Jones, R. Gounder, Temperature dependence of Cu(I) oxidation and Cu(II) reduction kinetics in the selective catalytic reduction of NOx with NH3 on Cu-chabazite zeolites, J. Catal. 404 (2021) 873–882. https://doi.org/10.1016/J.JCAT.2021.08.042.
[18] G. Zakem, I. Ro, J. Finzel, P. Christopher, Support functionalization as an approach for modifying activation entropies of catalytic reactions on atomically dispersed metal sites, J. Catal. (2021). https://doi.org/10.1016/j.jcat.2021.07.030.
[19] C. Paolucci, I. Khurana, A.A. Parekh, S. Li, A.J. Shih, H. Li, J.R. Di Iorio, J.D. Albarracin-Caballero, A. Yezerets, J.T. Miller, W.N. Delgass, F.H. Ribeiro, W.F. Schneider, R. Gounder, Dynamic multinuclear sites formed by mobilized copper ions in NOx selective catalytic reduction, Science. 357 (2017) 898–903. https://doi.org/10.1126/science.aan5630.
[20] A. Suzuki, Y. Inada, A. Yamaguchi, T. Chihara, M. Yuasa, M. Nomura, Y. Iwasawa, Time Scale and Elementary Steps of CO-Induced Disintegration of Surface Rhodium Clusters, Angew. Chemie - Int. Ed. 115 (2003) 4943–4947. https://doi.org/10.1002/anie.200352318.
[21] R.R. Cavanagh, J.T. Yates, Site distribution studies of Rh supported on Al2O3 - An infrared study of chemisorbed CO, J. Chem. Phys. (1981). https://doi.org/10.1063/1.441544.
[22] J.T. Yates, T.M. Duncan, S.D. Worley, R.W. Vaughan, Infrared spectra of chemisorbed CO on Rh, J. Chem. Phys. (1979). https://doi.org/10.1063/1.437603.
[23] F. Solymosi, M. Pásztor, M. Pasztor, An Infrared Study of the Influence of CO Chemisorption on the Topology of Supported Rhodium, J. Phys. Chem. 89 (1985) 4789–4793. https://doi.org/10.1021/J100268A026.
[24] I. Ro, M. Xu, G.W. Graham, X. Pan, P. Christopher, Synthesis of Heteroatom Rh–ReO_x Atomically Dispersed Species on Al_2O_3 and Their Tunable Catalytic Reactivity in Ethylene Hydroformylation, ACS Catal. 9 (2019) 10899–10912. https://doi.org/10.1021/acscatal.9b02111.
[25] I. Ro, J. Qi, S. Lee, M. Xu, X. Yan, Z. Xie, G. Zakem, A. Morales, J.G. Chen, X. Pan, D.G. Vlachos, S. Caratzoulas, P. Christopher, Bifunctional hydroformylation on heterogeneous Rh-WOx pair site catalysts, Nat. 2022 6097926. 609 (2022) 287–292. https://doi.org/10.1038/s41586-022-05075-4.
[26] S. Lee, A. Patra, P. Christopher, D.G. Vlachos, S. Caratzoulas, Theoretical study of ethylene hydroformylation on atomically dispersed Rh/Al2O3 catalysts: Reaction mechanism and influence of ReOx promoter, ACS Catal. (2021) 9506–9518. https://doi.org/10.1021/acscatal.1c00705.
[27] P.K. Ghorai, S.C. Glotzer, Molecular dynamics simulation study of self-assembled monolayers of alkanethiol surfactants on spherical gold nanoparticles, J. Phys. Chem. C. 111 (2007) 15857–15862. https://doi.org/10.1021/jp0746289.
[28] R.L. Jones, N.C. Pearsall, J.D. Batteas, Disorder in alkylsilane monolayers assembled

on surfaces with nanoscopic curvature, J. Phys. Chem. C. 113 (2009) 4507–4514. https://doi.org/10.1021/jp8081358.
[29] B.W. Ewers, J.D. Batteas, Molecular dynamics simulations of alkylsilane monolayers on silica nanoasperities: Impact of surface curvature on monolayer structure and pathways for energy dissipation in tribological contacts, J. Phys. Chem. C. 116 (2012) 25165–25177. https://doi.org/10.1021/jp303097v.
[30] L. DeRita, S. Dai, K. Lopez-Zepeda, N. Pham, G.W. Graham, X. Pan, P. Christopher, Catalyst Architecture for Stable Single Atom Dispersion Enables Site-Specific Spectroscopic and Reactivity Measurements of CO Adsorbed to Pt Atoms, Oxidized Pt Clusters, and Metallic Pt Clusters on TiO2, J. Am. Chem. Soc. 139 (2017) 14150–14165. https://doi.org/10.1021/jacs.7b07093.
[31] L. DeRita, J. Resasco, S. Dai, A. Boubnov, H.V. Thang, A.S. Hoffman, I. Ro, G.W. Graham, S.R. Bare, G. Pacchioni, X. Pan, P. Christopher, Structural evolution of atomically dispersed Pt catalysts dictates reactivity, Nat. Mater. (2019). https://doi.org/10.1038/s41563-019-0349-9.
[32] J. Resasco, L. Derita, S. Dai, J.P. Chada, M. Xu, X. Yan, J. Finzel, S. Hanukovich, A.S. Hoffman, G.W. Graham, S.R. Bare, X. Pan, P. Christopher, Uniformity Is Key in Defining Structure-Function Relationships for Atomically Dispersed Metal Catalysts: The Case of Pt/CeO2, J. Am. Chem. Soc. 142 (2020) 169–184. https://doi.org/10.1021/jacs.9b09156.
[33] J. Zhang, L.D. Ellis, B. Wang, M.J. Dzara, C. Sievers, S. Pylypenko, E. Nikolla, J.W. Medlin, Control of interfacial acid–metal catalysis with organic monolayers, Nat. Catal. 1 (2018). https://doi.org/10.1038/s41929-017-0019-8.
[34] Y. Izumi, K. Asakura, Y. Iwasawa, Promoting effects of Se on Rh/ZrO2 catalysis for ethene hydroformylation, J. Catal. (1991). https://doi.org/10.1016/0021-9517(91)90188-A.
[35] C. Asokan, M. Xu, S. Dai, X. Pan, P. Christopher, Synthesis of Atomically Dispersed Rh Catalysts on Oxide Supports via Strong Electrostatic Adsorption and Characterization by Cryogenic Infrared Spectroscopy, J. Phys. Chem. C. (2022). https://doi.org/10.1021/ACS.JPCC.2C05426.
[36] S. Khoobiar, J.L. Carter, P.J. Lucchesi, The electronic properties of aluminum oxide and the chemisorption of water, hydrogen, and oxygen, J. Phys. Chem. 72 (1968) 1682–1688. https://doi.org/10.1021/j100851a051.
[37] X. Wan, I. Lieberman, A. Asyuda, S. Resch, H. Seim, P. Kirsch, M. Zharnikov, Thermal Stability of Phosphonic Acid Self-Assembled Monolayers on Alumina Substrates, J. Phys. Chem. C. 124 (2020) 2531–2542. https://doi.org/10.1021/acs.jpcc.9b10628.
[38] Y. Tang, C. Asokan, M. Xu, G.W. Graham, X. Pan, P. Christopher, J. Li, P. Sautet, Rh single atoms on TiO2 dynamically respond to reaction conditions by adapting their site, Nat. Commun. 10 (2019) 1–10. https://doi.org/10.1038/s41467-019-12461-6.
[39] H.F.J. van't Blik, T. Huizinga, J.B.A.D. van Zon, J.C. Vis, D.C. Koningsberger, R. Prins, Structure of Rhodium in an Ultradispersed Rh/Al2O3 Catalyst as Studied by EXAFS and Other Techniques, J. Am. Chem. Soc. 107 (1985) 3139–3147. https://doi.org/10.1021/ja00297a020.
[40] J.L. Robbins, Rhodium dicarbonyl sites on alumina surfaces. 1. Preparation and characterization of a model system, J. Phys. Chem. 90 (1986) 3381–3386.

https://doi.org/10.1021/j100406a016.
[41] D.A. Buchanan, M.E. Hernandez, F. Solymosi, J.M. White, CO-induced structural changes of Rh on TiO2 Support, J. Catal. 125 (1990) 456–466. https://doi.org/10.1016/0021-9517(90)90318-E.
[42] H. Guan, J. Lin, B. Qiao, S. Miao, A. Wang, X. Wang, T. Zhang, Enhanced performance of Rh $_1$ /TiO $_2$ catalyst without methanation in water-gas shift reaction, AIChE J. 63 (2017) 2081–2088. https://doi.org/10.1002/aic.15585.
[43] J.C. Matsubu, V.N. Yang, P. Christopher, Isolated metal active site concentration and stability control catalytic CO2 reduction selectivity, J. Am. Chem. Soc. 137 (2015) 3076–3084. https://doi.org/10.1021/ja5128133.
[44] Y. Kwon, T.Y. Kim, G. Kwon, J. Yi, H. Lee, Selective Activation of Methane on Single-Atom Catalyst of Rhodium Dispersed on Zirconia for Direct Conversion, J. Am. Chem. Soc. (2017). https://doi.org/10.1021/jacs.7b11010.
[45] J.T. Yates, K. Kolasinski, Infrared spectroscopic investigation of the rhodium gem-dicarbonyl surface species, J. Chem. Phys. (1983). https://doi.org/10.1063/1.445844.
[46] T.M. Duncan, J.T. Yates, R.W. Vaughan, A 13C NMR study of the adsorbed states of CO on Rh dispersed on Al203, J. Chem. Phys. (1980). https://doi.org/10.1063/1.440746.
[47] C. Asokan, L. Derita, P. Christopher, Using probe molecule FTIR spectroscopy to identify and characterize Pt - group metal based single atom catalysts, Chinese J. Catal. 38 (2017) 1473–1480. https://doi.org/10.1016/S1872-2067(17)62882-1.
[48] C. Asokan, Y. Yang, A. Dang, A. Getsoian, P. Christopher, Low-Temperature Ammonia Production during NO Reduction by CO Is Due to Atomically Dispersed Rhodium Active Sites, ACS Catal. 10 (2020) 5217–5222. https://doi.org/10.1021/acscatal.0c01249.
[49] C. Hansch, A. Leo, R.W. Taft, R.W. Hansch, Corwin; Leo, A; Taft, A Survey of Hammett Substituent Constants and Resonance and Field Parameters, Chem. Rev. 91 (1991) 165–195. https://doi.org/10.1021/cr00002a004 (accessed March 27, 2020).
[50] C. Asokan, H.V. Thang, G. Pacchioni, P. Christopher, Reductant composition influences the coordination of atomically dispersed Rh on anatase TiO2, Catal. Sci. Technol. 10 (2020) 1597–1601. https://doi.org/10.1039/d0cy00146e.
[51] S. Hanf, L.A. Rupflin, R. Gläser, S.A. Schunk, L. Alvarado Rupflin, R. Gläser, S.A. Schunk, L.A. Rupflin, R. Gläser, S.A. Schunk, Current State of the Art of the Solid Rh-Based Catalyzed Hydroformylation of Short-Chain Olefins, 10 (2020) 510. https://doi.org/10.3390/catal10050510.
[52] M. Ichikawa, A.J. Lang, D.F. Shriver, W.M.H. Sachtler, Selective hydroformylation of ethylene on rhodium-zinc-silica. An apparent example of site isolation of rhodium and Lewis acid-promoted carbonyl insertion, J. Am. Chem. Soc. 107 (2005) 7216–7218. https://doi.org/10.1021/ja00310a098.
[53] S.S.C. Chuang, S.I. Pien, Infrared spectroscopic studies of ethylene hydroformylation on Rh/SiO2: An investigation of the relationships between homogeneous and heterogeneous hydroformylation, J. Mol. Catal. (1989). https://doi.org/10.1016/0304-5102(89)80238-X.
[54] S.S.C. Chuang, R.W. Stevens, R. Khatri, Mechanism of C2+ oxygenate synthesis on Rh catalysts, Top. Catal. 32 (2005) 225–232. https://doi.org/10.1007/s11244-005-2897-2.

[55] Y. Konishi, M. Ichikawa, W.M.H. Sachtler, Hydrogenation and hydroformylation with supported rhodium catalysts. Effect of adsorbed sulfur, J. Phys. Chem. (1987). https://doi.org/10.1021/j100308a041.
[56] S.S.C. Chuang, S.I. Pien, Role of silver promoter in carbon monoxide hydrogenation and ethylene hydroformylation over Rh/SiO2 catalysts, J. Catal. (1992). https://doi.org/10.1016/0021-9517(92)90305-2.
[57] G. Pieters, L.J. Prins, Catalytic self-assembled monolayers on gold nanoparticles, New J. Chem. 36 (2012) 1931–1939. https://doi.org/10.1039/C2NJ40424A.
[58] C.N.R. Rao, G. V. Subba Rao, Electrical conduction in metal oxides, Phys. Status Solidi. 1 (1970) 597–652. https://doi.org/10.1002/pssa.19700010402.
[59] R.G. Nuzzo, F.A. Fusco, D.L. Allara, Spontaneously Organized Molecular Assemblies. 3. Preparation and Properties of Solution Adsorbed Monolayers of Organic Disulfides on Gold Surfaces, J. Am. Chem. Soc. 109 (1987) 2358–2368. https://doi.org/10.1021/ja00242a020.
[60] A. Ulman, Formation and structure of self-assembled monolayers, Chem. Rev. 96 (1996) 1533–1554. https://doi.org/10.1021/cr9502357.
[61] B. Liu, Y. Wang, N. Huang, X. Lan, Z. Xie, J.G. Chen, T. Wang, Heterogeneous hydroformylation of alkenes by Rh-based catalysts, Chem. (2022). https://doi.org/10.1016/J.CHEMPR.2022.07.020.

Chapter 5: Improving the Productivity and Stability of Atomically Dispersed Rh Catalysts for Ethylene Hydroformylation: Support Structure, Rh Weight Loading, and Promoters

5.1 INTRODUCTION

Numerous publications have demonstrated the unique reactivity of supported atomically dispersed catalysts. Some examples include:(i) in the presence of H_2O, NO_x, and CO, Rh clusters preferentially reduce NO_x to N_2 and oxidize CO to CO_2 while atomically dispersed Rh is selective towards NH_3[1], (ii) in the presence of CO_2 and H_2, Rh clusters are selective towards CH_4, while atomically disperse Rh is selective towards CO[2], (iii) atomically dispersed Au on TiO_2 was demonstrated to be several times more active for low temperature formaldehyde oxidation[3], (iv) atomically dispersed Pd was shown to be selective towards C_2H_4 in the partial hydrogenation of C_2H_2, while nanoparticles formed almost exclusively C_2H_6[4], (v) and many more.[5–11] Recently, a set of guidelines was released to help researchers contextualize the performance and sustainability of a catalyst for a particular chemical process.[12] One metric of particular relevance for atomically dispersed catalysts is reactor productivity. Specifically, novel catalysts should exhibit a productivity of at least $0.1 g/(hr \cdot cm^3)$. As this metric is on a per volume basis, the spatial density of active sites is critical to meeting this metric. In this work, "productivity" will refer to product formation rates normalized by volume, while "activity" will refer to per-site rates. Low metal loadings make many atomically dispersed catalysts uneconomical for use in industry, where the unique activity of an atomically dispersed catalyst may not be sufficient to justify the decrease in metal loading required to maintain atomic dispersion of metals.

There are challenges to increasing the loading of atomically dispersed catalysts which differ based on the metal of interest and by environmental conditions Early transition metals are highly oxophillic,[13–15] and their oxides can often maintain dispersion under relatively harsh reductive and oxidative conditions. Conversely, late transition metals are quite facilely

reduced and oxidized, such that the environment has a large impact on the dispersion and oxidation state of the metal.[8,16] Rh in particular exhibits 3 common oxidation states (0, +1, and +3) which correspond to metallic Rh, atomically dispersed Rh, and atomically dispersed Rh coordinated to oxidizing species (oxides, halides, etc.).[17,18] To maintain atomic dispersion of Rh at higher loadings, the environmental conditions must favor interactions between Rh and adsorbates that are stronger than interactions between Rh and other Rh atoms. As such, the stability of atomically dispersed catalysts is often a concern, and different strategies have been used to minimize the probability of particle growth. To maintain complete dispersion, low weight loadings are often utilized, sometimes as low as hundredths of a percent.[19–21]

Low loadings (<0.3%) of Rh on γ-Al_2O_3 have previously been demonstrated to exhibit improved selectivity towards propanal for ethylene hydroformylation (EHF, $C_2H_4 + CO + H_2 \rightarrow CH_3CH_2CHO$) compared to clusters/nanoparticles of Rh.[7,17,22,23] Despite this improved selectivity, the total activity of Rh diminished when compared to small nanoparticles,[24–28] such that the total productivity of these catalysts are low. As such, strategies to increase Rh loading and activity are necessary for catalysts to meet the guidelines for novel catalytic processes.

EHF is an ideal probe reaction for studying the stability of atomically dispersed species, as atomically dispersed Rh produces only ethane and propanal, while clusters/nanoparticles of Rh produce propanol.[25,29–31] As such, through a combination of CO probe molecule FTIR measurements, in which CO adsorbed on atomically dispersed Rh exhibits stretching frequencies distinct from CO adsorbed on Rh clusters/nanoparticles, [1,2,32–38] and EHF in

which atomically dispersed Rh exhibits unique activity, are well suited for qualitatively characterizing the dispersion of Rh as prepared and under reaction conditions.

Several reports have demonstrated means by which EHF over atomically dispersed Rh on 5nm spherical γ-Al_2O_3 can be promoted. Firstly, it was demonstrated that forming atomically dispersed Rh-ReO_x pair sites improved the activity for EHF by ~10x, with some improvement to the selectivity towards propanal. These changes were attributed to modifications in the electronic structure of Rh due to the proximity of ReO_x species.[7,39] Later, it was demonstrated that decorating the alumina surface around atomically dispersed Rh with phosphonic acid (PA) self-assembled monolayers (SAMs) improved activity by up to ~1000x and selectivity by up to ~50%. These improvements were attributed to PAs lowering the mobility, and therefore the entropy of $Rh(CO)_2$, lowering the entropic barriers for CO desorption, the initiating step in EHF.[22,23] Unfortunately, it was also observed that PA SAMs blocked a significant fraction of the Rh sites, such that catalyst productivity only increased by ~5x. Lastly, the synthesis of atomically dispersed Rh-WO_x pair sites was demonstrated to drastically improve the activity of Rh by nearly 100x, and selectivity by nearly 60%. These improvements were attributed to a change in the catalytic mechanism, in which ethylene can adsorb on WO_x, such that CO desorption is no longer necessary for the initiation of the EHF catalytic cycle. This resulted in drastic decreases in the apparent activation barrier for propanal formation (~60 kJ/mol to ~25 kJ/mol). [17]

In all of the previously discussed methodologies for improving EHF reactivity over Rh/γ-Al_2O_3, a Rh loading of 0.25% or less was used and supported on 5nm, nonporous support particles. In these works, the use of the small support assisted in maintaining dispersion by ensuring that on average, there were few Rh atoms on each support particle, such that sintering

was kinetically challenging.[8,36,37,40,41] While this approach is useful at low loadings, the converse is true at high loadings, in which having high numbers of Rh atoms on a single support particle would encourage sintering. As such, the use of a porous, tortuous support may better maintain dispersion at these higher loadings.

Here, we demonstrate a methodology by which choice of support (higher surface area mesoporous Al_2O_3) pretreatment conditions that maintain the stability of atomically dispersed species, and support modifications are used to improve the loading and stability of atomically dispersed Rh, such that atomically dispersed catalysts with loadings up to 20% Rh were synthesized and evaluated for EHF productivity. The transferability of previously demonstrated WO_x and phosphonic acid modifications to higher Rh loading, higher surface area catalysts was evaluated. Further, as previously demonstrated, modification by methylphosphonic acid (MPA) was used to improve the stability of atomically dispersed sites at elevated pressures.[42] This system portrays a unique situation, in which increasing the metal loading has little effect on the structure, and therefore the activity of a catalyst.

5.2 EXPERIMENTAL

5.2.1 Catalyst Preparation

5.2.1.1 Rh/Al_2O_3 Preparation

Catalysts consisting of Rh on Al_2O_3 were prepared via a modified strong electrostatic adsorption (SEA) approach using rhodium (III) chloride hydrate (Sigma Aldrich, 206261) as a precursor.[8,41,43] Mesoporous Al_2O_3 (Sigma Aldrich, 517747) (referred to as m-Al_2O_3) or 5 nm diameter γ-Al_2O_3 nanoparticles (US Research Nanomaterials, US3007) were used as supports. Catalysts were prepared in 1.0 g batches. Rh precursor was dissolved in 40 mL of high-performance liquid chromatography (HPLC) grade water (JT4218-3, J.T. Baker) and the

pH of the precursor solution was adjusted to a pH slightly over 10 by the addition of NH_4OH. 1.0 g of support was added to 60 mL of HPLC grade water, and the suspension was stirred well in a round-bottomed porcelain dish. The pH of the support suspension was adjusted to slightly over a pH of 10 using NH_4OH and allowed to equilibrate for 1 hour. Additional NH_4OH was added at the end of the equilibration period to bring the pH back to slightly above 10. The 40 mL precursor solution was added via syringe pump to the support solution at a rate of 40.0 mL/hour. High injections rates were required to minimize precipitation of the high-concentration precursor in the syringe during synthesis. Additional NH_4OH was added as needed throughout injection to ensure that a pH of above 10 was maintained. After injection was complete, the catalyst suspension was heated to 60°C and allowed to evaporate while maintaining stirring. Dried catalysts were placed in a 120°C oven overnight to remove residual moisture.

5.2.1.2 Phosphonic Acid Support Functionalization

PA functionalization was achieved via liquid phase condensation onto pre-prepared Rh/m-Al_2O_3 catalysts.[44] An appropriate amount (as described in detail previously[22]) of methyl PA (MPA; Sigma Aldrich 289868) was dissolved in a well stirred beaker of an appropriate volume of tetrahydrofuran (THF) (Sigma Aldrich, 401757) to form a complete self-assembled monolayer. Catalyst was added to the THF solution, and the suspension was stirred for 24 hours. The suspension was centrifuged to separate the solid catalyst and was washed with THF several times to remove physically bound PAs. The dried catalyst was then treated at 120°C in air for at least 6 hours.

5.2.1.3 Rh/W/Al_2O_3 Preparation

W was deposited onto the m-Al_2O_3 via an incipient wetness impregnation of $(NH_4)_6H_2W_{12}O_{40}\cdot xH_2O$ (Sigma Aldrich, 463922) as previously described in detail.[17,45] Samples were allowed to dry overnight at room temperature, followed by calcination at 500°C for 4 h in air. Resultant samples are referred to as xW/m-Al_2O_3, where x is the mass percentage of W in the sample.

Rh was deposited via strong electrostatic adsorption, as previously described in detail.[17] Tris(ethylenediamine) Rhodium(III) chloride (Alfa Aesar, 10553) was dissolved in 10mL of HPLC grade water, and the pH of the solution was adjusted to a just above 9.5 via dropwise addition of NH_4OH. A support suspension of xW/m-Al_2O_3 in HPLC grade water was prepared, such that the surface loading of the resultant suspension and precursor solution combined was 500 m^2/L (Equation 5.1) The pH of the support suspension was adjusted to just above 9.5 by the dropwise addition of NH_4OH under magnetic stirring in a sealed bottle. The support suspension was allowed to stir for thirty minutes. After these thirty minutes, the pH was measured again, and the pH of the support suspension was again adjusted to just above 9.5 by the dropwise addition of NH_4OH. This process was repeated until the support suspension maintained a pH above 9.5 thirty minutes after addition of NH_4OH. Once the pH of both the precursor solution have been pH adjusted, the precursor solution was added to the support suspension, and allowed to stir for at least one hour. Afterward, the suspension was vacuum filtered using a 0.45μm membrane filter and allowed to dry overnight at room temperature. Afterward the resultant sample (referred to as yRh/x/W/m-Al_2O_3, where y is the nominal Rh loading, and x is the nominal W loading before Rh deposition).

$$Surface\ Loading\ \left(\frac{m^2}{L}\right) = \frac{Surface\ Area\ of\ Support\left(\frac{m^2}{g}\right) * support\ mass\ (g)}{Total\ Volume\ of\ Solution\ (L)} \qquad (5.1)$$

5.2.2 Catalyst Characterization

5.2.2.1 Fourier-Transform Infrared Spectroscopy (FTIR)

Catalysts were loaded into a Harrick Praying Mantis low temperature reaction chamber with ZnSe windows mounted inside of a Thermo Scientific Praying Mantis diffuse reflectance adapter set inside of a Thermo Scientific Nicolet iS10 FT-IR spectrometer with a mercury cadmium telluride (MCT) detector cooled by liquid nitrogen. All samples were measured in a diffuse reflectance infrared Fourier-transform spectroscopy (DRIFTS) configuration. Before characterization, catalysts were heated to 150°C at 3°C/min in in Ar and held at 150°C for 15 minutes, and then cooled to 50°C. A background spectrum was recorded, then catalysts were heated to 150°C at 2°C/min in 10% CO in Ar and held at 150°C for 1 hours, and then cooled to 50°C. The reaction cell was purged with Ar for 10 minutes before spectra were taken. In all measurements, spectra were obtained by averaging at least scans at a resolution of 4 cm^{-1}.

5.2.2.2 Brunauer-Emmett-Teller (BET)

Support surface area was measured via nitrogen physisorption in a Micromeritics 3Flex Porosimeter. Supports were degassed at 350°C in vacuum before BET measurements.

5.2.3 Reactivity Measurements

Catalytic rates and selectivity for EHF were evaluated in a fixed-bed 316 stainless steel tube (0.26 Inch ID) in the temperature range of 100-170°C at 10 bar pressure (absolute). An ultra-high purity (UHP) grade reactant gas mixture of C_2H_4, H_2, and CO at a molar ratio of 1:1:1 was used with a total flow rate of 30 SCCM for all experiments. The CO gas was housed in an aluminum-lined cylinder to avoid potential contamination by iron and nickel carbonyls. Catalysts were diluted in purified sand (SiO_2, Sigma Aldrich, 84878) to ensure that heat and

mass transfer limitations were absent. Measurements of the influence of reaction rate on total flow rate, with constant partial pressures, evidenced no external mass transfer limitations.[7][17] Prior to reactivity measurements, catalysts were heated at 2°C/min to 150°C in 10 SSCM CO at and allowed to dwell for 1 hour. Afterward, the reactor was heated to 170°C at 1°C/min. The reaction was allowed to proceed for approximately 36 hours at ambient pressure to allow for surface bound propanal species to saturate, as previously noted for this reaction.[46] Experiments at elevated pressures were performed after the 36-hour induction period. Partial pressure dependence studies were conducted at 150°C with flow rates of the gas of interest ranging from 3-10 SCCM while balanced by argon to maintain partial pressure of other species and a total flow rate of 30 SCCM at ambient pressure. Products were quantified using an SRI Multiple Gas Analyzer #3 gas chromatographer equipped with a 3' packed alumina column in series with a MXT wax capillary column and FID detector.

5.3 RESULTS

5.3.1 Synthesis and Characterization of Rh/m-Al_2O_3

In all of the previously discussed methodologies for improving EHF reactivity over Rh/γ-Al_2O_3, a Rh loading of 0.25% or less was used and supported on 5nm, nonporous support particles. The rationale behind using this support was that isolating small amounts of Rh on each particle may make the formation of clusters kinetically difficult. However, we have consistently observed that at higher loadings (>0.5%), Rh sinters on these supports. As such, we wanted to explore the influence of support structure on maintaining atomic dispersion by comparing the previously reported results for EHF using atomically dispersed Rh on 5nm γ-Al_2O_3 (~130 m^2/g. nonporous) with a more tortuous support that might better keep Rh atoms separated. As such, the use of a mesoporous Al_2O_3 (m-Al_2O_3, ~250 m^2/g, 4 nm pore diameters) was explored.

A modified strong electrostatic adsorption approach was used to deposit atomically dispersed $RhCl_3$ onto a mesoporous alumina (m-Al_2O_3) support. This approach has previously been used to synthesize low weight loading (<0.5%) atomically dispersed Rh or Pt,[8,36,37,40,41] and while the nature of the supports in these works (non-porous, small nanoparticles) assisted in maintaining high metal dispersions at low loadings (few metal atoms per support particle, low chances of sintering), at high loadings, there are many metal atoms on the same support particle, facilitating sintering. Unlike in previous works, the synthesized Rh/m-Al_2O_3 was not calcined because Rh was observed to sinter after exposure to oxidative conditions at 350°C. Reactivity data presented later in this work suggests that removing this step had little impact on EHF activity.

0.25, 1, 2.5, 5, 10, and 20% Rh/m-Al_2O_3 catalysts were synthesized, and the atomic dispersion of the catalysts was characterized via CO probe molecule diffuse reflectance infrared Fourier-transform spectroscopy (DRIFTS). This technique has repeatedly been demonstrated to be a surface sensitive method to examine the relative abundance of surface species. Rh in particular exhibits unique stretching frequencies for atomically dispersed $Rh(CO)_2$ (a symmetric and asymmetric feature at ~2090 cm^{-1} and ~2020 cm^{-1}, respectively) and CO adsorbed linearly (~2050 cm^{-1}) or bridge-bound on Rh clusters/nanoparticles (~1800 cm^{-1}). [1,2,32–38] Thus, the sole presence of stretches associated with $Rh(CO)_2$, in combination with the reactivity presented later, are sufficient to demonstrate the predominance of atomically dispersed species.

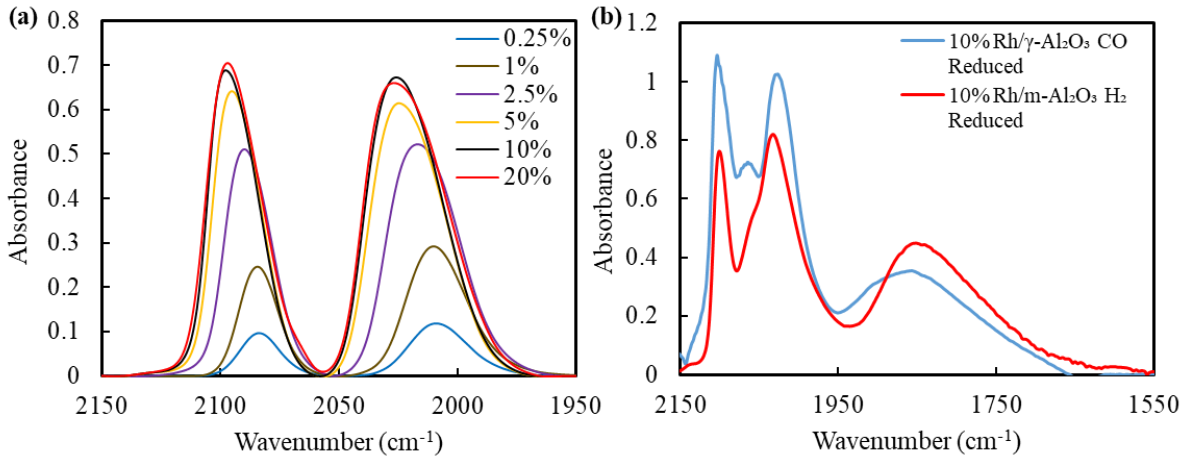

Figure 5.1: (a) Before characterization, catalysts were heated to 150°C at 3°C/min in in Ar and held at 150°C for 15 minutes, and then cooled to 50°C. A background spectrum was recorded, then catalysts were heated to 150°C at 2°C/min in 10% CO in Ar and held at 150°C for 1 hours, and then cooled to 50°C. The reaction cell was purged with Ar for 10 minutes before spectra were taken. CO probe molecule FTIR spectra of Rh/m-Al_2O_3 with 0.25, 1, 2.5, 5, 10, and 20% Rh. (b) CO probe molecule FTIR spectra of 10% Rh/m-Al_2O_3 pretreated at 100°C in H_2, and 10% Rh/γ-Al_2O_3 pretreated at 100°C in CO.

Before characterization, catalysts were heated to 150°C at 3°C/min in in Ar and held at 150°C for 15 minutes, and then cooled to 50°C. A background spectrum was recorded, then catalysts were heated to 150°C at 2°C/min in 10% CO in Ar and held at 150°C for 1 hours, and then cooled to 50°C. Slow temperature ramp rates were used to ensure that Rh species would

have more time to react with CO and form $Rh(CO)_2$ before reaching the highest temperatures (at which sintering is more likely). Once $Rh(CO)_2$ is formed, it is expected that Rh species will remain dispersed at sufficiently mild conditions, as CO has been demonstrated to disperse small Rh particles at these temperatures where CO desorption is slow.[47] The reaction cell was purged with Ar for 10 minutes before spectra were taken. Figure 1a presents FTIR spectra of 0.25, 1, 2.5, 5, 10, and 20% Rh/m-Al_2O_3. All samples exhibited only features associated with $Rh(CO)_2$, suggesting that Rh remains atomically dispersed despite the high Rh loadings. The stretch positions of $Rh(CO)_2$ blueshift to higher wavenumbers with increasing loading. Shifts in metal-carbonyl wavenumbers are often associated with changes in the electronic structure of the metal (redshifts indicate increased electron density, while blueshifts indicate decreased electron density.[34,48,49] We hypothesize that this is due to dipole coupling between adjacent $Rh(CO)_2$ species,[50] and not changes in the electronic state of Rh., as the reactivity presented later suggests that Rh electronic states are constant across all loadings. This is evidenced by the similar per-site reactivity of Rh (presented later in this document) across all Rh loadings. Dipole coupling between COs on neighboring $Rh(CO)_2$ complexes is reasonable, as $Rh(CO)_2$ surface coverages exceed 1 Rh/nm^2 at 5% or greater loading. An increase in $Rh(CO)_2$ stretch area with Rh loading is observed, but the area appears to saturate above 10% Rh. Although stretch absorbance areas in DRIFTS measurements are not usually linearly correlated with absorber concentrations due to changes in geometric and optical properties between different samples, previous reports have demonstrated positive correlations between $Rh(CO)_2$ loading and $Rh(CO)_2$ stretch area.[22,23] The range of absorbances are between ~0.1 and ~0.7, which is problematic for linear interpretations of concentrations from DRIFTS. Absorbance is linear with concentrations below ~0.4, but becomes non-linear above

those ranges.[51] This may be causing the asymptotic behavior of stretch area vs concentration that is seen here.

To demonstrate the importance of the m-Al_2O_3 support and the CO pretreatments used in Figure 5.1a, two other experiments were performed (Figure 5.1b). A 10% Rh/γ-Al_2O_3 using 5nm support particles was synthesized, and was treated with a milder, 100°C reduction in 10% CO. Despite this milder treatment, which should diminish the propensity for sintering,[40] the resulting spectra exhibits significant linear and bridge-bound CO features. This demonstrates the importance of the mesoporous support in maintaining dispersion. Interestingly, the m-Al_2O_3 only has twice the surface area of the γ-Al_2O_3, ~250 m^2/g and ~130 m^2/g, respectively. Since the 20% Rh/m-Al_2O_3 should exhibit similar Rh surface density (Rh/nm^2) to the 10% γ-Al_2O_3, this suggests that the mesoporous structure better prevents sintering than the non-porous, spherical particles beyond the role of the increased surface area. This may be due to the mesoporous geometry making Rh-Rh coordination kinetically difficult, or possibly due to sites on the support that more strongly interact with Rh (although the similar $Rh(CO)_2$ stretch positions and reactivity make this seem less likely). A 10% Rh/m-Al_2O_3 catalyst was treated at 100°C with 10% H_2, followed by exposure to CO at 50°C. This also resulted in significant linear and bridge-bound CO features, suggesting that both the use of a mesoporous alumina support, and a dispersive CO treatment at relatively slow temperature ramp rates are required to maintain atomic dispersion. It was expected that H_2 pretreatments would induce sintering, as the reductive treatment encourages the formation of metallic Rh. While CO is also a reductant, the strong coordination to two COs in $Rh(CO)_2$ encourages an incomplete reduction from Rh(III) to Rh(I).

5.3.2 Reactivity of Rh/m-Al_2O_3

Ethylene hydroformylation (EHF) was used as a probe reaction because $Rh(CO)_2$ is the most abundant surface species under EHF conditions, which should assist in maintaining the dispersion of Rh during the reaction.[7,17,22] Additionally, EHF performed on atomically dispersed Rh/Al_2O_3 has been demonstrated to produce only ethane and propanal, while nanoparticles or clusters often produce a variety of other products due to the ability of vicinal metal sites to facilitate secondary reactions. [25,29–31] Thus this reaction is suitable for evaluating the atomic dispersion and stability of Rh under reaction conditions from the absence/presence of additional products.

Despite the orders of magnitude difference in Rh content, the total mass of Rh in the reactor was managed to keep the conversion of ethylene below 0.2% to ensure differential kinetics, and to lower the likelihood of internal heat transfer limitations and thermal gradients within the reactor bed. Catalysts were loaded and heated at 2°C/min from room temperature to 150°C in 10 SCCM of semiconductor grade CO. After dwelling at 150°C for one hour, the catalyst was heated at 0.33°C/min to 170°C, at which point the catalyst was exposed to an 30 SCCM equimolar reaction mixture of CO, H_2, and C_2H_4. As previously observed,[7,17,22,23,52,53] an induction period spanning between 12 and 36 hours was observed before the catalytic behavior reached a steady state. This behavior has previously been attributed to the formation of surface aldehyde species. As such, all sample were allowed at least 36 hours of time on stream before measurements were recorded.

Reactor productivities were calculated using Equation 5.2, in which the bulk density of $Rh/m\text{-}Al_2O_3$ is approximately 0.6 g/cm^3. It is important to note that these reactor productivities

are theoretical because catalysts tested were diluted in SiO_2 for reactive characterization to avoid potential mass and heat transfer limitations.

$$Reactor\ Productivity\ \left[\frac{g}{cm^3 hr}\right] = rate\ \left[\frac{mol}{g_{cat} hr}\right] * \rho\ \left[\frac{g_{cat}}{cm^3}\right] * MW\ \left[\frac{g}{mol}\right] \qquad (5.2)$$

Where: rate=product production rate per mass of catalyst (mol/(g·hr))
ρ=bulk density of catalyst (g/cm^3)
MW= Molecular weight of product (g/mol)

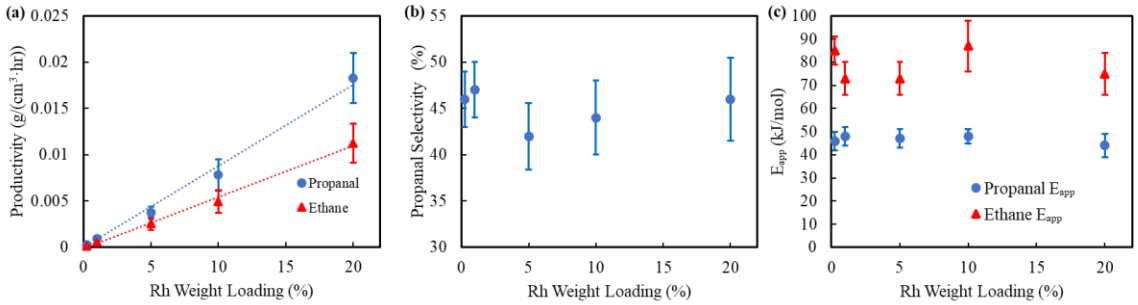

Figure 5.2: All uncertainties represent the standard error from 3 repeat experiments using samples synthesized in different batches. Prior to reactivity measurements, catalysts were heated at 2°C/min to 150°C in 10 SSCM CO at and allowed to dwell for 1 hour. Afterward, the reactor was heated to 170°C at 1°C/min. The reaction was allowed to proceed for approximately 36 hours at ambient pressure before rates, selectivities, and barriers were characterized. (a) Reactor productivity of 0.25, 1, 5, 10, and 20% Rh/m-Al_2O_3 for propanal (blue/circle) and ethane (red/triangle) at 150°C and 30 SCCM 1:1:1 H_2:CO:C_2H_4 at ambient pressure. The dashed lines are meant to illustrate a trend, not to represent recorded data. (b) Molar selectivity towards propanal of 0.25, 1, 5, 10, and 20% Rh/m-Al_2O_3 at 150°C and 30 SCCM 1:1:1 H_2:CO:C_2H_4 at ambient pressure. (c) Activation energies for propanal (blue/circle) and ethane (red/triangle) formation measured from 140-170°C and 30 SCCM 1:1:1 H_2:CO:C_2H_4 at ambient pressure.

Figure 5.2 presents the productivity, selectivity, and activation energies for 0.25, 1, 5, 10, and 20% Rh/m-Al_2O_3. At 150°C and ambient pressure, only propanal and ethane were detected, suggesting that all active Rh remained atomically dispersed. Additionally, the linear growth of catalyst formation rates, constant selectivities, and constant activation energies with Rh weight loading suggests that activity of individual Rh sites is not changing with increased loading (as would be expected for non-interacting sites), suggesting that the blueshift in Rh stretch center observed in FTIR is not representative of changes in Rh reactivity. For this reason, increasing the Rh loading from 0.25% to 20% results in an ~75x increase in

productivity. Interestingly, at the same loading, Rh/m-Al_2O_3 exhibits lower activity for ethane formation than Rh/γ-Al_2O_3 despite insignificant differences in propanal activity. This may be due to the geometry/confinement of $Rh(CO)_2$ species inside of the mesoporous material, as it has previously been suggested that ethane formation rates are sensitive to the steric environment of Rh.[39] As the energetic barriers and reaction orders (Appendix Table 5.4) are similar for both Rh/γ-Al_2O_3 and Rh/m-Al_2O_3, this suggests that differences in entropic barriers are responsible for the differences in ethane formation rates. This might be due to differences in the steric environment of $Rh(CO)_2$, as previous microkinetic modeling has suggested that ethane formation pathways can be sterically hindered.[39] The rates, selectivities, and barriers for Rh/m-Al_2O_3 are presented in Table 5.1.

Table 5.1: Tabular summary of Rh/m-Al_2O_3 reactivity. All uncertainties represent the standard error from 3 repeat experiments using samples synthesized in different batches. Prior to reactivity measurements, catalysts were heated at 2°C/min to 150°C in 10 SSCM CO at and allowed to dwell for 1 hour. Afterward, the reactor was heated to 170°C at 1°C/min. The reaction was allowed to proceed for approximately 36 hours at ambient pressure before rates, selectivities, and barriers were characterized. All rates/selectivities reported were measured at 150°C and 30 SCCM 1:1:1 H_2:CO:C_2H_4 at ambient pressure. Energetic barrier measurements were collected from 140-170°C and 30 SCCM 1:1:1 H_2:CO:C_2H_4 at ambient pressure.

Sample	Ethane Production (μmol/(g·hr))	Propanal Production (μmol/(g·hr))	Ethane Production $(g/c(m^3 \cdot hr)) \cdot 10^{-4}$	Propanal Production $(g/(cm^3 \cdot hr)) \cdot 10^{-4}$	Molar Selectivity (%)	Ethane Eapp (kJ/mol)	Propanal Eapp (kJ/mol)
0.25% Rh/γ-Al_2O_3	17±2	7±1	3.0±0.4	2.0±0.3	30±3	80±10	46±4
0.25% Rh/m-Al_2O_3	8±2	7±1	1.4±0.3	2.4±0.3	46±3	85±6	45±3
1% Rh/m-Al_2O_3	32±7	28±5	6±1	9.7±1.6	47±3	73±7	48±4
5% Rh/m-Al_2O_3	141±39	107±19	25±7	37±6	42±5	73±7	47±4
10% Rh/m-Al_2O_3	272±68	224±49	49±12	78±16	44±4	87±11	48±3
20% Rh/m-Al_2O_3	622±117	524±78	112±21	180±30	46±5	75±9	44±5

Despite the ~75x increase in production rates due to increased Rh loading, the resulting catalyst is still significantly below the desired productivity of 0.1 $g/(hr \cdot cm^3)$. Previous works

have demonstrated that the activity and selectivity for EHF over Rh/γ-Al_2O_3 benefits from increased total reaction pressure.[17,23] Unfortunately, all loadings of Rh/m-Al_2O_3 were observed to begin forming propanol and other side products at elevated pressures (by 2.5 bar), suggesting Rh sintering. Chromatograms with and without the presence of propanol are presented in the Appendix as Figure 5.6. To further improve the productivity of Rh, the stability, activity, or both need to be improved. As such, we attempt to apply methodologies that have previously been demonstrated to improve the stability and activity of atomically dispersed Rh/γ-Al_2O_3 catalysts under EHF conditions at low Rh loadings, to this high Rh loading system.

5.3.3 Rh/W/m-Al_2O_3

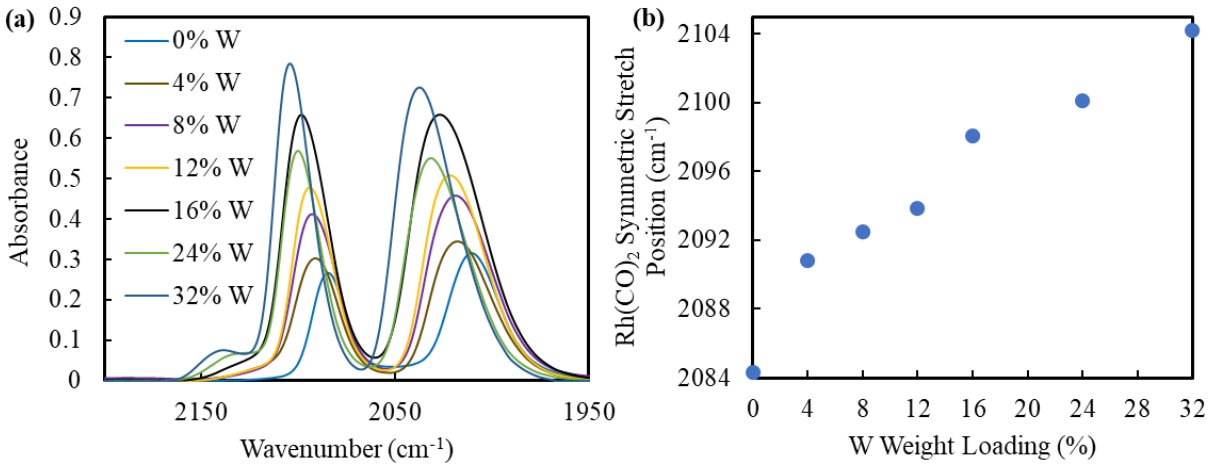

Figure 5.3: (a) Before characterization, catalysts were heated to 150°C at 3°C/min in in Ar and held at 150°C for 15 minutes, and then cooled to 50°C. A background spectrum was recorded, then catalysts were heated to 150°C at 2°C/min in 10% CO in Ar and held at 150°C for 1 hours, and then cooled to 50°C. The reaction cell was purged with Ar for 10 minutes before spectra were taken. CO probe molecule FTIR spectra of 1Rh/xW/m-Al_2O_3 with 0, 4, 8, 12, 16, 24, and 32% W. (b) Symmetric stretch position of $Rh(CO)_2$ on 1Rh/xW/m-Al_2O_3 as a function of W loading. The increase in wavenumber suggests that W is decreasing the electron density of Rh.

Previously, the deposition of atomically dispersed Rh onto γ-Al_2O_3 carrying atomically dispersed WO_x was used to synthesize Rh-W pair sites, facilitating a lower barrier pathway for propanal formation.[17] The resultant catalyst (0.25% Rh/1%W/γ-Al_2O_3) exhibited increased

activity, selectivity, and improved stability under EHF conditions, and was capable of maintaining atomic dispersion at higher pressures than unmodified Rh/γ-Al_2O_3. As such, forming Rh-W pair sites on m-Al_2O_3 may allow for high loadings of Rh with improved activity, selectivity, and stability.

W/m-Al_2O_3 at 0, 4, 8, 16, 24, and 32% W was synthesized via an incipient wetness method using $(NH_4)_6H_2W_{12}O_{40}$ as the tungsten precursor, followed by a calcination in air at 500°C. Afterward, tris(ethylenediamine) Rhodium(III) chloride was deposited using strong electrostatic adsorption as previously described in great detail. [17] The Rh concentration during synthesis was chosen such that the final catalyst was nominally 1% Rh/xW/Al_2O_3. 4% W was chosen as the lowest W in order to have a ~2:1 W:Rh ratio, as the previous work demonstrated that ratio resulted in the formation of the Rh-W pair sites.

Using the same procedure as for Rh/m-Al_2O_3, CO probe molecule FTIR experiments were performed for all 1% Rh/xW/m-Al_2O_3 samples for (Figure 5.3). In the previous work, 0.25% Rh/xW/γ-Al_2O_3 was examined, in which the $Rh(CO)_2$ stretches were observed to blueshift (>20 cm^{-1}) with increased W loading up until 2% W, at which point further increasing the W loading did not result in further shifts in wavenumber. This behavior was attributed to all Rh interacting with W at 2% W, such that adding additional W did not increase Rh-W interactions, despite changes in the structure of WO_x with increase W loading. Unlike in that case, smaller shifts in the stretch positions are observed for 1% Rh/4%W/m-Al_2O_3 (~7 cm^{-1}), and the stretch continues to blueshift with increased W loading, even up to 32%. This suggests that increased Rh-W interactions are occurring even when a large excess of W exists relative to Rh. This behavior is not explained by the increased surface area of the m-Al_2O_3 (~250 m^2/g) compared to the γ-Al_2O_3 (~130 m^2/g) leading to lower W densities, as several times the W

loading was used. This may suggest an uneven distribution of Rh and W within the porous catalyst particles. Additionally, the $Rh(CO)_2$ stretch area increases with increased W loading. This may be due to changes in the extinction coefficient of CO as the electronic state of Rh is modified, changes in the uptake of Rh during strong electrostatic adsorption, or both. Another feature of note is the appearance of a stretch around 2140 cm^{-1} at higher W loadings. This feature has previously been attributed to a Rh(CO) species in which Rh is coordinated to an additional oxygen.[54] In the previous work, this feature only appeared for the 1 and 2% W samples, which were the samples that were hypothesized to have formed the Rh-W pair sites. As such, the appearance of this feature may be indicative of further Rh-W interactions.

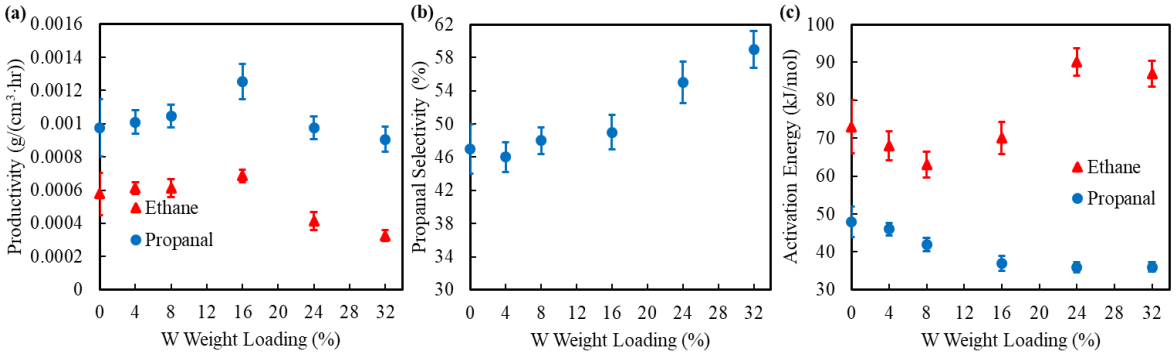

Figure 5.4: Prior to reactivity measurements, catalysts were heated at 2°C/min to 150°C in 10 SSCM CO at and allowed to dwell for 1 hour. Afterward, the reactor was heated to 170°C at 1°C/min. The reaction was allowed to proceed for approximately 36 hours at ambient pressure before rates and selectivites were characterized. (a) (blue/circle) Product formation rates of 1% Rh/xW/m-Al_2O_3 with 0, 4, 8, 16, 24, and 32% W at 170°C and 30 SCCM 1:1:1 H_2:CO:C_2H_4 at ambient pressure. (black/diamond) Reactor productivity of 2.5 and 5% Rh/MPA/m-Al_2O_3 at 170°C and 30 SCCM 1:1:1 H_2:CO:C_2H_4 at 10bar. (b) (blue/circle) Molar selectivity towards propanal of 0.25, 1, 5, 10, and 20% Rh/m-Al_2O_3 at 150°C and 30 SCCM 1:1:1 H_2:CO:C_2H_4 at ambient pressure. (black/diamond) Selectivity towards propanal of 2.5 and 5% Rh/MPA/m-Al_2O_3 at 150°C and 30 SCCM 1:1:1 H_2:CO:C_2H_4 at 10bar.(c) Activation energies for propanal (blue/circle) and ethane (red/triangle) formation measured from 140-170°C and 30 SCCM 1:1:1 H_2:CO:C_2H_4 at ambient pressure.

The reactivity of synthesized 1%Rh/xW/m-Al_2O_3 catalysts was characterized in an identical manner to the Rh/m-Al_2O_3 catalysts (Figure 5.4). Unlike what was observed for the previous work (order of magnitude increases in activity), the presence of 8% or less W has an insignificant effect on any characterized metric. At higher W loadings, a decrease in the

activation energy for propanal formation is observed, corresponding to an increased selectivity towards propanal. This coincided with an increase in energetic barriers for ethane formation, and a decrease in ethane formation rate, but the propanal formation rates stayed constant. After characterizing the reactivity of the 1% Rh/xW/Al_2O_3 catalysts at ambient pressure, the pressure was raised to 2.5 bar. Samples with 8% or more W exhibited increased stability with pressure, and remained atomically dispersed at 2.5 bar, but all Rh/W/m-Al_2O_3 samples exhibited evidence of sintering by 5 bar. A summary of Rh/W/m-Al_2O_3 reactivity is presented as Table 5.2.

There was no W loading at which the catalytic behavior was consistent with the formation of Rh-W pair sites that was previously observed. In that work, more than an order of magnitude increase in formation rates was observed at W loadings consistent with Rh-W pair site formation, and energetic barriers were lowered to <30 kJ/mol for propanal formation. Despite the observed shifts in $Rh(CO)_2$ stretch areas indicating a change in the electronic structure of Rh, which has previously been demonstrated to significantly alter Rh/γ-Al_2O_3 reactivity for EHF,[7] very little effect is observed from the addition of Rh. We hypothesize that same support characteristics that allow for high weight loadings of Rh to remain atomically dispersed on m-Al_2O_3, also provides hindrances to the formation of Rh-W pair sites. The constant propanal formation rate with increased W loading despite a decrease in activation barriers merits further discussion. It is likely that at higher W loadings, there exists large, three dimensional WO_x structures on which Rh may be coordinated to. These WOx structures are known to decorate/encapsulate active metals via SMSI under reductive conditions,[55] as such, we hypothesize that any increase in Rh activity due to WO_x is offset by a loss in active sites

Despite the promise of these modifications for stabilizing and improving the activity or Rh/m-Al_2O_3, it was synthetically difficult to ensure that all Rh was interacting with WO_x on the mesoporous alumina support, such that the expected improvements in catalytic behavior were unrealized. As such, a different methodology for improving the stability of atomically dispersed Rh is required. The negative result using W modification suggests that well-defined modifications (such as forming distinct pair sites) may be synthetically challenging in this system. As such, a more homogeneous modification to the catalyst might be favorable.

Table 5.2: Tabular summary of Rh/W/m-Al_2O_3 reactivity. Rh loadings are nominal. All uncertainties represent the standard error of at least 3 data points at that condition (for activities/selectivities) or the standard error of the linear regression (for activation energies). Prior to reactivity measurements, catalysts were heated at 2°C/min to 150°C in 10 SSCM CO at and allowed to dwell for 1 hour. Afterward, the reactor was heated to 170°C at 1°C/min. The reaction was allowed to proceed for approximately 36 hours at ambient pressure before rates, selectivities, and barriers were characterized. All rates/selectivities reported were measured at 150°C and 30 SCCM 1:1:1 H_2:CO:C_2H_4 at ambient pressure. Energetic barrier measurements were collected from 140-170°C and 30 SCCM 1:1:1 H_2:CO:C_2H_4 at ambient pressure.

Sample	Ethane Production (µmol/(g·hr))	Propanal Production (µmol/(g·hr))	Ethane Production (g/(cm^3·hr))·10^{-4}	Propanal Production (g/(cm^3·hr))·10^{-4}	Molar Selectivity (%)	Ethane Ea (kJ/mol)	Propanal Ea (kJ/mol)
1% Rh/m-Al_2O_3	32±7	28±5	6±1	9.7±1.6	47±3	73±7	48±4
1% Rh/4%W/m-Al_2O_3	34±2	29±2	6.1±0.3	10±1	46±2	68±4	46±2
1% Rh/8%W/m-Al_2O_3	34±3	30±2	6.1±0.5	10±1	48±2	63±3	42±2
1% Rh/16%W/m-Al_2O_3	38±2	36±2	6.9±0.3	12±1	49±2	70±4	37±2
1% Rh/24%W/m-Al_2O_3	23±3	28±2	4.1±0.5	9.8±0.7	55±3	90±4	36±1
1% Rh/32%W/m-Al_2O_3	18±2	26±3	3.3±0.3	9.1±0.8	59±2	87±3	36±1

5.3.4 Rh/MPA/m-Al_2O_3

An alternative means of stabilizing atomically dispersed Rh/Al_2O_3 has been to decorate the support surrounding Rh with phosphonic acids (PAs).[42] It was observed that Rh exhibited less sintering under reductive conditions when Rh/γ-Al_2O_3 was decorated with methylphosphonic acid (MPA). Additionally, it was observed that decorating atomically dispersed Rh/γ-Al_2O_3 with MPA (resulting samples referred to as Rh/MPA/γ-Al_2O_3) improved the activity and selectivity under EHF conditions by modifying mobility of $Rh(CO)_2$ on the alumina surface.[23] As such, this modification may improve the stability and activity of Rh/m-Al_2O_3 Importantly, the deposition of MPA forms a self-assembled monolayer (SAM), such that the Al_2O_3 surface should be uniformly (support and monolayer defects not withstanding) modified. This should help avoid the problems of uneven distribution of Rh and modifiers that was encountered with Rh/W/m-Al_2O_3 system.

Rh/MPA/m-Al_2O_3 was synthesized by first synthesizing the desired weight loading of Rh/m-Al_2O_3, followed by the deposition of MPA onto the support. MPA deposition was performed through liquid phase condensation onto surface hydroxyls of Rh/m-Al_2O_3. An excess of MPA was used to fully saturate the catalyst surface. MPA is a suitable anchoring group to m-Al_2O_3 for this reaction as it exhibits high stability at elevated temperatures in inert and reducing environments.[56]

Using the same procedure as for Rh/m-Al_2O_3, CO probe molecule FTIR experiments were performed for 2.5, 5, and 10% Rh/MPA/m-Al_2O_3 (Figure 5.5a). All samples exhibited only features associated with $Rh(CO)_2$, suggesting that Rh remains atomically dispersed. As observed with the Rh/m-Al_2O_3 samples, $Rh(CO)_2$ stretch areas increase slightly with increased loading, but above 2.5% Rh, increases are minimal. The $Rh(CO)_2$ stretch positions blueshift

less with Rh loading on the MPA modified catalyst, than the unmodified catalyst. If this shift is due to dipole coupling, then this suggests that the presence of MPA is screening some of those interactions. It should be noted that in the previous study, approximately 65% of Rh on 0.25% Rh/γ-Al_2O_3 was inaccessible to CO (and therefore not visible in FTIR or catalytically active), but improvements in turnover frequencies of the remaining sites still resulted in improvements rates per gram of catalyst.[23]

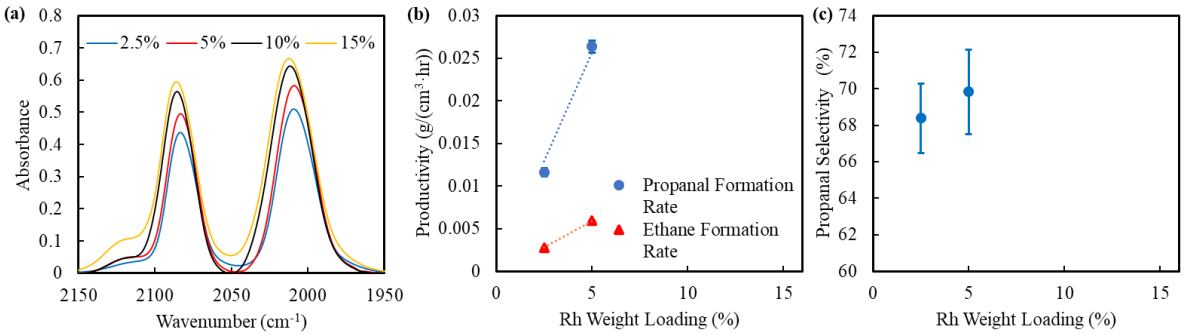

Figure 5.5: (a) Before characterization, catalysts were heated to 150°C at 3°C/min in in Ar and held at 150°C for 15 minutes, and then cooled to 50°C. A background spectrum was recorded, then catalysts were heated to 150°C at 2°C/min in 10% CO in Ar and held at 150°C for 1 hours, and then cooled to 50°C. The reaction cell was purged with Ar for 10 minutes before spectra were taken. CO probe molecule FTIR spectra of 2.5, 5, and 10% Rh/MPA/m-Al_2O_3. The dashed lines are meant to illustrate a trend, not to represent recorded data. (b and c) Prior to reactivity measurements, catalysts were heated at 2°C/min to 150°C in 10 SSCM CO at and allowed to dwell for 1 hour. Afterward, the reactor was heated to 170°C at 1°C/min. The reaction was allowed to proceed for approximately 36 hours at ambient pressure. Afterward, kinetic barriers were characterized, and then the total pressure was increased from 1 to 10 bar before rates and selectivities were measured. All uncertainties represent the standard error of at least 3 data points at that condition. (b) Product formation rates for 2.5 and 5% Rh/MPA/m-Al_2O_3 at 150°C and 30 SCCM 1:1:1 H_2:CO:C_2H_4 at 10 bar. (c) Selectivity towards propanal for 2.5 and 5% Rh/MPA/m-Al_2O_3 at 150°C and 30 SCCM 1:1:1 H_2:CO:C_2H_4 at 10 bar.

The reactivity of 2.5 and 5% Rh/MPA/m-Al_2O_3 catalysts was characterized in an identical manner to the Rh/m-Al_2O_3 catalysts (Figure 5.5), except after characterization at ambient pressure, the pressure was increased in increments of 2.5 bar, up to 10 bar. 10% and 15% Rh/MPA/m-Al_2O_3 will be evaluated at a future date. Rates, selectivities, and kinetic barriers for all Rh/MPA/m-Al_2O_3 samples can be found in Table 5.3. Evaluated Rh/MPA/m-Al_2O_3 samples exhibited no propanol formation up to 10 bar total pressure, suggesting that modification with MPA successfully stabilized atomically dispersed $Rh(CO)_2$. At 10 bar and

150°C, Rh/MPA/m-Al_2O_3 catalysts exhibit ~7x the propanal formation rate of the same loading of Rh/MPA/m-Al_2O_3 at ambient pressure, while only exhibiting ~2.4x as much ethane formation. These enhancements in rates are consistent with the reaction orders measured at ambient pressure for Rh/m-Al_2O_3 (Appendix Table 5.4), which suggest that, at least initially, propanal formation rates should scale as ~$P^{1.1}$ while ethane formation rates should scale as $P^{0.3}$. The rates likely scale with pressure less than the initial reaction orders predict because the CO reaction order becomes more negative at higher pressures.[17,23] This resulted in an increase in selectivities towards propanal. Activation energies for Rh/MPA/m-Al_2O_3 were not significantly different than activation energies for Rh/m-Al_2O_3, consistent with previous work demonstrating changes solely to entropic barriers due to PA deposition.

Interestingly, the enhancement in per gram rates that were previously observed due to the presence of MPA seem absent in this system, and increased pressure is likely responsible for all increase in product formation rates. We hypothesize that this is due to the already constrained state of $Rh(CO)_2$ on high loading Rh/m-Al_2O_3 (as evidenced by the presence of dipole coupling in FTIR), such that the addition of MPA does not have as large of an impact on the mobility/entropy of $Rh(CO)_2$ species in this system than occurred in the 0.25% Rh/γ-Al_2O_3 system. While this does mean that modification with MPA was less impactful than expected, the stabilization of atomically dispersed species was the primary goal of this modification and was successful.

Table 5.3: Tabular summary of Rh/W/m-Al_2O_3 reactivity. All uncertainties represent the standard error of at least 3 data points at that condition (for activities/selectivities) or the standard error of the linear regression (for activation energies). Prior to reactivity measurements, catalysts were heated at 2°C/min to 150°C in 10 SSCM CO at and allowed to dwell for 1 hour. Afterward, the reactor was heated to 170°C at 1°C/min. The reaction was allowed to proceed for approximately 36 hours at ambient pressure. Afterward, the total pressure was increased from 1 to 10 bar before rates and selectivities were measured. All rates/selectivities reported were measured at 150°C and 30 SCCM 1:1:1 H_2:CO:C_2H_4 at 10 bar. Energetic barrier measurements were collected from 140-170°C and 30 SCCM 1:1:1 H_2:CO:C_2H_4 at ambient pressure.

Sample	Ethane Production (μmol/(g·hr))	Propanal Production (μmol/(g·hr))	Ethane Production $(g/(cm^3 \cdot hr)) \cdot 10^{-3}$	Propanal Production $(g/(cm^3 \cdot hr)) \cdot 10^{-3}$	Molar Selectivity (%)	Ethane Eapp (kJ/mol)	Propanal Eapp (kJ/mol)
2.5% Rh/MPA/m-Al_2O_3	154±7	334±14	2.7±0.1	12±1	68±2	80±3	41±2
5% Rh/MPA/m-Al_2O_3	327±15	757±23	10.1±0.3	26±2	70±2	83±3	43±2

5.3.5 Outlook

While experimental verification is necessary, a 15% Rh/MPA/Al_2O_3 would theoretically meet the proposed productivity metric of 0.1 $g/(cm^3 \cdot hr)$. It is important to note that this study exclusively evaluated catalysts at low conversions, and that as an exothermic reaction, local heating may change the reactivity and stability of these catalyst. As such, while these systems may represent a useful starting point, further study and optimization is required. The uniform addition of promoters to induce a more positive charge on Rh, in combination with the MPA modification may allow for more active and selective catalysts and lower Rh loadings, but this may be synthetically difficult.

5.4 CONCLUSION

In conclusion, we have examined a system in which the choice of support, support modifications, and pretreatment/reaction conditions allow for the maintenance of atomic dispersion on catalysts up to 20% Rh by weight on a mesoporous alumina (m-Al_2O_3). Product formation rates grew linearly with Rh content, suggesting that the structure and reactivity of Rh was not changing with total Rh loading, consistent with atomically dispersed active sites. Unmodified Rh/m-Al_2O_3 samples were unstable at elevated reaction pressures, such that additional support modifications were required. Two successful modifications from literature, support modification with either W or methylphosphonic acid (MPA), were applied to this system in an attempt to improve stability at higher pressures. Despite the previous success at lower Rh loadings, the W modification was unable to selectively form the Rh-W pair sites at higher loadings. As such, it was concluded that it is synthetically difficult to ensure that high loadings of W and Rh are distributed equally such that the specific Rh-W interactions can be uniformly applied. Modification with MPA was not reliant on specific interactions, and the uniform application of self-assembled monolayers made this approach more synthetically feasible. Although MPA modification did not enhance rates in the manner that was expected, it successfully stabilized dispersed Rh species at higher pressures, allowing for improved product formation rates and selectivities. While experimental verification is necessary, a 15% Rh/MPA/Al_2O_3 would theoretically meet the proposed productivity metric of 0.1 g/(cm^3·hr), and further use of promoters may allow for more active and selective catalysts.

5.5 APPENDIX

Table 5.4: Reaction orders calculated for 0.25% Rh/γ-Al_2O_3 and 0.25% Rh/m-Al_2O_3 at 150°C and ambient pressure. Uncertainties represent the standard error from at least 3 repeat experiments using batches of catalyst synthesized separately.

Sample	Product	CO Order	C2H4 Order	H2 Order
0.25% Rh/γ-Al_2O_3	Ethane	-1.3±0.1	0.6±0.1	0.9±0.1
	Propanal	-0.6±0.1	0.8±0.1	0.8±0.1
0.25% Rh/m-Al_2O_3	Ethane	-1.4±0.1	0.7±0.1	1±0.1
	Propanal	-0.7±0.1	0.9±0.1	0.9±0.1

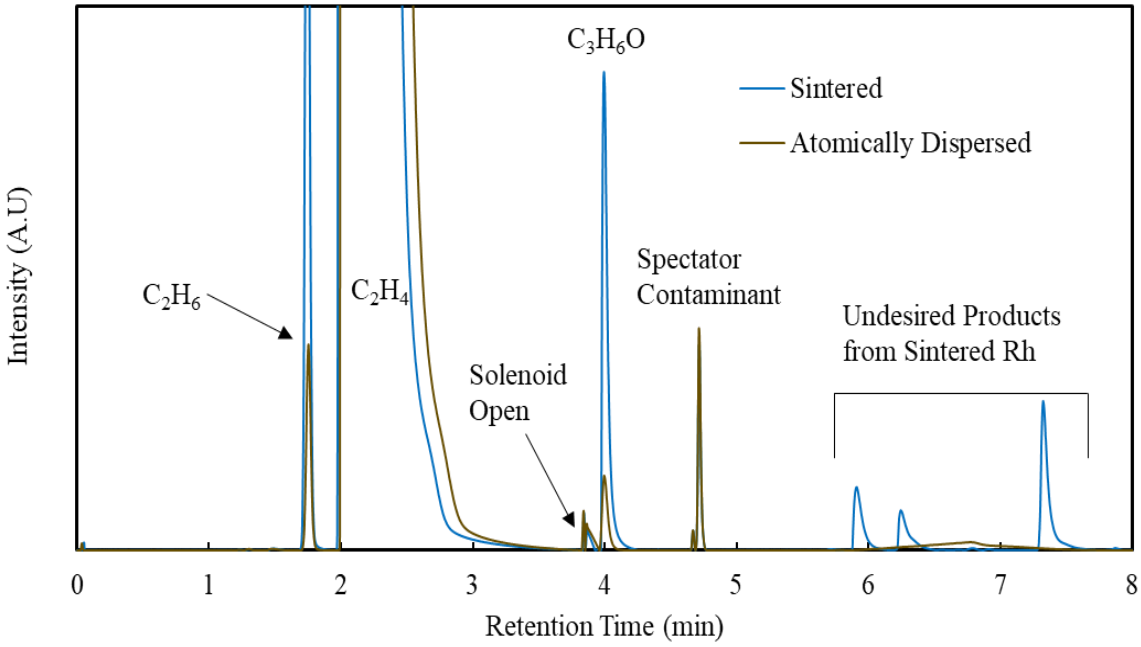

Figure 5.5: Example chromatogram of products from 5% Rh/m-Al_2O_3 at 150°C 30 SCCM 1:1:1 H_2:CO:C_2H_4 at 2.5 bar (Blue/Sintered). Example chromatogram of products from 5% Rh/m-Al_2O_3 at 150°C 30 SCCM 1:1:1 H_2:CO:C_2H_4 at 1 bar (Black/Atomically Dispersed).

5.6 REFERENCES

[1] C. Asokan, Y. Yang, A. Dang, A. Getsoian, P. Christopher, Low-Temperature Ammonia Production during NO Reduction by CO Is Due to Atomically Dispersed Rhodium Active Sites, ACS Catal. 10 (2020) 5217–5222. https://doi.org/10.1021/acscatal.0c01249.

[2] J.C. Matsubu, V.N. Yang, P. Christopher, Isolated metal active site concentration and stability control catalytic CO2 reduction selectivity, J. Am. Chem. Soc. 137 (2015) 3076–3084. https://doi.org/10.1021/ja5128133.

[3] Huixia Li, Shaofan Fang, Guimin Jiang, Zuotai Zhang, Enhanced oxygen activation on an atomically dispersed Au catalyst with dual active sites for room-temperature formaldehyde oxidation, Environ. Sci. Nano. 10 (2023) 80–91. https://doi.org/10.1039/D2EN00805J.

[4] F. Huang, Y. Deng, Y. Chen, X. Cai, M. Peng, Z. Jia, P. Ren, D. Xiao, X. Wen, N. Wang, H. Liu, D. Ma, Atomically Dispersed Pd on Nanodiamond/Graphene Hybrid for Selective Hydrogenation of Acetylene, J. Am. Chem. Soc. 140 (2018) 13142–13146. https://doi.org/10.1021/jacs.8b07476.

[5] J. Resasco, F. Yang, T. Mou, B. Wang, P. Christopher, D.E. Resasco, Relationship between Atomic Scale Structure and Reactivity of Pt Catalysts: Hydrodeoxygenation of m-Cresol over Isolated Pt Cations and Clusters, ACS Catal. 10 (2020) 595–603. https://doi.org/10.1021/acscatal.9b04330.

[6] M.T. Darby, M. Stamatakis, A. Michaelides, E.C.H. Sykes, Lonely Atoms with Special Gifts: Breaking Linear Scaling Relationships in Heterogeneous Catalysis with Single-Atom Alloys, J. Phys. Chem. Lett. (2018). https://doi.org/10.1021/acs.jpclett.8b01888.

[7] I. Ro, M. Xu, G.W. Graham, X. Pan, P. Christopher, Synthesis of Heteroatom Rh-ReOx Atomically Dispersed Species on Al2O3 and Their Tunable Catalytic Reactivity in Ethylene Hydroformylation, ACS Catal. 9 (2019) 10899–10912. https://doi.org/10.1021/acscatal.9b02111.

[8] L. DeRita, J. Resasco, S. Dai, A. Boubnov, H.V. Thang, A.S. Hoffman, I. Ro, G.W. Graham, S.R. Bare, G. Pacchioni, X. Pan, P. Christopher, Structural evolution of atomically dispersed Pt catalysts dictates reactivity, Nat. Mater. (2019). https://doi.org/10.1038/s41563-019-0349-9.

[9] B.C. Gates, Atomically Dispersed Supported Metal Catalysts: Seeing Is Believing, Trends Chem. 1 (2019) 99–110. https://doi.org/10.1016/J.TRECHM.2019.01.004.

[10] E.J. Peterson, A.T. DeLaRiva, S. Lin, R.S. Johnson, H. Guo, J.T. Miller, J.H. Kwak, C.H.F. Peden, B. Kiefer, L.F. Allard, F.H. Ribeiro, A.K. Datye, Low-temperature carbon monoxide oxidation catalysed by regenerable atomically dispersed palladium on alumina, Nat. Commun. (2014). https://doi.org/10.1038/ncomms5885.

[11] X. Xue, Y. Song, Y. Xu, Y. Wang, High-performance and long-lived Rh nanocatalyst for hydroformylation of styrene, New J. Chem. (2018). https://doi.org/10.1039/C8NJ00447A.

[12] J.P. Lange, Performance metrics for sustainable catalysis in industry, Nat. Catal. 4 (2021) 186–192. https://doi.org/10.1038/s41929-021-00585-2.

[13] K.A. Moltved, K.P. Kepp, The chemical bond between transition metals and Oxygen: Electronegativity, d-Orbital Effects, and Oxophilicity as Descriptors of Metal-Oxygen Interactions, J. Phys. Chem. C. 123 (2019) 18432–18444.

https://doi.org/10.1021/ACS.JPCC.9B04317/ASSET/IMAGES/LARGE/JP-2019-043179_0005.JPEG.
[14] H.S. Lacheen, P.J. Cordeiro, E. Iglesia, Isolation of rhenium and ReO x species within ZSM5 channels and their catalytic function in the activation of alkanes and alkanols, Chem. - A Eur. J. (2007). https://doi.org/10.1002/chem.200601602.
[15] S.R. Bare, S.D. Kelly, F. D.vila, E. Boldingh, E. Karapetrova, J. Kas, G.E. Mickelson, F.S. Modica, N. Yang, J.J. Rehr, Experimental (XAS, STEM, TPR, and XPS) and theoretical (DFT) characterization of supported rhenium catalysts, J. Phys. Chem. C. (2011). https://doi.org/10.1021/jp1105218.
[16] C. Asokan, H.V. Thang, G. Pacchioni, P. Christopher, Reductant composition influences the coordination of atomically dispersed Rh on anatase TiO2, Catal. Sci. Technol. 10 (2020) 1597–1601. https://doi.org/10.1039/d0cy00146e.
[17] I. Ro, J. Qi, S. Lee, M. Xu, X. Yan, Z. Xie, G. Zakem, A. Morales, J.G. Chen, X. Pan, D.G. Vlachos, S. Caratzoulas, P. Christopher, Bifunctional hydroformylation on heterogeneous Rh-WOx pair site catalysts, Nat. 2022 6097926. 609 (2022) 287–292. https://doi.org/10.1038/s41586-022-05075-4.
[18] E.K. Schroeder, J. Finzel, P. Christopher, Photolysis of Atomically Dispersed Rh/Al2O3 Catalysts: Controlling CO Coverage in Situ and Promoting Reaction Rates, J. Phys. Chem. C. (2022). https://doi.org/10.1021/ACS.JPCC.2C04642.
[19] F. Zaera, Designing Sites in Heterogeneous Catalysis: Are We Reaching Selectivities Competitive with Those of Homogeneous Catalysts?, Chem. Rev. (2021). https://doi.org/10.1021/acs.chemrev.1c00905.
[20] R. Lang, T. Li, D. Matsumura, S. Miao, Y. Ren, Y.T. Cui, Y. Tan, B. Qiao, L. Li, A. Wang, X. Wang, T. Zhang, Hydroformylation of Olefins by a Rhodium Single-Atom Catalyst with Activity Comparable to RhCl(PPh3)3, Angew. Chemie - Int. Ed. 55 (2016) 16054–16058. https://doi.org/10.1002/anie.201607885.
[21] Z. Zhang, H. Li, D. Wu, L. Zhang, J. Li, J. Xu, S. Lin, A.K. Datye, H. Xiong, Coordination structure at work: Atomically dispersed heterogeneous catalysts, Coord. Chem. Rev. 460 (2022) 214469. https://doi.org/10.1016/J.CCR.2022.214469.
[22] G. Zakem, I. Ro, J. Finzel, P. Christopher, Support functionalization as an approach for modifying activation entropies of catalytic reactions on atomically dispersed metal sites, J. Catal. (2021). https://doi.org/10.1016/j.jcat.2021.07.030.
[23] G. Zakem, P. Christopher, Active Site Entropy of Atomically Dispersed Rh/Al2O3 Catalysts Dictates Activity for Ethylene Hydroformylation, ACS Catal. (2023).
[24] S.S.C. Chuang, G. Srinivas, A. Mukherjee, Infrared studies of the interactions of C2H4 and H2 with Rh+(CO)2 and CO adsorbed on RhCl3/SiO2 and Rh(NO3)3/SiO2, J. Catal. 139 (1993) 490–503. https://doi.org/10.1006/jcat.1993.1043.
[25] S.S.C. Chuang, R.W. Stevens, R. Khatri, Mechanism of C2+ oxygenate synthesis on Rh catalysts, Top. Catal. 32 (2005) 225–232. https://doi.org/10.1007/s11244-005-2897-2.
[26] S.S.C. Chuang, S.I. Pien, Infrared study of the CO insertion reaction on reduced, oxidized, and sulfided Rh/SiO2 catalysts, J. Catal. 135 (1992) 618–634. https://doi.org/10.1016/0021-9517(92)90058-P.
[27] M.W. Balakos, S.S.C. Chuang, Transient response of propionaldehyde formation during CO/H2/C2H4 reaction on Rh/SiO2, J. Catal. 151 (1995) 253–265. https://doi.org/10.1006/jcat.1995.1026.

[28] S.M. McClure, M.J. Lundwall, D.W. Goodman, Planar oxide supported rhodium nanoparticles as model catalysts, Proc. Natl. Acad. Sci. (2011). https://doi.org/10.1073/pnas.1006635107.
[29] S.S.C. Chuang, S.I. Pien, Infrared spectroscopic studies of ethylene hydroformylation on Rh/SiO2: An investigation of the relationships between homogeneous and heterogeneous hydroformylation, J. Mol. Catal. (1989). https://doi.org/10.1016/0304-5102(89)80238-X.
[30] Y. Konishi, M. Ichikawa, W.M.H. Sachtler, Hydrogenation and hydroformylation with supported rhodium catalysts. Effect of adsorbed sulfur, J. Phys. Chem. (1987). https://doi.org/10.1021/j100308a041.
[31] S.S.C. Chuang, S.I. Pien, Role of silver promoter in carbon monoxide hydrogenation and ethylene hydroformylation over Rh/SiO2 catalysts, J. Catal. (1992). https://doi.org/10.1016/0021-9517(92)90305-2.
[32] Y. Kwon, T.Y. Kim, G. Kwon, J. Yi, H. Lee, Selective Activation of Methane on Single-Atom Catalyst of Rhodium Dispersed on Zirconia for Direct Conversion, J. Am. Chem. Soc. (2017). https://doi.org/10.1021/jacs.7b11010.
[33] J.T. Yates, K. Kolasinski, Infrared spectroscopic investigation of the rhodium gem-dicarbonyl surface species, J. Chem. Phys. (1983). https://doi.org/10.1063/1.445844.
[34] J.T. Yates, T.M. Duncan, S.D. Worley, R.W. Vaughan, Infrared spectra of chemisorbed CO on Rh, J. Chem. Phys. (1979). https://doi.org/10.1063/1.437603.
[35] T.M. Duncan, J.T. Yates, R.W. Vaughan, A 13C NMR study of the adsorbed states of CO on Rh dispersed on Al203, J. Chem. Phys. 73 (1980) 975. https://doi.org/10.1063/1.440746.
[36] C. Asokan, L. Derita, P. Christopher, Using probe molecule FTIR spectroscopy to identify and characterize Pt - group metal based single atom catalysts, Chinese J. Catal. 38 (2017) 1473–1480. https://doi.org/10.1016/S1872-2067(17)62882-1.
[37] C. Asokan, M. Xu, S. Dai, X. Pan, P. Christopher, Synthesis of Atomically Dispersed Rh Catalysts on Oxide Supports via Strong Electrostatic Adsorption and Characterization by Cryogenic Infrared Spectroscopy, J. Phys. Chem. C. (2022). https://doi.org/10.1021/ACS.JPCC.2C05426.
[38] R.R. Cavanagh, J.T. Yates, Site distribution studies of Rh supported on Al2O3 - An infrared study of chemisorbed CO, J. Chem. Phys. (1981). https://doi.org/10.1063/1.441544.
[39] S. Lee, A. Patra, P. Christopher, D.G. Vlachos, S. Caratzoulas, Theoretical study of ethylene hydroformylation on atomically dispersed Rh/Al2O3 catalysts: Reaction mechanism and influence of ReOx promoter, ACS Catal. (2021) 9506–9518. https://doi.org/10.1021/acscatal.1c00705.
[40] Y. Tang, C. Asokan, M. Xu, G.W. Graham, X. Pan, P. Christopher, J. Li, P. Sautet, Rh single atoms on TiO2 dynamically respond to reaction conditions by adapting their site, Nat. Commun. 10 (2019) 1–10. https://doi.org/10.1038/s41467-019-12461-6.
[41] L. DeRita, S. Dai, K. Lopez-Zepeda, N. Pham, G.W. Graham, X. Pan, P. Christopher, Catalyst Architecture for Stable Single Atom Dispersion Enables Site-Specific Spectroscopic and Reactivity Measurements of CO Adsorbed to Pt Atoms, Oxidized Pt Clusters, and Metallic Pt Clusters on TiO2, J. Am. Chem. Soc. 139 (2017) 14150–14165. https://doi.org/10.1021/jacs.7b07093.
[42] J. Zhang, C. Asokan, G. Zakem, P. Christopher, J.W. Medlin, Enhancing Sintering

Resistance of Atomically Dispersed Catalysts in Reducing Environments with Organic Monolayers, Green Energy Environ. (2021). https://doi.org/10.1016/j.gee.2021.01.022.
[43] J. Resasco, L. Derita, S. Dai, J.P. Chada, M. Xu, X. Yan, J. Finzel, S. Hanukovich, A.S. Hoffman, G.W. Graham, S.R. Bare, X. Pan, P. Christopher, Uniformity Is Key in Defining Structure-Function Relationships for Atomically Dispersed Metal Catalysts: The Case of Pt/CeO2, J. Am. Chem. Soc. 142 (2020) 169–184. https://doi.org/10.1021/jacs.9b09156.
[44] J. Zhang, L.D. Ellis, B. Wang, M.J. Dzara, C. Sievers, S. Pylypenko, E. Nikolla, J.W. Medlin, Control of interfacial acid–metal catalysis with organic monolayers, Nat. Catal. 1 (2018). https://doi.org/10.1038/s41929-017-0019-8.
[45] S. Lwin, Y. Li, A.I. Frenkel, I.E. Wachs, Nature of WOx Sites on SiO2 and Their Molecular Structure-Reactivity/Selectivity Relationships for Propylene Metathesis, ACS Catal. 6 (2016) 3061–3071. https://doi.org/10.1021/acscatal.6b00389.
[46] Y. Izumi, K. Asakura, Y. Iwasawa, Promoting effects of Se on Rh/ZrO2 catalysis for ethene hydroformylation, J. Catal. (1991). https://doi.org/10.1016/0021-9517(91)90188-A.
[47] A. Suzuki, Y. Inada, A. Yamaguchi, T. Chihara, M. Yuasa, M. Nomura, Y. Iwasawa, Time Scale and Elementary Steps of CO-Induced Disintegration of Surface Rhodium Clusters, Angew. Chemie - Int. Ed. 115 (2003) 4943–4947. https://doi.org/10.1002/anie.200352318.
[48] P. Serna, B.C. Gates, Zeolite- and MgO-supported rhodium complexes and rhodium clusters: Tuning catalytic properties to control carbon-carbon vs. carbon-hydrogen bond formation reactions of ethene in the presence of H2, J. Catal. (2013). https://doi.org/10.1016/j.jcat.2013.07.005.
[49] M. Babucci, A.S. Hoffman, L.M. Debefve, S.F. Kurtoglu, S.R. Bare, B.C. Gates, A. Uzun, Unraveling the individual influences of supports and ionic liquid coatings on the catalytic properties of supported iridium complexes and iridium clusters, J. Catal. 387 (2020) 186–195. https://doi.org/10.1016/j.jcat.2020.04.022.
[50] P. Hollins, The Influence of Dipole Coupling on the Infrared Spectra of Adsorbed Species and its Significance for the Interpretation of Transmission Spectra from Supported Metal Catalysts, Http://Dx.Doi.Org/10.1177/026361748500200304. 2 (2016) 177–193. https://doi.org/10.1177/026361748500200304.
[51] J. Sirita, S. Phanichphant, F.C. Meunier, Quantitative analysis of adsorbate concentrations by diffuse reflectance FT-IR, Anal. Chem. 79 (2007) 3912–3918. https://doi.org/10.1021/AC0702802/ASSET/IMAGES/LARGE/AC0702802F00013.JPEG.
[52] M.W. Balakos, S.S.C. Chuang, Dynamic and LHHW kinetic analysis of heterogeneous catalytic hydroformylation, J. Catal. 151 (1995) 266–278. https://doi.org/10.1006/jcat.1995.1027.
[53] M. Ichikawa, A.J. Lang, D.F. Shriver, W.M.H. Sachtler, Selective hydroformylation of ethylene on rhodium-zinc-silica. An apparent example of site isolation of rhodium and Lewis acid-promoted carbonyl insertion, J. Am. Chem. Soc. 107 (2005) 7216–7218. https://doi.org/10.1021/ja00310a098.
[54] E.A. Wovchko, J.T. Yates, Chemical bond activation on surface sites generated photochemically from RhI(CO)2 species, Langmuir. 15 (1999) 3506–3520.

https://doi.org/10.1021/la9810197.
[55] D.C. Calabro, J.C. Vartuli, J.G. Santiesteban, The characterization of tungsten-oxide-modified zirconia supports for dual functional catalysis, Top. Catal. 18 (2002) 231–242. https://doi.org/10.1023/A:1013890606038.
[56] X. Wan, I. Lieberman, A. Asyuda, S. Resch, H. Seim, P. Kirsch, M. Zharnikov, Thermal Stability of Phosphonic Acid Self-Assembled Monolayers on Alumina Substrates, J. Phys. Chem. C. 124 (2020) 2531–2542. https://doi.org/10.1021/acs.jpcc.9b10628.

Chapter 6: Conclusion and Continued Work

6.1 CONCLUSION

Significant efforts have been made to modify atomically dispersed catalysts electronically via changes in support or promoters to alter active site electronic properties, and subsequently enthalpic reaction barriers. While these modifications are impactful, they ignore the role of active site mobility in the reactivity of these catalysts, which may influence entropic reaction barriers.

Our work demonstrates changes in the activation entropies for CO desorption, and subsequently ethylene hydroformylation on atomically dispersed $Rh(CO)_2$ catalysts that are attributed to changes in the mobility of the $Rh(CO)_2$ active site on the Al_2O_3 support. The mobility of $Rh(CO)_2$ was altered by modifying the Al_2O_3 support around atomically dispersed Rh with straight chain alkylphosphonic acid self-assembled monolayers, such that the mobility of the $Rh(CO)_2$ was decreased, subsequently lowering entropic barriers for CO desorption and ethylene hydroformylation. This resulted in lower temperature desorption of CO, and increased rates and selectivities towards propanal formation. Additionally, the extent by which $Rh(CO)_2$ mobility was modified was observed to change with the length of the phosphonic acid tail, in which longer tails were better able to restrict the mobility of $Rh(CO)_2$. This behavior was attributed to intermolecular interactions between PA tails increasing the rigidity of longer tail PAs, better restricting $Rh(CO)_2$ mobility.

Despite the improvements in activity and selectivity, the productivity of atomically dispersed catalysts is often too low for industrial viability due to the low metal loadings required to stabilize atomic dispersion under reaction conditions. As such we also explored methodologies by which we could increase the loading of Rh on Al_2O_3 while maintaining atomic dispersion. Modifications to existing syntheses, changes in support morphology,

gentle and dispersive pretreatments, and modifications with phosphonic acids were all used to maintain atomic dispersion, and significantly greater (~80x) loadings of atomically dispersed Rh was synthesized and characterized via CO probe molecule Fourier-Transform infrared spectroscopy and ethylene hydroformylation reactivity. Broadly, these studies establish the relevance of mobility in supported atomically dispersed species, methodologies by which to modify mobility to decrease entropic reaction barriers and subsequently reaction rates, and methodologies by which to improve the density of atomically dispersed active sites to increase the productivity of atomically dispersed catalysts.

6.2 CONTINUED WORK

6.2.1 Further Studies on Active Site Mobility

The conclusions in this thesis rely on inferences from kinetic data, but there are aspects of these systems that cannot be examined from kinetic data alone due to the complexity of the SAMs. As such, more evidence of the differences in mobility of $Rh(CO)_2$ under different confinements than those provided by SAMs would help to support the conclusions from this work. One system that might merit further study is $Rh/Re/Al_2O_3$, in which atomically dispersed $Rh\text{-}ReO_x$ pairs were formed, and improvements in EHF activity were observed.[1] Changes in activity were primarily attributed to differences in the electronic density of $Rh(CO)_2$ due to its proximity to ReO_x, as evidenced by shifts in $Rh(CO)_2$ stretch positions and decreases in CO desorption temperatures, but changes in EHF energetic barriers were not observed. This suggests that the changes in activity are due to changes in the entropic barriers for EHF, but this was not examined in this work. Performing an analysis of both the energetic and entropic barriers for both EHF and CO desorption may

yield similar results as to those observed in Chapters 3 and 4, further supporting that active site mobility is relevant to the reactivity of Rh/Al_2O_3.

6.2.2 Understanding Dynamic SAM Behavior

Another aspect of this system that could use additional examinations is the behavior of the PA SAM, as our observations in this work do little to tell us about the dynamic behavior of the SAMs. As such, molecular dynamics simulations may help us to better understand the structure of SAMs under reaction conditions. The exact mechanism by which gas phase species can access the catalyst surface through the SAMs is unknown. We can imagine two possibilities: (i) mobility of individual PA tails creates spaces for gas phase species to access the surface, (ii) active $Rh(CO)_2$ sites exist at domain boundaries between SAMs, such that they are always accessible, but still confined. The former case seems unlikely, as the interaction strength of alkyl tails has been estimated at ~6-7 kJ/mol per CH_2 pair.[2] In this case, individual tails of longer PAs would have interaction strengths on the order of 80 kJ/mol, which would likely affect apparent kinetic barriers if rearrangement was necessary for the reaction to proceed. The latter case seems likely, as we demonstrated in this work that $Rh(CO)_2$ concentrations are roughly constant between 100 and 170°C, suggesting that rearrangement of the SAM to allow access of additional COs is unlikely.

6.2.3 C6+ Olefin Hydroformylation

While propylene is the highest volume feedstock for hydroformylation, it would benefit less from a heterogeneous catalyst than larger olefin feedstocks. This is because propylene hydroformylation reactors are designed such that the homogeneous catalyst never exits the reactor, such that the homogeneous catalyst does not require additional separations. [3,4] As such, heterogeneous catalysts are best suited for replacing the Co catalysts used for

hydroformylation of larger olefins, as more significant separations are required. Additionally, homogeneous Co catalysts require higher temperatures and pressures than Rh catalysts.[5] As such, implementing a heterogeneous Rh catalyst would be advantageous for reducing separations and conversion costs.

While the work presented in this document does not demonstrate regioselectivity, it did demonstrate steric hindrance to $Rh(CO)_2$ mobility due to PA SAMs, suggesting that sufficiently large adsorbates may be restricted in access or orientation. If these olefins selectively adsorb on the terminal carbon of the double bond, then regioselectivity may be possible. Unfortunately, hydroformylation of larger olefins typically exhibit lower turnover frequencies than hydroformylation of ethylene.[6] This means that the improved reactor productivity presented in Chapter 5 may be necessary.

These larger olefin hydroformylation reactions are exclusively performed in the liquid phase, such that the leaching of both Rh and the PAs might be a concern. The choice of solvent will also be important to determining the structure of SAMs, as PA ligands may interact with solvent molecules. The choice of solvent can have significant effects on the stability, activity, and selectivity of the catalyst. Fortunately, several works have demonstrated significant impacts on catalyst reactivity due to solvent effects, such that these catalysts in the liquid phase may perform better than in the gas phase.[7]

6.2.4 Experimental and Computational Studies of DRIFTS Sampling Depth

Many of the inferences made in this thesis rely on kinetic data from TPD experiments in which the relative surface coverage of species was probed using DRIFTS. The accuracy of kinetic data extracted this way is dependent on a limited probe depth (<15μm) to assert that readsorption is not significant. While this thesis does present an argument for why the

penetration depth should be much shorter than that for nanometer scale particles, experimental and computational evidence would be useful for obtaining more precise estimates of penetration depth, along with developing guidelines for estimating penetration depths for different materials.

Experimental verification might be achieved by placing thin (<15 μm) layers of support particles above a catalyst and comparing how the absorption of associated catalyst stretches decreases with increased layer thickness above catalyst. The formation of these thin films may be synthetically difficult, and likely requires the use of catalyst pellets, rather than a packed catalyst bed. It will be important that the catalyst is dilute to ensure that there are minimal changes to the optical properties between the bare support and catalyst, as changes in refractive indices will promote reflections. From these experiments, one could examine the absorbance as a function of film thickness, allowing for determination the depth of probing, but also the contribution of the catalyst to the absorbance as a function of depth. Even if DRIFTS is probing sufficiently deeply that readsorption may be a concern, if those depths only contribute to a small fraction of the examined signal, then they will not have a major effect on the extracted TPD data.

Computational simulations of light interacting with a bed of particles might provide more first-principles insight onto how light interacts with the initial surface, and subsequent interactions inside of the bed. This is especially so for larger particles, in which the behavior of light will alter as a function particle size. A simulation of light behavior for different sized particles between the Rayleigh scattering and Mie scattering regime may provide insight into the penetration depth. As of now, it is difficult to predict the behavior of light in this transitionary range.

6.3 REFERENCES

[1] I. Ro, M. Xu, G.W. Graham, X. Pan, P. Christopher, Synthesis of Heteroatom Rh-ReOx Atomically Dispersed Species on Al2O3 and Their Tunable Catalytic Reactivity in Ethylene Hydroformylation, ACS Catal. 9 (2019) 10899–10912. https://doi.org/10.1021/acscatal.9b02111.

[2] D.J. Lavrich, S.M. Wetterer, S.L. Bernasek, G. Scoles, Physisorption and chemisorption of alkanethiols and alkyl sulfides on Au(111), J. Phys. Chem. B. 102 (1998) 3456–3465. https://doi.org/10.1021/JP980047V/ASSET/IMAGES/LARGE/JP980047VF00010.JPEG.

[3] F.J. Smith, NEW TECHNOLOGY FOR INDUSTRIAL HYDROFORMYLATION., Platin. Met. Rev. 19 (1975) 93–95. https://www.ingentaconnect.com/content/matthey/pmr/1975/00000019/00000003/art00004 (accessed July 17, 2019).

[4] R. Tudor, M. Ashley, Enhancement of industrial hydroformylation processes by the adoption of rhodium-based catalyst: Part II, Platin. Met. Rev. 51 (2007) 164–171. https://doi.org/10.1595/147106707X238211.

[5] J. Falbe, New Syntheses with Carbon Monoxide, Springer Berlin Heidelberg, Berlin, Heidelberg, 1980. https://doi.org/10.1007/978-3-642-67452-5.

[6] Z. Mao, Z. Xie, J.G. Chen, Comparison of Heterogeneous Hydroformylation of Ethylene and Propylene over RhCo3/MCM-41 Catalysts, ACS Catal. 11 (2021) 14575–14585. https://doi.org/10.1021/acscatal.1c04359.

[7] R. Franke, D. Selent, A. Börner, Applied hydroformylation, Chem. Rev. 112 (2012) 5675–5732.